

DESIGN OF DIAPHRAGM DIELECTRIC ELASTOMER ACTUATORS (DEAs) AND EXPERIMENTAL CHARACTERIZATION TECHNIQUES

Dissertation

zur Erlangung des Grades
des Doktors der Ingenieurwissenschaften (Dr.-Ing.)
der Naturwissenschaftlich-Technischen Fakultät
der Universität des Saarlandes

von

Micah Hodgins, M.Sc.

Saarbrücken

2016

Tag des Kolloquiums: 05.12.2016

Dekan: Univ.-Prof. Dr. Guido Kickelbick
Mitglieder des
Prüfungsausschusses: Univ.-Prof. Dr.-Ing. Stefan Seelecke
Univ.-Prof. Dr.-Ing. Stefan Diebels
Univ.-Prof. Dr. Andreas Schütze
Dr. Felix Felgner

EIDESSTATTLICHE VERSICHERUNG

Hiermit versichere ich an Eides statt, dass ich die vorliegende Arbeit selbstständig und ohne Benutzung anderer als der angegebenen Hilfsmittel angefertigt habe. Die aus anderen Quellen oder indirekt übernommenen Daten und Konzepte sind unter Angabe der Quelle gekennzeichnet. Die Arbeit wurde bisher weder im In- noch im Ausland in gleicher oder ähnlicher Form in einem Verfahren zur Erlangung eines akademischen Grades vorgelegt.

Saarbrücken, Dezember 2016

Micah Hodgins

ZUSAMMENFASSUNG

Dielektrische Elastomer (DE) Wandler stellen eine neue Technologie dar, die viele Vorteile im Bereich der Aktorik sowie Sensorik bietet. Diese Arbeit fokussiert auf DE Aktoren (DEAs), welche durch hohe Dehnungen und Reaktionsgeschwindigkeiten während der Auslenkung charakterisiert werden.

Eine spezielle Art der DEAs, die Diaphragma DEAs, sind aus der Ebene heraus betriebene Membrane. Um dabei einen grossen Hub erzeugen zu können, muss die Membran mit einem flexiblen Vorspannungsmechanismus ausgerüstet werden. Beide Teile bilden das Aktorsystem.

Im ersten Teil dieser Arbeit wird die Funktion von DEA Aktorsystemen und der Einfluss verschiedener Vorspannungsmechanismen untersucht. Unterschiedliche Mechanismen werden vorgestellt und experimentell verglichen. Die besten Ergebnisse konnten mit dem Einsatz einer bistabilen Feder (NBS, Negative-rate Biased Spring) erzielt werden

Der zweite Teil dieser Arbeit präsentiert zwei Testgeräte, die zur elektromechanischen Charakterisierung von DE Membranen entwickelt wurden. Eines ist ein steuerbarer elektromagnetischer Motor, der DEAs unter verschiedenen Lastbedingungen charakterisieren und testen kann. Das zweite Gerät wurde entwickelt, um DEs unter wiederholbaren Bedingungen in einem planaren Zugversuch zu charakterisieren. Dabei wird ein Membrandickenprofil kontinuierlich für jede Auslenkung aufgenommen. Der Tester ermöglicht einen Vergleich der wesentlichen Leistungsparameter und damit eine Verbesserung zukünftiger DEA Anwendungen.

ABSTRACT

Dielectric elastomer (DE) transducers are a new technology offering many benefits for actuation and sensing devices. This work focuses on DE actuators (or DEAs) which have been shown to exhibit high-strain and high-speed characteristics.

Diaphragm DEAs are a type of membrane DEA configured to operate out-of-plane. However, to produce reasonable stroke, membrane DEAs should be pre-stretched with a compliant mechanism. Therefore, the actuator system consists of the DEA and the necessary compliant mechanism.

The first focus of this work to investigate how DEA membranes operate as a system and how they can be improved by designing compliant mechanisms which, when coupled with the DEA, give higher performance. Several compliant mechanisms are presented and experimentally compared. A bistable mechanism called a negative-rate bias spring (NBS) is shown to greatly increase the output of the DEA.

The second part of this work presents two test devices and techniques for electromechanically characterizing DE membranes. One is a programmable electromagnetic motor to characterize diaphragm DEAs and test them under different loading conditions. The second device is designed to repeatably characterize planar DEs through a tensile test. The work includes a novel technique for obtaining a membrane thickness profile while stretching and/or actuating the DEA. The tester allows for a comparison of material performance parameters which aid in more informed design recommendations for future DEAs.

DEDICATION

To my beloved wife, Julie

BIOGRAPHY

Micah William Hodgins was born in South Carolina on April 6, 1986. He graduated from the University of South Carolina-Columbia in May 2008 with a BS in Mechanical Engineering and from North Carolina State University December 2010 with a MS in Mechanical Engineering.

ACKNOWLEDGEMENTS

First and foremost, I would like to thank my personal Lord and Savior Jesus Christ for His goodness and for His care throughout my years in Saarbrücken, Germany. I also would like to thank my advisor Dr. Stefan Seelecke for giving me this opportunity to do my doctoral research in Germany and for his patience, guidance and backing throughout my time in his lab. I also would like to thank Alex York and Gianluca Rizzello for our discussions and their valuable collaboration.

I would like to express my appreciation to my committee members for supporting me and taking the time to be on my advisory committee.

To my wife, family and close friends I am grateful for your support, encouragement and understanding through the ups and downs of life in graduate school.

Parts of this work have been published in the following papers:

Peer-reviewed journal papers:

M. Hodgins and S. Seelecke, "Systematic experimental study of pure shear type dielectric elastomer membranes with different electrode and film thicknesses," *Smart Mater. Struct.*, vol. 25, no. 9, p. 095001, Aug. 2016. doi:10.1088/0964-1726/25/9/095001

M. Hodgins, A. York, and S. Seelecke, "Systematic experimental characterization of dielectric elastomer membranes using a custom-built tensile test rig," *Journal of Intelligent Material Systems and Structures*, 2016, accepted, pp. 1-23.

M. Hodgins, G. Rizzello, A. York, D. Naso, and S. Seelecke, "A smart experimental technique for the optimization of dielectric elastomer actuator (DEA) systems," *Smart Mater. Struct.*, vol. 24, no. 9, p. 094002, Sep. 2015. doi:10.1088/0964-1726/24/9/094002

G. Rizzello, **M. Hodgins**, D. Naso, A. York, and S. Seelecke, "Modeling of the effects of the electrical dynamics on the electromechanical response of a DEAP circular actuator with a mass-spring load," *Smart Mater. Struct.*, vol. 24, no. 9, p. 094003, Sep. 2015. doi:10.1088/0964-1726/24/9/094003

G. Rizzello, **M. Hodgins**, D. Naso, A. York, and S. Seelecke, "Dynamic Modeling and Experimental Validation of an Annular Dielectric Elastomer Actuator With a Biasing Mass," *J. Vib. Acoust.*, vol. 137, no. 1, p. 011014, Feb. 2015. doi: 10.1115/1.4028456

M. Hodgins, G. Rizzello, D. Naso, A. York, and S. Seelecke, "An electro-mechanically coupled model for the dynamic behavior of a dielectric electro-active polymer actuator," *Smart Mater. Struct.*, vol. 23, no. 10, p. 104006, Oct. 2014. doi:10.1088/0964-1726/23/10/104006

M. Hodgins, A. York, and S. Seelecke, "Experimental comparison of bias elements for out-of-plane DEAP actuator system," *Smart Mater. Struct.*, vol. 22, no. 9, p. 094016, Sep. 2013. doi:10.1088/0964-1726/22/9/094016

M. Hodgins, A York, and S. Seelecke, "Modeling and experimental validation of a bi-stable out-of-plane DEAP actuator system," *Smart Mater. Struct.*, vol. 20, no. 9, p. 094012, Sep. 2011. doi:10.1088/0964-1726/20/9/094012

International conference proceedings:

B. Fasolt, **M. Hodgins**, and S. Seelecke, "Characterization of screen-printed electrodes for Dielectric Elastomer (DE) membranes: influence of screen dimensions and electrode thickness on actuator performance," in Proc. SPIE 9798, Electroactive Polymer Actuators and Devices (EAPAD), 2016, p. 97983E.

M. Hodgins, A. York, and S. Seelecke, "Systematic experimental investigation of Dielectric electroactive polymers using a custom-built uniaxial tensile test rig," in ASME 2015 Conference on Smart Materials, Adaptive Structures and Intelligent Systems (SMASIS2015), pp. 1-8, September 21-23, 2015, Colorado Springs, Colorado, USA.

S. Hau, **M. Hodgins**, G. Rizzello, A. York, S. Seelecke: "Entwicklung einer durch dielektrische elektroaktive Polymeraktoren (DEAP) angetriebenen Hochgeschwindigkeitsmikropositionierbühne", VDI Fachtagung Mechatronik 2015, Dortmund, Germany, March 12-13, 2015.

M. Hodgins, G. Rizzello, A. York, and S. Seelecke, "Experimental Analysis and Validation of a Circular Dielectric Electroactive Polymer Actuator Operating Against Various Loading Conditions," in ASME 2014 Conference on Smart Materials, Adaptive Structures and Intelligent Systems (SMASIS2014), pp. 1-8, September 8-10, 2014, Newport, Rhode Island, USA.

G. Rizzello, **M. Hodgins**, A. York, and S. Seelecke, "Dynamic Electromechanical Modeling of a Spring-Biased Dielectric Electroactive Polymer Actuator System," in ASME 2014 Conference on Smart Materials, Adaptive Structures and Intelligent Systems (SMASIS2014), pp. 1-10, September 8-10, 2014 Newport, Rhode Island, USA.

M. Hodgins, G. Rizzello, A. York, D. Naso, S. Seelecke: "Modeling of Actuator System Based on a Dielectric Electro-active Polymer Circular Membrane when Operating Against a Constant Loading Force", ACTUATOR 2014, 14th International Conference on New Actuators & 8th Exhibition on Smart Actuators and Drive Systems, pp. 1-4, June 23-25, Bremen, Germany.

M. Hodgins, G. Rizzello, A. York, and S. Seelecke, "High-Frequency Dynamic Model of a Pre-Loaded Circular Dielectric Electro-active Polymer Actuator," in ASME 2013 Conference on Smart Materials, Adaptive Structures and Intelligent Systems (SMASIS2013), pp. 1-10, September 16-18, 2013, Snowbird, Utah, USA.

M. Hodgins, A. York, and S. Seelecke, "Experimental Investigation of a Loaded Circular Dielectric Electro-Active Polymer Actuator Coupled to Negative-Rate bias Spring Mechanism," in ASME 2012 Conference on Smart Materials, Adaptive Structures and Intelligent Systems (SMASIS2012), pp. 1-6. September 19-21, 2012. Stone Mountain, Georgia, USA.

M. Hodgins, A. York, and S. Seelecke, "Improved Force-Displacement of a Dielectric Electroactive Polymer Actuator using a Negative- Rate Bias Spring Mechanism," in ACTUATOR 2012, 13th International Conference on New Actuators & 7th Exhibition on Smart Actuators and Drive Systems, pp. 1-4, June 18-20, Bremen, Germany.

M. Hodgins and S. Seelecke, "Experimental Analysis of Biasing Elements for Dielectric Electro-Active Polymers," in Proc. SPIE 7976, Electroactive Polymer Actuators and Devices (EAPAD) 2011, 797639 (29 March 2011).

A. Deodhar, A. York, **M. Hodgins**, and S. Seelecke, "Finite Element modeling of electromechanical behavior of a dielectric Electroactive Polymer Actuator," in Proc. SPIE 7978, Behavior and Mechanics of Multifunctional Materials and Composites 2011, 79780D (28 April 2011).

Poster presentations:

B. Fasolt, **M. Hodgins**, and S. Seelecke, "Characterization of screen-printed electrodes for Dielectric Elastomer (DE) membranes: influence of screen dimensions and electrode thickness on actuator performance," at SPIE, Electroactive Polymer Actuators and Devices (EAPAD) 2016, April, Las Vegas, NV, USA.

M. Hodgins, A. York, and S. Seelecke, "Systematic experimental investigation of dielectric electroactive polymers using a custom-built uniaxial tensile-test rig," in EuroEAP 2015, June, Tallinn, Estonia.

B. Fasolt, **M. Hodgins**, A. York, and S. Seelecke, "Screen Printing Electrodes on Silicone Film: Influence of Screen Dimensions and Multiple-Layer-Prints on Resistance," in EuroEAP 2015, June, Tallinn, Estonia.

M. Hodgins, S. Hau, G. Rizzello, A. York, S. Seelecke, and F. Stage, "Design, Fabrication, Testing and Control of a High Speed Micro-Positioning Stage Driven by Dielectric Electro-Active Polymer (DEAP) Actuators," in EuroEAP 2014, June, Linköping, Sweden.

M. Hodgins, S. Hau, A. York, and S. Seelecke, "Improving the stroke of dielectric electro-active polymer actuators using a non-linear spring," in EuroEAP 2013, Dübendorf (Zürich), Switzerland.

* Underlined name denotes role as presenter.

TABLE OF CONTENTS

Table of Contents.....	i
List of Tables	iv
List of Figures	v
Chapter 1 Introduction.....	1
1.1 Motivation.....	2
1.2 Background and Literature	2
1.2.1 Challenges.....	5
1.3 Research Objective and Thesis Structure.....	6
Part 1: Design of Dielectric Elastomer Actuators.....	8
Chapter 2 Fundamentals of Dielectric Elastomer Actuators (DEA).....	9
2.1 Electro-Mechanical Behavior of DE Actuators	9
2.2 Configurations.....	10
2.2.1 Stacked Actuator.....	11
2.2.2 Planar Actuator	12
2.2.3 Roll/Tube Actuators.....	13
2.2.4 Out-of-plane Actuators	14
2.3 Elastomer Materials	15
2.4 Electrode Materials	16
Chapter 3 DEA Design and Stroke Analysis.....	17
3.1 Membrane DEA Operation and Stroke.....	17
3.2 Experimental comparison of bias elements.....	20
3.2.1 Introduction.....	20
3.2.2 Bias Elements.....	21
3.2.3 Experiments and Results	22
3.2.4 Stroke Analysis.....	26
3.2.5 Summary	30
3.3 Conclusions.....	30
Chapter 4 Negative-rate Bias Spring Mechanism	31
4.1 Introduction and Motivation.....	31
4.2 Design and Fabrication	32
4.3 Mechanism Coupled to DEA	35
4.3.1 Approach.....	35
4.3.2 Background.....	35
4.3.3 Stroke Analysis.....	37
4.4 Results and Experimental Validation	42
4.4.1 NBS + Mech. Stop.....	42
4.4.2 NBS + Linear spring.....	48
4.5 Conclusions.....	54

Chapter 5 DEA Prototypes.....	55
5.1 Design	55
5.2 Experimental Investigation of Actuator Force	57
5.2.1 Results.....	59
5.3 Modeling.....	63
5.4 Discussion and Outlook	65
Part 2: Advanced Experimental Techniques for Characterization of DEAs.....	68
Chapter 6 Smart Experimental Technique to Optimize Diaphragm DEAs	69
6.1 Introduction	69
6.2 Design of a Programmable Electromagnetic Motor	70
6.2.1 Linear motor characterization	70
6.2.2 Control implementation	72
6.3 Pre-loaded DEA Experiments.....	73
6.3.1 Test Setup	73
6.3.2 DEA Characterization.....	74
6.3.3 Programmable loads	75
6.4 Results and Discussion	76
6.5 Further Discussion	81
6.6 Conclusion.....	82
Chapter 7 DE Membrane Characterization Suite	85
7.1 Introduction	85
7.2 Background and Motivation.....	85
7.3 Specimen Design/Fabrication, Clamps and Test Rig	87
7.3.1 Specimen Design/Fabrication	88
7.3.2 Clamp Design	91
7.3.3 Devices and Instrumentation.....	92
7.4 Experimental Results	95
7.4.1 Thickness profile test	96
7.4.2 Force vs. displacement test	98
7.4.3 Isometric tests	101
7.4.4 Isotonic tests	102
7.5 Conclusions	104
Chapter 8 Discussion and Outlook.....	105
8.1 Summary of Work.....	105
8.2 Future work in Designing membrane DEAs.....	106
8.3 Further work in Experimental Techniques.....	107
Appendices	110
Appendix A: Miniaturization through Inclined Beam Flexures.....	111
Appendix B: Magnetic Bias Force	115
Bibliography.....	119

Curriculum Vitae	130
-------------------------------	------------

LIST OF TABLES

Table 4.1: Stroke landscapes for different hanging mass loads. Stroke for different hanging mass levels (0-100grams) when using linear spring $k=0.24\text{N/mm}$	52
Table 5.1: NBS and LS parameters for three stability cases	59

LIST OF FIGURES

Figure 1.1: DE or DEA Google Scholar search results.....	3
Figure 2.1: Operating principle of DE transducers.....	9
Figure 2.2: Operating principle of a DEA	10
Figure 2.3: DE membranes with various boundary constraints	10
Figure 2.4: Stacked actuator type	11
Figure 2.5: Stacked actuators seen in literature.....	12
Figure 2.6: Planar actuator type with multiple layers.....	12
Figure 2.7: Planar actuators seen in literature	13
Figure 2.8: Roll actuator with coil spring core	13
Figure 2.9: Photos of Roll/Tube actuators seen in literature.....	14
Figure 2.10: Photos of out-of-plane actuators.....	14
Figure 2.11: Diaphragm out-of-plane actuator.....	15
Figure 3.1: Cross sectional sketch of circular/diaphragm DEA	18
Figure 3.2: Force vs. controlled out-of-plane displacement	18
Figure 3.3: Stroke development of a pre-loaded DEA	19
Figure 3.4: Diaphragm Membrane DEA workable region	19
Figure 3.5: Scaling force output by stacking diaphragm DEAs.....	20
Figure 3.6: Photo of DEA with different inner disk diameters.	20
Figure 3.7: Three biasing mechanisms	21
Figure 3.8: Force vs. controlled out-of-plane displacement of NBS	22
Figure 3.9: Hanging mass test setup	23
Figure 3.10: Stroke results for each hanging mass.....	23
Figure 3.11: Positive-rate spring (PBS) test setup	24
Figure 3.12: Stroke results for each PBS pre-deflection.....	24
Figure 3.13: Negative-rate bias spring (NBS) test setup	25
Figure 3.14: Bistable stroke results.....	25
Figure 3.15: Comparison of Stroke vs. inactivated DEA Pre-deflection.....	26
Figure 3.16: Stroke vs. DEA pre-deflection.....	26
Figure 3.17: Displacement stroke for two bias elements	27
Figure 3.18: Sketch of small stroke possible using NBS without mechanical stop	28
Figure 3.19: Stabilized NBS and DEA by mechanical stop.....	28
Figure 3.20: DEA-NBS stroke behavior for one cycle.....	29
Figure 4.1: Force and stored potential energy of a typical NBS.....	31
Figure 4.2: Examples of compliant mechanisms in literature	32
Figure 4.3 Bistable mechanisms and the force-displacement.....	33
Figure 4.4: X-shaped bistable mechanism.....	33
Figure 4.5: NBS parameter variation	34
Figure 4.8: NBS energy landscape	37
Figure 4.9: Combination of NBS and linear force	38

Figure 4.10: Transformation of energy landscape	38
Figure 4.11: Influence of linear spring on NBS behavior.	39
Figure 4.12: Sketch of tuned NBS+LS mechanism with DEA	40
Figure 4.13: Sketch of loaded DEA.....	40
Figure 4.14: DEA actuator force.....	41
Figure 4.15: Actuator force produced by linear spring	41
Figure 4.16: Actuator force produced by NBS+LS mechanism	42
Figure 4.17: NBS with mechanical stop test setup	43
Figure 4.18: Photo of test rig with mass attached.....	44
Figure 4.19: Test result of NBS without mass	44
Figure 4.20: Test result of NBS with mass	45
Figure 4.21: Comparison of stroke output with mass and without mass	45
Figure 4.22: Stroke development when adding mass (with mech. stop)	46
Figure 4.23: Effect of mass on actuator	47
Figure 4.24: Test results for NBS+LS bias element	48
Figure 4.25: DEA biased by combination of NBS and linear spring.....	49
Figure 4.26: NBS with linear spring test setup	49
Figure 4.27: Photos of setup	50
Figure 4.28: NBS + Linear spring stroke results without mass added.....	51
Figure 4.29: NBS + Linear spring stroke results with mass added	51
Figure 4.30: 3D surface plots of stroke.....	53
Figure 4.31: Stroke and work output	53
Figure 4.32: DEA performing work against increasing loads	54
Figure 5.1: DEA demonstrator design	55
Figure 5.2: Views for demonstrator assembly	56
Figure 5.3: Photos of various sized DEA demonstrators.	56
Figure 5.4: DEA demonstrator	57
Figure 5.5: Actuation force test setup	57
Figure 5.6: Photo of tested elements	58
Figure 5.7: Force response of DEA	58
Figure 5.8: Force response of NBS+LS cases	58
Figure 5.9: Actuation stroke test setup	59
Figure 5.10: Demo results compared	60
Figure 5.11: Comparison of stroke	60
Figure 5.12: Bistable actuator force output,	61
Figure 5.13: Semi-stable actuator force output	62
Figure 5.14: Stable actuator force output.....	63
Figure 5.15: DEA experimental and model results	63
Figure 5.16: NBS model fits.....	64
Figure 5.17: Modeled force and actuator potential energies	64
Figure 5.18: Experimental and model results	65

Figure 5.19: Actuator with linear load.....	65
Figure 6.1: Photo of linear motor	70
Figure 6.2: Motor characterization when blocked	71
Figure 6.3: Motor characterization against spring.....	71
Figure 6.4: Force control implementation.....	73
Figure 6.5: Force control test setup	74
Figure 6.6. DEA Force response to sinusoidal displacement	75
Figure 6.7: Sketch of DEA loaded with an arbitrary linear load.....	75
Figure 6.8: Frequency variation test for DEA at constant force	76
Figure 6.9: Time-resolved response of DEA loaded with a simulated linear spring	77
Figure 6.10: Simulated spring response (F_c^*)	78
Figure 6.11: DEA actuation results for different springs	79
Figure 6.12: Stroke results compared	80
Figure 6.13: Surface plot of stroke data	80
Figure 6.14: Diaphragm DEA geometry	81
Figure 6.15: Actuation strain results.....	81
Figure 6.16: DEA stroke vs. stiffness vs. pre-deflection.....	82
Figure 7.1: Range of DEA specimens the test rig can accommodate	88
Figure 7.2: Screen development	89
Figure 7.3: Electrode application process	89
Figure 7.4: Photo summary of applying reinforcing frame to DE film.....	90
Figure 7.5: Pure-shear specimen assembly	90
Figure 7.6: 3D sketch of clamp design with various sized specimens	91
Figure 7.7: Photos of clamps.....	91
Figure 7.8: Electrode connections in clamps.....	92
Figure 7.9: Planar actuator experimental setup	93
Figure 7.10: Calibrating thickness measurement sensors.....	94
Figure 7.11: Thickness scan of membrane	95
Figure 7.12: View of specimen (with electrodes) in clamps	96
Figure 7.13: Average membrane thickness measurements when un-stretched ($\lambda = 1$)	97
Figure 7.14: Measured thickness profile when stretched	98
Figure 7.15: Time resolved force-displacement results.....	99
Figure 7.16: Force-Elongation plot for sinusoidal displacement	100
Figure 7.17: Measurement of capacitance and resistance change when sinusoidally stretched	100
Figure 7.18: Comparing the blocking force results for.....	101
Figure 7.19: Blocking force measurement results	102
Figure 7.20: Time resolved constant force actuation test results	103
Figure 7.21: Actuation strain vs. Electric field for three isotonic tests	104
Figure A.1: Comparing the actuator length for two bias mechanism designs	111
Figure A.2: Buckling frame design	112
Figure A.3: Inclined NBS test results.....	112

Figure A.4: Solidworks sketch of demonstrator	113
Figure A.5: Photo of inclined NBS demonstrator.....	113
Figure A.6: Photo of inclined NBS demonstrator from rear	113
Figure A.7: Stroke results for iNBS demonstrator for different voltage inputs	114
Figure B.1: Bias mechanism force profiles.	115
Figure B.2: Measuring magnet attraction force	115
Figure B.3: Magnet demo tests and sketch.....	116
Figure B.4: Photos of magnetic bias demonstrator	116
Figure B.5: Sketches of various magnetically biased DEAs.....	117

Chapter 1 INTRODUCTION

This thesis presents the systematic study and development of Dielectric Elastomer (DE) as actuator systems. Dielectric elastomers are a multi-functional material that can serve as actuators and as sensors or generators. They are commonly referred to as dielectric elastomer transducers (DET). DE material can undergo a large change in shape in response to electrical energy, therefore acting as an actuator [1]. It can also transform mechanical energy into electrical energy, acting as a sensor [2]–[4] or generator [5]–[7]. In the realm of actuators, which is the focus of this work, the intended applications for DE actuators (DEAs) are fluidic pumps, valves, micro-positioning stages, robotic end effectors and many more.

DE film actuators can be designed in different configurations. For membrane actuators the film is clamped at the edge. Diaphragm actuators, which are studied here, are a type of membrane actuator. These membrane actuators can generate reasonable stroke in-plane and out-of-plane (with respect to the plane defined by the clamped boundary). The mode and magnitude of actuation depends on the direction and magnitude of the force pre-stretching or pre-deflecting the film membrane. This applied force is what deforms the DE membrane.

In contrast, stacked actuators (see page 11), which are clamped or fixed at the ends, operate in the thickness direction (with respect to the film). These require no pre-deflection or loading mechanism for significant stroke because they contract due to the Maxwell force deforming the stack (see Section 1.2). Therefore, they are less dependent on the external load as are membrane actuators. This distinction is important to note as this work focuses primarily on a type of *membrane actuator*.

Firstly, this research focuses on the design, fabrication, testing and optimization of *diaphragm membrane* DEAs. It is shown that for a well-performing membrane actuator system the choice of the compliant mechanism to bias or pre-load the DEA is highly deterministic in the resulting output. Therefore, this work includes a systematic investigation of various compliant mechanisms which can be used with membrane DEAs. A so-called negative-rate bias spring or bistable spring is studied extensively and its benefits on the DEA performance are shown experimentally and theoretically. Finally, lab-tested actuator prototypes are presented to provide the reader with examples of how such DEAs can be achieved and applied to real-world situations.

Secondly, this research includes an experimental investigation into techniques for characterizing DE membrane behavior. Electro-mechanical characterization tests are performed using two custom-built high-performance DE film testing suites. One is a

programmable electromagnetic motor to characterize diaphragm DEA membranes and to simulate loads. This showed the importance of mechanical loads on membrane actuators. The second setup and test procedure detailed is used to test and compare commercially available elastomer thin films. Actuator strain and force output were measured along with resistance and capacitance. Actuator design parameters such as pre-stretch and electrode thickness were studied. The work details a novel test technique for obtaining a membrane thickness profile while straining and/or actuating the DEA by utilizing dual confocal displacement sensors. The tester allows for comparison of material performance parameters which leads to informed design recommendations for future DEAs.

Overall this work seeks to present and equip the reader with some key principles on how to design, fabricate, test and build a high-performing membrane DEA system to provide the desired output for a given application.

1.1 MOTIVATION

Conventional actuator technologies such as pneumatic motors, linear solenoids and DC-motors are generally well-established, well-understood and marketable in the industries where they are found. Despite this, consumers continue to demand smaller, lighter, faster, quieter, smarter and more efficient products. However, since conventional electromagnetic motors generally have poor efficiencies at small scales (not to mention many parts, difficult assembly, noise and high-friction forces) there is a growing interest in other actuator technologies to save money and gain a technological advantage. Companies are considering the area of unconventional actuator systems or “smart material” technologies to do this. A “smart material” is one that changes one or more of its properties under the influence of external stimuli [8]. There are dozens of smart materials including piezo-ceramics, shape-memory alloys, and magneto rheological fluids which are continually being researched and gradually applied to industrial and commercial solutions [9]–[12].

Dielectric elastomer transducers (DETs), one of these smart materials, have many attractive characteristics. In addition to their overall low cost, DETs demonstrate inherent advantages over conventional transducers which include their high work/energy density, silent operation, form-flexibility and scalability. These traits promise applications which have been impracticable with standard actuator technologies. Such applications, among others, include DEA powered pumps [13]–[17], valves [18]–[20], loudspeakers [21], [22], robots [23]–[25], flapping wing insects [26], [27], variable stiffness devices [28]–[30], optical positioning systems [31]–[34] and micro-positioning stages [35].

1.2 BACKGROUND AND LITERATURE

The actuation effect of electrostatic forces on dielectrics was first reported by Röntgen in 1880 [36] but it was not until the mid-1990s that several researchers began studying the potential of using DEs as actuators. It began primarily with the research performed by Pelrine *et. al.* [1],

[37] at Stanford Research Institute (SRI) International. They were not the first to study the effect of electrostatic forces on soft dielectrics [38] but they were the first to investigate and publish primarily on its potential as an actuator. The findings of these groups and others since have been presented at conferences and published in journals around the world. Research of DEs is now rapidly spreading to research institutions and industrial companies around the world. Figure 1.1 shows internet search results (www.google.com/scholar) per annum for the query “Dielectric elastomer” or “Dielectric elastomer actuator”. It is a clear attestation to the attention the technology is increasingly receiving.

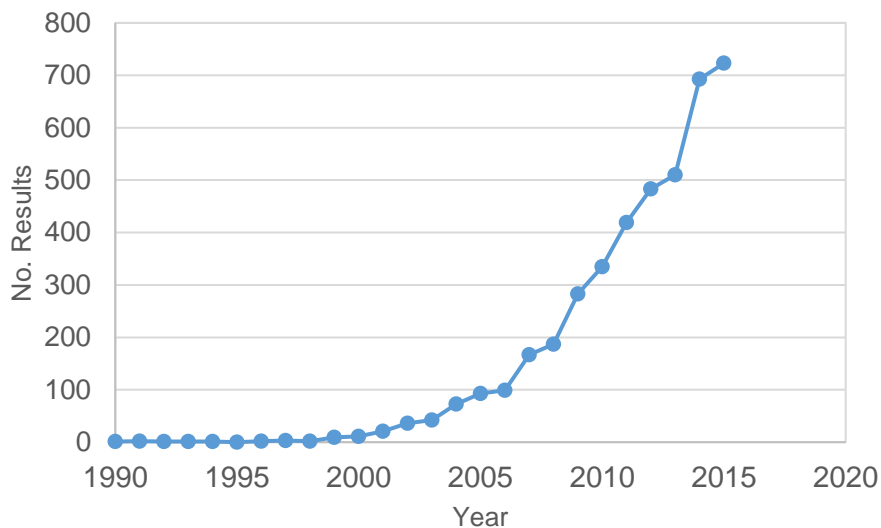


Figure 1.1: DE or DEA Google Scholar search results (per annum)

In the following paragraphs a literature survey is presented and current challenges for DEA technology are discussed.

Pelrine *et. al.* demonstrated the high-strain capability of the several DE materials while presenting actuators in a variety of configurations such as planar, stacks, rolls and tubes [1]. Two years later (in 2000) Pelrine and his colleagues published a landmark paper in *Science*. They demonstrated high actuation strains (>30%), fast response times (<1ms) and high specific energy densities (up to 0.15J/g) of DE actuators when using acrylic and silicone films [37]. These studies and others [39]–[41] led to a scientific and technological leap forward in the field of polymer actuators. Several annual, multi-day conferences in North America (SPIE Smart Structures/NDE, [42]) and in Europe (EuroEAP, [43]) have helped in communicating advancements in DE materials and applications to actuator/sensor technologies. The conference sessions facilitate collaboration between engineers and researchers since there are many active research areas (from better understanding DE materials to fabrication methods, modeling/simulation and improving the overall actuator system performance).

Rubber-like soft-dielectrics (such as natural rubber, polyurethane, acrylic, or silicone elastomers) display a non-linear stress-strain characteristic. As mentioned before they are capable of very high strains (ex. 3M™ VHB 4910 has been shown to endure strains up to 500%

[44]). Much of the initial DEA research used the commercially available “Very High Bonding” 3M tape as the DE. Even to this day some continue to use this material although it has been shown that the acrylic VHB tapes exhibit a much higher viscoelastic behavior than silicone based elastomers [45]. As with most other rubber-like materials, elastomers are viscoelastic. Many groups have proposed constitutive behavior models (several based on Yeoh, Ogden and Gent hyperelastic models) to represent the elastomer non-linear and viscoelastic behavior [46]–[53]. Typically the electromechanical coupling between the stretch and the applied electric field is made via Maxwell’s equation [1], [54]. This equation applies when the DEA is approximated as a parallel plate capacitor, with the elastomer serving as the dielectric and the conductive compliant electrodes on both sides of the film (which have their own stiffness) serving as the parallel plates. The dielectric constant (or relative permittivity, ϵ_r) is an important parameter since in the Maxwell equation it is directly related to the electrostatic attractive force through the film thickness. Efforts to measure the change in dielectric constant at different temperatures, film thicknesses and/or pre-stretch have been made but with varying results [54]–[58]. Dielectric films with higher dielectric constants are more desirable because they require lower electric fields for the same Maxwell stress. Additionally, low-modulus films are favorable for the reason of increasing the electromechanical performance [59]. It is however difficult to make soft materials with high dielectric constants (e.g. >10). Therefore, enhancing the dielectric constant has been the subject of considerable research. This involves modifying the chemistry of the elastomer with the goal of making it more polarizable. One common method is loading the elastomer with a high-permittivity filler [60]–[63] however this often comes at cost of increasing the modulus of the film. Another method, that of blending the elastomer with a highly polarizable copolymer, has shown promising results by enabling an increase in relative permittivity and a decrease in elastic modulus [64]. Other work has filled the elastomer with ceramic coated polarizable filler spheres [65].

Various failure modes of DE elastomer actuators have been observed and studied [51], [66]–[70]. Understanding the conditions and why an actuator fails is paramount in designing optimal long-lasting actuators. Most DE actuator failures are initiated due to electrical failure and not mechanical rupture. The dielectric breakdown limit, which ultimately constrains the achievable actuation stretch, has been shown to vary with thickness and pre-stretch [71]–[73]. On the other hand, pre-stretching has been shown to increase electromechanical stability and thereby enabling higher actuation stretch [74].

According to literature only a handful of investigations have been made on the behavior of DEAs in warm/cold or humid/dry environments [56], [75], [76]. The DE was shown to have a different viscoelastic response at different temperatures. The hysteresis was lower at higher temperatures. The DEA system behavior in different climates needs to be studied further in order to move toward applying the technology in functional areas like the automotive, aerospace, and space industry. In particular, some elastomers, like polydimethylsiloxane (PDMS), a common silicon based elastomer used in DEAs, are gas permeable and will swell

when confronted with some nonpolar solvents [77], [78]. The impact of climate on the electrode material has yet to be studied.

Electrodes play a crucial role in a well-functioning DEA. The conductivity must allow free-flow and distribution of charge on the surface, but the bulk stiffness should be low enough to not inhibit the desired actuation strain. The preferred electrode material has primarily been carbon based (such as carbon black, i.e. soot) but alternative materials are growing. By dispersing carbon black or graphite particles into a viscous oil/grease the electrodes can easily be applied by hand, but this is can be messy, may remain wet and over time will dry out and lose conductivity [79]. However, two-part silicone elastomer mixes (from companies like Dow Chemical, DuPont, NuSil, Wacker etc.) can be combined and filled with conductive particles, and cured with heat to serve as conductive and compliant rubber electrodes [79], [80]. These are more robust and stable over time. Common methods of depositing and patterning the electrodes on the elastomer film range from painting (by hand), blade casting, spraying and laser ablation [81] to screen printing, pad printing and drop-on-demand printing [79]. The last three are the most mass-producible [79].

The loading conditions of DEAs play a key role in the actuator performance, particularly in membrane actuators. Numerous studies have shown this to be true [39], [82], [83]. The compliant mechanism (also called the bias element) is used to pre-stretch or pre-load the DE membrane and can be optimized to maximize the desired force or stroke output of the actuator [84]. This topic will be expounded upon in this thesis.

1.2.1 Challenges

A major challenge for DEA technology is lowering the driving voltage required for DEAs. If this is achieved voltage amplifiers could be cheaper, smaller and more efficient, and DEAs would be more appropriate for applications in the human body. This challenge is in part a material problem and in part a fabrication problem. The solution using the material approach seeks to increase the dielectric constant (which would then theoretically lead to lower driving voltages), while not drastically increasing the Young's modulus or adding unwanted negative effects (like viscoelasticity, high dielectric loss or decreasing the breakdown voltage). The fabrication approach seeks to decrease the polymeric film thickness so the driving voltages may be lower but generate the same electric field needed for actuation. Ultra-thin films [85], [86] are more difficult to consistently fabricate and handle which leads to difficulty in making functional devices. Furthermore, the thinner the dielectric film is the larger the impact the electrodes have on the mechanical response for the film [79], [87], [88]. This requires the electrodes to be much thinner, relative to the film thickness. Poor electrode mechanical behavior (stiff, viscoelastic etc.) can lead to the overall actuators behaving poorly. The thinner the electrodes are, the higher the electrode surface resistance becomes, changing the electrical dynamics of the DEAs. These design challenges are essentially interrelated and should be addressed together.

1.3 RESEARCH OBJECTIVE AND THESIS STRUCTURE

This work aims to present a systematic investigation of the operating principles and the practical methods to improve the performance of diaphragm DEAs. The design, fabrication, modeling, testing and application of negative-rate (bias) springs coupled with DEAs are presented alongside qualitative and empirical results. The impact of the mechanical loading conditions on DEA stroke is studied. Lastly this research concludes with advanced techniques and test rig designs to perform experimental characterization of diaphragm DEAs and planar configured DE membranes.

Much of the analysis and experimental results in the thesis have been published in the author's following papers: [82], [89]–[96].

PART 1: DESIGN OF DIELECTRIC ELASTOMER ACTUATORS

Chapter 2 FUNDAMENTALS OF DIELECTRIC ELASTOMER ACTUATORS (DEA)

DE transducers (DETs) are multi-functional, meaning they have the ability to change electrical energy into mechanical energy—an actuator (DEA), and transfer mechanical energy to electrical energy—a generator (DEG) or sensor (DES).

Figure 2.1 illustrates this.

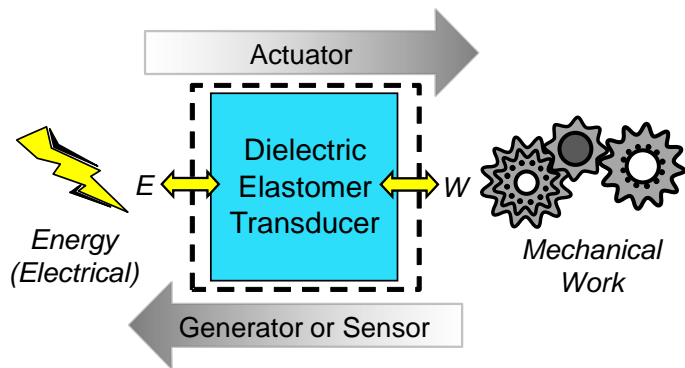


Figure 2.1: Operating principle of DE transducers

Section 2.1 introduces how DEAs work and Section 2.2 provides an overview of common configurations. Section 2.3 and 2.4 discuss the key role electrodes and elastomer materials play in DEAs.

2.1 ELECTRO-MECHANICAL BEHAVIOR OF DE ACTUATORS

Dielectric elastomer actuators undergo a shape change due to electrostatic forces. They consist of an elastomer film as the dielectric and compliant electrodes which coat both sides of the film. When a potential difference is applied across the film, opposite charges accumulate on the conductive electrodes. If this electric field is high enough to overcome the bulk stiffness of the dielectric material, the electrostatic pressure will squeeze the two electrodes together, reducing the thickness and causing an increase in surface area (assuming compliant electrodes and free boundary conditions). In Figure 2.2, a sample actuator is shown for the high-voltage circuit when open and closed. Since the electrode is highly flexible and conductive, and the elastomer has a low-stiffness (Young's modulus <1MPa), the electrostatic pressure or Maxwell stress squeezes the film and the elastomer reacts by changing in shape. The effective pressure on the electrode surface is given by the Peltine equation [97]:

$$p = \epsilon_0 \epsilon E^2 \quad (1)$$

where p is the electrostatic pressure (acting on the electrode area), ϵ_0 is the free-space permittivity, ϵ is the relative dielectric constant of the elastomer and E is the electric field (voltage/film thickness). This is the basic operating principle of DEAs.

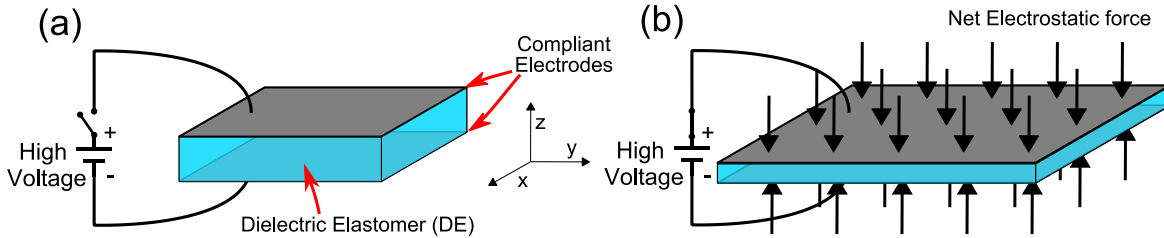


Figure 2.2: Operating principle of a DEA with free-boundaries, (a) No voltage, (b) Voltage applied

The goal of DEAs is to harness this electrostatic-induced shape change of the elastomer film to perform mechanical work. Well-performing dielectric elastomer materials are normally soft, thin dielectrics which should demonstrate as little viscoelastic behavior as possible. Electrode material should likewise be thin relative to the polymer thickness, highly conductive and very compliant.

2.2 CONFIGURATIONS

An attractive feature of DEAs is that they can be fabricated into different configurations to meet the demands of the application. Figure 2.2 above, shows an idealized case of a single DE membrane flat sheet with no boundary constraints. In non-idealized (real-life) cases the film is bounded in a particular manner to make it handleable and functional—able to perform mechanical work.

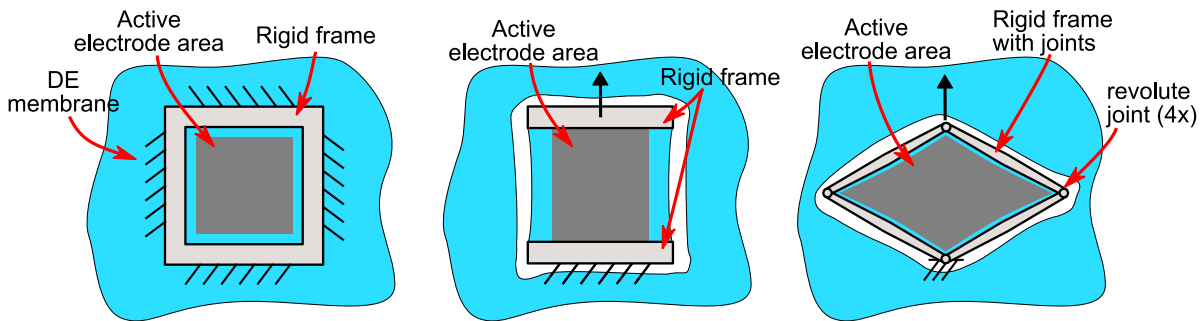


Figure 2.3: DE membranes with various boundary constraints

These boundaries or constraints can be applied differently to produce a shape/geometry and end output motion which meets the requirements Figure 2.3. The adaptability and formability of DEAs, as well as the characteristics listed in Section 1.1, are great selling points to companies seeking to incorporate DEAs into consumer or industrial products.

Further configurations are possible such multi-segmented electrodes which can be actuated to make more complex shapes and motions [98], [99]. The following sub-sections present several types of actuator configurations as seen in the literature with a brief explanation.

2.2.1 Stacked Actuator

Stacked actuators produce linear motion through the change in film thickness when the voltage is applied. This means the output motion is contractile and is in the direction of the film thickness. Since the films are normally thin ($1\text{-}100\mu\text{m}$) and the maximum thickness strains are generally less than 30% [39] the resulting stroke for a single layer would be microscopic. Therefore, the stroke is made more prominent by increasing the number of film layers—leading to a stack formation. The layers are mechanically in series meaning the force output can be scaled up by increasing the electrode area footprint.

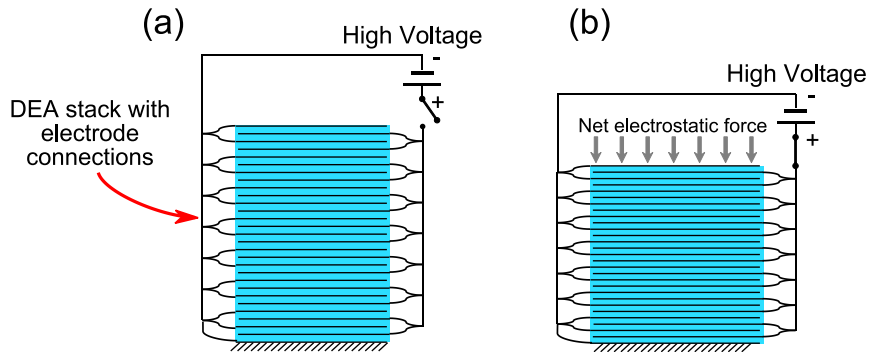


Figure 2.4: Stacked actuator type (a) No Voltage, (b) With Voltage

The stack has the advantage of being compact, monolithic, and capable of carrying compressive loads. However, because the actuator is fixed at the ends there is very little actuation in the planar direction. A stack can bulge at the middle when voltage is applied [100], [101], which can be problematic. Several groups have studied various aspects of stack actuators, including fabrication [16], [102], [103], using them in pump/valve applications [16], [20], and dynamic applications [104].

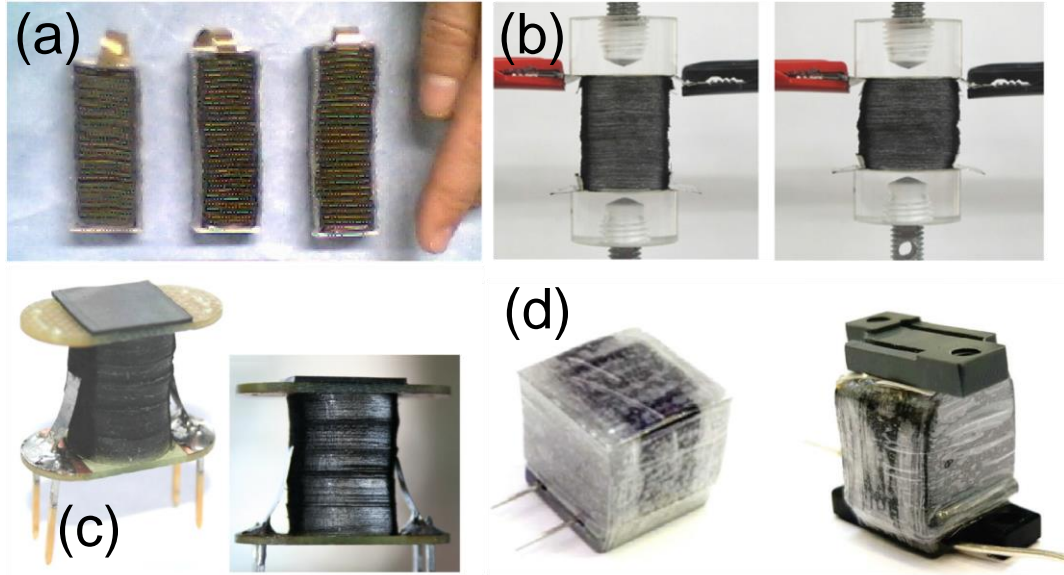


Figure 2.5: Stacked actuators seen in literature, (a) Stack formed by folding [102], (b) stack lifting a weight [105], (c) miniature stack to close and open a pneumatic valve [20], (d) machine fabricated stack actuator [103].

2.2.2 Planar Actuator

While the stack actuators use primarily the change in thickness, planar actuators take advantage of the increase in area upon activation. This configuration has many different varieties since the frame surrounding the active areas can vary in shape. Figure 2.6 shows an actuator strip which is held in tension by a spring. In this configuration the dominant actuation stroke is perpendicular to the membrane thickness—in the planar direction, mostly in the direction of the applied force. The force can be scaled up by adding more layers.

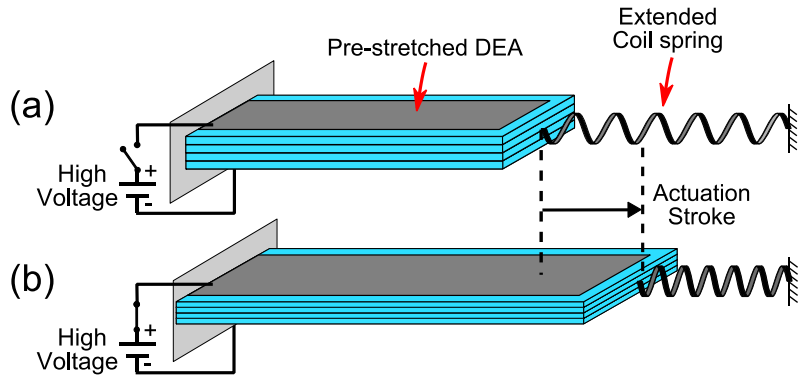


Figure 2.6: Planar actuator type with multiple layers (a) pre-stretched with voltage off, (b) voltage on, showing stroke.

The frame holding the membrane can be flexible [48], [106], rigid and may partially (or completely) surround the membrane. Flexible frames allow for an increase in stroke because the compliant frame surrounding the planar actuator deforms with the film. However the frame-film interface near the moving joints can be subject to high fatigue, delamination issues and lead to premature film breakdown in that area [25]. It is important to develop a frame with low-hysteresis to minimize the mechanical losses. Figure 2.7 shows some planar type actuators seen in literature.

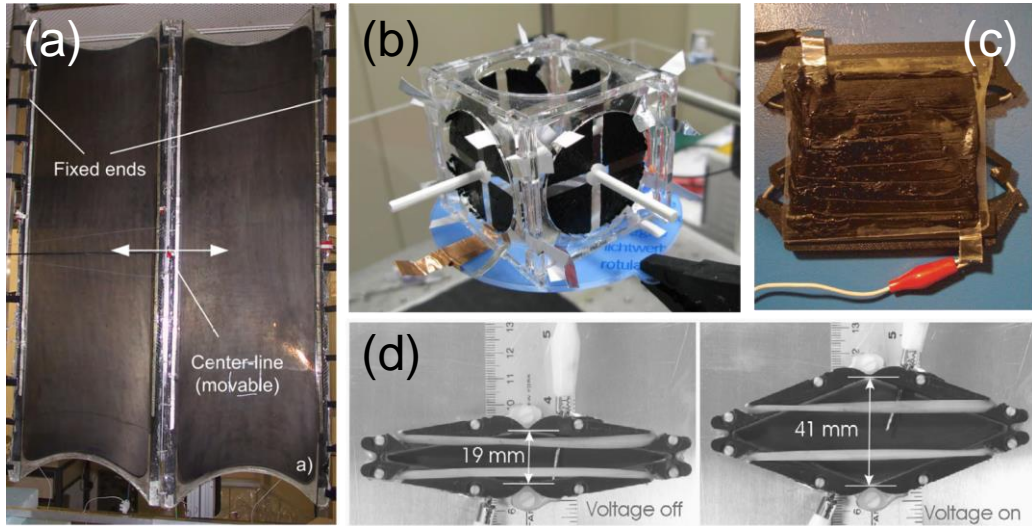


Figure 2.7: Planar actuators seen in literature (a) for actuating a tail of a fish-like blimp [107], (b) patterned-electrode planar actuator with six degrees of freedom [108]; (c) Rectangular actuator with compliant mechanism to apply output force [109], (d) diamond shaped actuator to study performance of viscoelastic DEAs [110].

2.2.3 Roll/Tube Actuators

By rolling a DEA sheet on itself or around a flexible structure, such as a spring, a tubular actuator can be formed [111]–[116]. This actuator produces stroke primarily in the axial direction of the roll. This was the actuator type used in the much popularized human versus artificial muscle arm wrestling competition at the 2005 EAPAD conference in San Diego, CA [114]. This configuration is similar to planar actuations as the layers of film are mechanically in parallel, meaning the force output can be scaled up by adding layers.

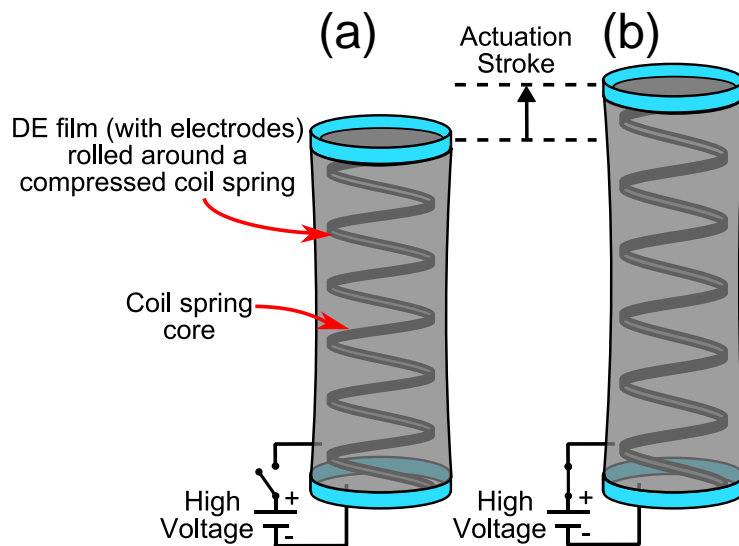


Figure 2.8: Roll actuator with coil spring core (a) voltage off, (b) voltage on showing actuation stroke

Some tests show that with certain materials with high pre-stretch (such as VHB types) the actuator creeps over its lifetime, reducing performance [114]. Additionally, DE breakdown, instabilities and mechanical failure may result at the elastomer-end caps and the core-film interface [114], [116]. Other drawbacks to the configuration are the empty space in the core, the complicated fabrication process (due to rolling and pre-stretching the film) and the

inability to interchange core springs once assembled. Nevertheless, this remains a promising configuration. Several designs are shown below.

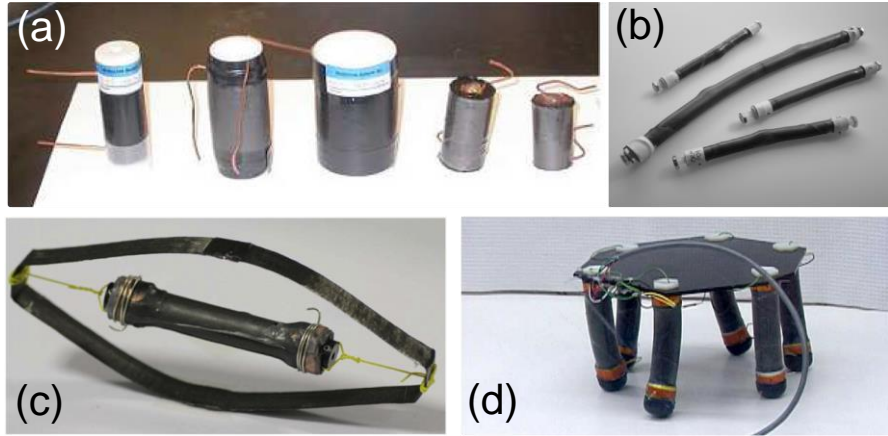


Figure 2.9: Photos of Roll/Tube actuators seen in literature, (a) Polyurethane stack actuators for vibration isolation [113], (b) actuators with spring core for driving robot arm [114], (c) rolled DEA for driving bio-inspired wing flapper [27], (d) multi-degree of freedom spring-core actuators operating as flexible legs of walking platform [112].

2.2.4 Out-of-plane Actuators

Out-of-plane actuators are, like planar actuators, membrane. As with the other configurations listed, several variations exist for out-of-plane actuators [49], [82], [94], [117]–[120], however they would all be considered membrane actuators. As the name indicates, these actuators operate out-of-plane and this can be achieved by a variety of means: from a compliant mechanism, like a spring or linkage, or with air or fluid pressure forming a bubble or bulge. One advantage of this type is that the outer boundary condition is usually fully-clamped which reduces the risk of membrane tearing because of the continuously fixed-edge. Below are a few examples of actuators operating in out-of-plane mode and producing linear actuation.

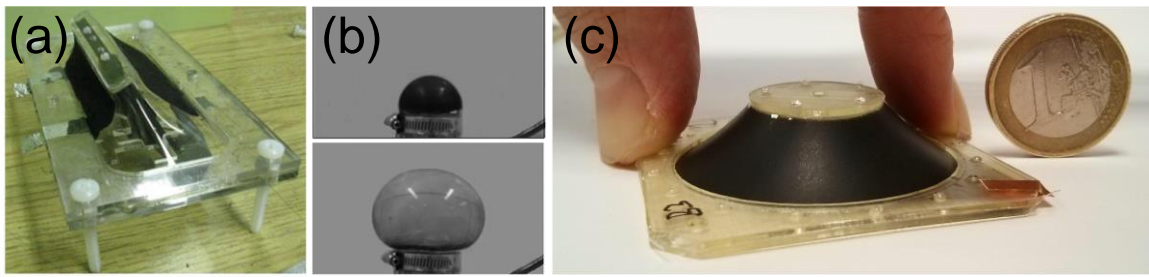


Figure 2.10: Photos of out-of-plane actuators: (a) flip-flop rotational mechanism [121], (b) pressurized membrane actuator showing giant deformation when voltage applied [122], (c) diaphragm actuator (from author).

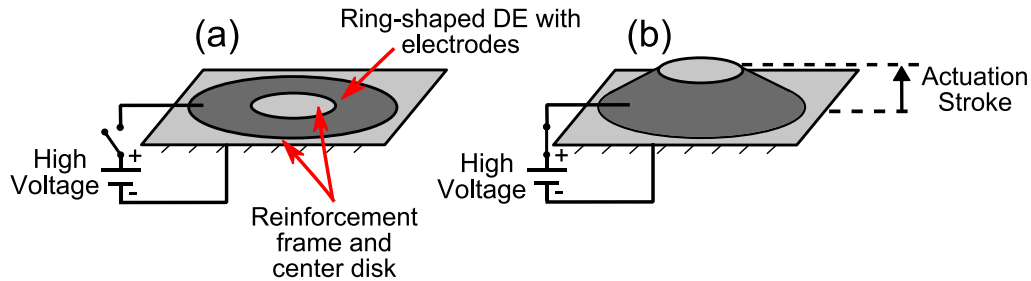


Figure 2.11: Diaphragm out-of-plane actuator (a) voltage off, (b) voltage on.

The so-called circular or diaphragm actuators (Figure 2.11) are used extensively in this work to produce linear motion. In this configuration there is a ring of active material surrounded by a stiff frame. The actuator exhibits out-of-plane motion when the center mount is displaced, as shown in Figure 2.11(b), thus stretching the DE membrane in the radial and circumferential directions.

2.3 ELASTOMER MATERIALS

Many rubber materials have been candidates for DEAs and a few have proven to be adequate for actuation [39]. The 3M VHB (“Very high bond”) acrylic adhesive is used by many researchers because of its availability, high-stretch capability and high breakdown strength. Still this material is highly viscoelastic [123]–[125], resulting in a slow response to voltage and high-creep over time. This is a major downside because the potential speed of the actuators (due to the charging of a capacitive load) cannot be realized due to the slow mechanical behavior [45].

A more appropriate material in recent days has been shown to be a silicone-based rubber compound called polydimethylsiloxane (PDMS). Wacker Chemie AG produces a PDMS elastomer called Elastosil® film at thicknesses as low as 20 μm . This and other silicone rubber (from companies such as NuSil, Dow Corning, etc.) have much shorter response times and less dissipation [45]. With a relative coefficient of about 3 and a low modulus the driving voltages only need to be around a few kV and not 10kV like VHB materials.

Other materials such as polyurethane [113], [126], [127] and natural rubber [5], [128] films have also been used. While polyurethanes usually exhibit a higher dielectric constant (~6-13) than silicones they also exhibit a higher elastic modulus and an increased sensitivity towards humidity [126] and temperature [129]. Natural rubbers are not so often reported in literature but some results show them as good candidates for energy harvesting because the high energy densities at a lower cost [130].

Rubber materials are inherently non-linear in their behavior. They can undergo large deformations but exhibit several hysteretic effects (hyperelasticity, viscoelasticity, creep, Mullin’s effect, etc) which can be exacerbated in different temperatures and humidity. Therefore, appropriate models are used to describe the behavior including normally

combining hyperelasticity models (Neo-hookean, Odgen, Mooney-Rivlin, and Gent models) with the induced Maxwell stress due to the applied electric field. (An example of this can be seen in the work of Rizzello and Hodgins [95], [131]).

2.4 ELECTRODE MATERIALS

As mentioned earlier, electrodes greatly impact the DE actuator performance and therefore need to be studied and well understood. This is a very open field and no perfect solution exists for each application. The goal and challenge in short is for an electrode material to exhibit high flexibility, low electrical resistance, good adhesion to the membrane, good patternability, low and uniform thickness relative to the membrane and robustness (will not degrade or rub off with use). Furthermore, to commercialize such devices, the fabrication process must be scalable—able to be manufactured uniformly at a large scale.

Carbon-based compliant electrode materials are most commonly used, likely due to their relatively good conductivity, mixability (with several polymer matrix materials) and availability. Other types of electrodes include metallic, ion implanted and hydrogels containing electrolytes. This work deals only with carbon based electrodes. A good summary of electrodes, which discusses the advantages and disadvantages common kinds, can be read in the following articles [79], [132].

Repeatable large-scale fabrication methods (which are dependent on the size of the device) include pad printing, screen printing and drop-on-demand printing (ie. Inkjet) [79], [133].

Chapter 3 DEA DESIGN AND STROKE ANALYSIS

As seen above in Section 2.2, several design configurations are possible. In each case the DEA operation is the same—using the transduction abilities of the DE film the electrical energy is converted to mechanical work.

However, in order to produce meaningful actuation for DE *membrane actuators*, the coupling with the surrounding structure should be correctly implemented. As mentioned on page 1 this is not as important for stacked actuators (page 11), but for membrane actuators, or other actuator configurations which extend when actuated, this is important. Realizing the most beneficial DEA loading conditions is not always trivial due to several reasons including the non-linear material behavior, space/size limitations and external loading conditions.

By performing a force-equilibrium study of the DE actuator system and the load (if any) the mechanical operating principle can be better understood. The following sections provide an explanation using this approach to help describe the operation of membrane DEA systems and additionally to show the importance of the surrounding structure (or bias mechanisms) chosen. (This view doesn't focus heavily on the electronics or the microscopic view of the actuator but rather takes a macroscopic view of the DEA and the supporting mechanical components which make up the actuator system.)

3.1 MEMBRANE DEA OPERATION AND STROKE

Since DEAs are designed to perform work it is necessary to measure and study the mechanical forces to understand their operation. Some configurations, such as the diaphragm configuration (Figure 2.11), rely heavily on a compliant bias mechanism (like a linear spring or hanging mass) to produce meaningful actuation stroke, in this case out-of-plane. The force characteristic of this bias element and the magnitude to which it pre-loads the DEA will dictate the displacement and force output of the actuator (when no other external forces are applied). To illustrate the operation, take the example of a positive-rate spring (linear coil spring) and a diaphragm DEA, as seen in Figure 3.1. The spring is compressed against the DEA with no voltage applied. When a high-voltage is applied to the DEA, its membrane expands radially which allows the coil spring to extend further to a new equilibrium position (Figure 3.1). If the spring was not compressed against the DEA virtually no stroke would occur. Therefore, the bias mechanism is vital to produce stroke for membrane actuators.

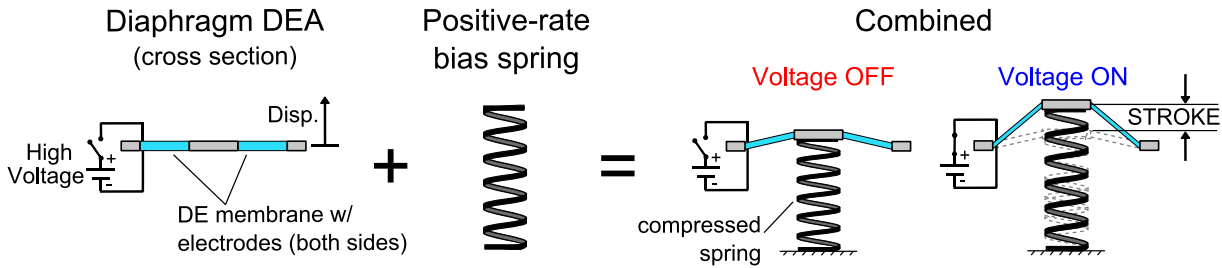


Figure 3.1: Cross sectional sketch of circular/diaphragm DEA coupled with a bias mechanism.

By performing a force-equilibrium analysis the force-equilibrium position can be determined. This is done by measuring the out-of-plane force of the membrane DEA as constant voltage is applied to the DEA. To perform this a linear actuator controlled the out-of-plane displacement of the DEA while the blocking force was measured with a load cell. Figure 3.2(a) shows a schematic of the test setup, Figure 3.2(b,c) shows photos of DEA being deflected out-of-plane and Figure 3.2(d) presents the measured force response to sinusoidal displacement at 1Hz. The effect of the voltage on the out-of-plane stiffness is clearly seen. The DEA is acting as a variable stiffness spring. The viscoelasticity of the actuator is also seen by the hysteresis in the force-displacement response.

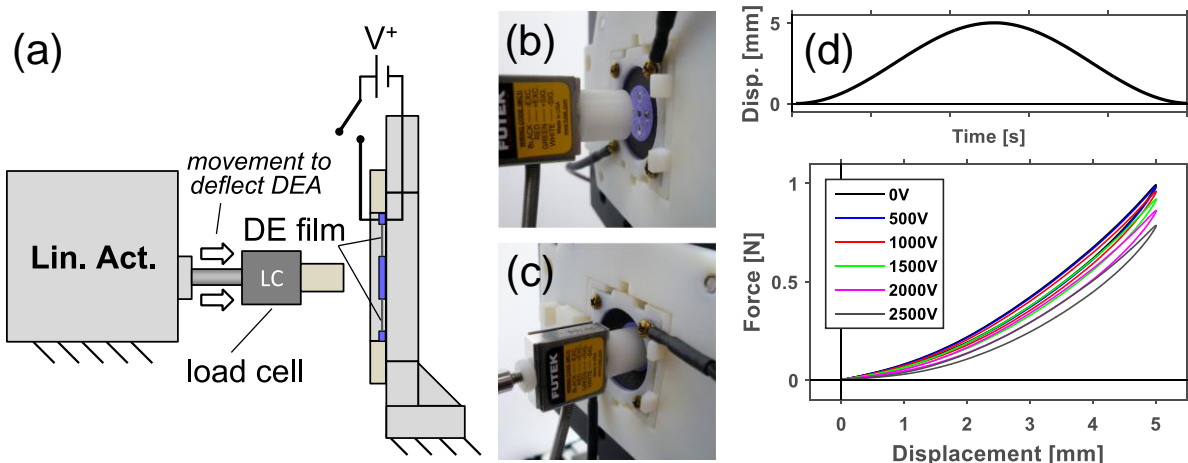


Figure 3.2: Force vs. controlled out-of-plane displacement of DEA setup and results.

The hysteresis can be neglected for quasi-static actuation cases. Figure 3.3 presents force-displacement (F-D) profiles for the individual components: the DEA as a single solution polynomial fit to the data, and the linear spring as a linear line with the stiffness k . By combining the F-D profiles (reversing the sign of the force for the spring) and locating the intersection points, the effective quasi-static actuator stroke can be approximated.

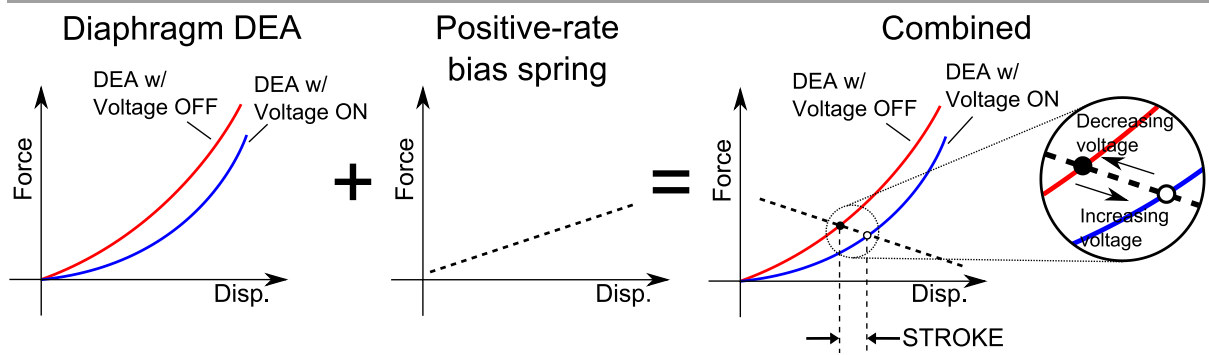


Figure 3.3: Stroke development of a pre-loaded DEA with a positive-rate bias spring (linear spring).

Figure 3.3 shows that increasing the voltage effectively softens the DEA membrane and results in a new force equilibrium position for the DEA-spring system. In other words, by increasing the voltage some of the stored energy in the compressed linear spring is released to stretch the now “softer” DEA. One can also note that while the linear spring is extending, the force is decreasing. At the maximum voltage the stroke or elongation of the elements is at its peak but the force and total stored energy are at their lowest point. When the voltage returns to zero, the starting force-equilibrium position is reached. This is how repeatable stroke is achieved with the DEA-spring system. As can be seen in Figure 3.3, at low-deflections there is little separation between the low and high-voltage profiles, meaning relatively low actuation stroke can be achieved in this region. Without an external bias force, little stroke could occur. The spring assists in deflecting the DEA into its working region highlighted in Figure 3.4.

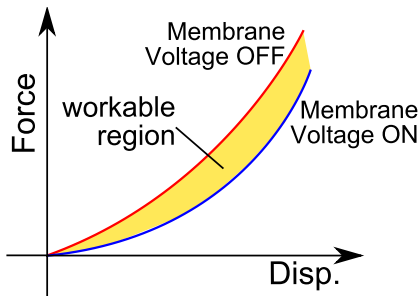


Figure 3.4: Diaphragm Membrane DEA workable region

The force range (and workable region size) can be increased by stacking diaphragm DEAs (Figure 3.5). This is useful when adapting the DEA to an application. One drawback to adding layers can be seen in Figure 3.5—an increase in viscoelasticity. This is seen by the larger hysteresis loops at constant voltage.

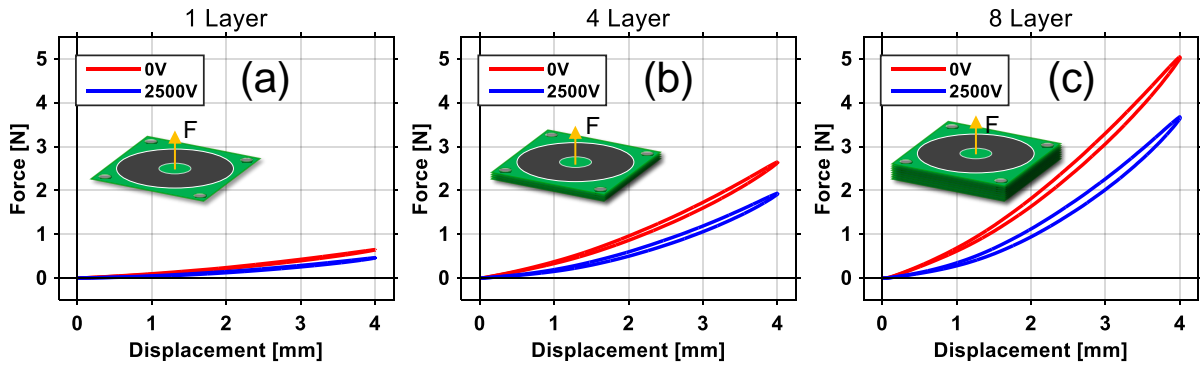


Figure 3.5: Scaling force output by stacking diaphragm DEAs. Sinusoidal displacement at 1Hz for (a) 1-layer, (b) 4-layer and 8-layer DEAs.

By changing the inner and outer diameter size the force response also changes. Hau *et al* found that increasing the inner diameter linearly increases the blocking force while linearly decreasing the stroke (at constant force) [134].



Figure 3.6: Photo of DEA with different inner disk diameters.

3.2 EXPERIMENTAL COMPARISON OF BIAS ELEMENTS

A linear spring is only one bias element. Others elements which can be used include a constant force (hanging mass) and non-linear springs. These are studied and compared in this section.

3.2.1 Introduction

Here an experimental comparison of 3 different bias elements producing actuation stroke is performed. A hanging mass, a linear coil spring, and a non-linear (bistable) mechanism are individually paired with a diaphragm DEA, pre-deflecting it out-of-plane. High-voltage (e.g. 2.5kV) is applied to the DEA and the out-of-plane stroke of the DEA is measured. The actuator stroke is notably different for each bias element. Results show that as the bias element's stiffness increases, the actuator stroke decreases. However, the bistable element, when coupled with the DEA, demonstrated improved actuation within a specific range of DEA pre-deflection. Not only was the stroke larger for this case, the stroke also did not attenuate as much as the linear coil spring element at higher actuation frequencies. This study demonstrates a promising method for obtaining high-performing DEA actuators.

3.2.2 Bias Elements

This section introduces and briefly details the bias elements to be used in the experiments, including the design and fabrication of the bistable spring.

3.2.2.1 Bias Elements

A hanging mass was used to provide a constant bias force, a compression spring a linear bias force, and a non-linear (bistable) spring provided a non-linear bias force (Figure 3.7). The hanging masses ranged from 10-100 grams in 10 gram increments. The range of masses permitted a gradual pre-deflection of the DEA up to approximately 5mm. Linear springs of stiffness 0.05N/mm, 0.24N/mm and 1.01N/mm were each tested with the DEA, also at different pre-deflections.

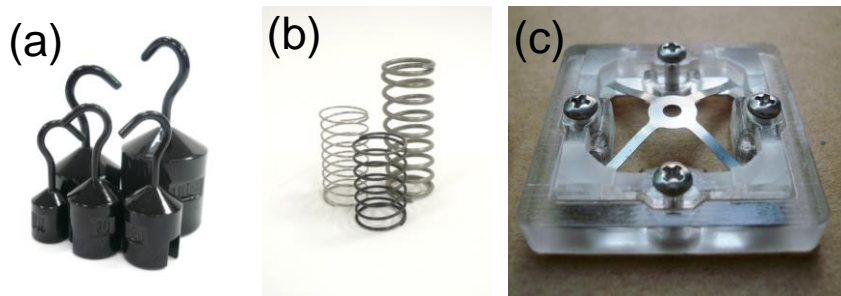


Figure 3.7: Three biasing mechanisms, (a) hanging masses, (b) compression Springs, and (c) post-buckled mechanism.

A miniature, custom made post-buckled beam mechanism was used as the bistable spring (Figure 3.7(c)). The thin stainless steel X-shaped form was mechanically buckled by inserting it into a smaller square shape and then constrained at the corners with a cover. Once inserted, the mechanism exhibits two stable post-buckled positions. Figure 3.7(c) shows the mechanism in the stable up position. (Further design and fabrication details are presented in Section 4.2.)

A force vs. controlled-displacement test was performed and revealed the expected non-linear force-displacement response. Figure 3.8(a, c) presents a sketch/photo of test setup and Figure 3.8(b) presents the measured force response highlighting the mechanical stability regions. The negative slope region of the spring explains the previously mentioned name of “negative-rate bias spring” or NBS.

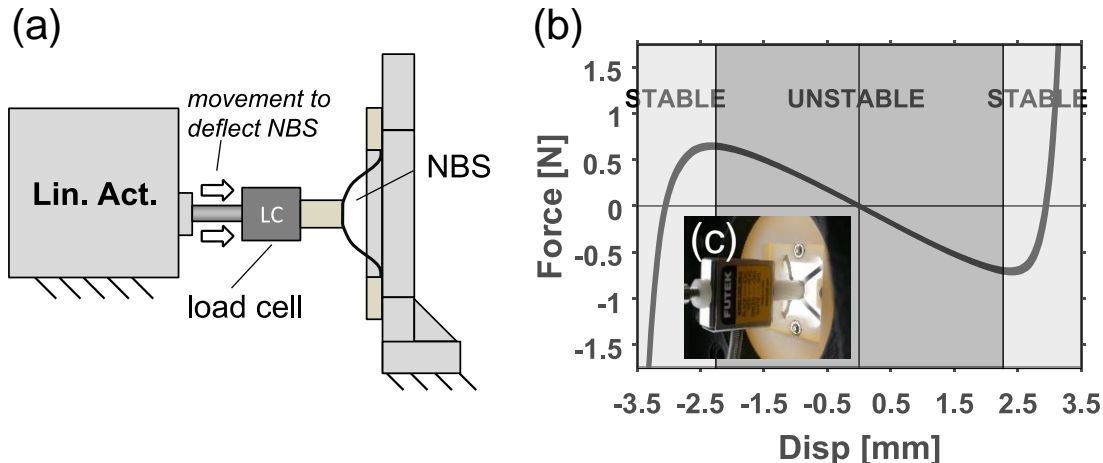


Figure 3.8: Force vs. controlled out-of-plane displacement of NBS, (a, c) setup and (b) results.

This region is inherently unstable while the outer stiff regions are stable like a linear spring. The mechanism can be snapped by hand from one stable position to the other, showing large motion quite suddenly when the critical force is exceeded.

3.2.3 Experiments and Results

This section presents the setup, procedure and actuation results for the three different bias elements. These three experiments were performed using one circular DEA. In each test the DEA was mounted to a frame and fully constrained around the stiff square-shaped epoxy region of the DEA to ensure no flexing. Then the DEA was biased (or pre-deflected at the center disk) while voltage was off. The voltage was then linearly ramped from 0V to 2.5kV and back to 0V (a triangle shape) for multiple cycles. The signal was digitally generated and was amplified with a Trek model 610E. The out-of-plane displacement of the DEA center disk was measured using a Keyence LK-G37 laser displacement sensor with 10nm resolution. The actuator and sensor signals were processed through a National Instruments 7852R FPGA board that was programmed from a Windows desktop computer running LabVIEW 2010.

3.2.3.1 Hanging Mass

The test setup for the hanging mass (constant bias force—CBF) is shown in Figure 3.9. Since the DEA was oriented vertically (i.e. the out-of-plane deflection was in the horizontal direction) a pulley was required to transfer the force from the hanging mass to the DEA. Masses were individually tested at a voltage frequency of 0.1Hz. The slow rate minimized any oscillations from the hanging mass which might be transferred to the DEA center disk.

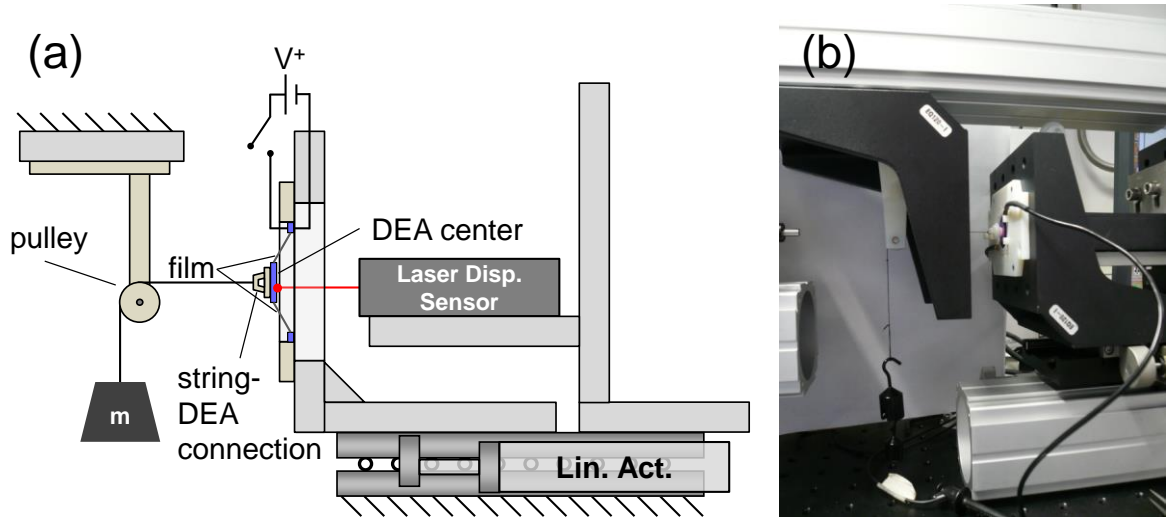


Figure 3.9: Hanging mass test setup (a) sketch, (b) photo.

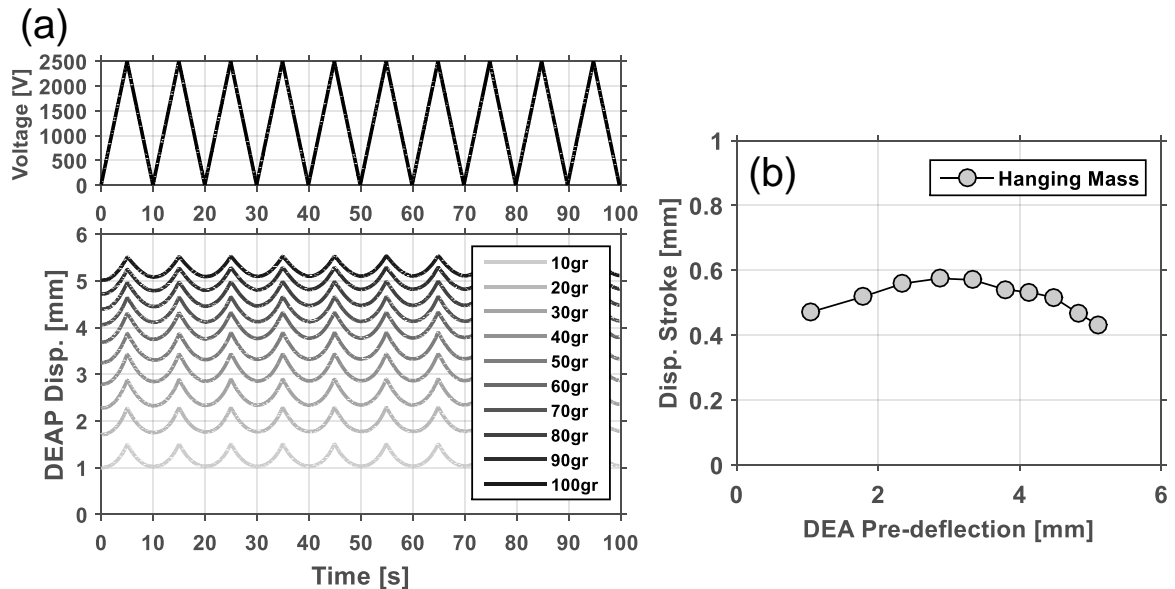


Figure 3.10: Stroke results for each hanging mass at 0.1Hz, (a) disp. vs time results, (b) stroke results vs pre-deflection.

Figure 3.10 shows the DEA displacement results for each hanging mass. The displacement stroke increased slightly with increasing mass and then decreased slightly after initial deflections exceeded approximately 3.5mm. It maintained a stroke of around 0.5mm.

3.2.3.2 Positive-rate Bias Spring (PBS)

In Figure 3.11 presents a sketch of the test setup and photos. For this test a linear actuator (Aerotech ANT-25LA) was used to compress the PBS against the DEA. With each PBS tested (0.05N/mm, 0.24N/mm and 1.01N/mm) the DEA was biased from 0mm to 5mm (out-of-plane).

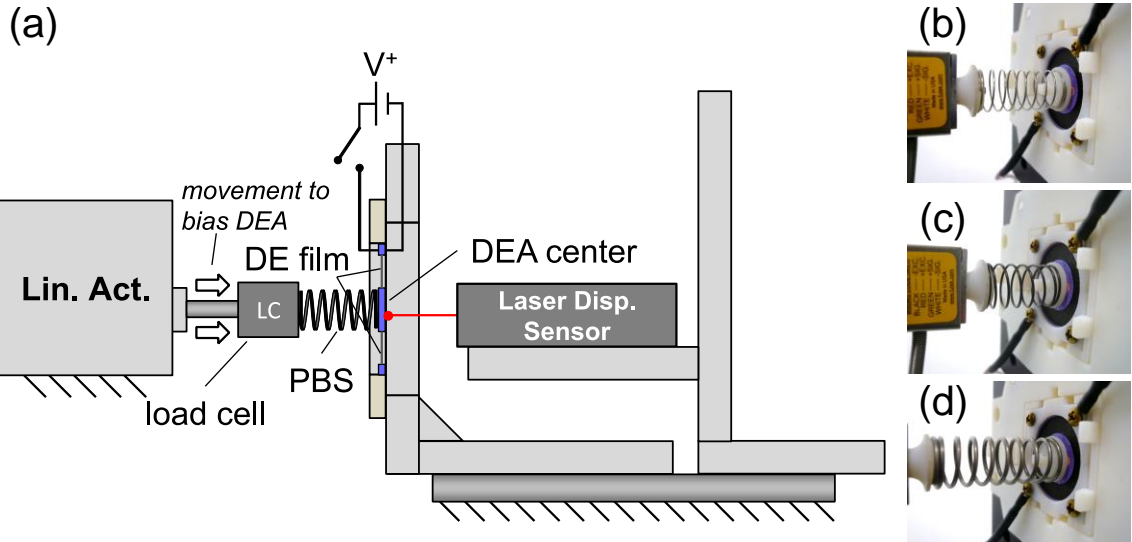


Figure 3.11: Positive-rate spring (PBS) test setup (a) sketch, (b-d) photos of setup with the 3 springs.

Figure 3.12 presents the time resolved DEA displacement results for the DEA biased (to various pre-deflection amounts) with a spring of $k=0.24\text{N/mm}$. Each line represents a different spring pre-deflection. The stroke clearly increases with an increase in DEA pre-deflection shown from the lower curves to the upper curves.

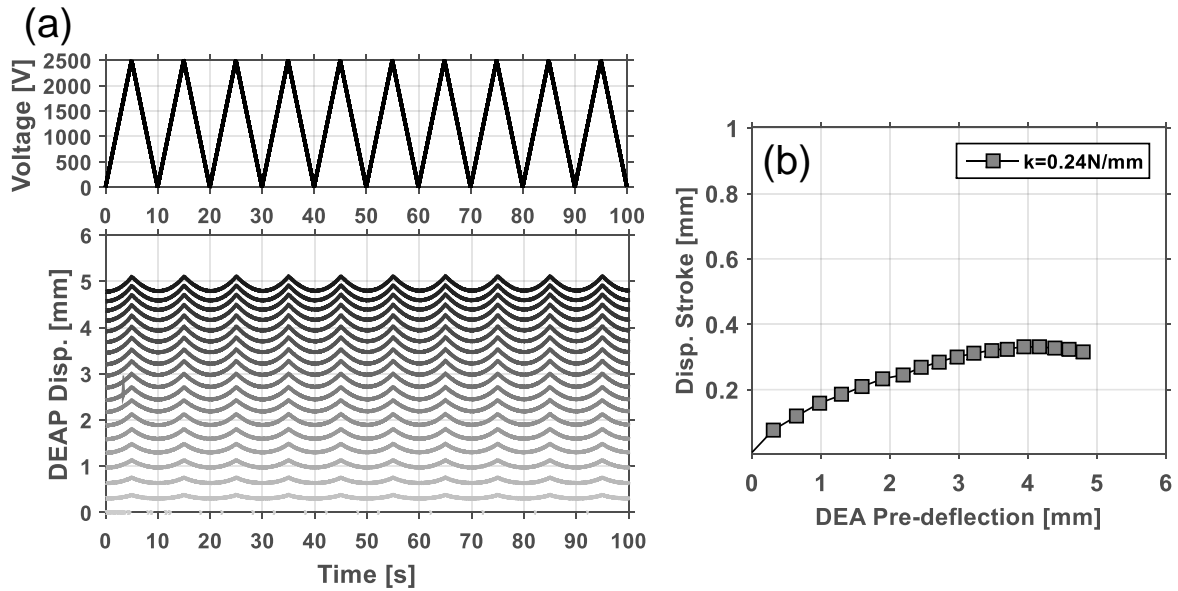


Figure 3.12: Stroke results for each PBS pre-deflection, $k=0.24\text{N/mm}$ at 0.1Hz , (a) time resolved, (b) stroke results vs. pre-deflection.

3.2.3.3 Negative-rate Bias Spring (NBS)

Next the NBS was tested as the bias element. This required a slightly more complicated setup because of the configuration of the NBS (i.e. the buckling frame should be fixed relative to NBS center deflection). To test the DEA at different pre-deflections the circular DEA was mounted onto a movable platform (Newport, model 443) which was actuated by a linear actuator (Zaber LA-28A) in the direction of the NBS, see Figure 3.13. The laser displacement sensor was mounted on the platform behind the DEA to track the out-of-plane displacement with respect to the DEA outer frame. Therefore, the absolute DEA out-of-plane deflection was

being measured precisely by the laser sensor. This moveable platform made it possible to bias the DEA by controlling the position of the outer frame of the DEA while the center disk of the DEA made contact with the NBS. A second linear actuator (Aerotech ANT-25LA) was positioned to the left of the NBS and served as an adjustable mechanical stop for the NBS (when needed).

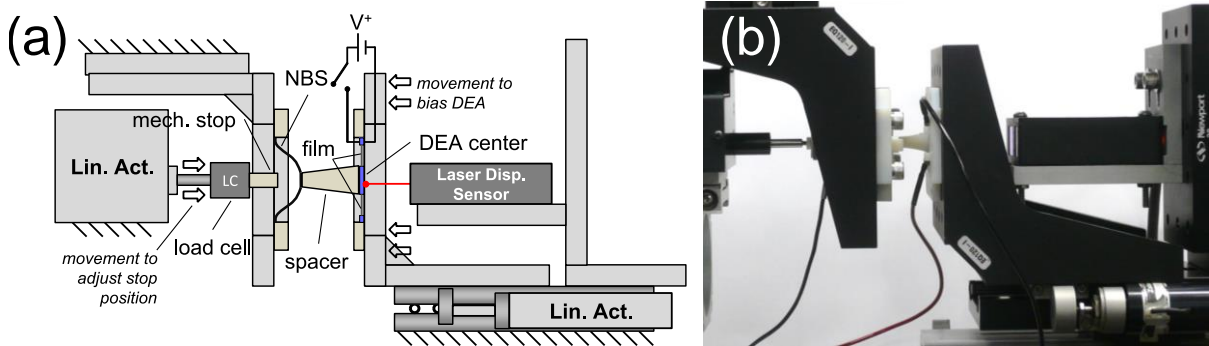


Figure 3.13: Negative-rate bias spring (NBS) test setup (a) sketch and (b) photo of setup.

The NBS used had a much higher stiffness than the DEA it was paired with, resulting in a mechanically unstable coupling when attempting to operate on the negative branch of the NBS. Therefore, a mechanical stop was used to provide a stable position for the NBS-DEA when unactuated. The mechanical stop was positioned so that when blocked, the DEA was still pre-deflected.

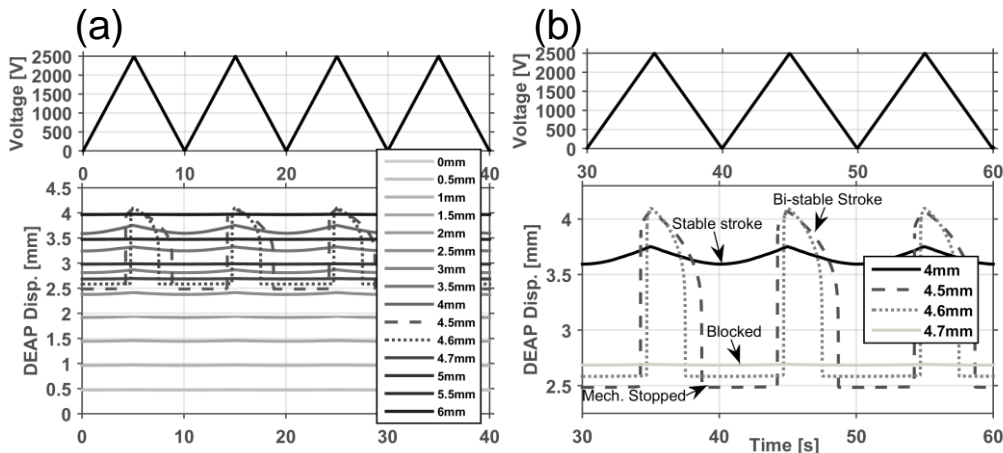


Figure 3.14: Bistable stroke results at (a) several DEA outer frame positions (0.1Hz) and (b) different modes of stroke possible.

The DEA was biased by the NBS while the mechanical stop was held constant. Figure 3.14 presents the time resolved displacement results for the NBS where each line represents different DEA outer frame position with respect to the neutral position Figure 3.14(b) highlights 3 types of stroke observed. At 4mm (DEA frame position with respect to the NBS frame) stable stroke is observed. At position 4.5 and 4.6mm bistable actuation occurred as seen by the sudden displacement at higher voltage levels. Suddenly at the next position (4.7mm) the stroke has vanished and no actuation occurs because the NBS is blocked against the stop.

3.2.3.4 Comparison

The stroke achieved vs. the initial out-of-plane deflection of the DEA (when voltage=0V) for each bias element is presented in Figure 3.15. The stiff PBS produces less displacement stroke than softer PBS. The hanging mass gives even larger stroke than the softest PBS. The NBS, however, far exceed the stroke of the hanging mass and PBS. It showed a 2.6x larger stroke than the hanging mass and 3.2x larger stroke than nearest performing PBS ($k=0.05\text{N/mm}$).

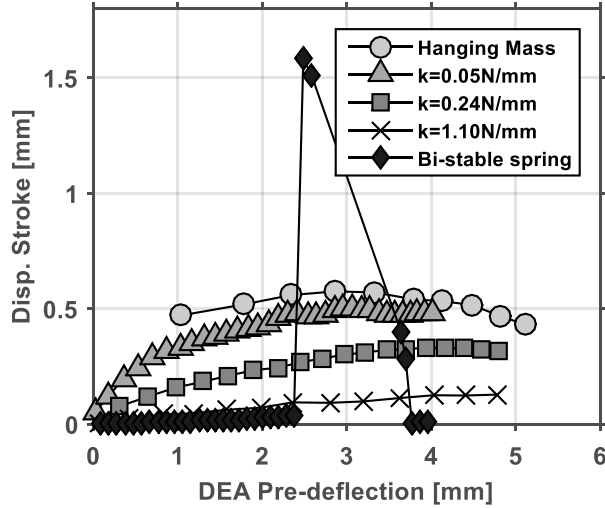


Figure 3.15: Comparison of Stroke vs. inactivated DEA Pre-deflection.

Additionally, when tested at higher frequencies the PBS showed a decrease in maximum stroke of nearly 40%, while the NBS showed only a minuscule 5% decrease.

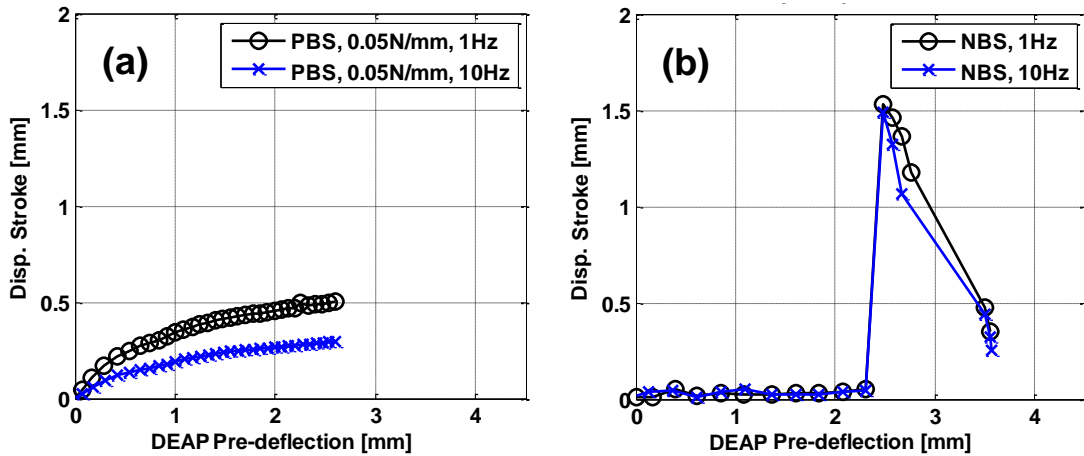


Figure 3.16: Stroke vs. DEA pre-deflection at 1Hz and 10Hz for: (a) PBS and (b) NBS.

The NBS shows virtually no decrease in performance at higher actuation frequency. These results clearly show the advantage of the NBS's bistable behavior to increase overall stroke and to maintain a higher operating bandwidth.

3.2.4 Stroke Analysis

In this section, a force-equilibrium (assuming a quasi-static equilibrium) analysis is performed in order to better understand how stroke results when each bias mechanism is coupled to the

DEA shown in Figure 3.10, Figure 3.12, and Figure 3.14. The area between the Voltage OFF and Voltage ON can be seen as the active operating area for a bias element. In order to plot the bias elements with the DEA together on the same plot, the sign for each bias element was flipped according to the force equilibrium equation.

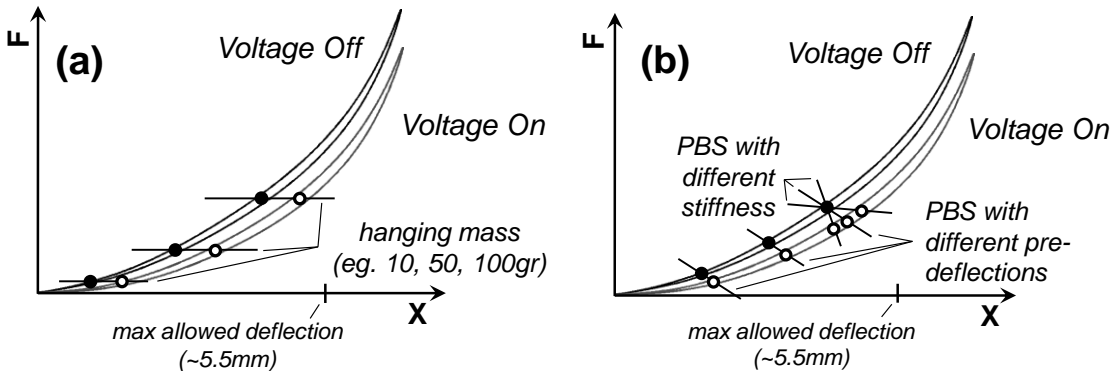


Figure 3.17: Displacement stroke for two bias elements (a) constant force and (b) linear springs.

Figure 3.17(a-b) visualizes the variation in stroke (between circles) by increasing DEA pre-deflection for a springs and masses.

3.2.4.1 Hanging Mass and Positive-rate Bias Spring

Figure 3.17(a) is a force equilibrium plot of the DEA (Voltage ON and Voltage OFF) biased showing 3 different hanging masses with their respective displacement stroke denoted. The user defined maximum out-of-plane displacement is shown for perspective. The hanging mass has zero stiffness and results in a reversible displacement stroke between the denoted force equilibrium points. The heavier masses pre-deflect the DEA more and tend to produce more displacement stroke. However, the experimental results (in Figure 3.10) show that for pre-deflections above 3mm the stroke decreases for the hanging mass. Graphically this can be seen from the convergence of the Voltage ON curve towards the Voltage OFF curve. In other words, the high-voltage has less of an effect on the DEA at these high stretches. This could be attributed to the high in-plane strain affecting the dielectric constant or film z-direction stiffness [44]. The effects of pre-strain and pre-deflection are discussed further in [49], [94], [135]. In Figure 3.17(b) the positive stiffness bias spring results in a reversible displacement stroke between the force equilibrium points. This stroke increases as the DEA bias force is increased. A larger displacement stroke can also be achieved by choosing a more compliant spring at the cost of a lower change in force.

3.2.4.2 Negative-rate Bias Spring with mechanical stop

The NBS, as seen in Figure 3.8(b), has a non-linear force characteristic. When a NBS is used to bias the DEA, this can result in multiple actuation “modes” when voltage is applied to the DEA. In Figure 3.18(a) the NBS is started in the stable right position and where it is just in contact with the DEA (i.e. no bias). (The reader should note that in Figure 3.18 the DEA constant voltage curves shapes are taken from deflections less than the 5.5mm maximum allowed deflection—hence the difference in appearance compared to the constant voltage curves of Figure 3.17. The smaller constant voltage curves of Figure 3.18 are more

distinguishable, showing such high deflections of the DEA are not necessary.) Figure 3.18(b) shows a case when the NBS pre-deflects the DEA so the force equilibrium is found on the stable branch of the NBS. This actuation mode is similar to when a stiff PBS is the bias element which produces small stroke (between points A and B). In Figure 3.18(c) the NBS is pre-deflected enough that the NBS is snapped to an equilibrium position on the left stable branch. When actuated, this results in very small stroke moving to the left direction (between points A and B).

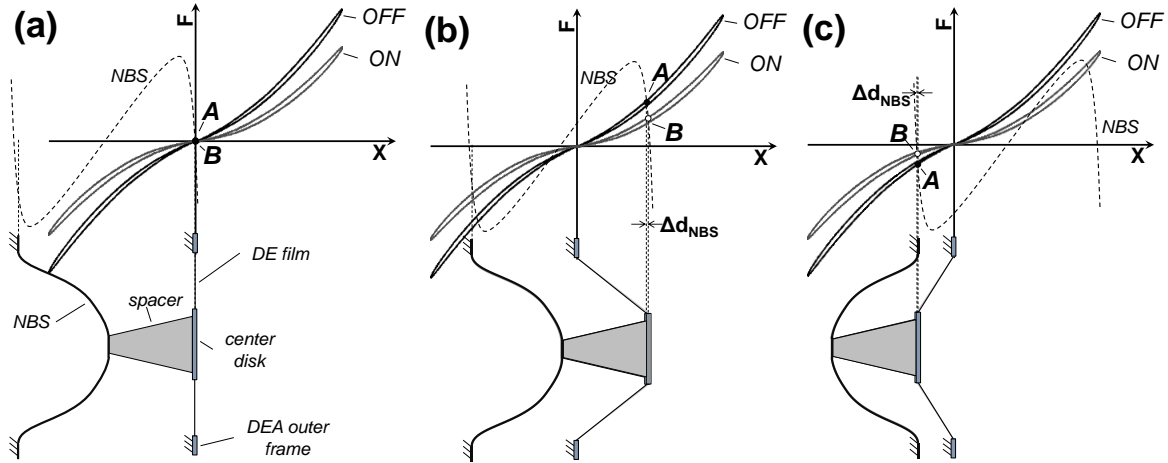


Figure 3.18: Sketch of small stroke possible using NBS without mechanical stop, (a) Initial condition (no pre-deflection), (b) NBS pre-deflecting DEA giving small stroke, (c) further deflected DEA such that peak NBS force overcome and NBS snapped to new stable condition on left side.

However, a mechanical stop can be added to constrain the NBS on the unstable branch as illustrated in Figure 3.19. The mechanical stop is positioned so that at low voltage (OFF) the actuator is blocked but at high voltage the only NBS-DEA intersection point is off the stop. Cycling voltage will produce a repeatable snapping action (between point A and B).

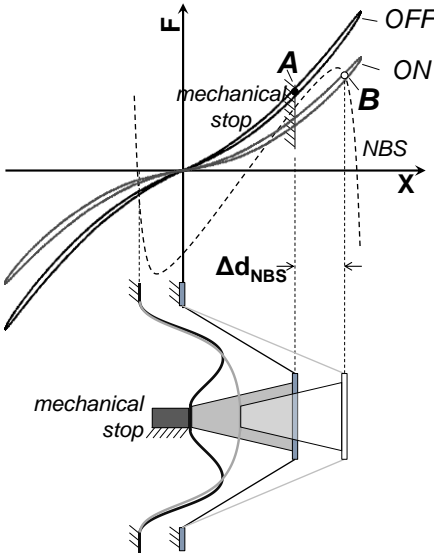


Figure 3.19: Stabilized NBS and DEA by mechanical stop.

Figure 3.20 presents the time-resolved steps for a single bistable actuation cycle when a mechanical stop is implemented. Each time step shows the force-equilibrium plots of the

DEA-NBS system synchronized with a sketch of the physical components beneath. In Figure 3.20(a-d) the bistable stroke is presented incrementally as voltage is increased to 2.5kV. Figure 3.20(d)-(f) present the position as the voltage is decreased.

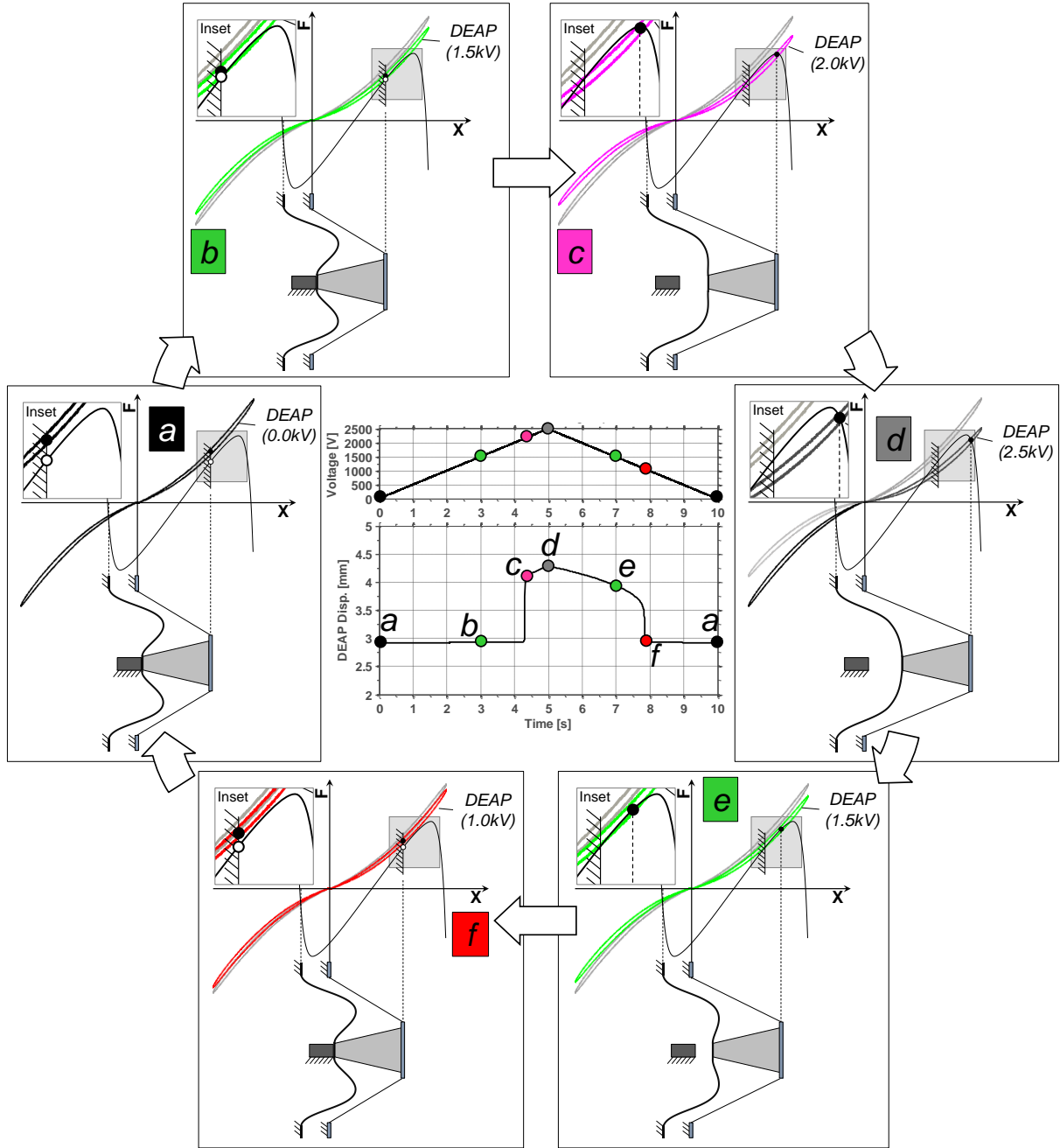


Figure 3.20: DEA-NBS stroke behavior for one cycle.

In Figure 3.20(a) the cycle begins at 0V with the DEA-NBS actuator at rest against the mechanical stop. The actuator remains blocked as the voltage is increased to 1.5kV as Figure 3.20(b) shows. In Figure 3.20(c) the voltage has reached 2.0kV. At this point the NBS has snapped away from mechanical stop (overcoming the DEA force) and has found a new equilibrium position on NBS characteristic curve. As the voltage increases to 2.5kV, the displacement steadily increases, Figure 3.20(d). The reverse happens when the voltage is decreased. Figure 3.20(e) shows the DEA-NBS soon before snapping back against the

mechanical stop. The snap occurs because there is no intersection point for the NBS and the DEA. From point (f) to point (a) the voltage decreases 1.0kV and the DEA stiffens up but remaining against the stop. As the center plot in Figure 3.20 shows the NBS behavior is quite hysteretic. Notice the difference in the voltage when the NBS snaps away and snaps back. This is due to the nonlinearity of the NBS.

3.2.5 Summary

In summary a small profile and scalable circular DEA actuator biased by a hanging mass, positive-rate bias spring, and negative-rate bias spring were systematically tested and compared. When electrically loaded at 0.1Hz the results showed the expected trends. The lower stiffness bias springs provided more displacement stroke than the stiff ones, and the hanging mass out-performed the softest spring. The non-linear or negative-rate bias spring (NBS) revealed the highest stroke of all the DEA bias elements. The NBS was bistable and used a mechanical stop to maintain stability on the negative stiffness branch. The NBS mechanism showed a decrease in stroke of less than 5% when the loading rate was increased from 1Hz to 10Hz. The linear spring showed a decrease of nearly 30% when the electrical loading rate was increased.

3.3 CONCLUSIONS

In conclusion, this chapter sought to analyze, explain and demonstrate the operation of a diaphragm membrane DEA in terms of the characteristic forces and those of the loading mechanism, or bias element. It was shown through qualitative analysis and systematic experimentation that the output (force and stroke) for a membrane DEA can be greatly improved by using a bias element with a profile aligned with the DEA force characteristic itself. A bistable element called a negative-rate bias spring (NBS) was introduced and, when coupled with the DEA, it produced over 50% more stroke than the constant load counterparts. The next chapter will examine non-linear bias elements more closely.

Chapter 4 NEGATIVE-RATE BIAS SPRING MECHANISM

In this chapter contains a detailed explanation of NBS mechanisms: how they are made and how they can be used most effectively to perform work with the diaphragm membrane DEA. The design of the NBS used is detailed and tested and trends are shown. A stroke analysis for the DEA operating against loads is presented along with experimental results.

4.1 INTRODUCTION AND MOTIVATION

It was demonstrated in Section 3.2 that the loading conditions of membrane DEAs are very important and in particular that negative-rate bias springs can provide a larger stroke. These compliant structures show large geometric change when switched between the stable configurations. They have the positive features of having high load carrying capacity, high speed, and sudden energy release [136]. For the case of a bistable mechanism there are two stable positions (S_1 and S_2) and an unstable point B as seen in Figure 4.1.

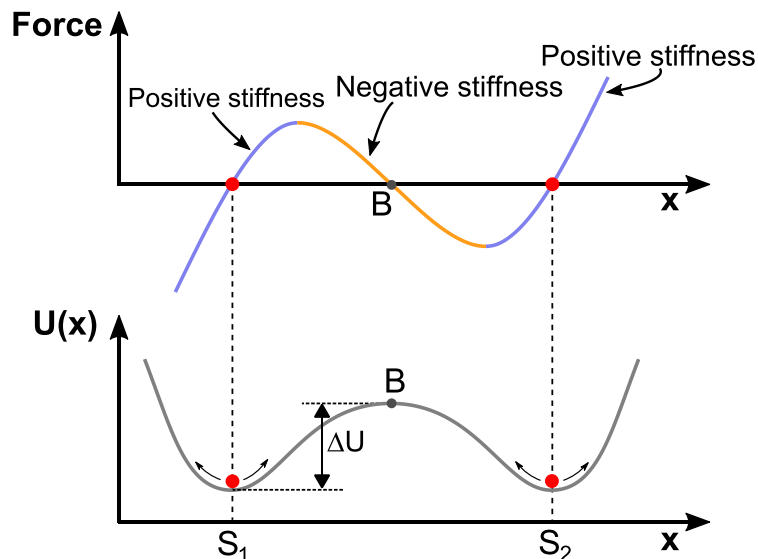


Figure 4.1: Force and stored potential energy of a typical NBS.

A switch will occur when the energy barrier ΔU is overcome. In the case above, the NBS is symmetric meaning the energy required is the same no matter the switching direction, however this is not always the case. For example, when the NBS is coupled to another mechanism, such as a spring or DEA, the $U(x)$ curve would be tilted and have one deeper well and one elevated well. This will be discussed and investigated further in Section 4.3.3.1.

As stated before, the NBS gets its name is due to the unstable region which predominately displays a negative stiffness. This provides an advantage when coupled with the DEA because the NBS force can increase when extending (as the DEA is actuated) and thereby perform more work against the DEA.

Since the NBS is a non-linear spring with at least 2 stable positions and the DEA is also non-linear (but stable) spring there are some extra challenges when designing a combined actuator system. The DEA+NBS system may or may not be bistable. One must choose the actuator mode based on the application. For example, if an open-close valve is required, possibly a bistable actuator would suffice, but if a proportional control valve is needed then a stable DEA mechanism would be more appropriate. One should also design the actuator with the component and external forces in mind. The challenge here lies in tuning (or designing) the NBS system to perform the desired work.

4.2 DESIGN AND FABRICATION

Bistable structures can come in many different forms and a variety of configurations have recently been built by researchers to match up with their respective membrane DEA configuration or application of interest. Some are made of four-bar linkages (rotational hinges, sliders and rollers) and springs [25], [137]–[139]. Some are built from bistable buckled members [24], [140]. The drawback of the linkages is that usually many parts must be assembled. As one would imagine this makes miniaturization challenging. For this reason, scalable mechanisms are very appealing for applications which need to be miniaturized, like DE actuators. One kind of scalable mechanism often found in applications are compliant mechanisms. These mechanisms are made to bend but do not undergo permanent deformation. Examples are buckled or post-buckled beams or monolithic structures with "living hinges" [141]. This is simply a bending joint which is thinned so that it is highly compliant. Figure 4.2 shows some examples of compliant mechanisms in literature.

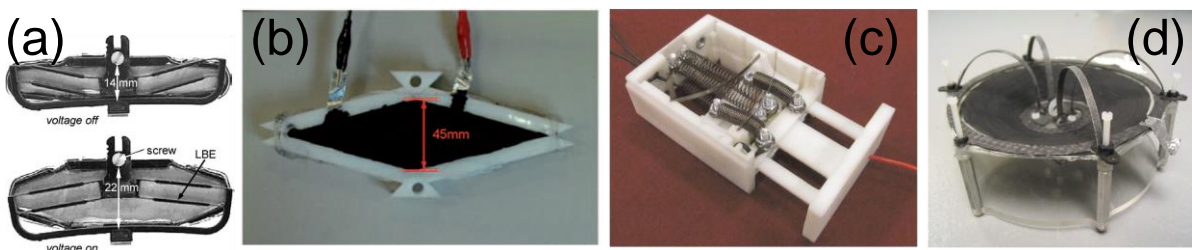


Figure 4.2: Examples of compliant mechanisms in literature (a) bistable element with parallel linkages [142], (b) Lozenge-shaped four bar linkage [106], (c) SMA compensating system which makes use of a system of post-buckled beams [143], (d) cone actuator deflected with carbon fiber leaf springs [144].

An advantage of these bistable mechanisms is that they contain fewer parts and there is no sliding or friction between parts. A disadvantage is that they sometimes undergo high stress when buckled.

Figure 4.3 presents sketches of two bistable mechanisms. One is realized through linear pre-compressed springs and rotational pivots/sliders and the other is made of slender post-

buckled beams. The figure presents the force profiles together showing some differences. The linear compressed spring mechanism exhibits more of a gradual change in force before reaching the critical force. The post-buckled beam profile is more abrupt because the beam suddenly begins to buckle resulting in a sharp decrease in force. These trends are discussed in the papers by Hodgins *et. al.* [94], [119].

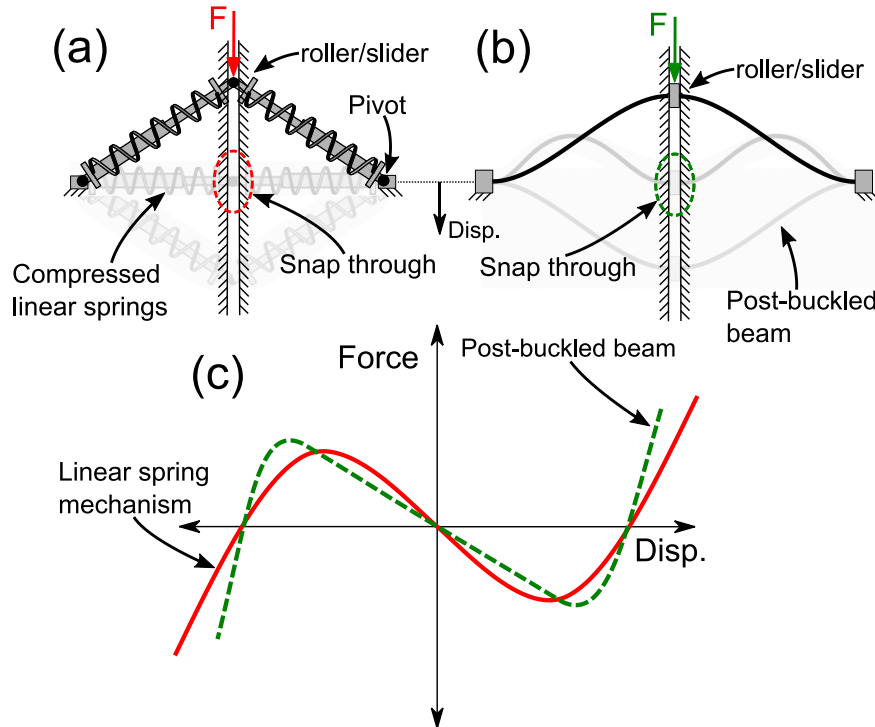


Figure 4.3 Bistable mechanisms and the force-displacement (a) Linear spring bistable mechanism, (b) Post-buckled beam bistable mechanism, (c) F-D response.

The NBS designed for this work is a post-buckled beam type. As already seen in Section 3.2.2.1. It consists of four beams (making an X-shape) which were wire electro-discharge machined (EDM) from a thin stainless steel sheet. Figure 4.4 presents the design.

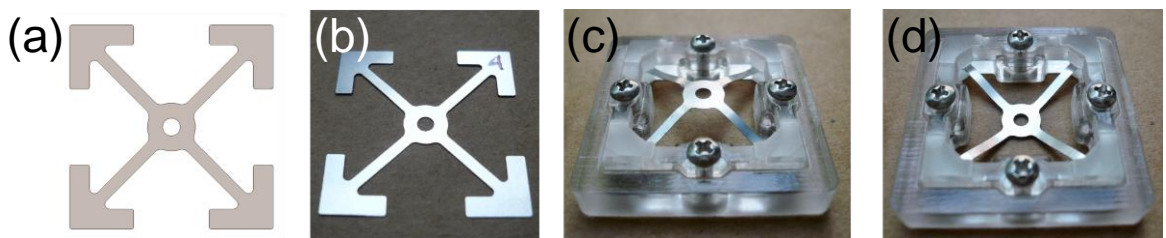


Figure 4.4: X-shaped bistable mechanism, (a) SolidWorks sketch of NBS, (b) photo unconstrained, (c-d) mechanically buckled and constrained into smaller frame, (c) shows upper stable position, and (d) shows lower stable position.

The thin X-shape is mechanically buckled into a square shape which is slightly smaller than the X-shape itself. This results in beams buckling out-of-plane Figure 4.4(c-d). The square frame was designed with SolidWorks and printed with a 3D-printer (OBJET Connex500). A 3D-printed cover frame is screwed down over the NBS to completely secure it. The force-displacement response of the mechanism is measured by controlling the position of the center of the mechanism and recording the force (as shown before in Figure 3.8).

Many different force profiles are achievable by varying the beam thickness (t), beam width (w) and the amount the beams are post-buckled (measured as a fraction of original beam length L_0). Figure 4.5(a-d) below shows some trends.

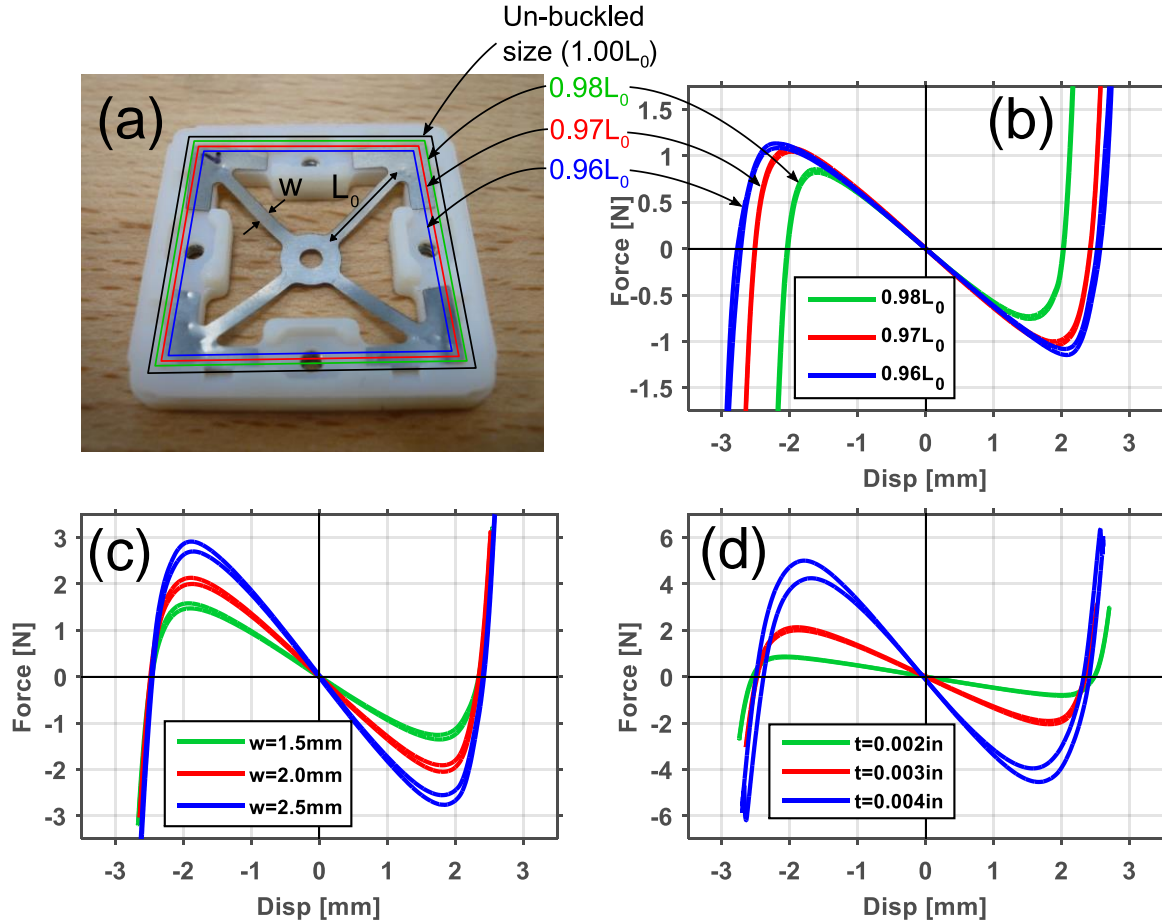


Figure 4.5: NBS parameter variation, (a) Buckling frame with dimensions; Force-displacement response and variation of (b) buckling amount, (c) beam width, (d) beam thickness.

By decreasing the size of the buckling frame (i.e. increasing the buckling amount) the stable equilibrium distance increases, Figure 4.5(b) but the negative slope remains constant (when $w=2.5\text{mm}$, $t=0.002\text{in}$). By increasing the beam width (w) the critical force increases, along with the negative slope (while $t=0.002\text{in}$ and Buckling = $0.97L_0$), Figure 4.5(c). Increasing the beam thickness results in a large increase in the peak force as well as an increase in negative stiffness (while $w=2\text{mm}$ and buckling= $0.97L_0$).

In summary, this simple X-shaped NBS design offers several tuning parameters to obtain other force responses. This is helpful for generating the NBS needed to match the DEA. The next section will discuss various ways to improve the DE actuation behavior by the use of this mechanism.

4.3 MECHANISM COUPLED TO DEA

4.3.1 Approach

In order to design and use a NBS mechanism appropriately with a membrane DEA to perform work, several considerations must be made at the beginning. For a given force/stroke requirement one can design the NBS for the DEA *or* design the DEA around the given NBS.

For this work and analysis, the membrane DEA is a diaphragm configuration with a fixed geometry. The actuators can be stacked together, as explained in Section 3.1 (p.20). This connects them mechanically in parallel which scales up the blocking force as well as the positive and negative behaviors observed (like hysteresis, capacitance, electrode resistance, probability to failure, etc.) Additionally the probability of failure is higher because of the increase in electrode surface area [145]. Similarly, the parallel capacitance increases with layers, meaning more charge is required and there will be a higher current draw to activate the actuators, especially at high rates. Therefore, it is advantageous to simply not add any unnecessary layers.

With a given DEA force response, one must design and adjust the NBS to fit the given diaphragm DEA for the given job. This is the approach applied here.

4.3.2 Background

When coupling a bias mechanism to the diaphragm DEA it must deflect the DEA out-of-plane—leading to a force equilibrium between the two mechanism or springs. If a linear spring and a DEA are coupled there is only one solution (Figure 4.6(a)). There can never be a bistable structure in this case because there is only a single equilibrium point. However, when a NBS and DEA are coupled there can be a case when the equilibrium paths cross more than once—giving *multiple solutions*. This case is represented by the sketch in Figure 4.6(b). The points S_2 and S_3 are *stable* solutions and S_1 is *unstable*. (It is possible to use a mechanical stop to stabilize this actuator on the negative branch and make a *bistable* actuator, as was shown in Section 3.2.) Point S_3 is not a viable solution from a practical standpoint because the actuator is intended to operate out-of-plane to the right (positive displacement), serving as a push actuator. However, if the NBS is not as stiff as the DEA to which it is coupled, it is possible to have a single *stable solution* on the normally unstable branch of the NBS. Here Figure 4.6(c) represents this case when the NBS is quite soft and exhibits only one solution when paired with the DEA. The Figure 4.6(c) solution might be advantageous for a stable actuator, though the size of the NBS is a drawback.

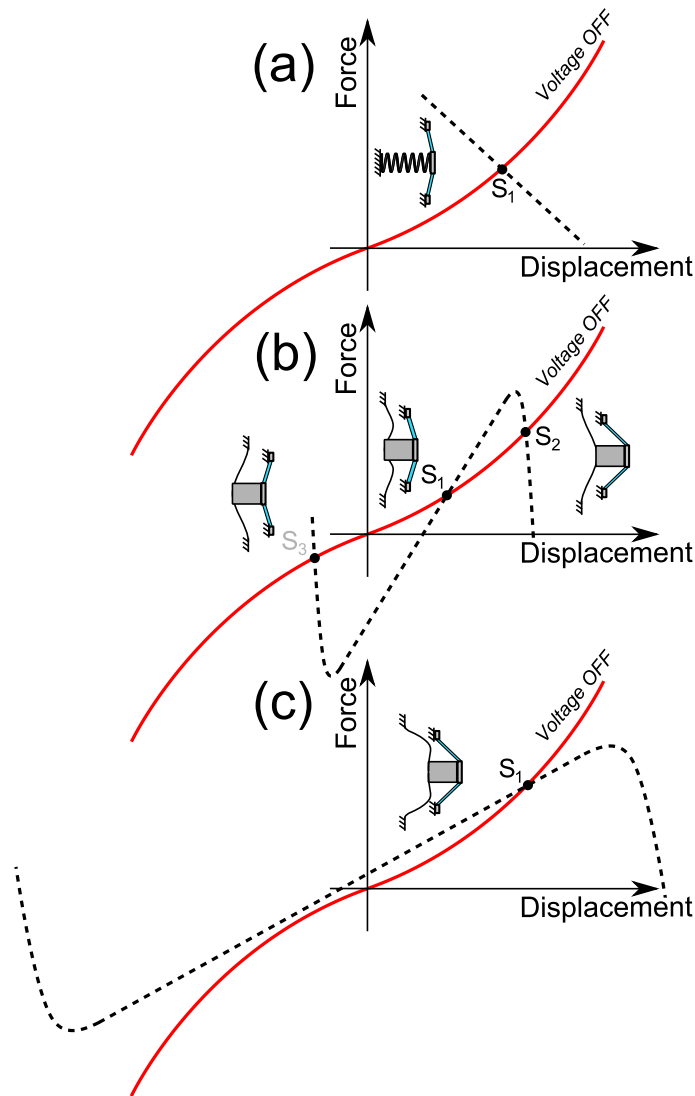


Figure 4.6: Graphical solutions when DEA and bias mechanisms are coupled, (a) linear spring and DEA, (b) stiff NBS and DEA, (c) soft NBS and DEA with one solution.

The NBS needs to be so large for two reasons. The first reason is that the DEA has a relatively low-stiffness, and to have a single stable solution on the negative branch, the NBS must have a local stiffness *less* than the DEA. To have a low-stiffness, the mechanism (assuming a post-buckled bistable mechanism) should have narrower post-buckled beams (as demonstrated in Figure 4.5(b-d)) or longer beams so the bending moment is reduced, and forces are lower. However, the longer the beam, the larger the geometric change between stable states.

The second reason for the large NBS size is due to the symmetric nature of the NBS. It needs to be bigger simply to achieve the correct stiffness can be achieved. But unfortunately since the left side of the DEA is not used, much of the NBS is wasted geometry.

On the whole, increasing the NBS size is not good (especially when miniaturization is considered). The longer the beams are, the larger the actuator footprint becomes. This is a critical consideration for product design.

One must also consider the required actuation force when designing an actuator. This is the force that the bias mechanism provides *in addition* to the force to stretch the activated DEA. See Figure 4.7 below.

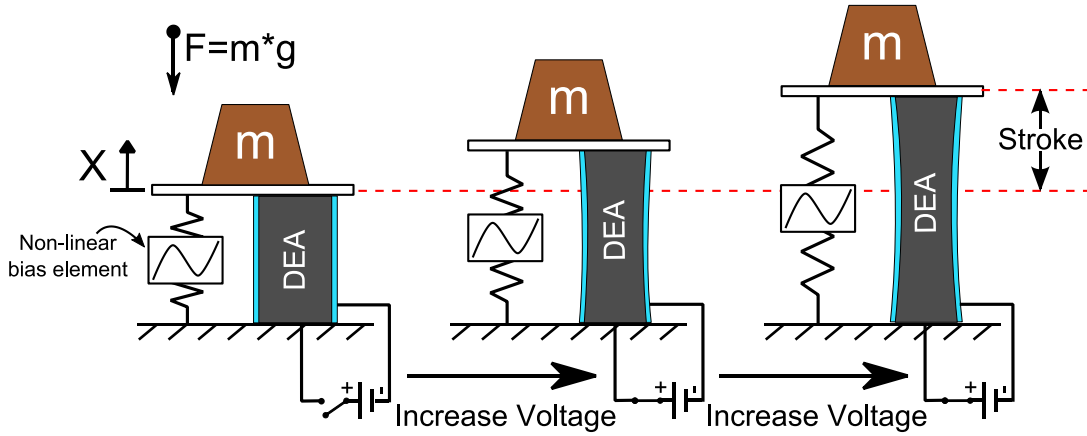


Figure 4.7: Generic membrane DEA+NBS system performing positive work as voltage is increased.

In this example, work is performed on the mass by the DEA+NBS system. The weight of the mass disturbs the DEA+NBS force equilibrium, so it must be accounted for in the stroke analysis. In maximizing actuator work output, the external forces should also be known so that they can be compensated for in the design of the DEA+NBS system.

4.3.3 Stroke Analysis

4.3.3.1 Influence of linear springs on NBS

A solution to the challenge of designing a NBS mechanism which accounts for the external force is to use an asymmetric bistable mechanism. This is a mechanism in which one stable potential energy state is higher than the other. It may look like the one shown in Figure 4.8(b). The energy difference between the wells is ΔU , which is also the net energy the mechanism can store/release.

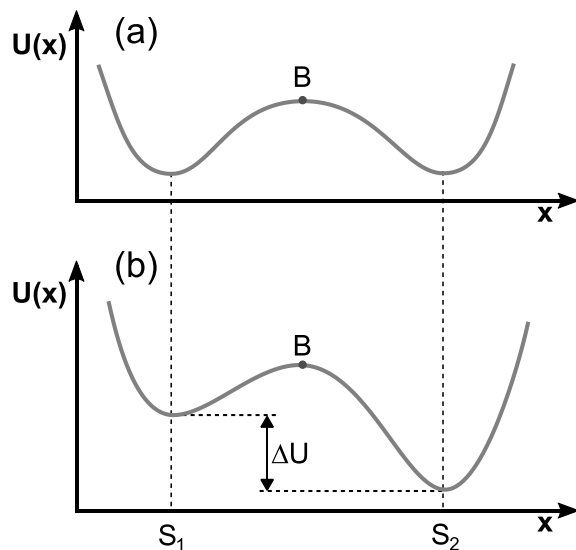


Figure 4.8: NBS energy landscape: (a) Symmetric vs (b) Asymmetric bistable mechanism showing tilted energy wells.

To make such a mechanism the NBS itself can be modified (through beam geometry and/or beam boundary conditions, see Appendix A) or by simply *adding another mechanism* (such as a linear spring) in series to the NBS (Figure 4.9).

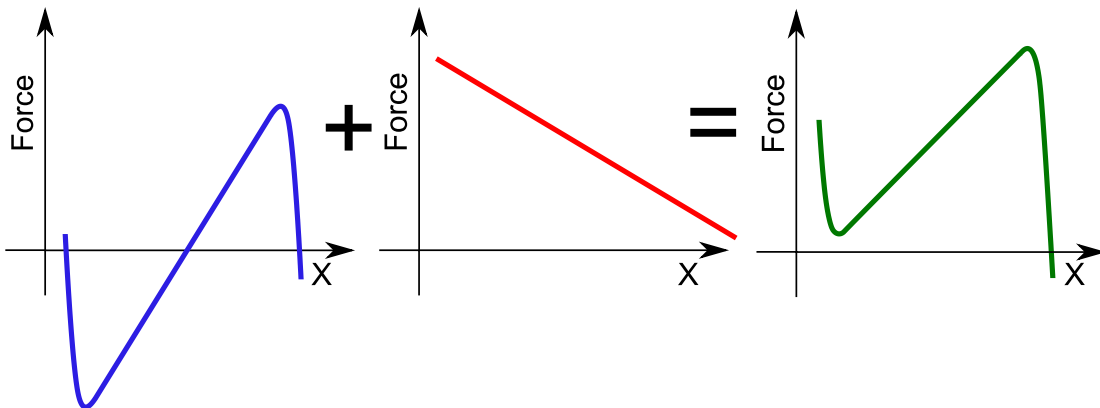


Figure 4.9: Combination of NBS and linear force resulting in a shifted or asymmetric bistable mechanism.

From the force perspective, the linear element shifts the NBS curve up and effectively "softens" the NBS negative stiffness branch. If the linear spring is compressed sufficiently against the NBS, one zero-force equilibrium can disappear altogether, as shown in Figure 4.9.

In terms of potential energy, the linear spring (with $U = x^2$ form, a parabola), when summed with the NBS, tilts the potential energy landscape, making one minimum more favorable than the other.

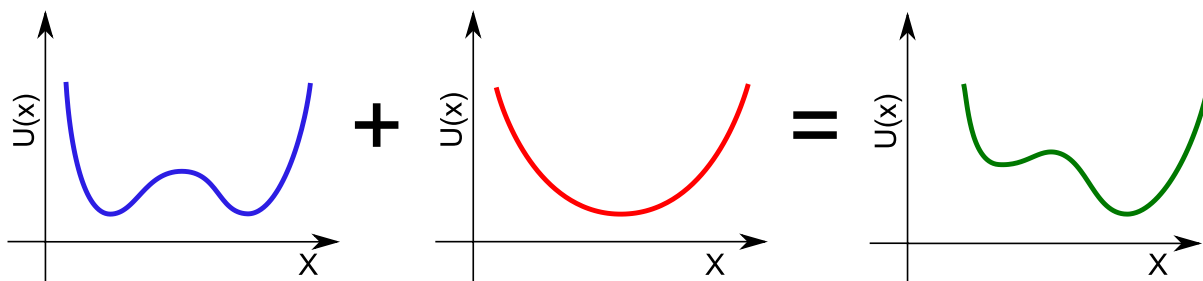


Figure 4.10: Transformation of energy landscape by combining a symmetric NBS and a linear spring to produce an asymmetric bistable mechanism.

The potential energy difference between wells can be used to the advantage of the actuator. For instance, the bistable structure can be used to store energy by being stabilized in the upper well (through work done by an actuator) and then can be released by exerting only enough energy to overcome the U-barrier from S₁ to B, Figure 4.8(b). Once the barrier is overcome, the energy is suddenly released and can, for example, be used against a load. (The load can be the combination of the DEA and an external force.) The deactivated actuator can then return the NBS to the upper energy well.

In summary, by adding a linear spring to a stiff NBS, a NBS can be "softened" and made adjustable. Since linear springs are a standard mechanical component sold by many suppliers adding them to the NBS is often more advantageous than redesigning and fabricating an entirely new NBS post-buckled mechanism with the appropriate stiffness to match the DEA.

The linear spring gives the engineer more freedom when designing the bias mechanism. Figure 4.11 below illustrates the impact the linear spring parameters (stiffness and pre-compression) have on the resulting NBS behavior. In particular, it is shown that the linear spring provides a way to adjust the NBS profile vertically with little impact to the NBS profile, i.e. it maintains a bistable region. By increasing the linear spring stiffness, it gradually cancels the negative-rate stiffness region—softening this region. If the linear spring is stiff enough, it can essentially negate the bistability altogether.

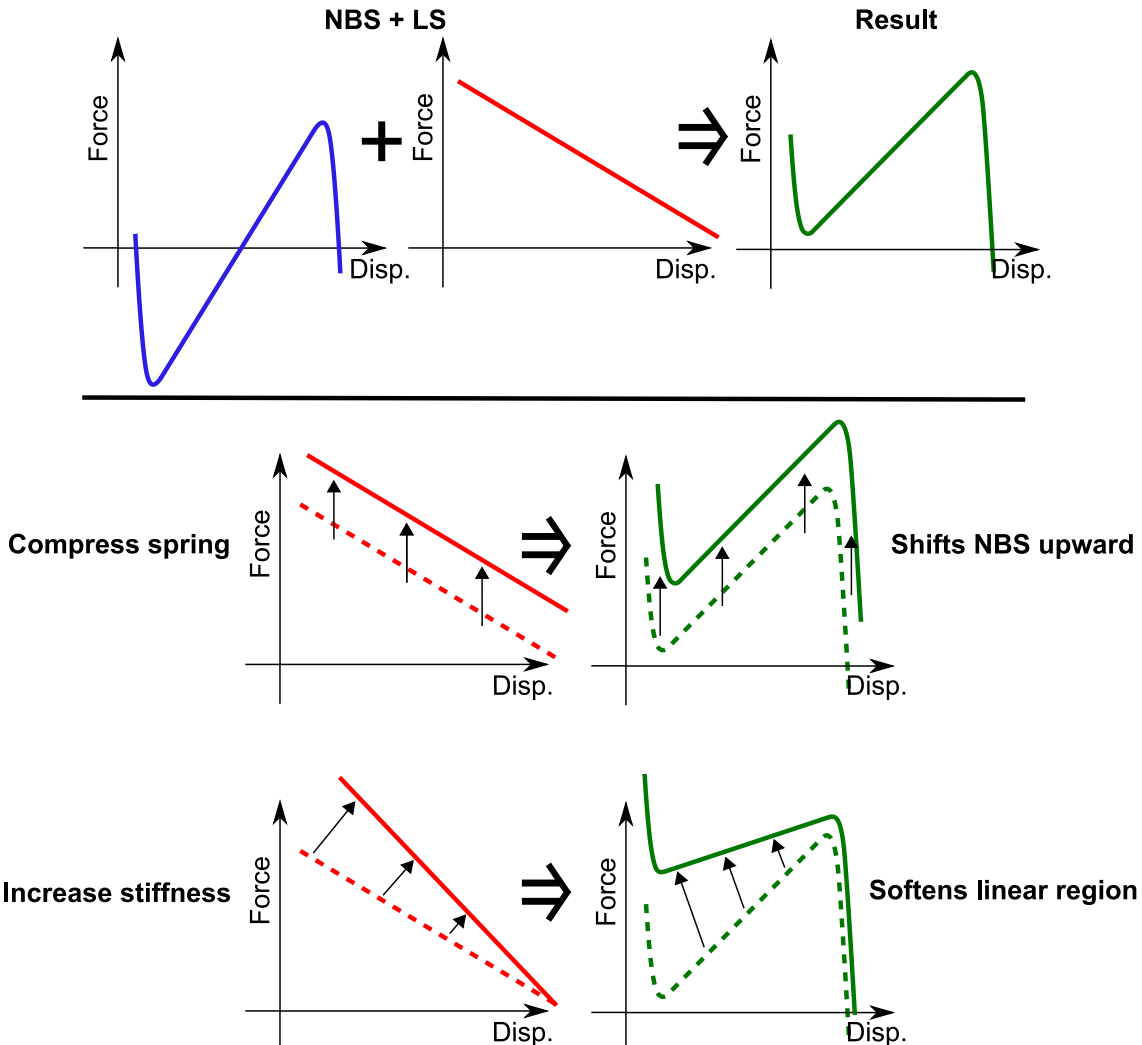


Figure 4.11: Influence of linear spring on NBS behavior.

Figure 4.12 shows the result of the NBS+LS system coupled with a DEA. Part (a) presents the bias elements just aligned with the DEA but without deflection. In Figure 4.12(b) the linear spring and NBS assemblies have been moved toward the DEA, deflecting the DEA and the NBS+LS system. One can see that this yields a much larger stroke than if any one component biases the DEA alone. Note that while the linear spring may add to the length of the actuator, the footprint does not necessarily increase because of the spring's small diameter.

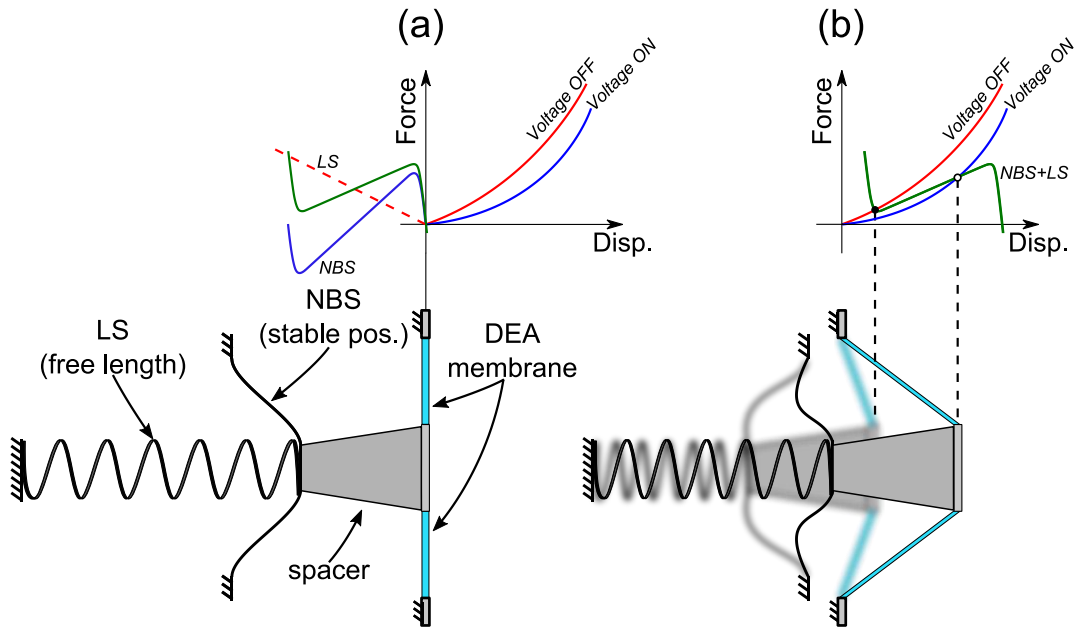


Figure 4.12: Sketch of tuned NBS+LS mechanism with DEA (a) Un-deflected and (b) deflected DEA and giving actuation stroke.

4.3.3.2 Influence of external forces on stroke

The analysis of the actuation of the DEA with the NBS system up to this point included no external forces. The NBS was working only against the DEA. For these actuators to be of any practical use, they must perform work—on external objects (see Figure 4.7), such as lifting a mass, closing a valve, or pumping fluid.

Assuming the work required (Force \times Distance) is known, this force should be included in the Force-Displacement plot when designing the biasing element. Below a sketch of a case when a DEA is loaded with a hanging mass.

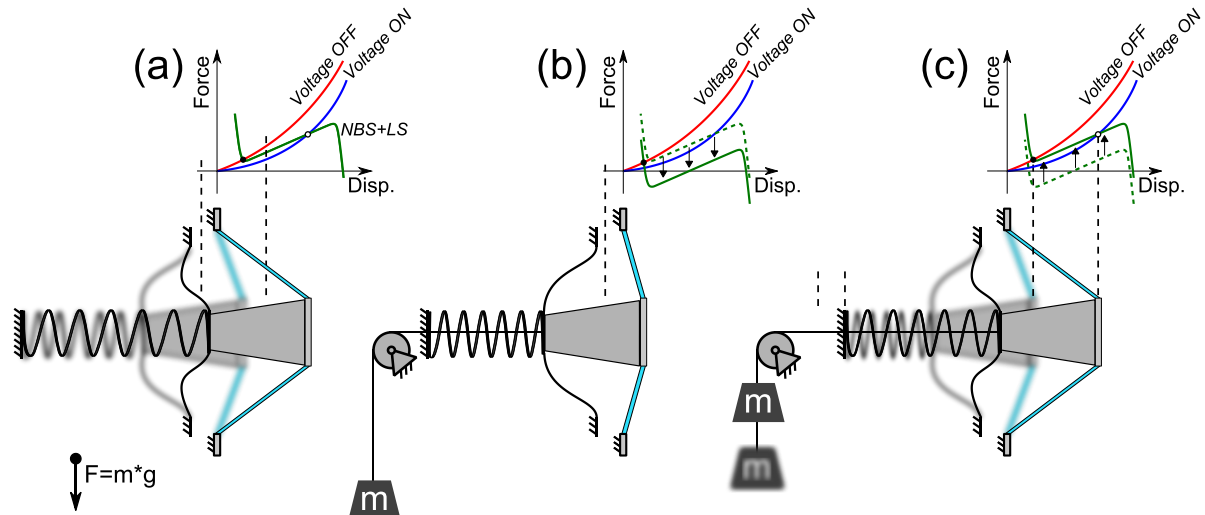


Figure 4.13: Sketch of loaded DEA (a) tuned DEA without mass, (b) mass loaded DEA not tuned to load, (c) mass loaded DEA tuned by compressing linear spring.

The force the mass adds to the DEA can be accounted for by compressing the linear spring, and thus shifting the NBS profile upward Figure 4.13(c). The linear spring is tunable and is

limited only by the blocked force of the linear spring (that is, when the spring is at the maximum compression).

An alternate way of representing the actuator behavior on a Force-Displacement graph is to plot the Actuator (output) Force, at the deactivated and activated states (LV and HV states). This is a quasi-static measurement, which when plotted clearly, shows the obtainable actuation forces. By plotting the load one can also see how the actuator would perform based on the intersection of the LV and HV curves with the load. Below is a free-body diagram of a generic actuator system (DEA biased with a linear spring) to show the derivation.

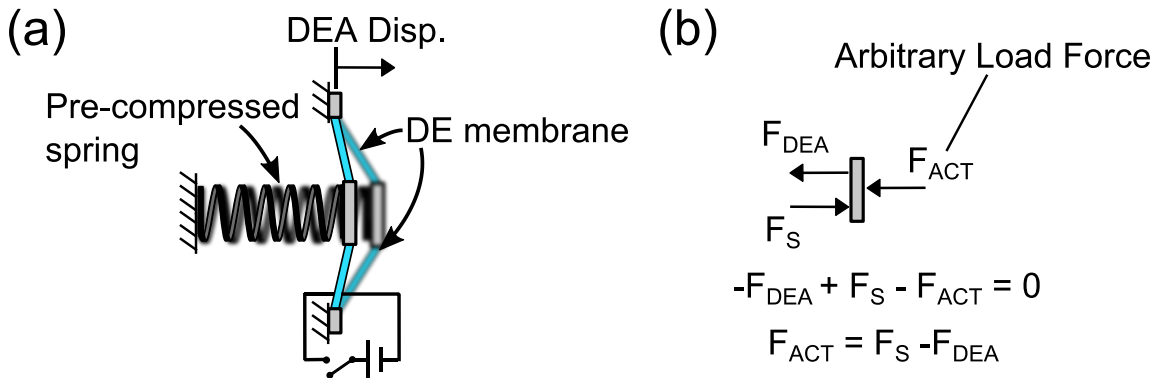


Figure 4.14: DEA actuator force (a) Sketch and (b) Free-body diagram of mechanism showing the actuator force (F_{ACT}).

The actuator force is the bias spring force less the DEA force. Figure 4.15 presents the F_{ACT} for a DEA biased with a linear spring.

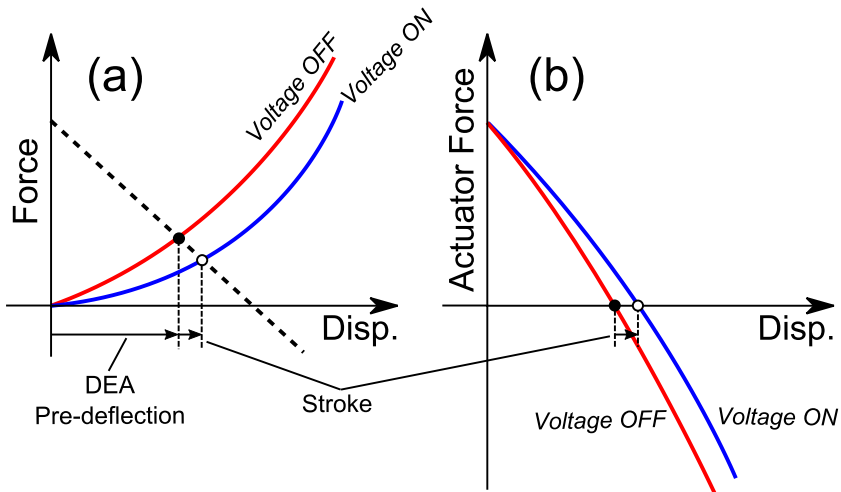


Figure 4.15: Actuator force produced by linear spring, (a) force equilibrium, (b) actuator force plot showing stroke with 0N load.

Figure 4.15(a) is the force-equilibrium of a linear spring. Figure 4.15(b) highlights the stroke for a no load case. The trends show that by increasing the load in the positive direction the stroke would decrease slightly, but by reversing and increasing the load in the other direction (making it negative) the stroke would increase slightly. It is possible to negate the stroke altogether by adding load negating pre-deflection and stroke.

When examining the actuator force for a NBS+LS system, one will note that the stroke is larger but more sensitive to external forces. Figure 4.16(a) shows the force equilibrium case of a NBS+LS system with large stroke. Figure 4.16(b) highlights the actuator output force for an unloaded case.

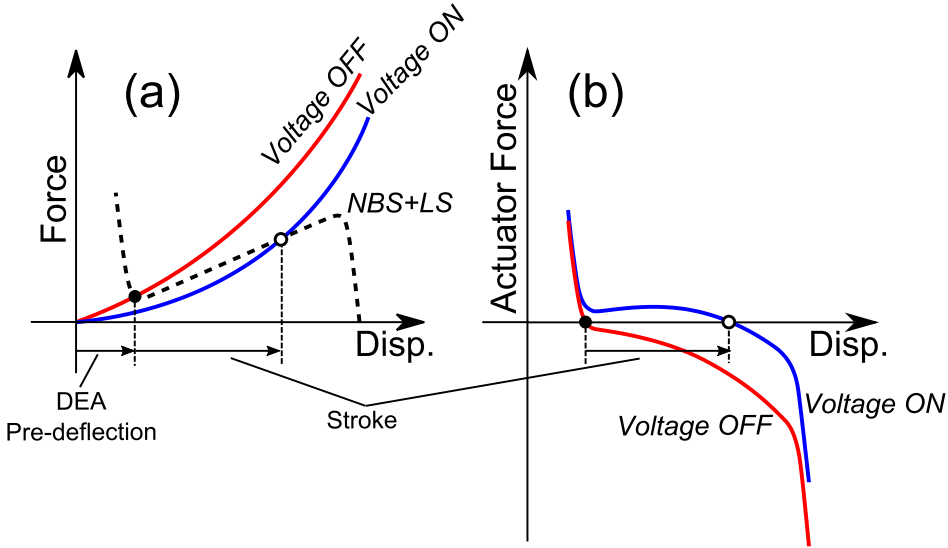


Figure 4.16: Actuator force produced by NBS+LS mechanism (a) Force equilibrium, (b) actuator force plot showing stroke with 0N load.

However, the actuator is very sensitive to any change in loading conditions because the bias element is quite compliant and has a stiffness similar to the DEA itself. If the load were increased (in the positive direction) the stroke would drop almost immediately to zero. If the load were reversed (pulling on the DEA), the stroke would still decrease eventually to zero, but not as quickly.

Therefore, the system must be tuned to each constant load applied. In the following sections a DEA with a NBS+LS bias system is tested against constant loads. The results serve as a validation of the theory presented in this section and empirically show the advantage of using a linear spring to tune the system against varying constant forces.

4.4 RESULTS AND EXPERIMENTAL VALIDATION

4.4.1 NBS + Mech. Stop

To illustrate the impact a small external force can have on a membrane actuator, this section presents a test with a NBS, a mechanical stop and an external force. The NBS and mechanical stop were appropriately coupled with the DEA to make a bistable DE actuator (as in Section 3.2.3.3) and a hanging mass was the external force.

4.4.1.1 Setup and Procedure

Figure 4.17 shows both a photo and a sketch of the test rig. The diaphragm DEA is mounted onto a movable platform (Newport) which is actuated by a Zaber LA-28A linear actuator. A Keyence LK-G37 laser displacement sensor is mounted on the platform behind the DEA. The

NBS is mounted and fixed in position relative to the moving platform and collinear with the center axis of the DEA. The center of the DEA is connected to the NBS with a plastic spacer. As the moving platform is actuated in the direction of the NBS, the spacer in between the NBS and DEA pre-deflects the DEA out-of-plane. The deflection of the center of the DEA is measured with the Keyence laser displacement sensor. A second linear actuator (Aerotech, model ANT-25LA with an Aerotech Ensemble ML controller) is positioned and fixed behind the NBS, serving as the adjustable mechanical stop. A plastic extender is attached to the end of the linear actuator to serve as the mechanical stop and its shape allows enough room for the pulley and a thread to hang the mass. The thread is tied to the center of the NBS and guided over a plastic pulley with low-friction needle roller bearing.

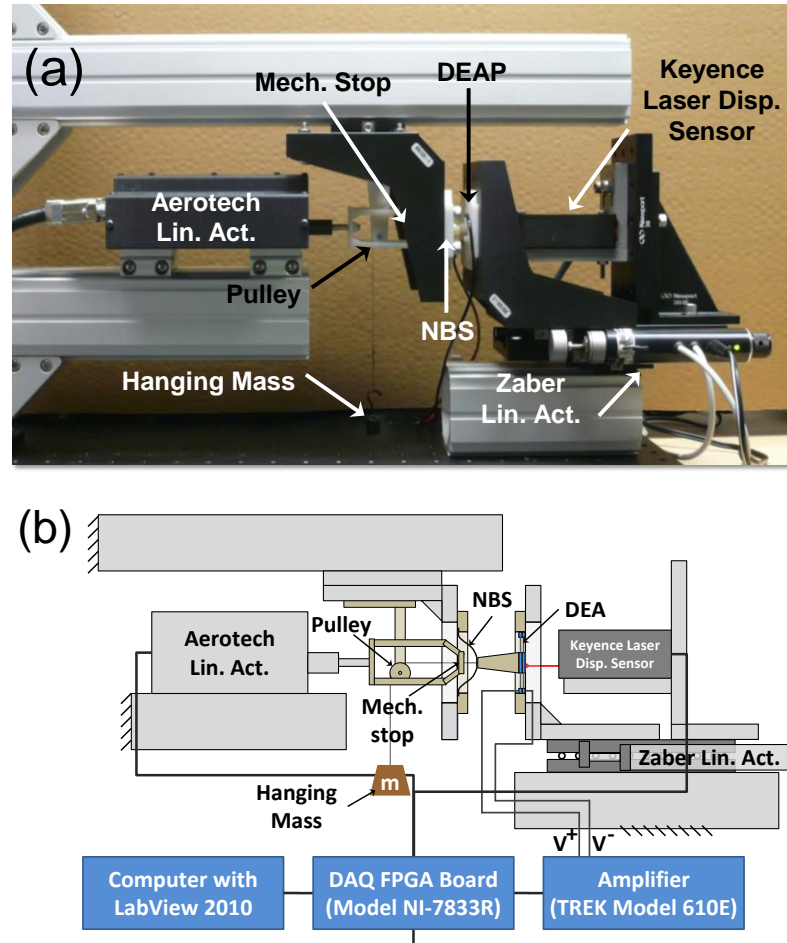


Figure 4.17: NBS with mechanical stop test setup (a) photo and, (b) schematic.

The DEA offset parameter is the position of the DEA outer frame which is controlled by the Zaber linear actuator. The x_1 parameter is the deflection of the center of the DEA from its un-deflected position. This is the value the laser sensor measured.

The DEA employed consisted of two stacked single-layer cartridges. The DEA was pre-deflected incrementally (with the Zaber linear actuator) and voltage on the DEA was linearly cycled from 0kV-2.5kV-0kV at rates of 0.1, 1.0 and 10Hz. The actuator was first tested without a hanging mass and then repeated with a hanging mass of 20 grams.

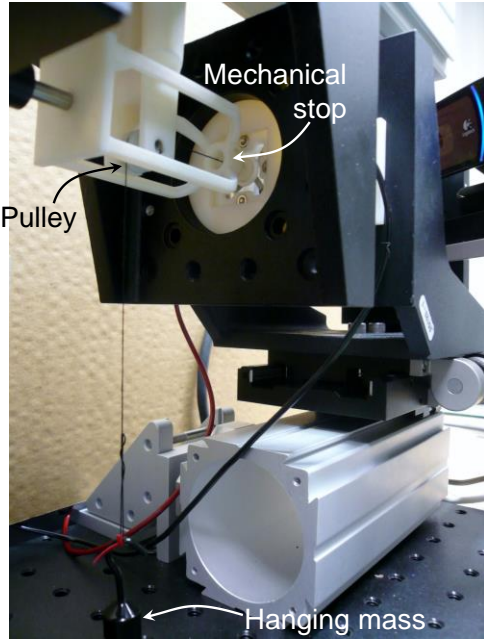


Figure 4.18: Photo of test rig with mass attached (20 gram) to NBS (DEA not visible).

4.4.1.2 Results

Results without mass for 0.1Hz are show in Figure 4.19(a-b). In the bistable region the largest displacement is approximately 1.5mm at a DEA offset of 4.8mm. Figure 4.19(a) presents the DEA output (x_1) (for 0.1Hz excitation) at various DEA offsets, highlighting the bistable region. In Figure 4.19(b) one cycle of DEA output vs. voltage is plotted. This clearly shows the large stroke for the bistable cases (DEA offset = 4.5 and 4.8). The higher DEA offsets (more pre-deflection, e.g. 5mm) results in a blocked actuator and low deflections behave like a linear spring.

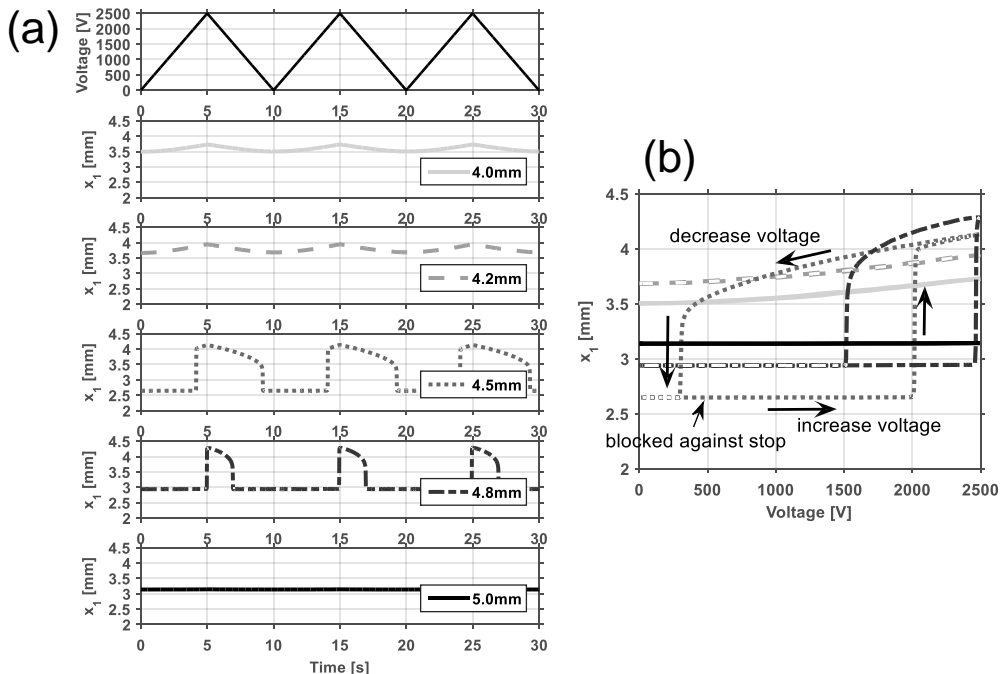


Figure 4.19: Test result of NBS without mass (a) time resolved stroke for different frame positions (DEA offsets), (b) stroke vs. voltage for same frame positions revealing stable, bistable and blocked cases.

When a 20 gram mass is added to the system the results are quite different (Figure 4.19(b)). The bistable stroke is no longer as it was with no mass. The maximum stroke is approximately 0.5mm at a DEA offset of 3.8mm.

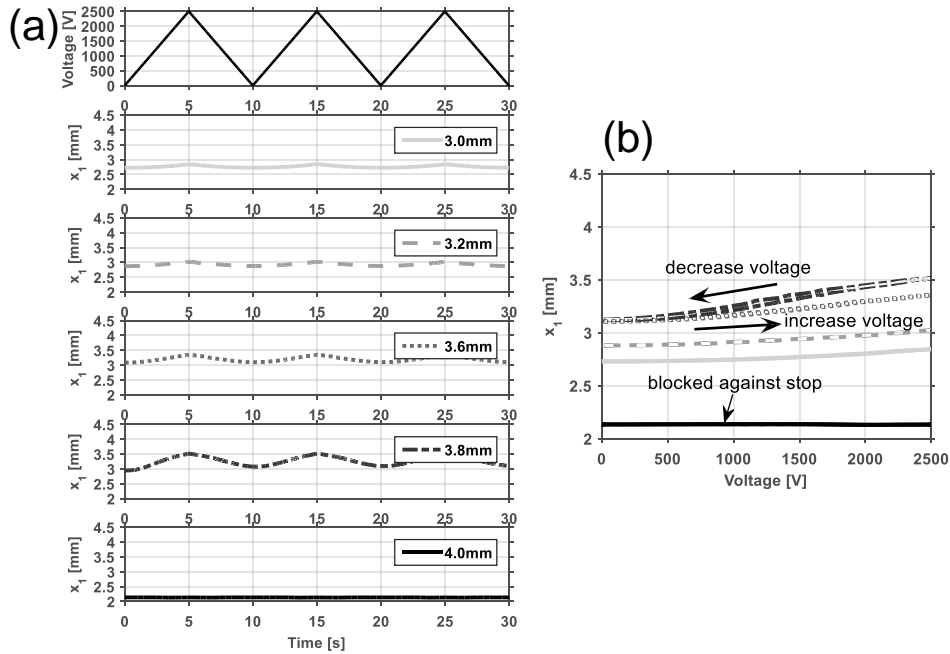


Figure 4.20: Test result of NBS with mass (a) time resolved stroke for different frame positions (DEA offsets), (b) Stroke vs. voltage for same frame positions revealing blocked or small actuation stroke.

A direct comparison of the stroke with a mass and without a mass is shown in Figure 4.21. The difference is clear. The external load on the actuator essentially removes the bistable behavior, substantially reducing the stroke over the range of pre-deflections.

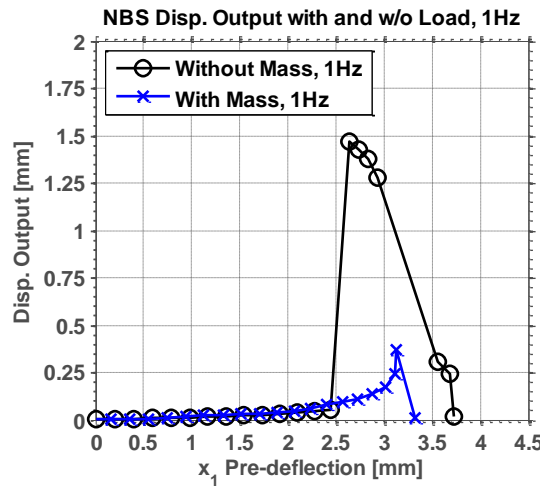


Figure 4.21: Comparison of stroke output with mass and without mass

4.4.1.3 Discussion

To understand failure of the DEA to perform work against a payload one should examine the force-equilibrium of the actuator.

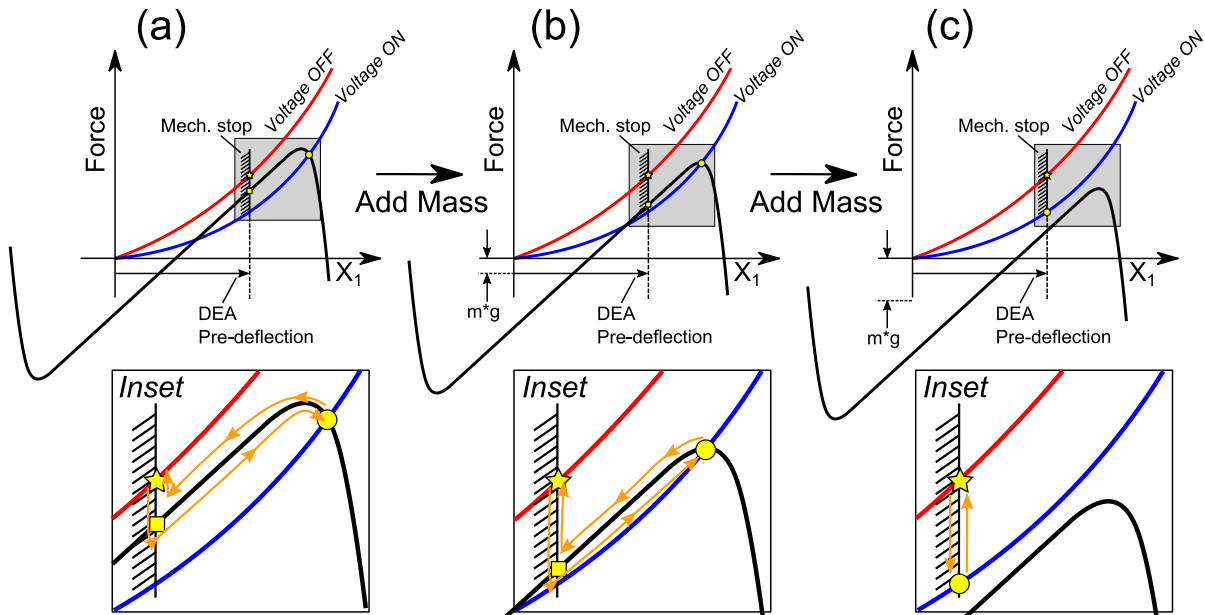


Figure 4.22: Stroke development when adding mass (with mech. stop), (a) no mass with large bistable stroke, (b) small mass reducing stroke slightly, (c) large mass with no displacement stroke (actuator blocked).

Figure 4.22 shows force-equilibrium sketches of the DEA with the NBS for a gradual addition of mass. The initial force equilibrium (at 0kV) is denoted by a star (*) symbol. The equilibrium point at the 2.5kV is denoted with a circle (°) symbol. The equilibrium point at which the NBS snaps away from the mechanical stop is denoted by a square (□) symbol.

Firstly, Figure 4.22(a) shows the DEA being pre-deflected by the NBS and being stabilized by the mechanical stop. In this position, the NBS begins against the mechanical stop because the DEA force is greater than the NBS force. As the voltage is increased, the stop force decreases until the force of the NBS overcomes the DEA (see □ symbol) and the NBS snaps away from the mechanical stop to a new equilibrium on a higher voltage curve. The force equilibrium position will continue to change until the voltage reaches the maximum of 2.5kV, denoted by the circle symbol (°). When the voltage is lowered the reverse happens. The NBS maintains equilibrium with the DEA until the DEA becomes so stiff that it overcomes the NBS force. Then the NBS must snap against the mechanical stop and return to equilibrium at the star (*) symbol.

The addition of a mass to the system (Figure 4.22(b)) results in the NBS force curve “falling down”. This is because the force from the mass (negative force) is added to NBS bias force and as a result it reduces the NBS force when plotted with the DEA curves, essentially softening the NBS with respect to the DEA. As the Figure 4.22(b) plot shows, this results in a snap behavior as before. However, the snapping away from the mechanical stop (see □ symbol) occurs at a lower force and also at a higher voltage level. As Figure 4.22(b) shows, this results in a slightly smaller stroke than the previous case, without the mass. As mass is gradually added to the system the stroke will continue to decrease until it becomes zero. There is a point when the NBS + m^*g force curve no longer intersects the mechanical stop within the DEA operating region (i.e. between the 0kV and 2.5kV curves). Therefore, even though the 2.5kV is

applied to the DEA, the NBS remains pressed against the stop. An example of this is seen in Figure 4.22(c), bottom. In this case, the force against the stop changes but it produces no stroke.

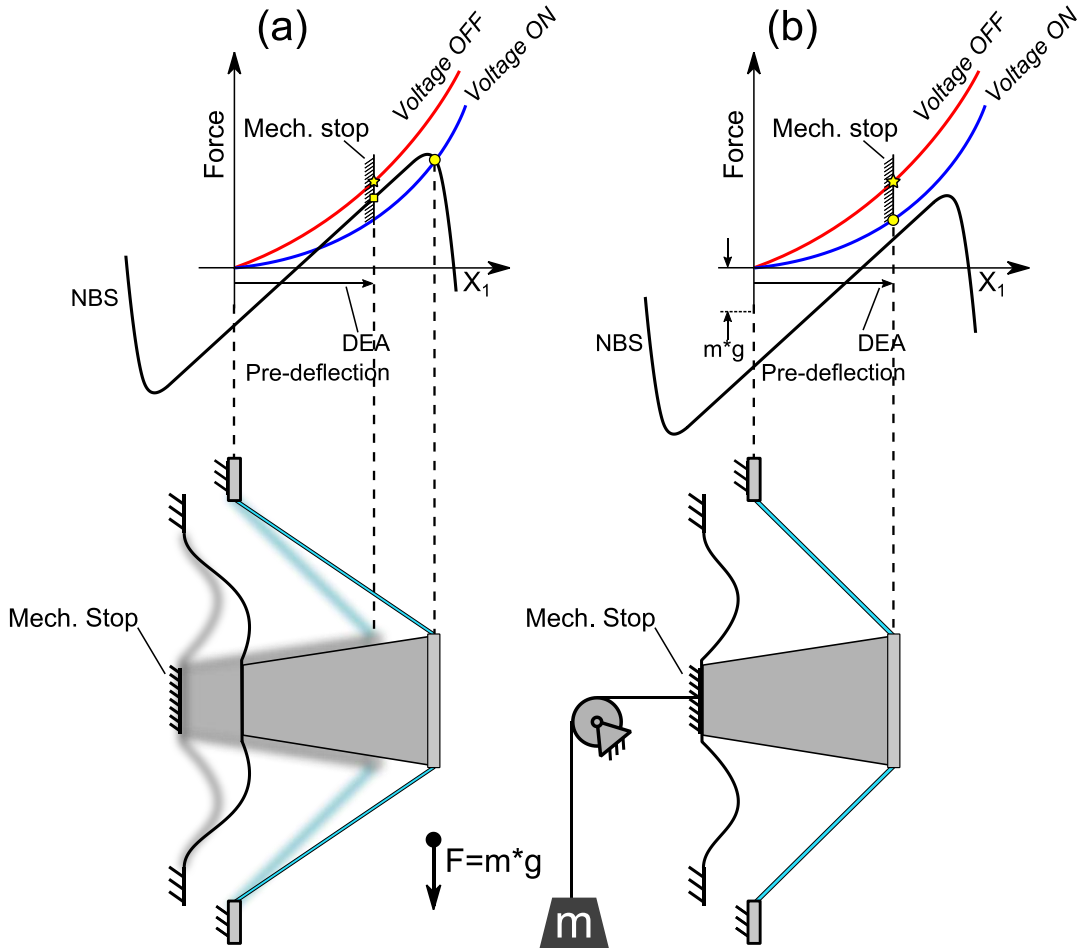


Figure 4.23: Effect of mass on actuator, (a) NBS + mechanical stop producing stroke, (b) mass added system resulting in blocked actuator.

Figure 4.23 shows a DEA without mass vs. a DEA with a mass. An unloaded DEA biased (to a particular pre-deflection) with an NBS reveals large stroke (Figure 4.23(a)). However, when a mass is added to the system Figure 4.23(b), the NBS force characteristic is shifted down with respect to the DEA characteristic curves. The loaded actuator produces no bistable displacement. This was demonstrated experimentally in the case shown in Figure 4.20 (blocked case).

One can clearly see from the tests, that the NBS biased DEA can produce large bistable stroke (with aid of a mechanical stop). It was also shown that when a 20gram mass was added to the previously bistable actuator the DEA large bistable stroke disappears. Theoretically, under the presence of a small enough mass (e.g. 10gr), bistable stroke could be obtainable but this was not shown experimentally.

4.4.1.4 Conclusions

These experimental results show the inadequacy of a NBS with a mechanical stop to bias the DEA and perform substantial work. When a payload was added to the system the bistable

behavior was nullified. The reason for the change was analyzed and qualitatively explained using a force-equilibrium argument. The suggestion to add a linear element (replacing the mechanical stop) to improve the stroke and obtain peak performance against a payload is covered in the following section.

4.4.2 NBS + Linear spring

As explained in Section 4.3.3.1 (page 37), when a linear spring is added to a NBS the mechanism can become asymmetrically bistable and the F-D curve will be softened and shifted upwards. To empirically document this effect, a force-displacement characterization was performed on a NBS+LS mechanism. A linear spring was simply aligned with the NBS and the force characteristic was measured, Figure 4.24(a-b). Figure 4.24(c) shows the results for a NBS and then the cases with linear spring at different compressions. Increasing the linear spring compression shifts the curve upwards. One case in literature where a similar mechanism (combination of a linear spring and bistable mechanism) is seen is in Chen *et al.* [146] where a monolithic constant force end-effector was designed.

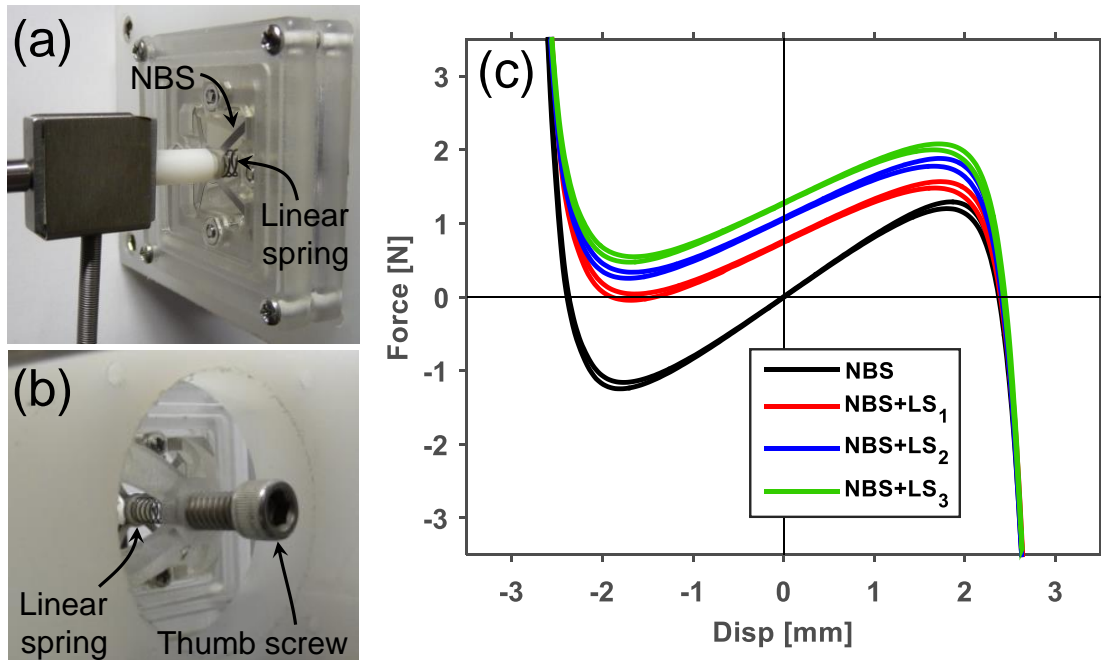


Figure 4.24: Test results for NBS+LS bias element (a) Photo of test rig from front showing NBS and LS being displaced by linear actuator, (b) Photo of test rig from rear revealing linear spring with adjustable thumb screw, (c) Force vs. controlled displacement results for NBS and NBS+LS at different linear spring pre-compressions.

The goal here is to perform a parameter study, in which the relevant bias mechanism parameters are studied. The linear spring has stiffness and length as inherent parameters and compressed length as an adjustable parameter. The NBS can likewise be positioned at varying distances from the DEA. Therefore, there are at least two independent parameters which need to be controlled in this test. Figure 4.25 shows a sketch of the DEA with the NBS and the linear spring.

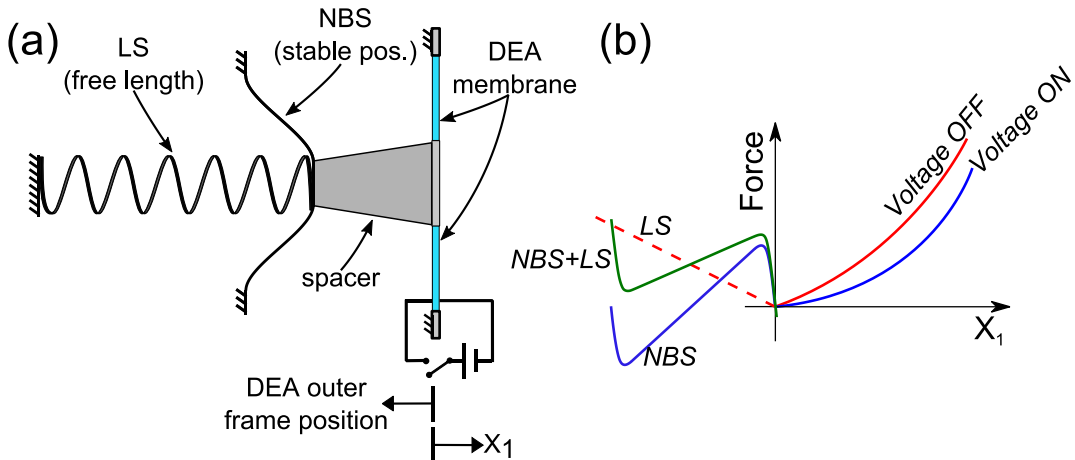


Figure 4.25: DEA biased by combination of NBS and linear spring (a) sketch, (b) Force vs- Displacement plot of individual elements.

The DEA outer frame position with respect to the NBS as well as the length (pre-compression) of the linear spring was varied. This enabled complete system characterization because the DEA pre-deflection and the linear spring deflection were variable. Additionally, the setup enabled an addition of a hanging mass to serve as the constant payload against the DEA.

4.4.2.1 Setup and Procedure

This combined NBS plus linear spring test setup was realized and is presented in the photo and sketch below.

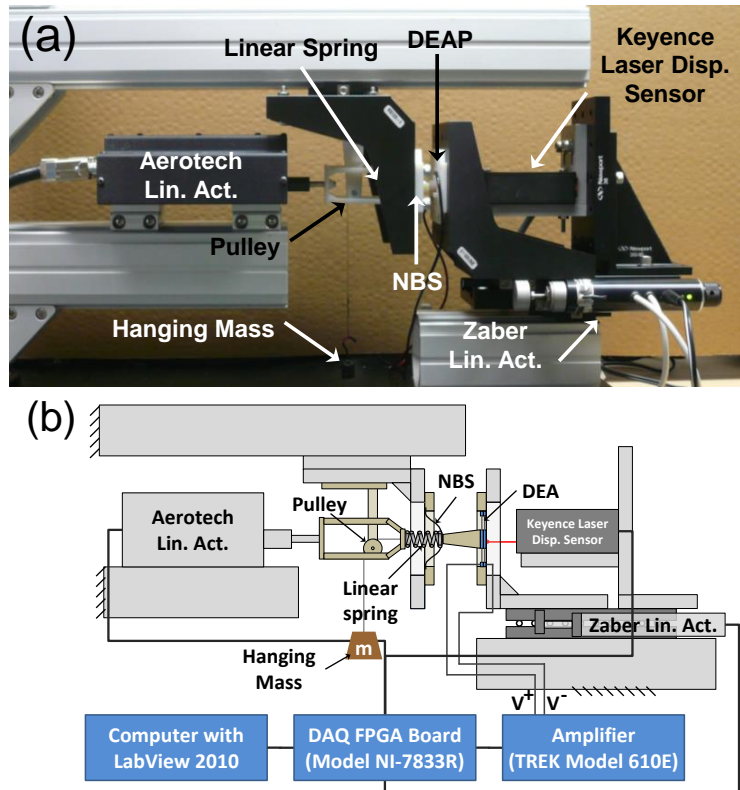


Figure 4.26: NBS with linear spring test setup (a) photo, (b) schematic.

The test was enabled by the two linear actuators to control the deflection of the DEA and the linear spring. The out-of-plane DEA displacement was tracked with a laser displacement

sensor which was mounted to the linear stage which was moving to deflect the DEA against the NBS. The setup was also designed to add a constant payload via a hanging mass and pulley system. See figure below for more visual details.

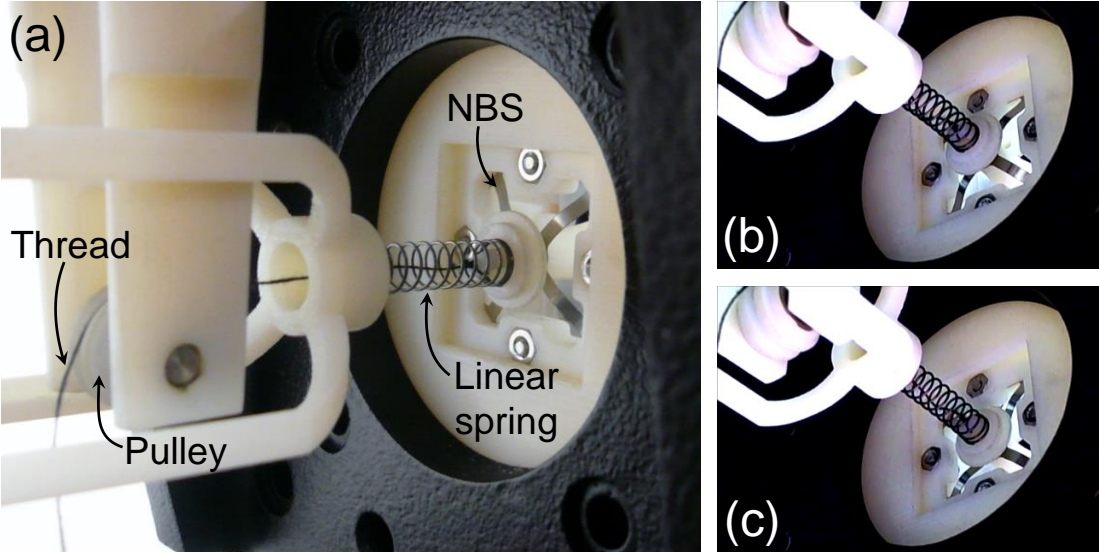


Figure 4.27: Photos of setup, (a) Close up of NBS and linear spring, (b) mechanism with low voltage, (c) mechanism snapped out when high voltage applied.

Before beginning the parameter study, the setup was initialized as follows. The NBS was manually snapped to the stable position to the right. The DEA frame was moved so that it was just in contact with the NBS (laser sensor used to sense contact). The linear spring was then moved to make contact with the NBS (load cell used to sense contact). These were the initial conditions (sketched in Figure 4.25). If a load was being tested, at this point the mass would be carefully hung on the thread.

Various combinations of DEA deflection (achieved by varying the DEA frame position) and linear spring compressions were set. Next, the voltage was applied linearly and the stroke was measured. For one NBS mechanism, three different linear springs (with stiffness constants $k= 0.174, 0.240, 0.377\text{N/mm}$) were coupled and tested. As before, measurements and control of the motors and sensors were performed using LabVIEW.

4.4.2.2 Results

Figure 4.28(a) shows the time resolved displacement results for a triangular voltage input. The figure shows the results for different linear spring, $k= 0.174\text{N/mm}$, compressions (1.1mm, 1.3mm...) while the NBS-DEA distance is fixed at 6.6mm. This plot reveals there are many types of displacements possible and they vary depending on the linear spring compression. The highest stroke in Figure 4.28(a) is approximately 2.5mm.

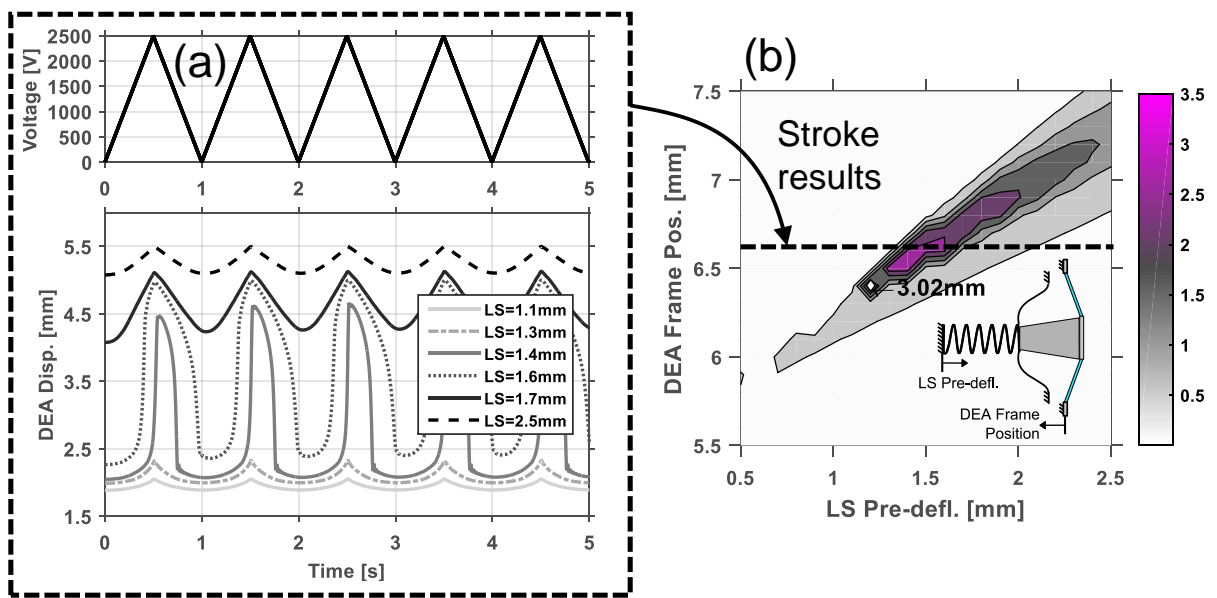


Figure 4.28: NBS + Linear spring stroke results without mass added at DEA frame position 6.6mm, (a) time resolved stroke at different LS pre-deflection levels, (b) Contour plot of stroke vs DEA frame position vs LS pre-deflection levels.

Figure 4.28(b) plots the measured stroke for a range of DEA frame positions and LS pre-deflections. The plethora of stroke results are summarized in this contour plot, showing that the optimum stroke has a magnitude of 3.02mm. The tuning of these two parameters are both quite sensitive. However there appears to be a small range of frame positions and LS pre-deflections that yields large results.

When a mass was added to the actuator, large stroke was still obtainable (as before) but at different linear spring pre-deflections. Figure 4.29 presents this case. The oscillations seen in the plot are due to the oscillations transferred to the center DEA disk from the hanging mass.

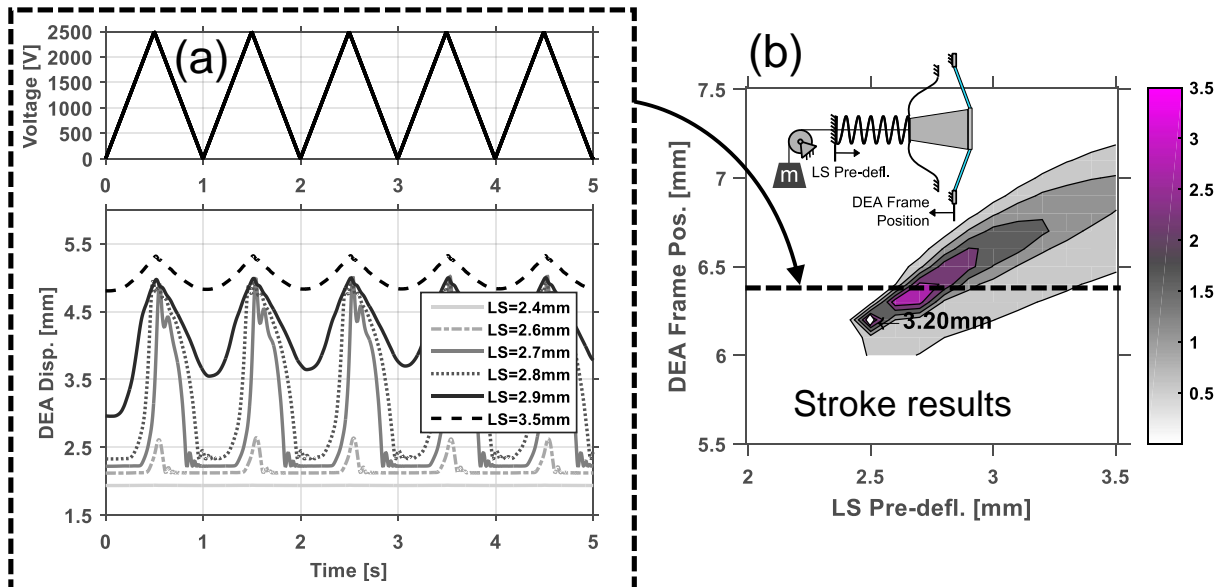
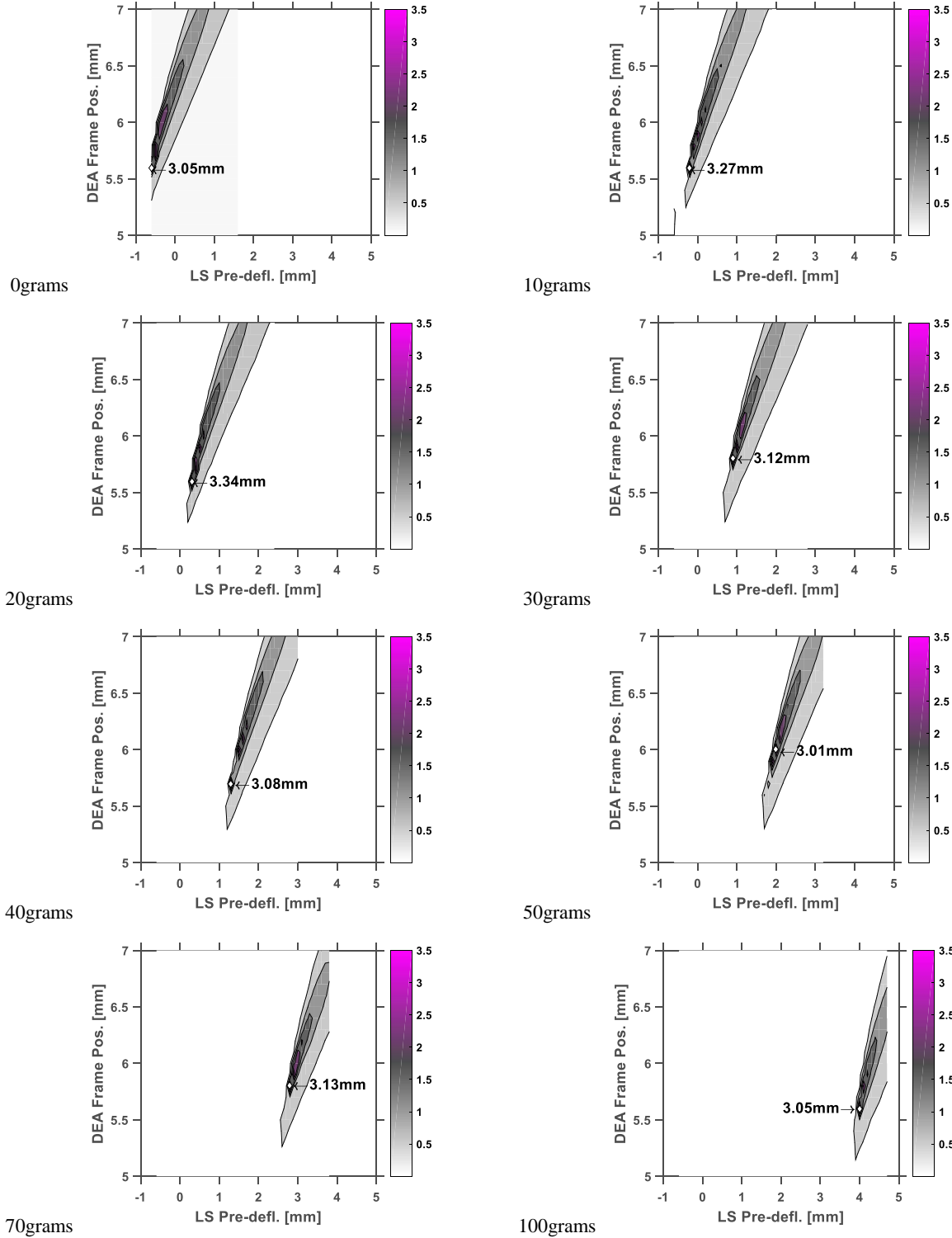


Figure 4.29: NBS + Linear spring stroke results with mass added (30grams) at DEA frame position 6.4mm, (a) time resolved stroke at different LS pre-deflection levels, (b) Contour plot of stroke vs DEA frame position vs LS pre-deflection levels.

By comparing the “ridge” of optimal values in Figure 4.28(b) and Figure 4.29(b), the main difference appears to be the higher LS pre-deflection. In order to illustrate this point further

Table 4.1 presents the stroke results when loaded by many different masses). Notice that a similar maximum stroke is obtainable at each level but at a higher linear spring pre-deflection.

Table 4.1: Stroke landscapes for different hanging mass loads. Stroke for different hanging mass levels (0-100grams) when using linear spring $k=0.24\text{N/mm}$.



The table of plots shows the ridge of optimal stroke moves to the right as mass is added. A stroke of at least 3mm is possible no matter the load faced. Figure 4.30 shows 3D surface plots of the stroke with different masses.

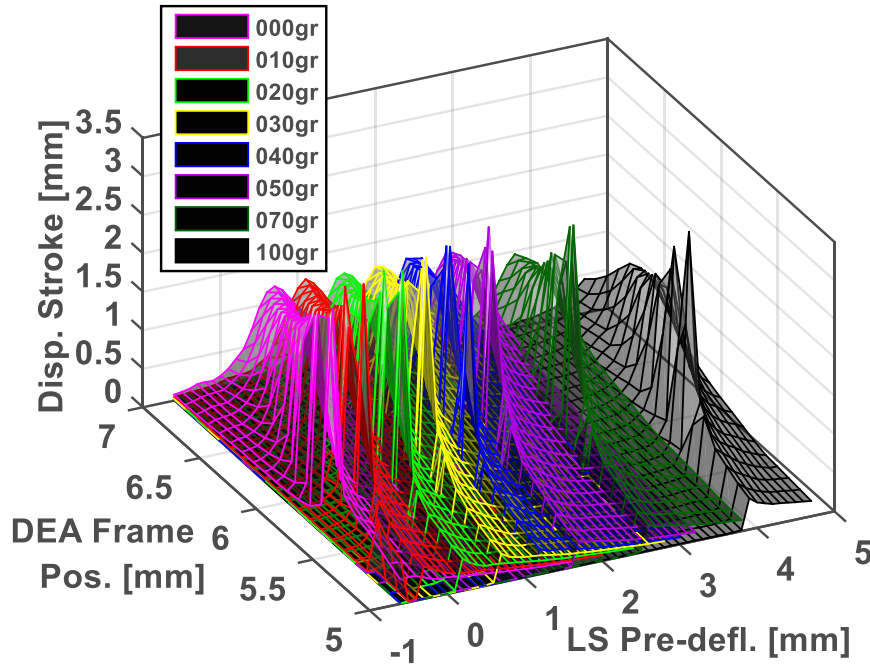


Figure 4.30: 3D surface plots of stroke at various constant loads.

Higher pre-deflections from the linear spring are required to compensate when larger constant loads are added.

4.4.2.3 Discussion

Since the linear spring counterbalances the applied load, more work can be performed for each stroke. Mechanical work is calculated as Force \times Displacement with the force being the weight of the mass and the displacement being the DEA stroke. Figure 4.31 presents the maximum stroke for each load and the corresponding work output.

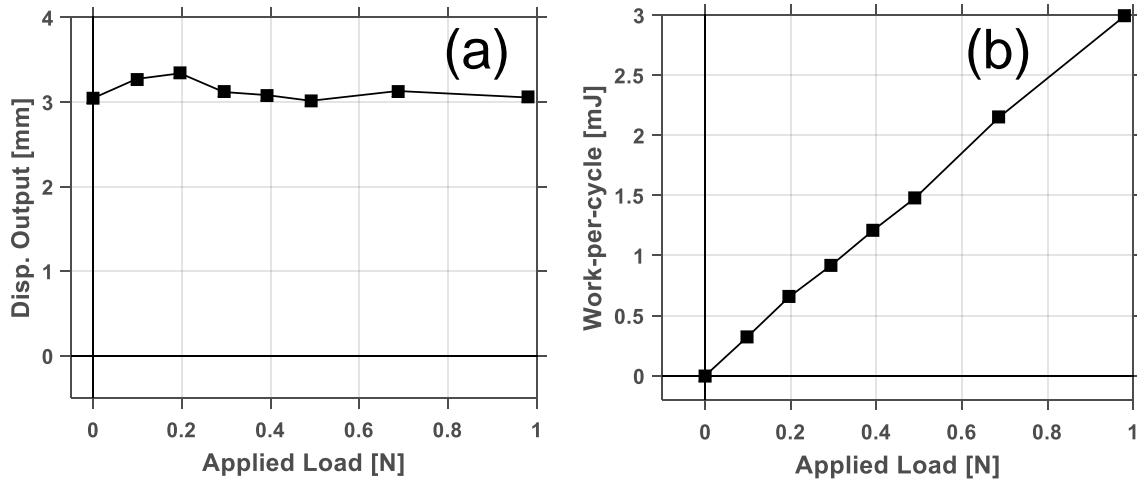


Figure 4.31: Stroke and work output (a) maximum displacement stroke vs. applied load, (b) calculated work-per-cycle vs. applied load.

The work performed can also be seen as the graphical area beneath the actuator force curve as presented in the Figure 4.32 below. In part (a) there is no load present. Once the load is applied (Figure 4.32(b-c)) work is being performed. The DEA is only allowing the *bias element* to perform the work against the load. If the load, for example, shown in (c) were to be removed

(i.e. 0N) the NBS would no longer be in balance with the DEA and it would snap and stretch the DEA until the actuator force reached null. Therefore, the load is required to maintain the desired stroke.

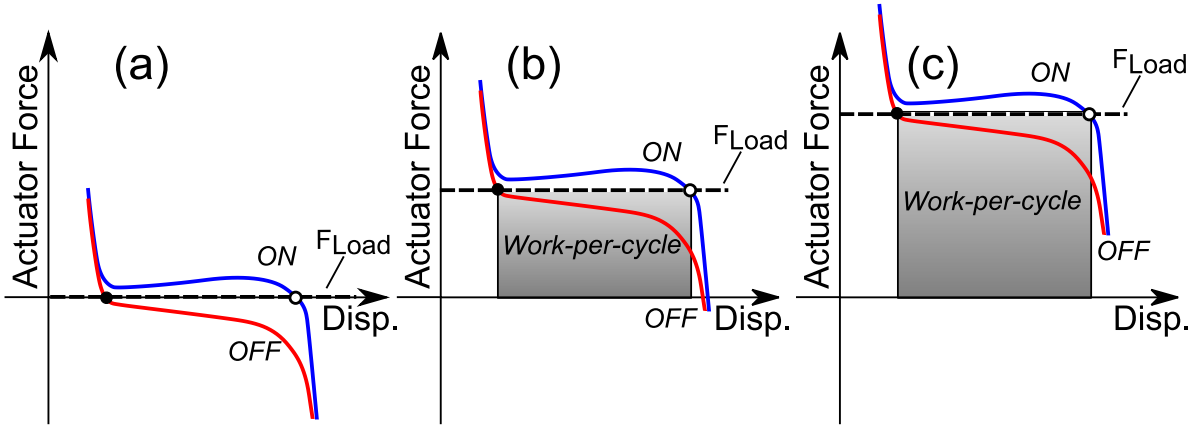


Figure 4.32: DEA performing work against increasing loads (F_{LOAD}) (a) no load, (b) medium load, (c) high load.

4.5 CONCLUSIONS

This chapter presented the design, fabrication, testing, and implementation of NBS mechanisms as bias elements for DEAs. An approach for tuning the NBS to the given DEA was explained and experimentally validated. This was performed by means of an asymmetric bistable spring. This was realized by combining linear spring elements with post-buckled bistable elements. This was motivated by the failure of the DEA with a NBS-mechanical stop to operate against a substantial load (i.e. more than 30grams). Therefore, the linear spring was added and tested. The linear element proved to be a good compensating mechanism when the DEA was operating against constant loads. It served as a tuning mechanism to adjust the bias mechanism to fit with the DEA and the external loads. An experimental test showed repeatable stroke of more than 3mm could be maintained even when loads up to 1N were applied.

Chapter 5 DEA PROTOTYPES

This chapter introduces demonstrator designs and uses them in a study to show the DE actuation theory explained in the previous chapters. Force-displacement measurements were performed for each individual component (DEA and bias components) and used in predicting the DEA stroke behavior. By using different NBS and linear spring combinations, *bi-stable*, *semi-stable* and *stable* stroke cases are achieved with the demonstrator. Furthermore, a quasi-static model is presented for each stability case by using polynomial fits to the empirical force data. The actuation stroke is modeled by examining the force-equilibrium condition at each voltage level. The qualitative actuation response matches the data well.

5.1 DESIGN

Having presented the theory of biasing diaphragm DEAs, now some further experimental results are presented. The DEA demonstrator devices designed are standalone, portable actuators which demonstrate how DEAs work. The DEA cartridge and appropriate bias elements are held together by a 3D printed structure designed in SolidWorks. The demonstrator makes a good display piece when seeking to explain how diaphragm membrane DEAs work. Contained in the demonstrator is the DEA and a bias element. Figure 5.1 highlights the main components with bright colors. There is a spacer between the DEA and the NBS to allow for some separation between the two and for pre-deflection.

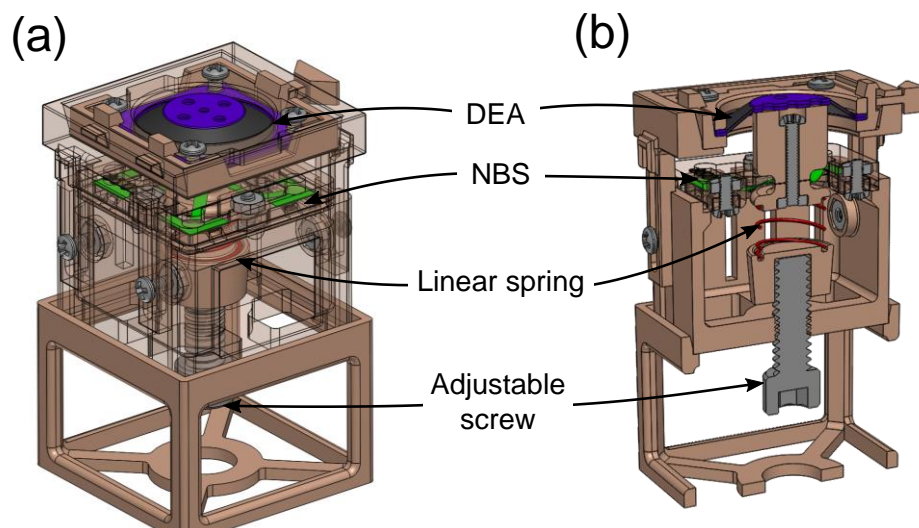


Figure 5.1: DEA demonstrator design (a) isometric view, (b) cross-sectional view.

The demonstrator was designed so that the DEA pre-deflection and linear spring deflection could be adjusted. The NBS was fixed, but the DEA could be lowered against the NBS+LS system to deflect it. The adjustable screw permitted linear spring pre-compression. The 3D

printed parts were fastened together with M2 fasteners and/or via snap/flexure mechanisms. Figure 5.2 shows the process of assembling the individual components.

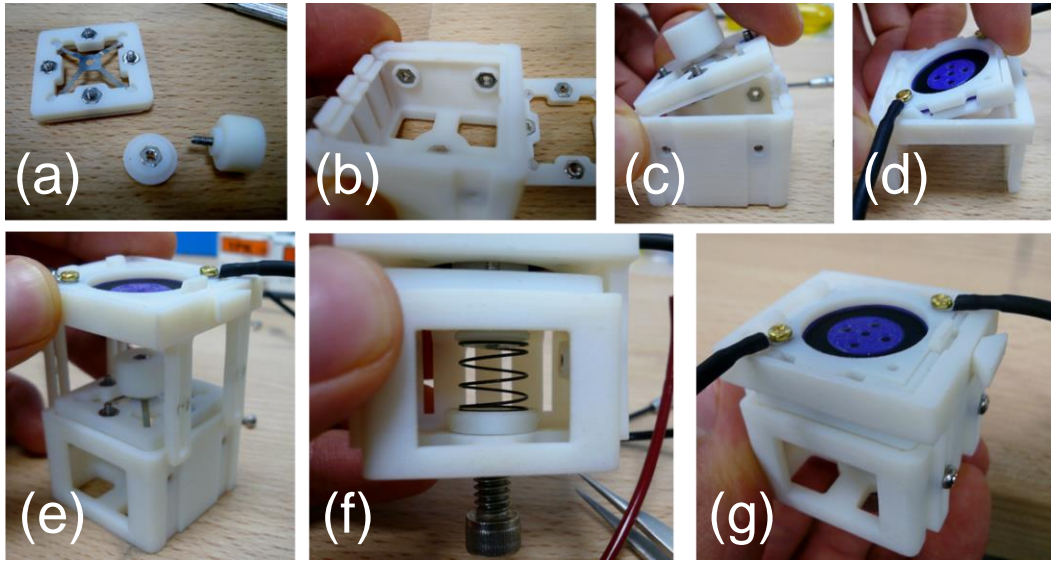


Figure 5.2: Views for demonstrator assembly (a) the NBS and push piece, (b) the base to hold the NBS, (c) snapping NBS into the base, (d) snapping DEA into seat, (e) guiding the DEA seat on to the base, (f) the linear spring and thumb screw, and (g) the fully assembled demonstrator.

Because of the use of snap-able parts, the DEA cartridge and NBS can be replaced easily when needed (see Figure 5.2(c-d)). The design had an open side to permit free access to the linear spring. The distance between the DEA seat and the NBS was adjustable via the grooves and the 4 screws could be tightened to lock the position. This allowed for freedom to adjust the DEA pre-deflection. This demonstrator design has been expanded and used for various sized diaphragm DEAs. Below is a series of DEA actuators with the same basic design as shown in Figure 5.1 and Figure 5.2 but with larger NBS and DEA components.



Figure 5.3: Photos of various sized DEA demonstrators.

Figure 5.4 presents three photos of the demonstrator producing stroke as voltage is increased.

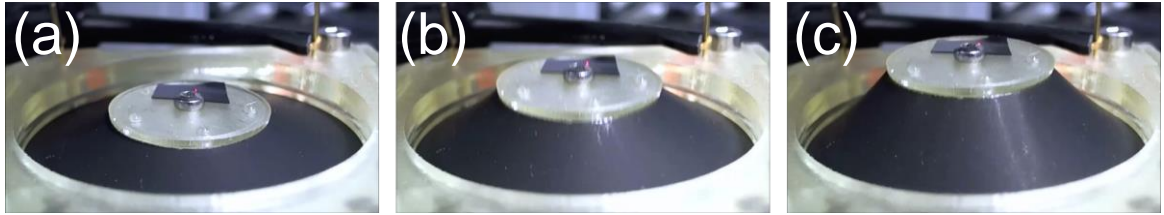


Figure 5.4: DEA demonstrator (a) no voltage applied, (b) voltage increasing, (c) maximum voltage.

The stability of the actuator depends on the DEA force behavior and the NBS + linear spring combination chosen. This will be briefly explored in the next section. Experimental results for bistable and stable actuators are shown along with actuator force response at different voltages.

5.2 EXPERIMENTAL INVESTIGATION OF ACTUATOR FORCE

Force measurements of the individual actuator components were performed and used in the force equilibrium analysis. First the force response of the DEA itself was measured (at constant voltage). Next the NBS+LS system force was measured. Finally, the DEA+NBS+LS force was measured at different voltage levels. The test setup is shown below for a DEA+NBS+LS test. While similar to the previously shown setups this one differs slightly. The motor may experience positive and negative loads due to the combined force measured. To maintain contact with the actuator, the motor shaft was secured to the DEA with two neodymium ($\text{Nd}_2\text{Fe}_{14}\text{B}$) magnets. When tension forces were required, the connection to the shaft would remain (up to a max holding force of $\sim 5.2\text{N}$) and the load cell would measure a tensile force. The magnets also allowed for quick connection and disconnection.

The linear motor with a shaft mounted load cell began the force-displacement experiment with the DEA at its zero or the minimum pre-deflection allowed by the NBS. The DEA (or NBS+LS) was displaced in a sinusoidal manner while the force was measured.

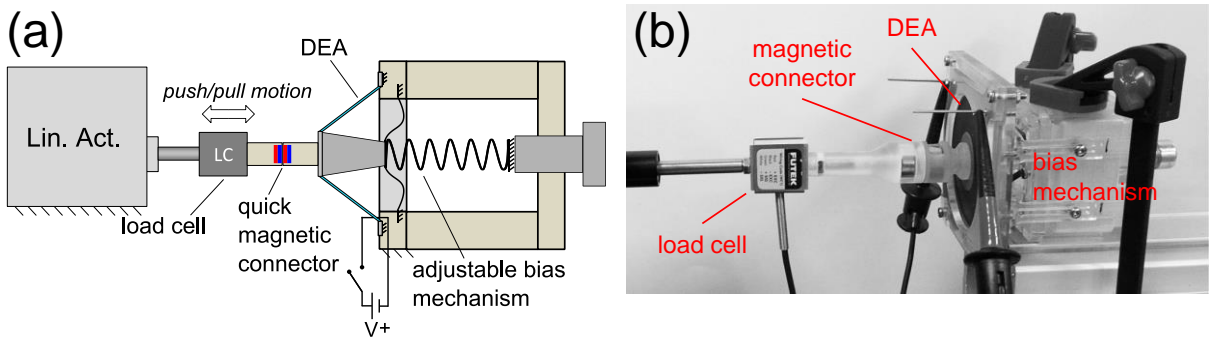


Figure 5.5: Actuation force test setup (a) Linear motor to push/pull the DEA+NBS+LS demonstrator, (b) photo of setup.

A NBS and a DEA used for this demonstrator are shown in the figure below. The NBS and the DEA were slightly larger than the ones used in previous chapters. This particular frame buckled the NBS by about 5% of the active beam length ($L_0 = 13.3\text{mm}$). The beam width was either 1.5 or 2.5mm. The shim stock thickness was 0.003in (76 μm). The exact NBS combination

will be listed for each stability case. The linear spring used for all three cases had a stiffness of, $k=0.38\text{N/mm}$.

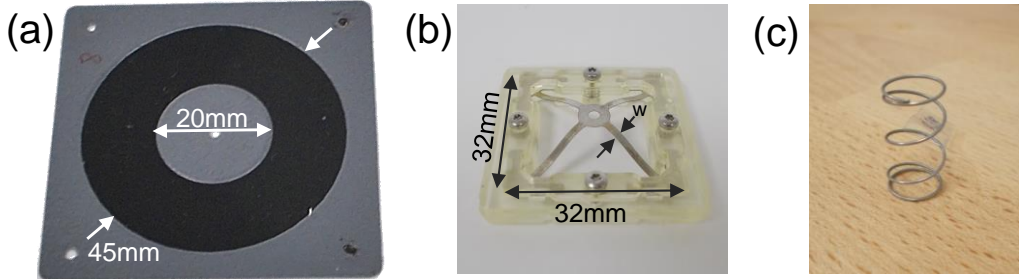


Figure 5.6: Photo of tested elements (a) DEA, (b) NBS, and (c) linear spring.

The force-displacement results for a two-layer DEA are presented below for voltage ranging from 0 to 2500V.

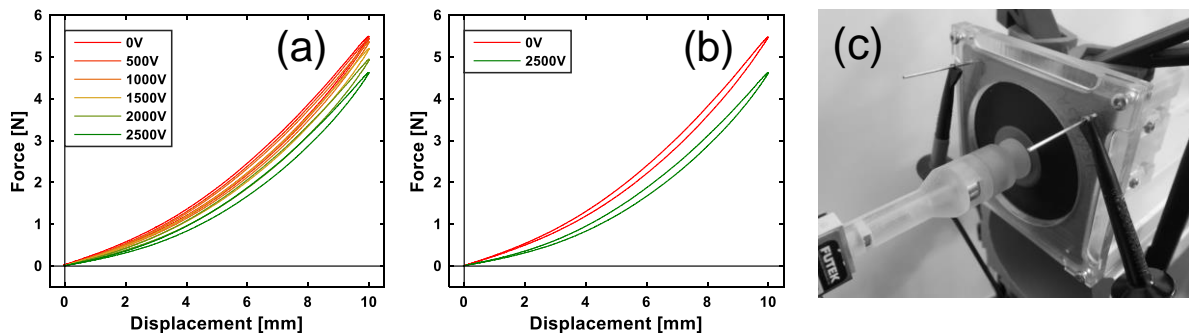


Figure 5.7: Force response of DEA (45mm diameter) to sinusoidal displacement (a) at 6 constant voltage levels (b) 0V and 2500V showing gap (workable area) and (c) photo of test.

The NBS and the NBS+LS were tested in the same manner. Figure 5.8(a-c) shows force measurements of the NBS+LS combination used with the DEA to produce a bistable, semi-stable and stable actuator, respectively.

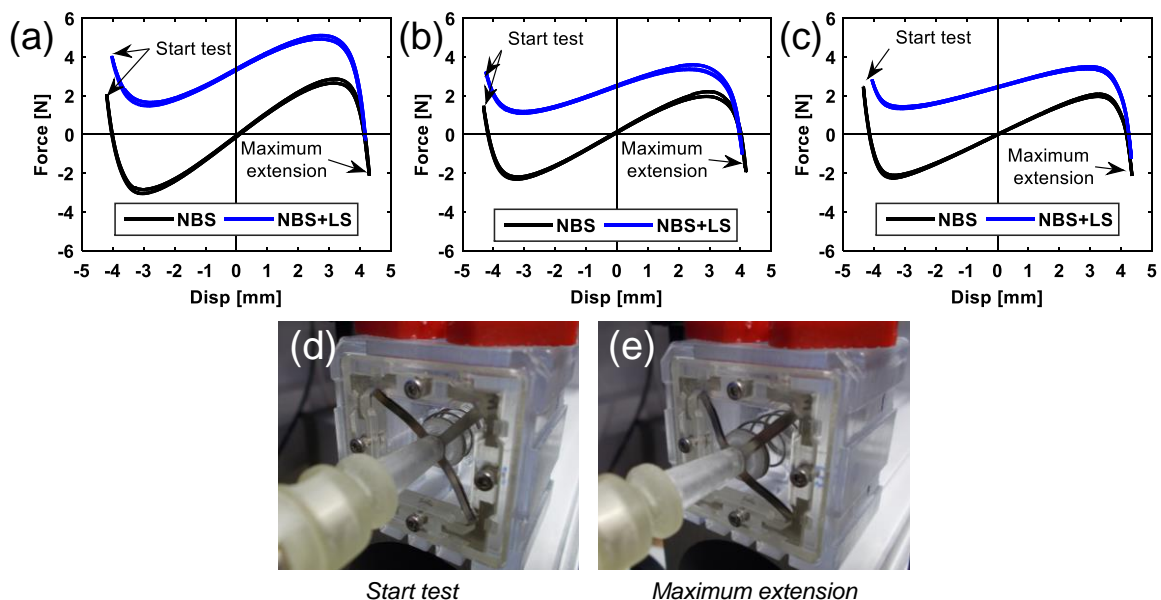


Figure 5.8: Force response of NBS+LS cases (a) bistable case, (b) semi-stable case, (c) stable case, (d) test at start (compressed spring) and (e) extended linear spring.

The table below lists the NBS and LS parameters. Two NBS elements were stacked and clamped together in the buckling frame to achieve the desired thickness and stiffness. (The linear spring compression was approximated from the data since the small workable area in the prototype did not allow for measurements of the spring length.)

Table 5.1: NBS and LS parameters for three stability cases

	Frame size	w [mm]	t [mm]	LS k [N/mm]	LS compression [mm]
Bistable	0.95L ₀	2.5	0.076	0.38	~4.61
	0.95L ₀	2.5	0.076		
Semi-stable	0.95L ₀	2.5	0.076	0.38	~2.18
	0.95L ₀	1.5	0.076		
Stable	0.95L ₀	1.5	0.076	0.38	~2.14
	0.95L ₀	1.5	0.076		

To test the free actuation stroke, a setup with a laser displacement sensor was used (as shown in Figure 5.9). The starting deflection of the DEA was not directly measured, since the DEA was deflected as the demonstrator was assembled by hand. For this reason, the absolute actuation stroke measured by the laser was compared with the DEA and NBS system force measurements to calculate the DEA starting deflection. In other words, the NBS system force measurements were shifted to the right with respect to the DEA coordinates (Figure 5.7).

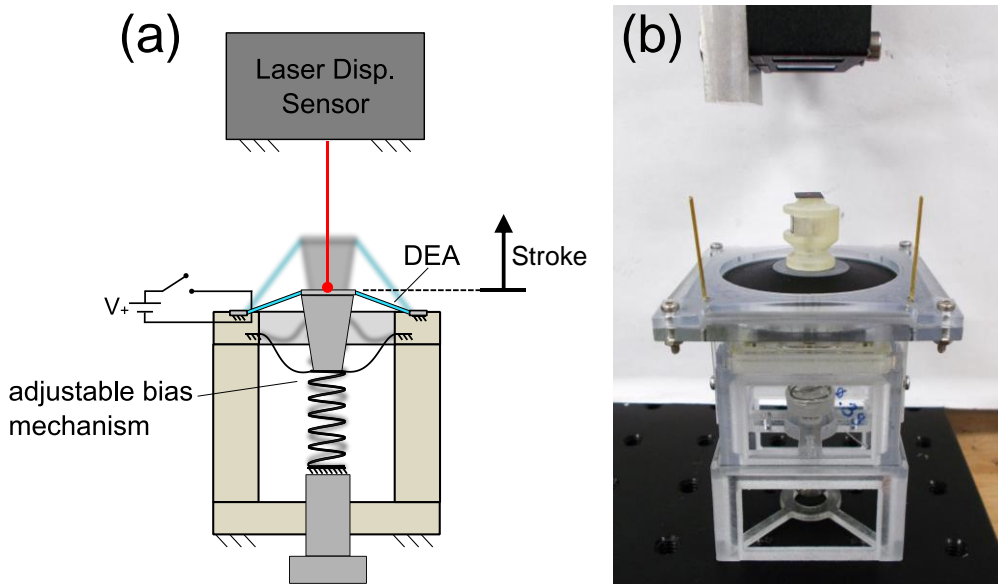


Figure 5.9: Actuation stroke test setup (a) sketch and (b) photo.

5.2.1 Results

In Figure 5.10 are the results for the three different cases. The time-resolved stroke is plotted for each case when a sinusoidal voltage input was applied and the actuation stroke is measured with the laser displacement sensor. The absolute stroke vs. voltage plot shows the stability of the system. The force-displacement plots present the DEA (Figure 5.7) with the NBS+LS results (Figure 5.8) plotted in the same coordinates. The intersection points show the start and max stroke obtained.

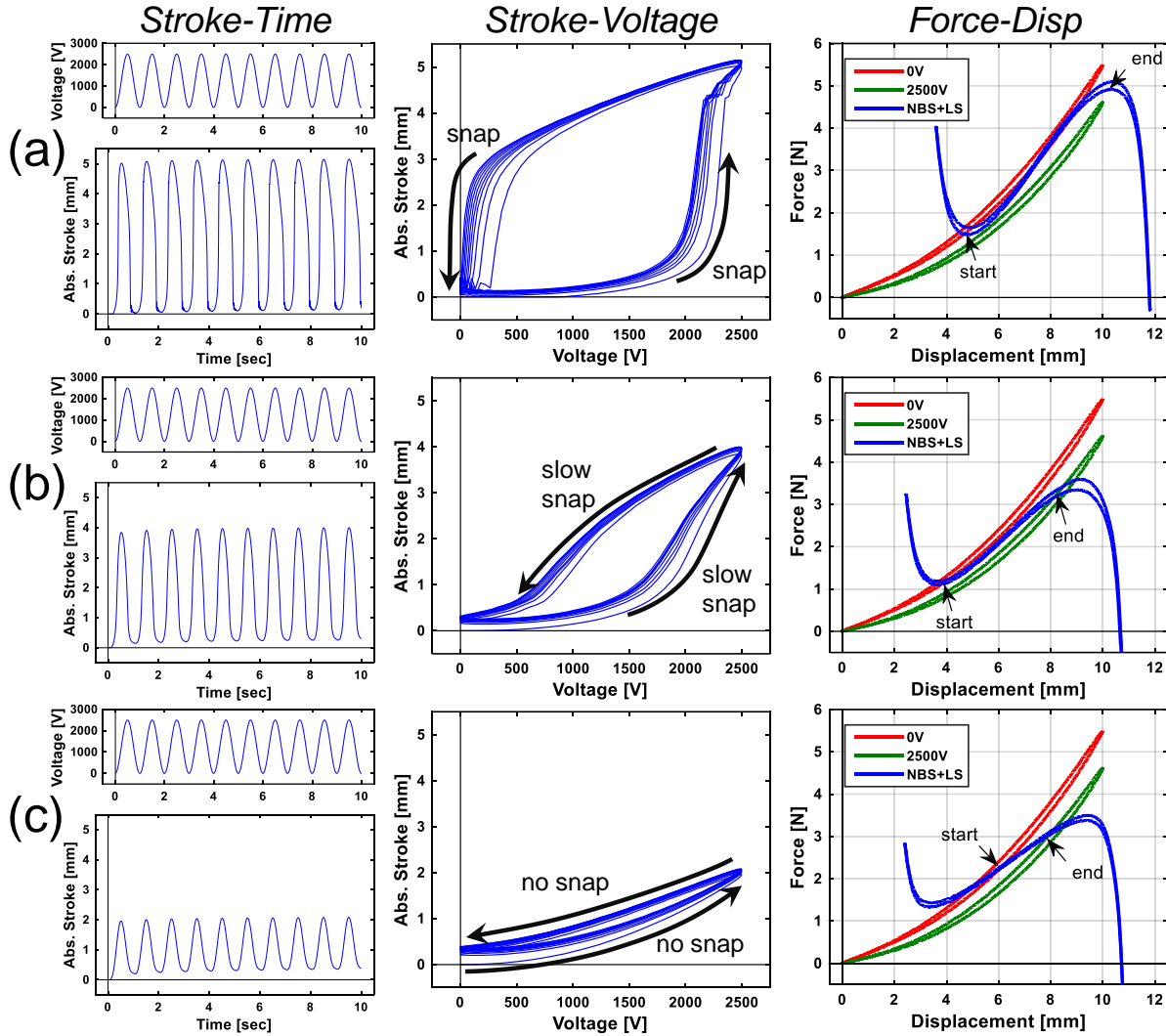


Figure 5.10: Demo results compared (a) bistable case, (b) semi-stable case and (c) stable case.

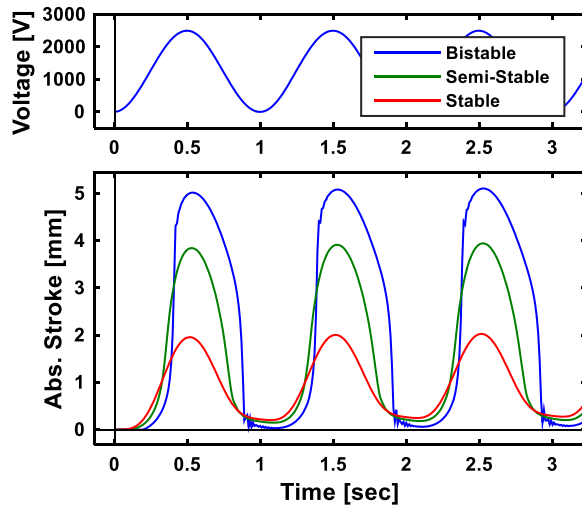


Figure 5.11: Comparison of stroke for each case.

5.2.1.1 Bistable DEA

Shown in Figure 5.10(a) is the case where the DEA was bistable due to the NBS+LS combination chosen (Figure 5.8(a)). The bistability is seen clearly in the voltage resolved plot.

There is a sudden large displacement around 2000V and a return around 250V. The stroke from the intersection points in the F-D plot appear to very similar to the actual stroke measured, ~5mm.

Examining the actuation force provides a deeper understanding of the actuator behavior at hand. Figure 5.12 presents the measured actuator force vs. the actuator displacement or elongation at different voltage levels. This can be used to predict the possible stroke of the actuator system under various loading cases. For this demonstrator the load was ~0N, hence the displacement must remain on the x -axis. The large overlapping hysteresis loops in Figure 5.12(a) are due to the combined hysteresis of the NBS and also partially due to the viscoelasticity of the DEA. To make the trends clearer, the force is averaged in Figure 5.12(b).

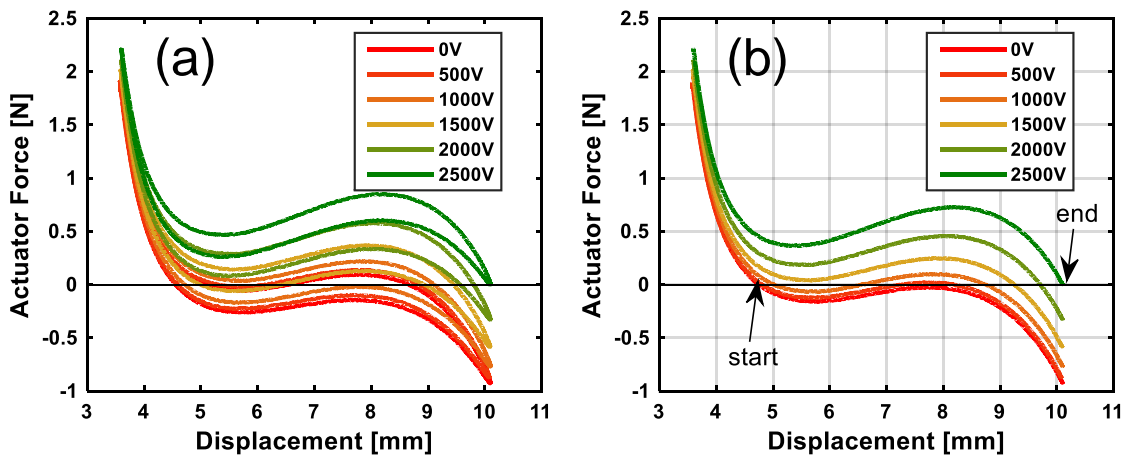


Figure 5.12: Bistable actuator force output, (a) force measurement to sinusoidal response at 6 constant voltage levels, (b) measurement average for each voltage level with start and end points for 0N load noted.

The multiple intersections of the constant voltage curves with the x -axis show that there can be instabilities. At 0V the actuator has one intersection point (~4.75mm), but at higher voltages up to 1500V there are three intersection points, with the middle one being an unstable equilibrium. However, beginning with 1500V, there is a switch back to one solution but at a higher deflection (~9.25mm). This switch in stability point results in a snap. Increasing the voltage further to 2500V gives a steady and minimal stroke.

Decreasing the voltage also results in a snap back to the start when the number of x -axis intersection points switch from three to one. On the return this happens at a much lower voltage; less than 500V.

5.2.1.2 Semi-stable DEA

In this case a different, slightly softer NBS mechanism was used (Figure 5.8(b), Table 5.1) so that the demonstrator revealed *semi*-stable stroke. This resulted in the negative stiffness being slightly less (than the bistable case) and therefore more similar to the DEA stiffness itself.

As seen in Figure 5.10 the stroke is more gradual than the fully bistable case. The cycle is still hysteretic, i.e. two solutions for each voltage level, but it is not as extreme as the bistable case. The hysteresis is attributed primarily to the viscoelasticity of the DEA and secondarily to the

NBS mechanism. It is also possible that the similarity in stiffness (between the DEA and the NBS+LS) exaggerates the DEA viscoelasticity because the ΔF is relatively small compared to the Δx due to the voltage change. In other words, the softness of the overall actuator system allows the viscoelasticity, and not the bias spring to dominate the system during actuation.

From the actuation force results (Figure 5.13) one can notice that the shape of the actuation force profile is flatter in the region of intersection with the x -axis and generally displays a single solution at 0N. Therefore, the actuation should not exhibit a large jump in position when actuated.

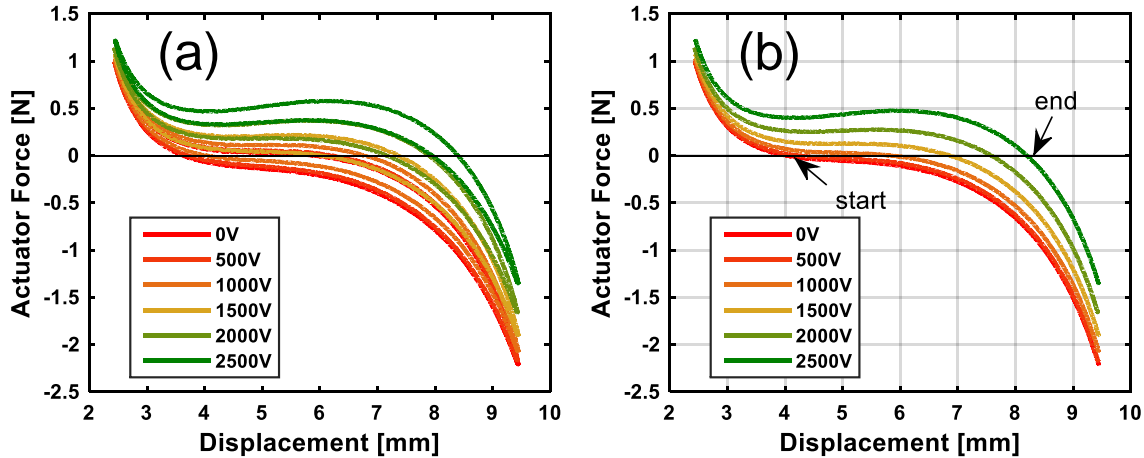


Figure 5.13: Semi-stable actuator force output (a), force measurement to sinusoidal response at 6 constant voltage levels, (b) measurement average for each voltage level with stroke start and end points for 0N load noted.

According to Figure 5.13(b) there is clearly one solution (with the 0N axis) from 1500V onward. This seems to suggest the acceleration in stroke from this point on as seen in Figure 5.10(b). This is due to the large decrease in DEA stiffness and not due to bistability.

5.2.1.3 Stable DEA

An increasingly stable response (and a much less-hysteretic response) therefore, is achieved with an even softer mechanism. The NBS here was slightly softer than the *semi-stable* case so that, when combined with the same linear spring ($k=0.38\text{N/mm}$), the negative stiffness was softer than the DEA stiffness at the same deflection.

In Figure 5.10(c) one can see that the stroke is quite stable (low-hysteresis), however this is at the cost of actuator stroke. The stroke is reduced to around 2mm. In the force-equilibrium plot of Figure 5.10(c) there appears to be a range of intersection points between the bias mechanism and the DEA at 0V (at the start). This is believed to lead to the large initial stroke which doesn't return completely to 0mm. This can be due again to the viscoelasticity of the DEA along with the bias force which practically matches the DEA stiffness at the start point.

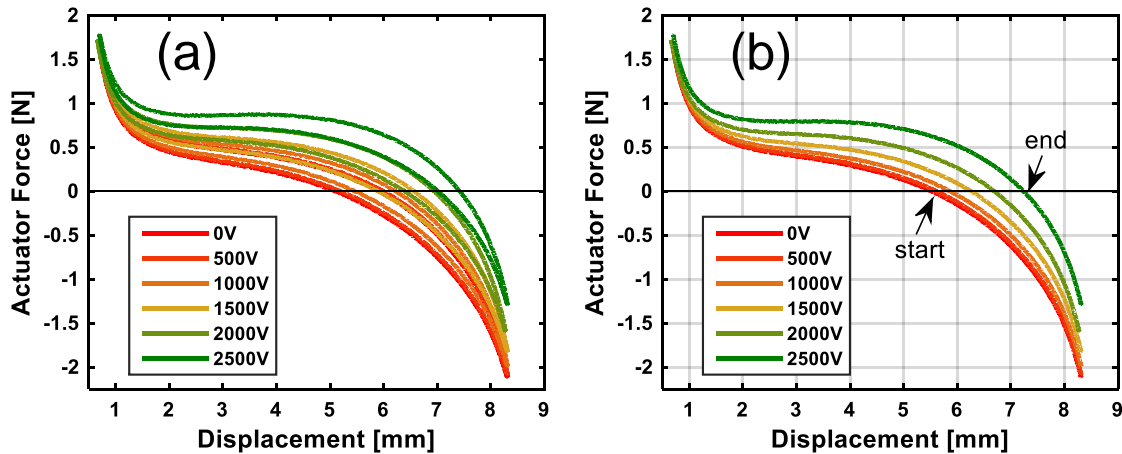


Figure 5.14: Stable actuator force output (a) Force measurement to sinusoidal response at 6 constant voltage levels, (b) measurement average for each voltage level with stroke start and end points for ON load.

In the actuation force interpretation, one can see that the actuator gives stable actuation because there is one clear intersection point at each voltage level with the 0N load. This means the hysteresis observed is primarily due to the DEA viscoelasticity and NBS hysteresis but not due to bistability or multiplicity of force equilibria.

5.3 MODELING

A quasi-static modeling of the stroke behavior can be performed by solving for the force equilibrium at each voltage level. However, when multiple solutions are possible, a more elegant way to solve for displacement is to track the minimum potential energy of the system when actuated. This is the approach taken here. Firstly, by using polynomial fits for the DEA force at constant voltage, the NBS force can be approximated. The linear spring is assumed to be linear. The total actuator potential energy expression can be found from these analytical force equations, by summing the integral of the force expression.

For the DEA a 5th order polynomial was used for fitting to the experimental data at each voltage level. Figure 5.15(a) shows the fits and data for low and high voltage. Figure 5.15(b) shows the fits at each voltage level. Notice the increasing separation at the higher voltages.

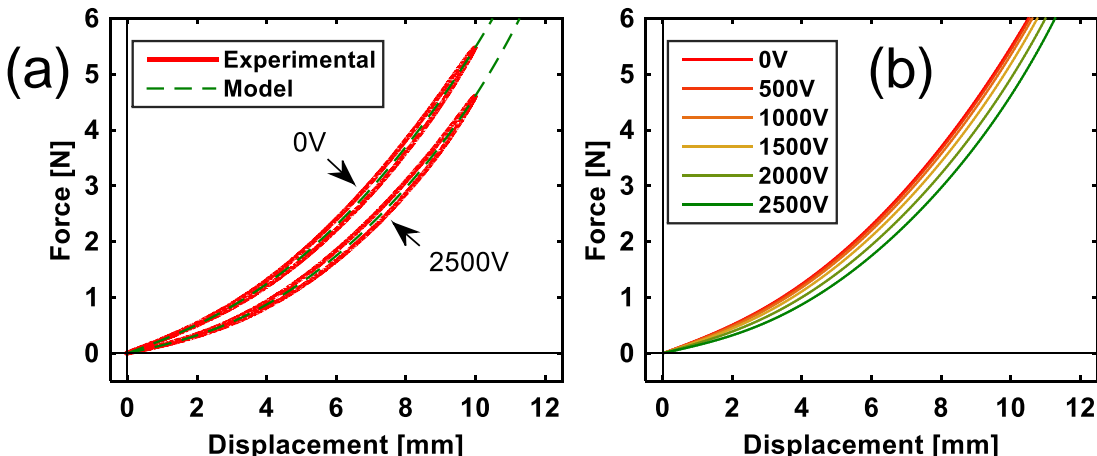


Figure 5.15: DEA experimental and model results (a) 0V and 2500V experimental and model fits, (b) model fits for intermediate voltages.

For the NBS data a 9th order polynomial fit was solved for each NBS combination used. Figure 5.16 shows the data and the resulting fit. Due to some slight asymmetry in the NBS mechanism, the fits have some small error but overall it represents the experiments well.

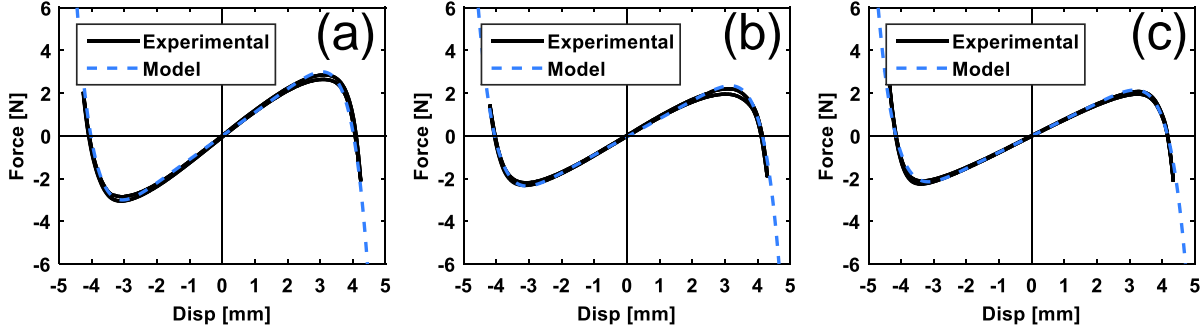


Figure 5.16: NBS model fits for (a) bistable, (b) semi-stable and (c) stable cases.

Using these polynomial fits, the potential energy was calculated using the following formula:

$$PE = \int F_{DEA} dx + \int F_B dx \quad (2)$$

Where F_{DEA} is the force of the DEA (a function of the voltage) and the F_B is the force of the bias mechanism (NBS+LS).

Figure 5.17 presents the modeled F-D plots with the total PE for 0kV to 2.5kV in increments of 500V. By tracking the minimum energy for all voltage levels the entire stroke profile can be known.

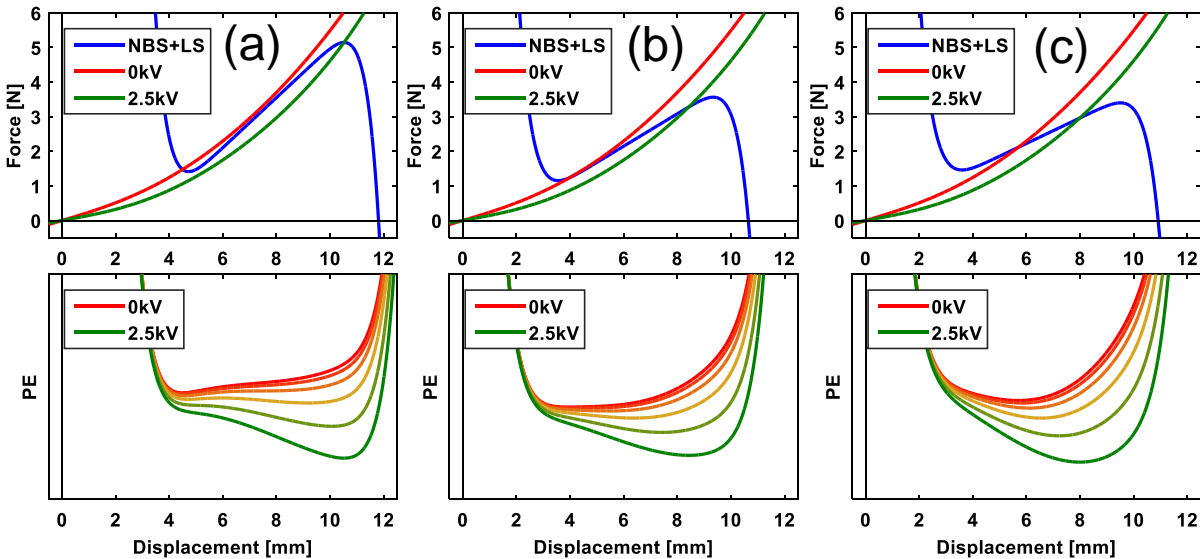


Figure 5.17: Modeled force and actuator potential energies at intermediate voltage levels for (a) bistable, (b) semi-stable, and (c) stable. The change in potential energy minimum is clearly seen.

The coefficients of the 5th order polynomial fits (Figure 5.15(b)) are linearly interpolated between the six constant voltage measurements. This provides a smooth change in the parabola shape as voltage is simulated.

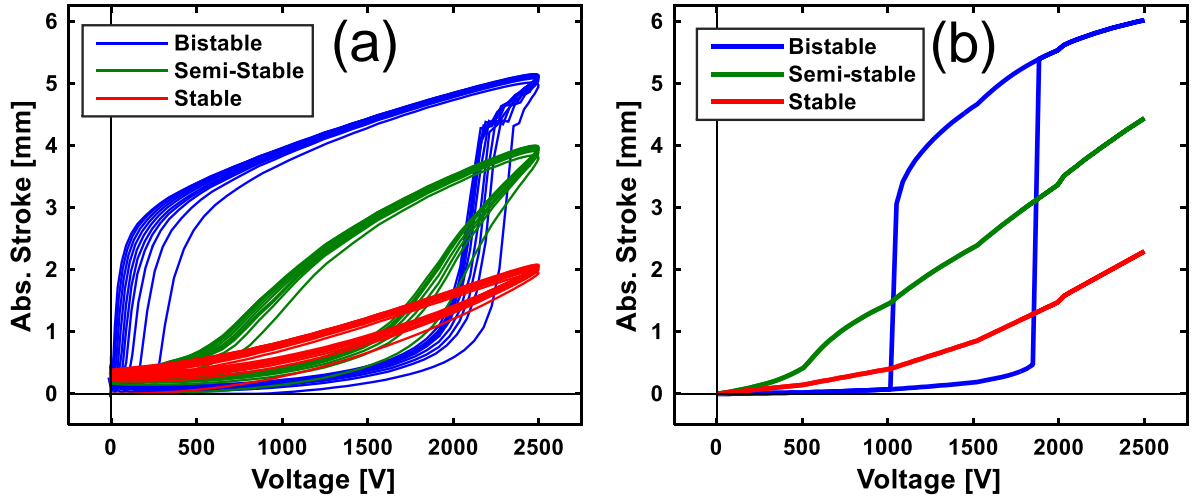


Figure 5.18: Experimental and model results (a, b).

For comparison, the results are presented side-by-side. The magnitudes are fairly similar considering the assumptions and data fits made. The bistable case shows the hysteretic behavior due to the instability. The model was purely quasi-static, so there are no viscoelastic effects seen in the results as in the experiments. It is interesting to note that the largest stroke also has the largest hysteresis. Such an actuator would perform well as a binary actuator or an “open-close” actuator unless stability was achieved using robust control as used in [147]. For a proportional actuator, the stable case would be preferable because of the continuous displacement with voltage. The control would be less complicated.

5.4 DISCUSSION AND OUTLOOK

When non-zero loads are applied, the actuation force plots can be useful to present the expected stroke. Consider the following case when a linear spring load is applied. Figure 5.19 shows the test scenario and the actuation force. The intersection points of the actuator force with the load show when there is a force equilibrium.

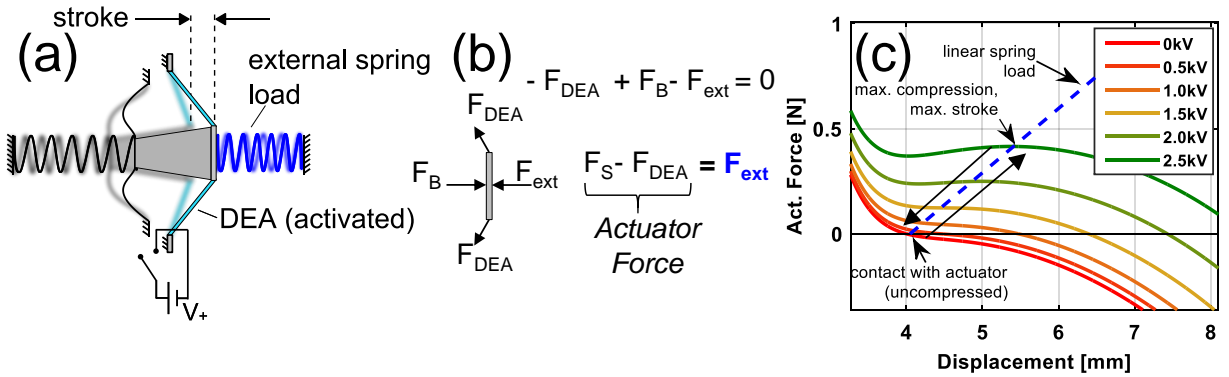


Figure 5.19: Actuator with linear load (a), FBD (b) and actuator force against linear load (c).

With the addition of a load the stability of the actuator can change. To study the stability, the same procedure of finding the minimum of the total potential energy can be used. Thus the stability can be ensured for all voltage levels.

This chapter presented experimental and modeling results for 3 demonstrators built from 3 different NBS mechanisms. The F-D diagrams along with the actuator force were used to analyze the actuator behavior. Using a potential energy approach, the actuators were modeled and showed good qualitative results for the different mechanisms.

Using this method of modeling the NBS and diaphragm DEA force with polynomial fits, the stroke can be estimated under different loading conditions. The time dependent effects like viscoelasticity and creep are neglected here so in reality the performance could be lower in applications. Further work in material modeling is should be performed to include the time dependent effects into this model.

PART 2: ADVANCED EXPERIMENTAL TECHNIQUES FOR CHARACTERIZATION OF DEAs

Experimental testing of DEAs is highly important not only because the field is fairly young but because it allows models to be created and verified. Validated models can then be used in the design and optimization of other DEA systems.

Part Two of this thesis highlights two newly-designed methods for benchmarking membrane DEAs. The first is a programmable force application device which was developed to characterize DEAs and to determine optimal loading conditions. The second is a standardized DEA tester which performs uniaxial tests on simple geometry DE materials. The device is capable of performing repeatable electromechanical tests of DEAs and DE materials. The development, utilization and studies from each setup are presented in the following chapters.

Chapter 6 SMART EXPERIMENTAL TECHNIQUE TO OPTIMIZE DIAPHRAGM DEAs

6.1 INTRODUCTION

As with most active or “smart” materials systems, DE Actuators (DEAs) exhibit non-linearities which are easily seen in stress-strain, voltage-force and voltage-stroke measurements [49], [123]. These non-linearities need to be analyzed and compensated for to maximize performance in applications and take full advantage of the attractive features of DEAs.

Research has shown that DEAs respond differently when coupled with different mechanical loads. Chapter 4 and [82] demonstrated how a negative stiffness spring (post-buckled beam mechanism) provided an order of magnitude increase in the DEA stroke over constant force or positive stiffness springs. However, to experimentally test a DEA to find the optimal bias mechanism configuration requires designing, fabricating and testing several pre-load mechanisms. This can often be a time consuming process. For instance, testing a DEA at different constant force levels requires attaching several test masses to the DEA (as performed in Section 3.2.3). Or testing a DEA with different linear spring rates requires aligning and repeating the tests for each spring tested. Each time a load or component is exchanged for the other, there is a risk of alignment and offset errors. Furthermore, given the variety of DEA geometries and the multitude of mass/spring configurations, the number of useful actuator designs that would need to be tested could reach the 1000’s.

In this chapter a novel solution is developed to couple any predefined load to a diaphragm DEA while simultaneously measuring the performance of the actuator (stroke, force, work etc.). This benchtop tool mechanically simulates realistic loading conditions via a programmable electromagnetic motor and can expedite testing of application specific devices. It limits the number of setups which need to be built and allows for enhanced dynamic testing of DEAs which was previously impossible.

To validate and demonstrate this tool, various mechanical loads were applied to a circular diaphragm DEA via the custom force controlled electromagnetic motor. The motor is programmed to simulate various biasing systems, such as a constant mass or linear spring, and proved to be capable of maintaining the desired loads as the DEA was actuated. The measured DEA stroke matched the measured DEA force-displacement profile. This study also

demonstrated that higher mechanical output can be achieved by matching the pre-load mechanism loading characteristic with that of the DEA—ultimately making an actuator system more sensitive to the applied voltage. This was in agreement with the work presented in Section 3.2.

6.2 DESIGN OF A PROGRAMMABLE ELECTROMAGNETIC MOTOR

Before testing the DEA under different biasing loads, careful experiments were conducted on a linear electromagnetic motor. The intent was to use the motor to apply mechanical loads to the DEA. This particular linear direct drive motor has a built-in encoder and an already implemented internal current control loop. It is designed to be operated in closed loop position control, with the position as the process variable and the current as the output of the controller. However, since force control is desired, in this case the motor current is the process variable. A load cell mounted on the motor shaft permits measuring the applied force. This section shows the experimental results which convinced the authors of the need to control the force with a closed loop PID law rather than exploiting the force-current correlation via a feedforward control. The control scheme implemented is explained in Section 6.2.2.

6.2.1 Linear motor characterization

Two tests for the motor were performed: a blocked and an unblocked test. The tests were primarily performed to verify the expected linear relationship between the motor output force and the commanded current, and eventually to determine the motor force constant.

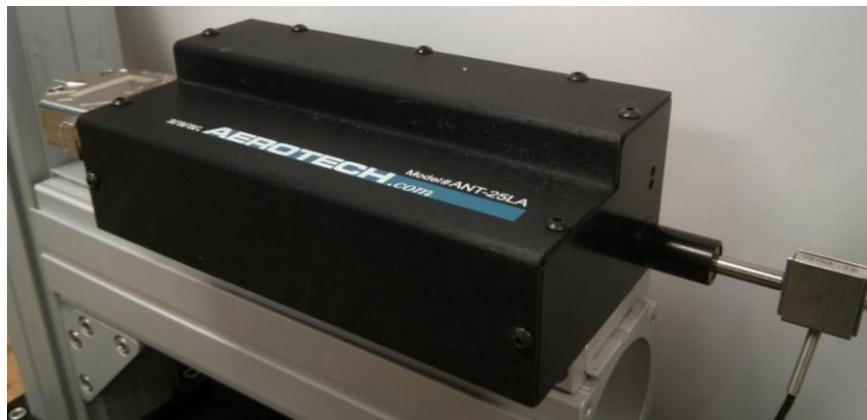


Figure 6.1: Photo of linear motor (Aerotech ANT-25LA) with load cell attached.

In the blocking force test the motor force was measured for fixed motor-current levels and at different motor shaft extensions. The results (Figure 6.2) show an almost linear relationship but with a small offset and small hysteresis, indicating that the motor's force (torque) constant [148] is actually variable and position dependent.

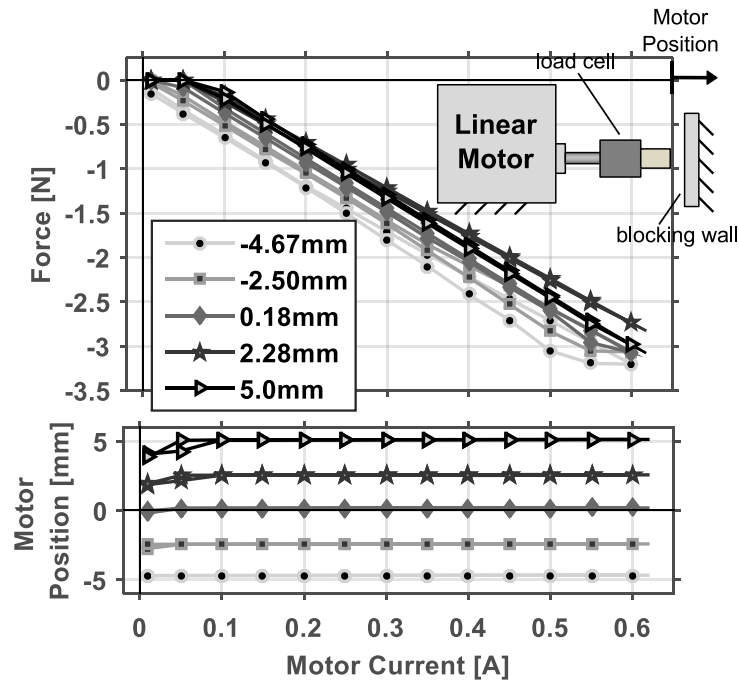


Figure 6.2: Motor characterization when blocked, Force vs. current at various motor extensions.

For the unblocked test, a linear coil spring was placed in front of the motor. The force output and displacement were measured while the motor current was commanded in a sinusoidal manner at different rates (see Figure 6.3). The hysteresis was independent of current frequency.

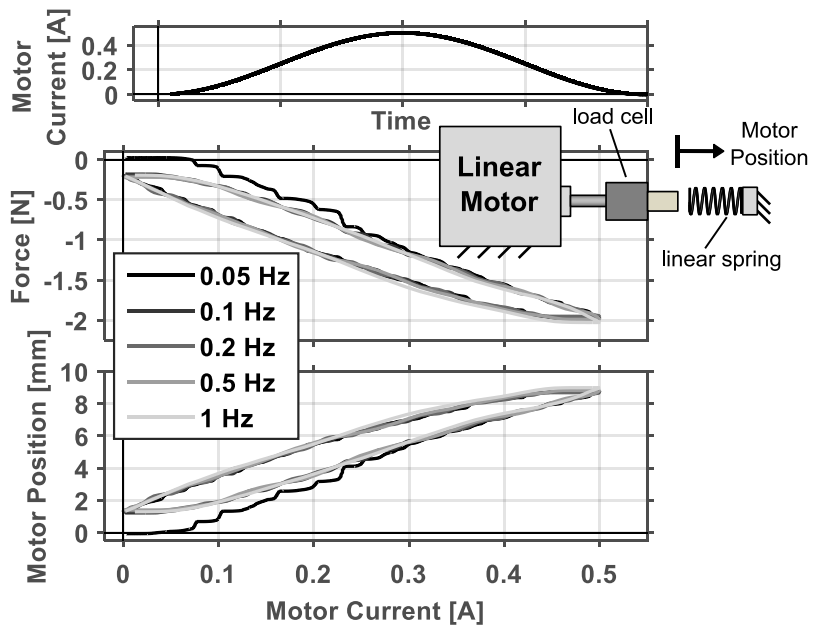


Figure 6.3: Motor characterization against spring, force vs. current at various rates.

As seen in Figure 6.3, the test resulted in large hysteresis in the force response when commanding the current of the motor. These losses are attributed to internal friction in the motor drive.

6.2.2 Control implementation

Following the above results, it was concluded that the motor force is not accurately controllable with open loop control of the motor current. This is due primarily to the observed shift in the blocking force, depending on the motor extension (Figure 6.2) and the hysteretic behavior when compressing a linear spring (Figure 6.3). Consequently, a closed loop force control is preferable in order to regulate the force output more accurately and repeatedly. Force applied to the DEA was measured via a load cell. (Details of the equipment and setup are given at the beginning of Section 6.3.) The current i is then generated according to the following PID law:

$$i = k_P (F_C^* - F_C) + k_I \int_0^t (F_C^* - F_C) d\tau + k_D \frac{d}{dt} (F_C^* - F_C) \quad (3)$$

where F_C^* and F_C are the desired and the measured force, respectively, and k_P , k_I , k_D are the controller gains. The integral action in the PID law ensures zero steady-state error in the force, provided that the closed loop system is stable. As this work represents a first attempt to address the problem, the controller was hand-tuned experimentally in order to achieve a sufficiently fast and overdamped response. (The design of more complex control solution with hysteresis compensation capability has not been explored, and represents a possible further optimization of the proposed setup.) If the PID controller is fast enough, we can assume that the applied force equals the set point, therefore

$$F_C \approx F_C^* \quad (4)$$

Assuming Eqn. 3 is true, the force equilibrium on the mass connected to the load cell results then in

$$F_C^* - F_{DEA} = m \frac{d^2}{dt^2} x \quad (5)$$

where x is the DEA out-of-plane deflection and m is the mass connected to the load cell. We have therefore different options in selecting the desired force F_C^* :

- 1) Constant force F_C^* , at steady state we have

$$\underline{F}_C^* = \underline{F}_{DEA} \quad (6)$$

- 2) A force profile $F_C^*(t)$, we expect that

$$\underline{F}_C^*(t) \approx \underline{F}_{DEA}(t) \quad (7)$$

with an error that becomes smaller for slower force reference frequencies;

- 3) Desired mechanical impedance, by setting

$$F_C^* = -b^* \frac{d}{dt} x - k^* (x - x_0^*) \quad (8)$$

the resulting force equation becomes

$$-F_{DEA} = m \frac{d^2}{dt^2} x + b^* \frac{d}{dt} x + k^* (x - x_0^*) \quad (9)$$

therefore the motor reacts to the DEA force as a mass-spring-damper system with desired stiffness k^* , equilibrium position x_0^* and viscous damping b^* , allowing the possibility to simulate a dynamic mechanical load. At steady-state, Eqn. 8 results in the DEA operating solely against an elastic load,

$$-F_{DEA} = k^* (x - x_0^*) \quad (10)$$

Note that k^* can be selected either positive or negative, allowing the possibility to simulate both positive-rate and negative-rate springs.

Figure 6.4 shows the scheme of the control loop with the linear motor. Here the motor is shown applying a pre-load force (F_c^*) to the DEA.

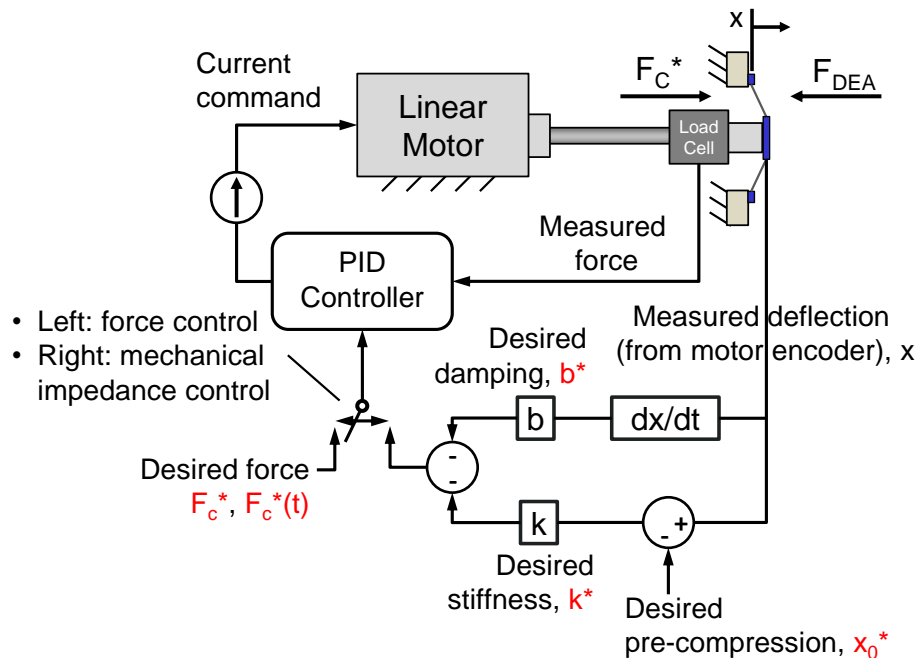


Figure 6.4: Force control implementation by commanding current to linear motor via the PID controller.

6.3 PRE-LOADED DEA EXPERIMENTS

The linear motor operating in force control was used to pre-load the DEA with various linear loads. This further validated of the force control, and provided previously unavailable insight into the DEA actuation under different mechanical loads.

6.3.1 Test Setup

Voltage was applied to the DEA and the resulting actuation strain (from the loading of the linear motor) was recorded via the linear motor encoder. The setup used is seen in Figure 6.5.

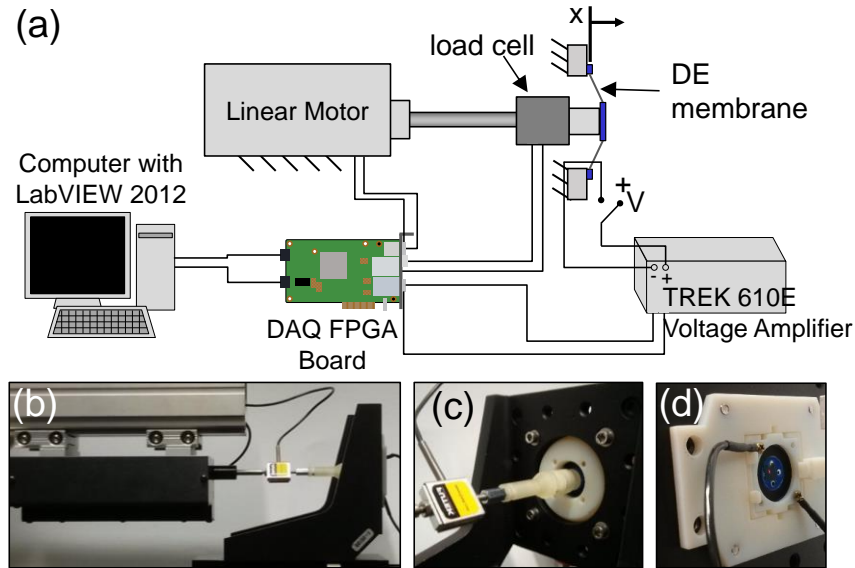


Figure 6.5: Force control test setup, (a) sketch, (b) picture of motor and load cell, (c) close-up of load cell and DEA, (d) DEA with electrical connections.

The electromagnetic linear motor used was an Aerotech® model ANT-25LA with an Aerotech® Ensemble™ ML controller. The direct drive motor is capable of 250mm/s, has 10nm linear resolution, and $\pm 12\text{mm}$ range. A Futek (LSB-200, 2lbf) load cell was fixed on the end of the linear motor to record the force of the DEA and provide feedback for the force control scheme. Voltage was applied to the DEA using a Trek® Model 610E amplifier. The actuator and sensor signals were processed through a National Instruments™ 7852R Field Programmable Gate Array (FPGA) board programmed from a Windows® desktop computer running LabVIEW 2012™.

6.3.2 DEA Characterization

A quasi-static (0.01Hz) force-displacement measurement of the DEA using the linear motor was performed with 0V and 2.5kV applied (Figure 6.6).

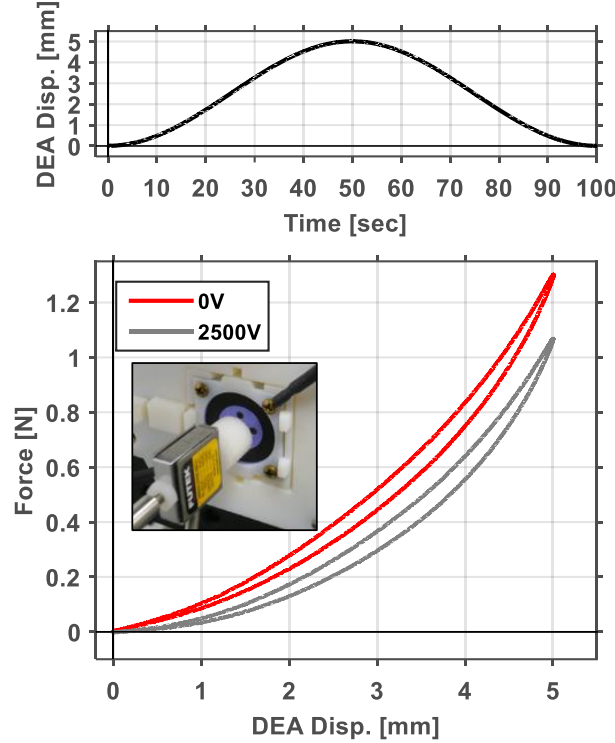


Figure 6.6. DEA Force response to sinusoidal displacement input while DEA at a constant voltage.

This result was later used when presenting the loaded actuation stroke. Since this force profile was measured with the same motor which would later simulate the loads, the force-displacement results can be plotted on the same coordinate system.

6.3.3 Programmable loads

Next, a linear force profile as seen in Figure 6.7 was simulated using the programmable motor. It was programmed to behave as a desired mass-spring-damper system. The encoder reading x was $x=0\text{mm}$ when the DEA was in the neutral position. Figure 6.7 shows a sketch of the DEA loaded with an arbitrary linear force, F_c^* . The figure neglects the dynamic contribution in F_c^* related to the viscous damping.

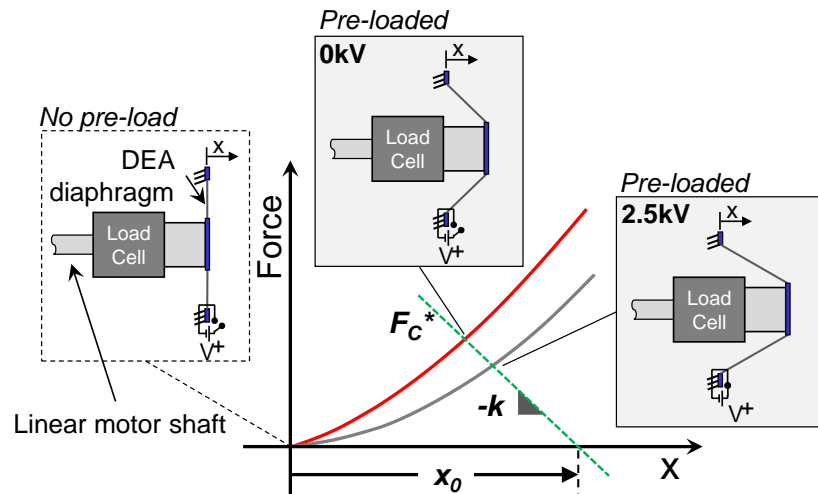


Figure 6.7: Sketch of DEA loaded with an arbitrary linear load (F_c^*) via the programmable Aerotech® linear motor.

Given the programmability of the motor, various linear springs with stiffness ranging from $-0.2N/mm < k^* < 0.4N/mm$ were systematically tested against the DEA at different x_0^* values (i.e. different DEA pre-deflections). The damping b^* was always selected in order to achieve an overdamped response. To do this, the F_c^* control was enabled (so that the equilibrium condition Eqn. 5 was met) and the DEA was allowed to rest for 30 seconds before receiving voltage each time. Next, voltage to the DEA was cycled from 0V to 2.5kV in a sinusoidal manner at a slow rate (0.05 or 0.10Hz). The slow rate was chosen based on initial tests performed which showed that the faster the DEA was activated the larger the error was in the force. Below are the results when the voltage frequency was varied and the motor was set to maintain constant force ($k^*=0$).

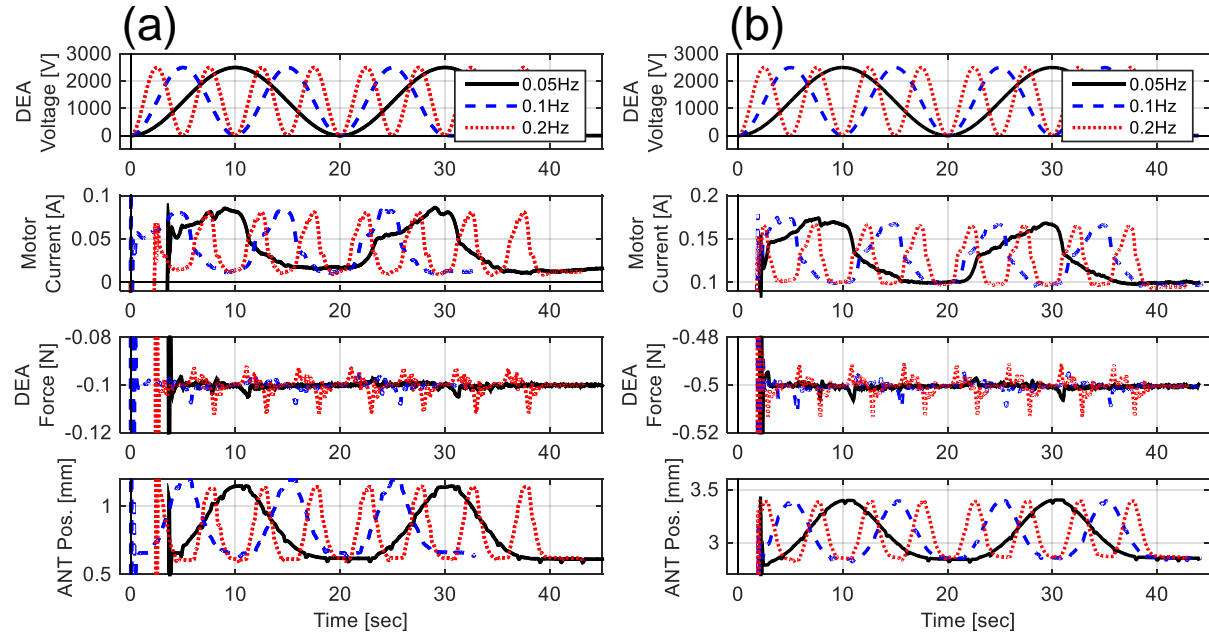


Figure 6.8: Frequency variation test for DEA at constant force (a) 0.1N and (b) 0.5N showing smaller force error for slower activation rates.

At the slower activation (e.g. 0.05Hz) there is less error in the force than there is at higher frequencies. Therefore, to better allow the controller to maintain the desired F_c^* as well as lessen the inherent DEA viscoelastic effects on the actuation results, a 0.05Hz activation frequency was used for the remainder of the tests.

To illustrate the actuation from the simulated springs, the results were plotted directly with the previously measured DEA force response (Figure 6.6). Combined they provide clearer understanding of the stroke trends.

6.4 RESULTS AND DISCUSSION

In this section a sampling of the results are presented and discussed first, followed by an overview of the results and concluding remarks.

Figure 6.9 shows the time resolved results for one simulated positive stiffness spring. The DEA voltage input, linear motor current command from controller, F_{DEA} and DEA

displacement for three actuation cycles are plotted. Included in the figure are three insets which show one second of data after the controller was enabled. The controller quickly increased the motor current, deflecting the DEA until the desired F_c^* was read by the load cell. Over the next 29 seconds the DEA relaxed slightly before 2.5kV was gradually applied to the electrodes, upon which the DEA “softened” and the motor extended further to a new force-equilibrium position. The motor current increased slightly with the applied voltage and then dropped when the voltage reversed. As the voltage cycled the DEA repeatedly responded with stroke because of the linear load applied by the motor.

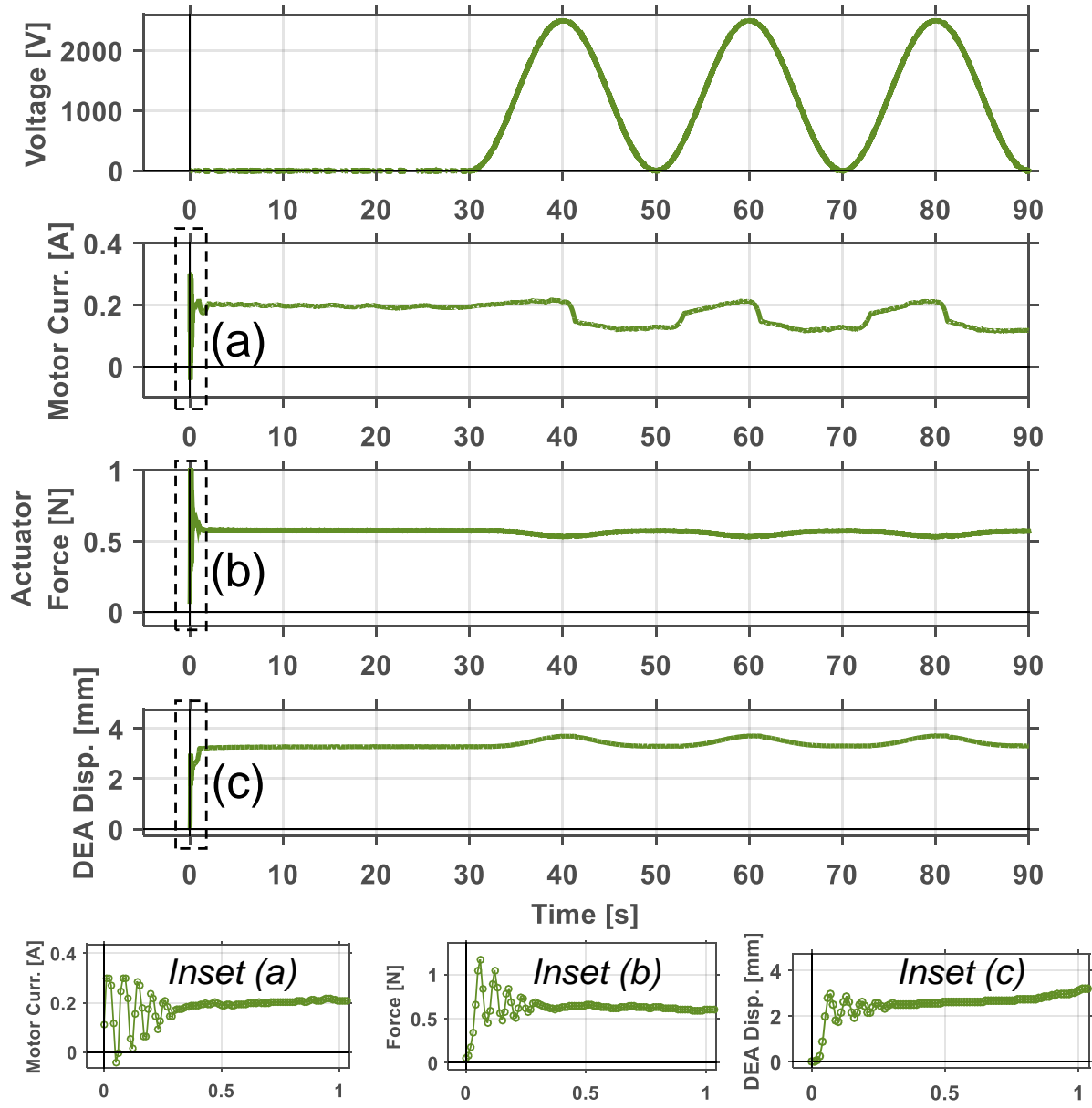


Figure 6.9: Time-resolved response of DEA loaded with a simulated linear spring of stiffness $k^*=0.10\text{N/mm}$. (a) rise of motor current, (b) rise of resulting force, (c) deflection of DEA.

Figure 6.10 presents the actuation results when plotted with the DEA force-displacement characteristic. It highlights the linear motor quickly moving into the force equilibrium position in about 1 second. By the time the voltage is applied ($t=30\text{sec}$) the motor has settled to the

coordinates which lie in the middle of the 0V hysteresis loop. (This is no surprise because the DEA is known to relax over time [49])

In this test a linear spring with $k^* = 0.10\text{N/mm}$ and $x_0^* = 9\text{mm}$ was simulated. The combined system behaves linearly as expected, demonstrating the programmed stiffness when operating between the 0V and 2.5kV DEA characteristic. The cycle 1 results begin in the middle of the 0V hysteresis loop and after increasing the voltage the maximum displacement achieved is on the edge of the 2.5kV loops. The reason the displacement didn't proceed further into the 2.5kV loop could be due to the lack of relaxation time at high voltage. The DEA had approximately 30 seconds to relax at 0V, sufficient time to stretch the DEA so that it was in the middle of the hysteresis loop. On the other hand, the DEA was at 2.5kV for only a moment.

Figure 6.10(c) shows three subsequent displacement cycles. They are steady and repeatable with an absolute stroke of approximately 0.4mm and a Δforce of about 0.035N.

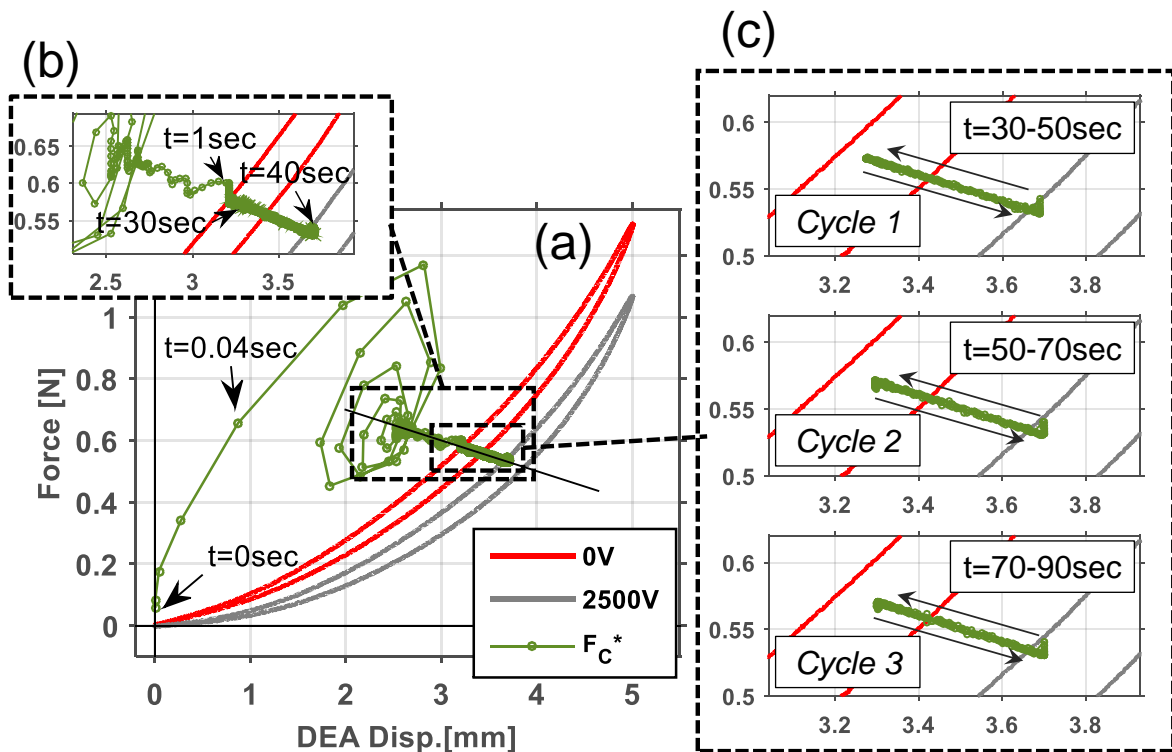


Figure 6.10: Simulated spring response (F_{c^*}), (a) plotted with DEA response, (b) close up of spring stroke, (c) stroke cycles 1-3.

The force-displacement results for a sampling of the springs simulated (at six different k^* 's and x_0^*) are presented in Figure 6.11 at varying pre-deflections. Each colored linear line reveals the simulated force profile as voltage was varied in a sinusoidal manner (third complete cycle shown). The results are very repeatable. The starting and ending points of the stroke lie within the pre-measured DEA constant voltage force-displacement curves (presented in Figure 6.6.) The stroke varies not only between different k^* but also at different pre-deflections.

The negative rates springs behaved as expected—producing a higher stroke than positive and constant rate bias mechanisms. Several simulated negative-rate springs were unstable when

the DEA had low-stiffness, i.e. at low-deflections; tests could not be performed in these cases. Negative-rate tests were performed when the motor and the DEA were able to be stabilized at 0V. These are included in Figure 6.11.

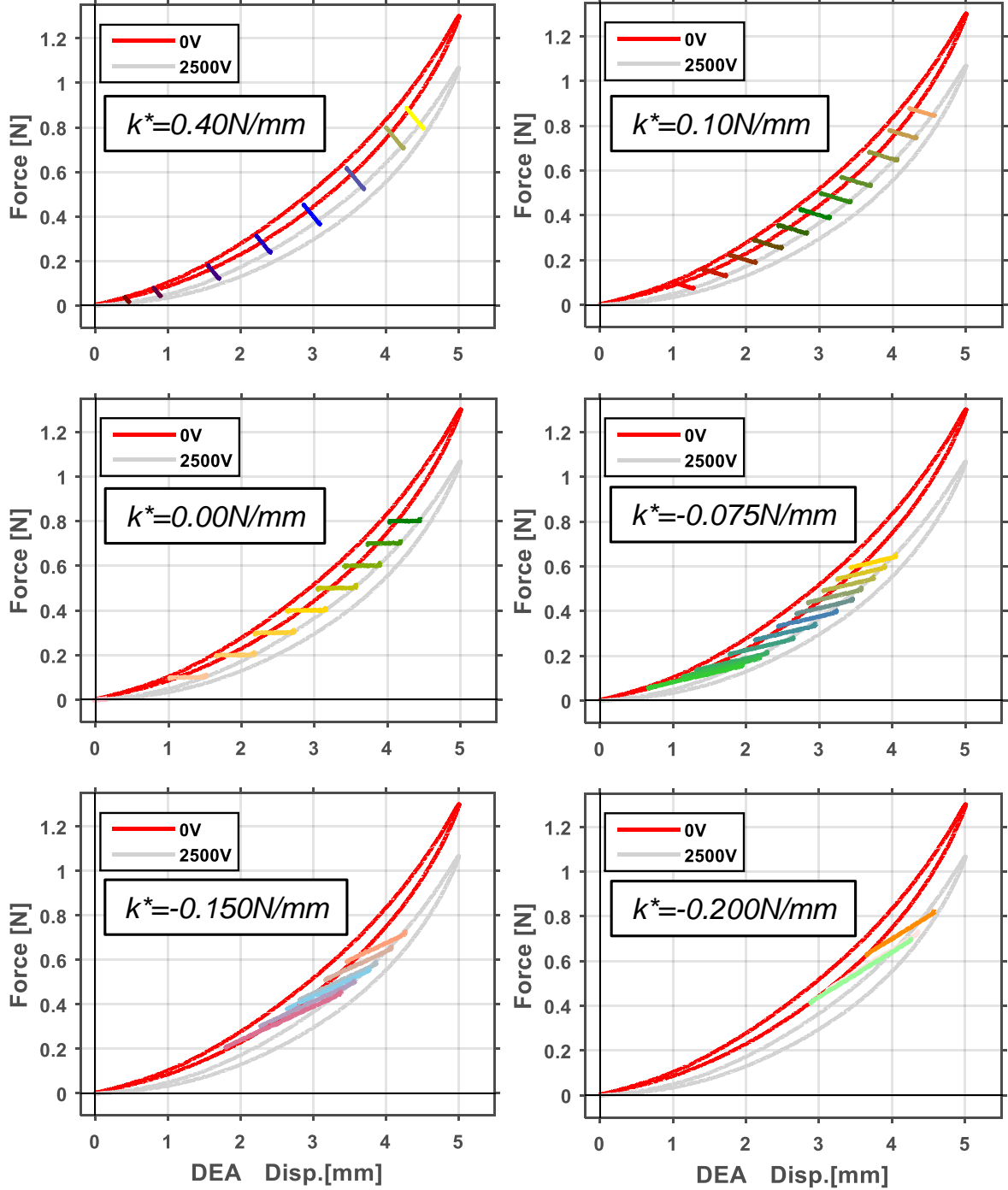


Figure 6.11: DEA actuation results for different springs (k^*) at different x_0^* values (pre-deflections).

Figure 6.12(a) compares the performance of all springs at the tested DEA pre-deflections in terms of absolute out-of-plane stroke in millimeters. The negative rate springs provided an overall improvement, but the stroke generally still decreases at higher pre-deflections due to the stiffening of the membrane. Pre-deflections above 4.5mm were not tested because of high failure rates due to high electric fields. Some negative stiffness springs could not be tested

because the stiffness of the NBS exceeded the stiffness of the DEA leading to an unstable system. At times the motor needed to be damped (in the first 30 seconds of force control) by hand in order to initially stabilize the linear motor at the desired DEA pre-deflection before applying voltage. Current limits were also implemented to protect the linear motor and DEA in case of mechanical instability.

Figure 6.12(b) presents one actuation cycle for the three stroke cases numbered in Figure 6.12(a). This clearly highlights why the stroke is larger in the case of the negative rate spring. The force increases when voltage increases, thereby giving more stroke.

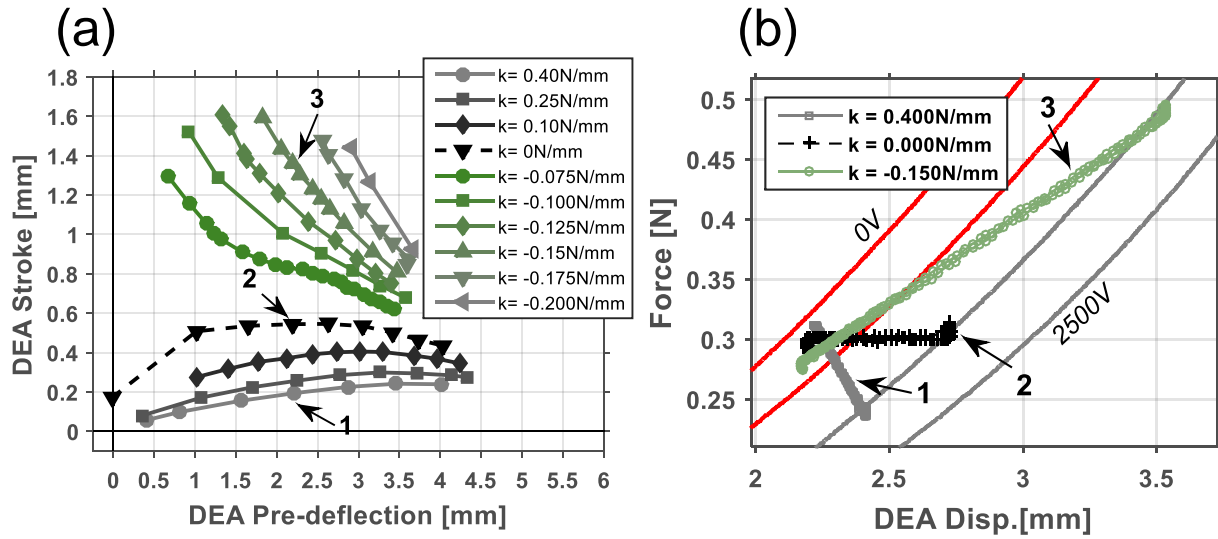


Figure 6.12: Stroke results compared (a) DEA Stroke vs. Pre-deflection, (b) Force-Disp.

Presenting the results in a different format, Figure 6.13 illustrates the stroke vs. the pre-deflection vs. the spring stiffness. This shows the dependence of the stroke on the bias mechanism characteristic (spring stiffness) and the amount the DEA is pre-deflected. A surface is interpolated over the data to show the trends.

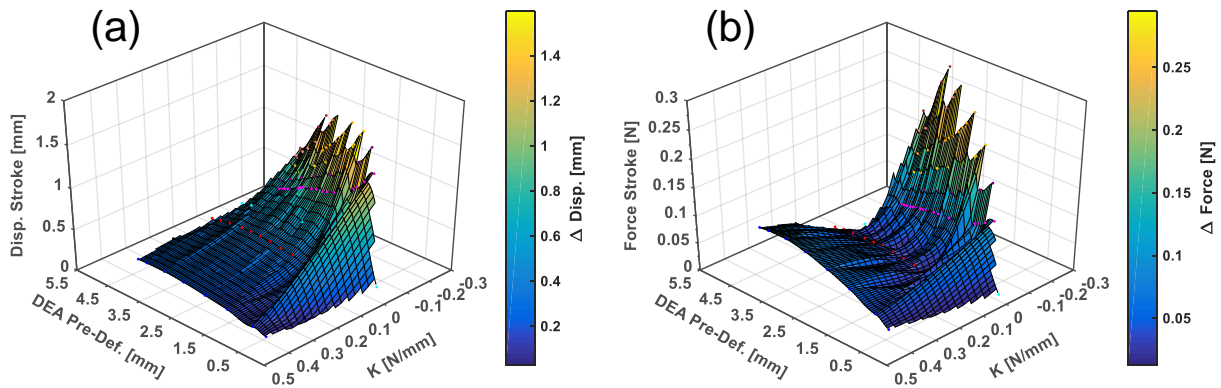


Figure 6.13: Surface plot of stroke data (a) displacement stroke, (b) force stroke.

The displacement and force stroke are highest for the more negative springs when the DEA is at a mid-DEA pre-deflection. The lowest displacement comes from the more positive stiffness springs. The lowest force stroke occurs when the constant load is applied (i.e. $k \sim 0$) as seen by the trough in Figure 6.13(b).

While the DEA diaphragm membrane undergoes multi-directional strain when deflected, the radial strain is most dominant. This can provide an approximation of the linear (uniaxial) strain and can be calculated based on the initial and final geometry. Figure 6.14 shows the geometry and values for deflected (Figure 6.14(a)) and undeflected (Figure 6.14(b)).

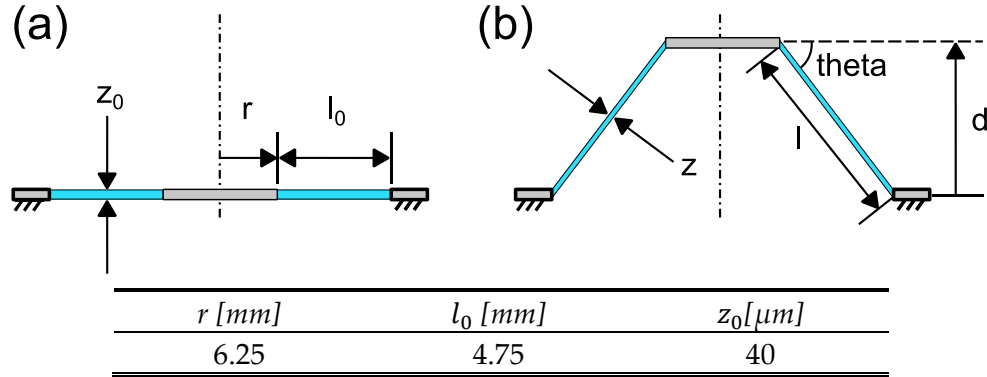


Figure 6.14: Diaphragm DEA geometry, (a) un-deflected, (b) deflected.

Using this information and the displacement/stroke data (in Figure 6.12) the stroke can be described in terms of elongation strain (Figure 6.15(a)). The general strain formula is $\varepsilon = l/\Delta l$. Additionally, by assuming constant DE membrane volume and approximating the membrane deformation as a truncated cone [95], the thickness can be approximated and therefore the electric field can be approximated when voltage is applied. This was calculated for three actuation results, as seen in Figure 6.15(b). This shows how the DEA loading system not only effects the overall stroke, but it can even make the system *more* electromechanically sensitive. The compared curves (#1, 2 & 3) are for different spring stiffnesses but each have been initially deflected the DEA to approximately the same pre-strain (~10%) for a fair comparison.

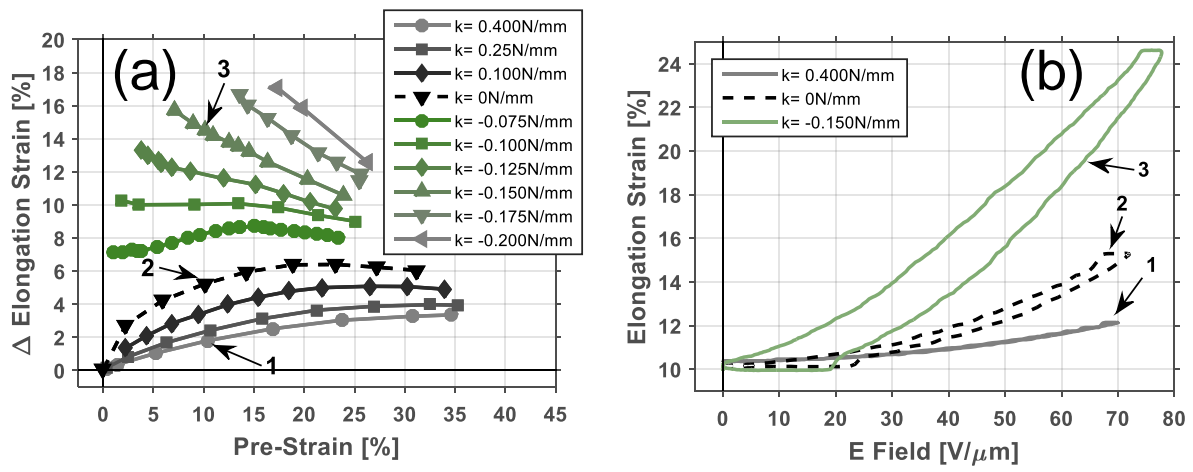


Figure 6.15: Actuation strain results (a) Elongation strain vs. Pre-strain, (b) Elongation strain vs. Electric field.

6.5 FURTHER DISCUSSION

As previously mentioned, during testing it was observed that the negative stiffness springs produce an unstable system overall if the stiffness of DEA (at 0V) is exceeded by the negative stiffness of the pre-load spring. In this case, the system will have at least two stable solutions.

In the author's previous work, it is shown that a bistable DEA system can be harnessed with the use of at least one mechanical stop [94]. If bi-stability should be avoided, then the design should take precautions that the DEA stiffness, for all viable actuator extensions (and applied voltages) will not be less than the negative stiffness of the pre-loading spring. Figure 6.16(a) presents a plot showing the stiffness of the DEA at a given pre-deflection; Figure 6.16(b) shows the DEA stroke output from the experimental results.

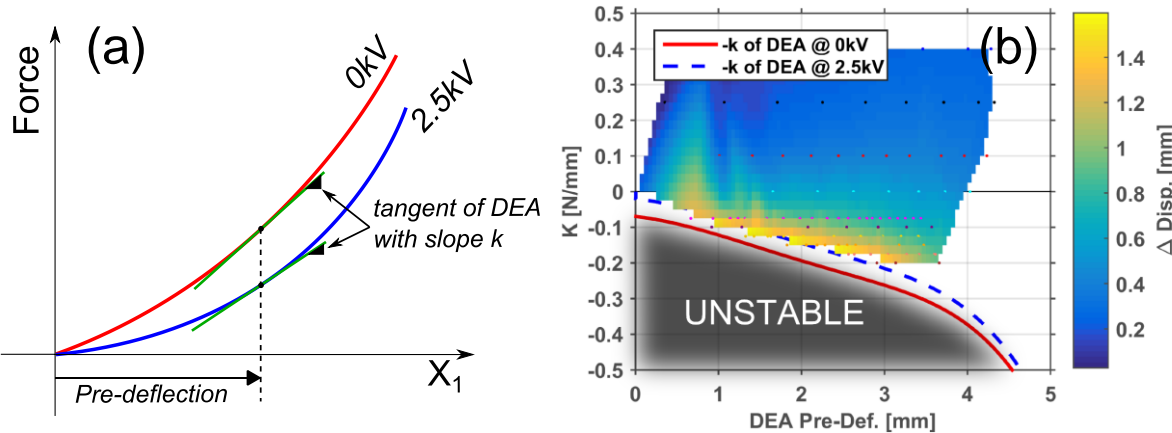


Figure 6.16: DEA stroke vs. stiffness vs. pre-deflection, (a) sketch showing DEA slope, (b) DEA stroke vs. Pre-load mechanism stiffness (k^*) vs. DEA Pre-deflection.

The figure includes two lines indicating the approximate negative stiffness of the DEA at each DEA deflection. The negative of the DEA stiffness is plotted in the xy -plane to show that the stable solutions must be less than the DEA stiffness. This is also the boundary along which the highest stable stroke occurs.

6.6 CONCLUSION

This work presented a benchtop tester and a novel method to load or pre-load diaphragm DEAs with programmable springs; the first of its kind as far as the authors know. This was realized by first testing the electromagnetic linear motor and designing a force control scheme. The multi-purpose setup performed well in both characterizing the DEA and applying the desired pre-loads to the DEA. The technique expedites testing, characterization and optimization of membrane DEAs.

Furthermore, the results of the actuation tests show that the actuator stroke is dependent on the actuation frequency and relaxation time, but can be accurately approximated using the intersection of the pre-load force-displacement profile with the DEA force-displacement characteristic, as has been done throughout this work. It was shown also that pre-load mechanisms can increase the electromechanical sensitivity of the DEA system by matching the stiffness of the pre-load device to the DEA stiffness. This actuator system approach for increasing the sensitivity is not dependent on the DE material (e.g. permittivity or E modulus,) *per se* but on the pre-load mechanism.

In the future, this new setup will be used to test and benchmark other DEAs in order to determine which biasing profile is optimal. Furthermore, this setup can be utilized to apply other loads to the DEA system, such as pure viscous or non-linear loads, which mimic the forces in the target applications.

Chapter 7 DE MEMBRANE CHARACTERIZATION SUITE

7.1 INTRODUCTION

New Dielectric Elastomers (DE) and compliant-electrode materials for dielectric elastomer transducers (DETs) are developing quickly as the technology grows. The many procedural steps in DE device fabrication, such as film pre-stretching, surface treatment, electrode patterning and membrane cutting can influence the actuator performance positively or negatively. To aid in understanding the impact the fabrication process parameters have on DE device performance, a systematic electro-mechanical study of the DE membrane is necessary. These elastomers are notoriously difficult to characterize in a repeatable manner due to their very compliant and often viscoelastic nature. Therefore, for reliable outcomes when testing multiple specimens there should be as little variation as possible so that correct conclusions can be drawn. Careful attention should be given to the test rig design (including motors, clamps, amplifier, load cell etc.) so that they enable repeatable placement and sufficient data acquisition for each test performed.

In this work an experimental test rig, with a procedure to systematically manufacture and test DE membranes in a standardized manner, is designed, fabricated and built. The steps to fabricate and prepare the specimens (while minimizing variations in geometry, clamping/boundary conditions, electrical contact) before testing are detailed. The test rig includes optical thickness sensors which provide the first known DE membrane thickness profile measurements of stretched and/or activated membranes. The work summarizes the tester design and presents measurements of several pure shear DE membrane specimens, which demonstrates the functionality of the test rig. This versatile programmable test rig results in a highly useful tool for further repeatable electro-mechanical characterization studies of DE membranes.

7.2 BACKGROUND AND MOTIVATION

DE transducers can be fabricated into many different configurations such as stacked, planar, rolled, and circular/cone/diaphragm configurations. The previous chapters studied bias mechanisms coupled to circular DE membranes. The DEAs had been mass manufactured via a screen printing process. Since the topic was focused on the bias mechanisms, the film/electrode behavior, and even production parameters were not investigated. Nevertheless, this is still a very important area to study. While the circular actuator

configuration exhibits many advantages, (e.g. having a fully-constrained active electrode area, being scalable/stackable and being easy to handle) it is a suboptimal configuration for direct material characterization. Due to the complex frustum shape of the deformed circular DE membrane the stress and strain fields are non-uniform and material parameters such as Young's modulus cannot be directly measured. Furthermore, membrane thickness measurement when deformed is not realistically achievable. Therefore, to help in modeling efforts and direct material characterization, a more appropriate form factor for obtaining DE material parameters is needed.

A planar, rectangular DE membrane with a rigid frame on each end and two free edges is a common configuration used for studying DE film transducers. This so-called pure shear test is recommended for DE and DEA characterization [149]. Kofod et al [44] showed a parabolic dependence of force upon applied voltage for a polyacrylic pure shear DEA. It supported the theoretical analysis but the low-force from the experimental piece was attributed to imperfections in the setup. Zhu et al [150] studied the wrinkle transitions in a simple clamped-clamped membrane setup. The study observed two types of wrinkle transitions in actuated states. Using a pure shear specimen Kollosche et al [51] conducted a many experiments and developed a model which describes the viscoelastic properties and instability effects of samples for different pre-stretches and voltage ramp rates. Stoyanov et al [151] performed isotonic test with a pure shear specimen of VHB4905 (3M, a polyacrylic elastomer). More than 140% actuation strain was obtained at 120V/um. Additionally, using a pure shear specimen, strain-dependent capacitance measurements of the specimen were performed. After grafting organic dipoles to the silicon network (in an attempt to increase the relative permittivity) Kussmaul et al [152] characterized a pure shear specimen (80mm wide, 10mm long) in an isotonic test. The improvement due to the grafting was determined from the slope β of the strain versus E^2 curve. In Wang et al [153] pure shear tensile experiments were performed to study dielectric elastomers with transparent electrodes made from PAAM hydrogel containing lithium chloride (LiCl) electrolytes. A maximum actuation strain of 67% was achieved for a specimen pre-stretched to $\{\lambda_{p1}, \lambda_{p2}\}=\{2.7, 5\}$. Yang et al [154] studied the elongation of uniaxial specimens vs pre-strain and compared them with FEA predictions. From the uniaxial tests and simulations, they observed that modeling actuator strain requires a hyperelastic expression and an optimized electrode/actuator geometry. Using a custom made tensometer Vertechy et al [128] mechanically tested pure shear DE membrane specimens made of commercially available natural rubber. The tester rig was used in populating an open-access DE material database.

Clearly as shown above, the pure shear planar specimen is a commonly used in DET experimentation. Still, a further motivation for choosing to build a test rig for testing planar DE membranes lies in the possible measurements the configuration enables. For example, an accurate non-contact thickness measurement of the DE membrane is very important as it allows for an estimation of the applied electric field. Due to the planar membrane

configuration, the electrode surface of pure shear specimen is easily observable from both sides; allowing for a thickness measurement. It should be noted that due to the challenging nature of the measurement (e.g. soft DE membrane and the high-voltage during actuation), thickness measurements of planar DEA membranes *during* actuation and/or deformation are typically not performed or seen in literature. One group in the literature presented an optical thickness strain measurement technique of an activated DEA, however this was a point measurement of a pre-stretched circular DEA and not a pure shear specimen [155]. No membrane thickness profile was taken. Most often in literature the initial DE membrane thickness (z_0) is said to be measured via a mechanical micrometer (or perhaps an optical method), and the deformed thickness (z) is calculated by assuming constant volume and measuring the planar deformation of the primary axis (tension direction). Consequently, the electric field calculation is approximated to be constant through the entire specimen because the thickness is approximated as uniform. Nonetheless, a non-contact measurement of the actual membrane thickness during electro-mechanical testing would lead to a better understanding the DEA specimen under test. For this reason, this contribution features an accurate, non-contact film thickness measurement device in the test rig, which can obtain a thickness profile of the stretched or un-stretched DE membrane.

It is possible to realize economical test rigs, as demonstrated by Moser using LEGO blocks [156], however this lacks the accuracy, speed and robustness which precision metal components can provide. Commercially available tensile testers can be used, but they were not employed in this work. Instead the test rig was designed to meet our particular needs and be able to accept future components. Commercially available key components such as linear drives were chosen based on the speeds, strains and force needed for typical film membrane tensile tests. Sufficient space around the specimen and clamps was reserved so that potential video capture and other measurement systems could be used in the future. Furthermore, custom programming of the sensors, data acquisition (DAQ) and synchronization in LabVIEW allowed for flexibility.

7.3 SPECIMEN DESIGN/FABRICATION, CLAMPS AND TEST RIG

The objective in designing the device and procedure were: repeatable results, ease of use and flexibility in the testing of DE membranes. The device was developed to accommodate planar specimens of varying geometries (e.g. from uniaxial to pure-shear), varying membrane stiffness/thickness and varying maximum strains. Figure 7.1 gives an example of the range of test specimen sizes the setup is designed to accommodate.

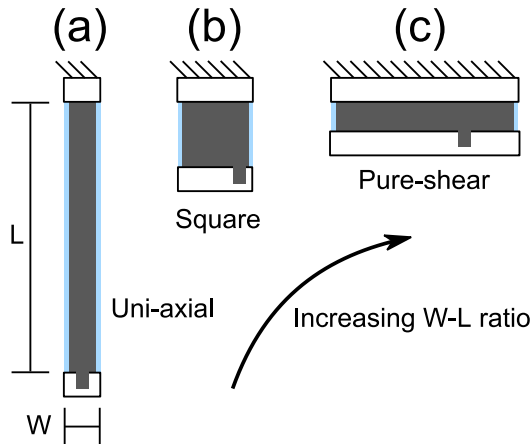


Figure 7.1: Range of DEA specimens the test rig can accommodate (a) uniaxial, (b) square, and (c) pure-shear. The setup should manage a reasonable span of stretches and forces so that various materials and geometries can be tested.

The choice of specimen geometry influenced several aspects of the test rig design such as the design of the clamps, choice of load cell and linear actuators. For example, the clamps should be wide enough for a pure shear specimen, the load cell should be sensitive enough to resolve the force of a narrow uniaxial specimen and the linear actuator should be capable of reaching high enough stretch levels for a uniaxial specimen of several centimeters length. In the following sections the specimen design/fabrication, clamp design and final devices with instrumentation are detailed.

7.3.1 Specimen Design/Fabrication

While several specimen geometries can be used in the test rig, for this study the electrode geometry was chosen to be 125mm wide and 25mm long (see Figure 7.1(c)). This geometry maintains the minimum 5:1 width-to-length ratio suggested by Carpi [149] for pure-shear tests.

7.3.1.1 Electrode patterning

A screen printing process was used to repeatably print the electrodes. The first step was to design and prepare the screen. The electrode geometry was designed on the computer with a vector graphics drawing software (Inkscape) and printed at 1:1 scale on a transparency film. Emulsion paper was applied to a new screen (with count of 90 nylon threads per centimeter) and allowed to dry in a dark cabinet for several hours. Next, the transparency/overlay was put into position over the screen before developing the emulsion layer with UV light. The undeveloped emulsion (under the overlay) was then washed off by rinsing the screen with water. See Figure 7.2 for photo of the developed screen.

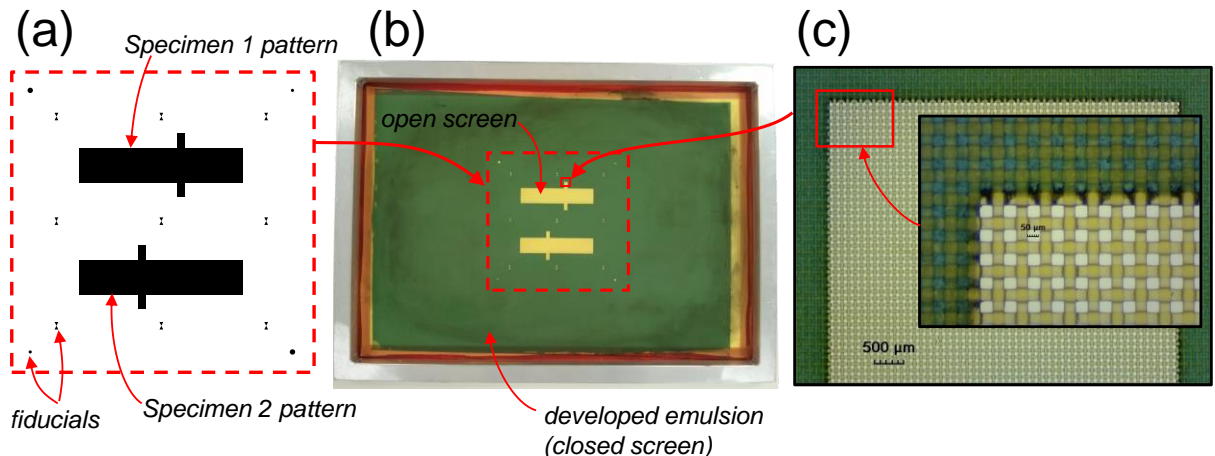


Figure 7.2: Screen development, (a) electrode designed on computer, (b) developed screen, (c) close-up of developed screen.

Next the DE film (Wacker Elastosil®, 50 μm nominal thickness [78]), in roll form was first cut to size (~200mmx200mm) and adhered directly to the aluminum carrier frame (Figure 7.3(a)) before carefully peeling the backing off.

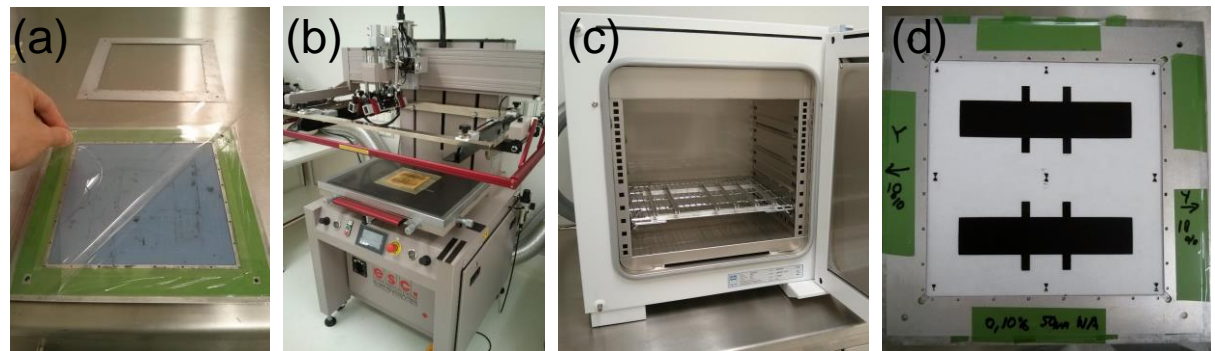


Figure 7.3: Electrode application process, (a) remove backing and tape film to carrier frame, (b) 1/2 automatic screen printer, (c) curing oven and (d) printed electrodes.

Two electrode (PDMS/carbon black mix) patterns were applied to the DE film via screen printing and with each layer cured in an oven at 150°C for 10 minutes (Figure 7.3, Figure 7.5(a,2)).

7.3.1.2 Reinforcement frame application

To handle the specimen, a reinforcing frame (3D-printed, Objet500 Connex, material: FullCure720) was precisely adhered to both sides of the DE film with double-sided tape (3M), sandwiching the specimens (Figure 7.4(b) and Figure 7.5(a,3)). The reinforcing frame was designed to fit exactly within the inner edge of the aluminum carrier frame by use of sacrificial tabs. This ensured good alignment of the frame with the electrode patterns. (The tabs would later be cut off, Figure 7.5(b,4)). Once sandwiched by the reinforcing frame, four straight-cuts through the DE film were made with a sharp razor blade to define the free-edges of the two pure-shear specimens (Figure 7.4(c-d)).

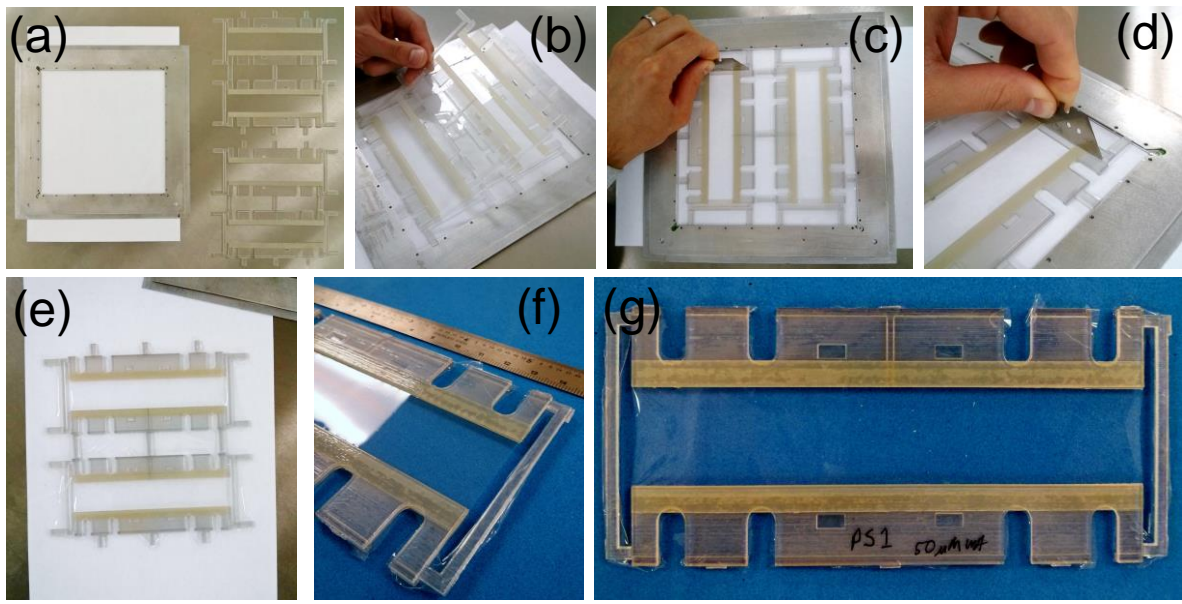


Figure 7.4: Photo summary of applying reinforcing frame to DE film (pictures show no electrodes but process is the same when electrodes are on film), (a) carrier frame with reinforcement frames, (b) applying reinforcement frame to film, (c) cutting free-edges of specimen with razor blade, (d) close-up of cutting, (e) whole reinforcement frame cutout/removed from carrier frame, (f) finished specimen showing free-edge/cut, (g) finished specimen.

After trimming the sacrificial alignment tabs away, the specimen was ready to be placed into the clamps. The specimen was aligned at the center of the clamps via the tongue feature of the reinforcement frame and the matching groove feature designed into the clamps. As soon as the clamps were securely tightened the linear motor was enabled in order to lock the initial position and length of the specimen. This would be the 0% strain position for all the subsequent tests. Next the two sacrificial connectors could be clipped. These connectors ensured that no pre-stretching of the specimen could occur during fabrication and handling. It also certified that each specimen would have the same initial length.

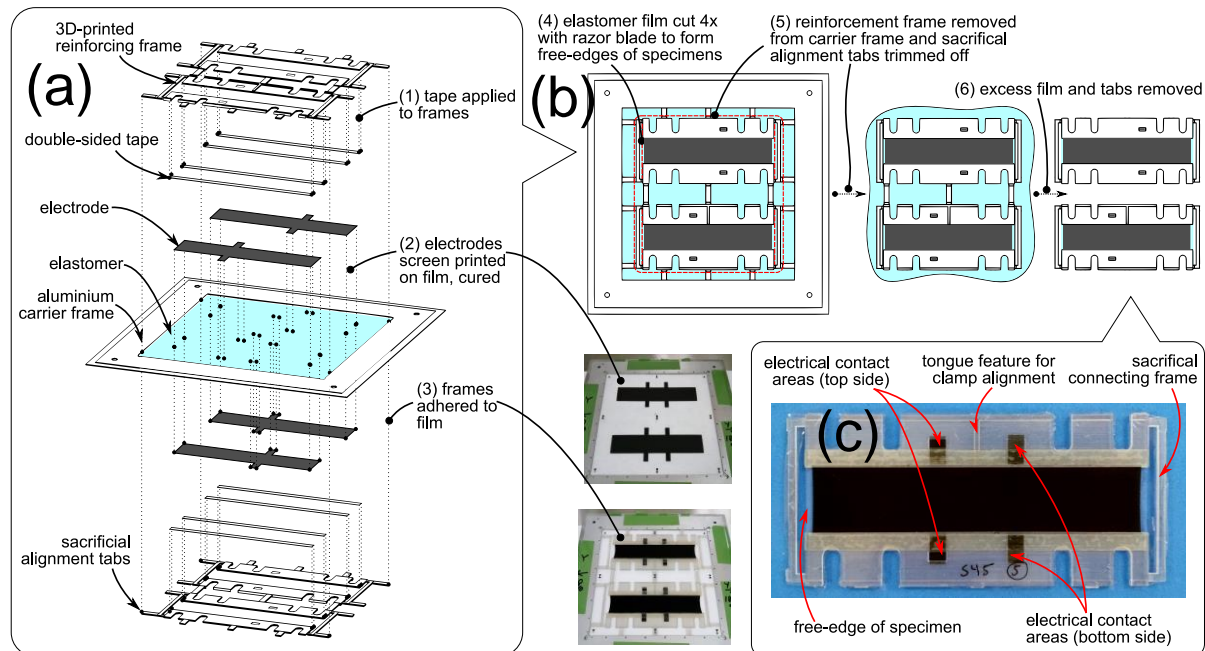


Figure 7.5: Pure-shear specimen assembly, (a) exploded view, (b) removal from carrier frame (c) and close-up of details/features.

While the procedure for forming the specimens explained above is for a pure-shear shaped specimen, the same process can be used for differently shaped specimens including those shown in Figure 7.1(a-c). In these cases, the electrode and reinforcing frame should be redesigned to fit together with the DE film spanning the carrier frame.

7.3.2 Clamp Design

The clamps were CNC-machined from Delrin® with a width of 130mm to enable a range of specimens from pure-shear to uniaxial test specimens as seen in Figure 7.6. Delrin was chosen for the clamp material because it is a high-modulus insulator. It could isolate the high-voltage from the load cell, linear actuator and any metal fasteners.

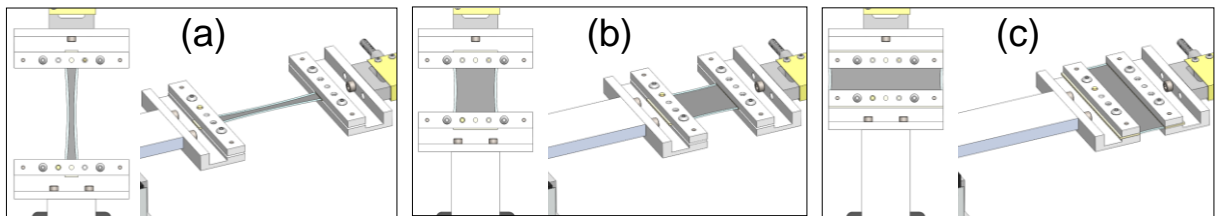


Figure 7.6: 3D sketch of clamp design with various sized specimens the clamps can accommodate (a-c).

As previously mentioned, the specimen and clamps were designed with a tongue and groove respectively which ensures proper specimen placement and alignment before clamping, Figure 7.7.

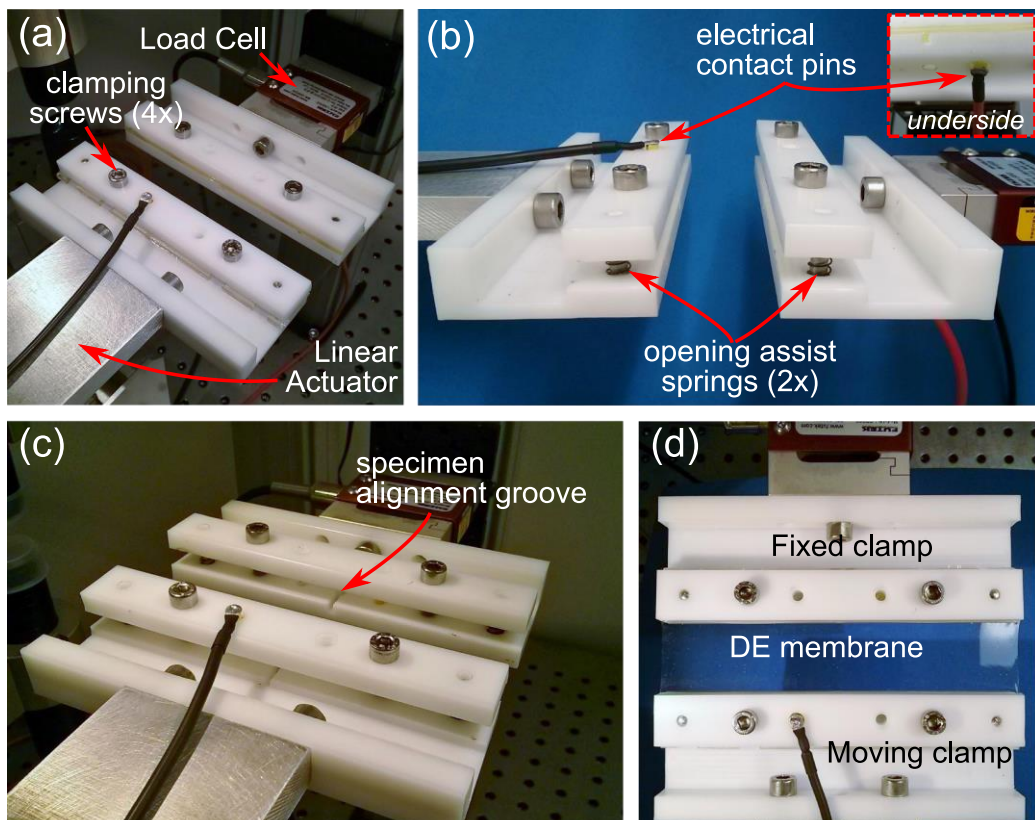


Figure 7.7: Photos of clamps, (a) Isometric view of clamps, (b) side-view of clamps highlighting opening assist springs and electrical contacts, (c) clamps open revealing specimen alignment groove for repeatable specimen alignment, (d) top-view showing stationary clamp, membrane and clamp mounted to linear motor.

The electrical connection to the specimen was built into the clamps. Gold-plated, spring-loaded contact pins (Figure 7.8) were fixed in the clamps so that upon mechanical clamping (tightening the two screws) the electrical connection was also made.

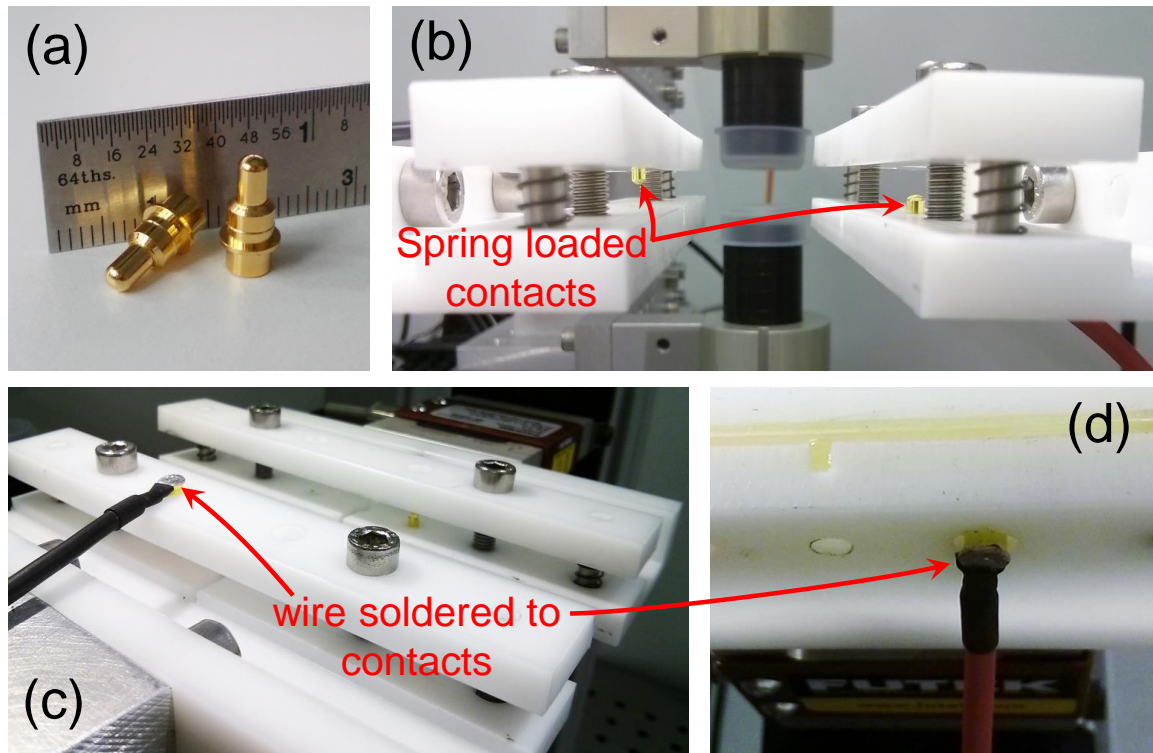


Figure 7.8: Electrode connections in clamps, (a) Close-up of gold-plated, spring loaded contacts used in clamps, (b) contacts in clamps, (c-d) wire connections to amplifier soldered to ends of contacts.

Lead wires with connections to the HV amplifier were soldered to the top of the gold plated contacts. The spring loaded contacts were used to reduce variation in electrical contact pressure to the electrode surface from specimen to specimen. This feature simplified the process of inserting the specimen into the clamps. The clamps had an overall height of less than 20mm which was needed to avoid a collision with the thickness sensors when scanning the specimen thickness.

7.3.3 Devices and Instrumentation

The setup was mounted to a vibration isolated optical table (air-cushioned) located in a climate controlled cleanroom (ISO 7). Extruded aluminum optical rails (Thorlabs) formed the structure on which the motors and sensors were attached. Several additional jigs were precision CNC-machined from 12mm thick aluminum plates. Two linear-servomotor-driven actuators (Aerotech ACT115DL) were employed in the setup. The *x*-axis actuator stage stretched the DE membrane and the *y*-axis stage carried the 2-confocal displacement sensors. The actuators have a travel range of 200mm, a resolution of $\pm 2 \mu\text{m}$, a maximum speed of 5m/s and a maximum continuous force of 105N. The entire setup is presented in Figure 7.9.

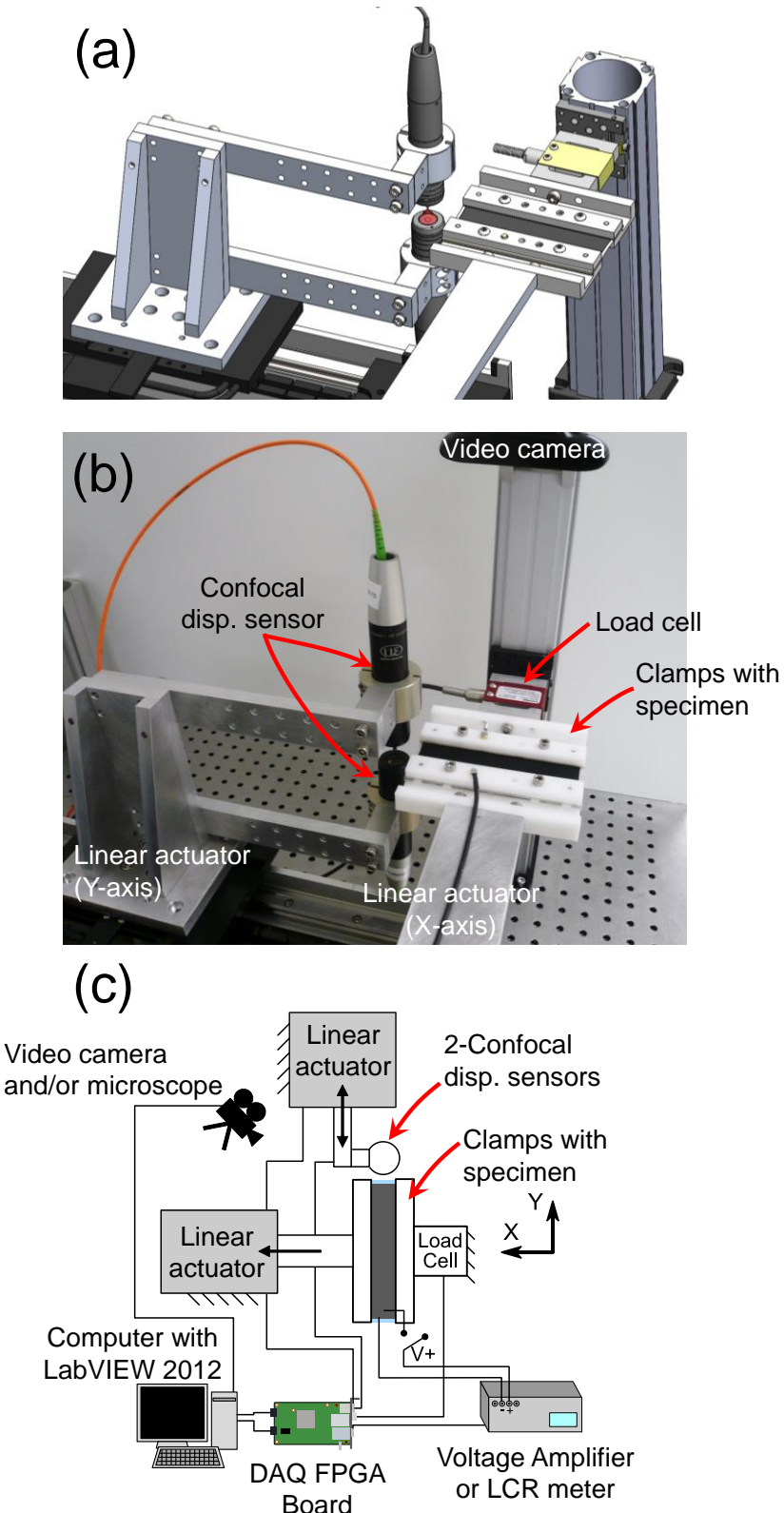


Figure 7.9: Planar actuator experimental setup, (a) CAD rendering, (b) photo and (c) sketch with equipment.

Two confocal displacement sensors (Micro-epsilon, confocalDT IFS 2405) were employed to perform the point-thickness measurement of the DE membrane. These sensors individually have measurement ranges of 1mm with a 10mm offset from the sensor, a resolution of 28nm and a linearity of 0.5 μ m. They were arranged in-line with overlapping measurement ranges

in order to measure the thickness of the DE membrane surface. For a transparent membrane (with known refractive index) only one sensor is needed for the thickness measurement due to the two reflective surfaces which the sensor recognizes. However, for non-transparent membranes (i.e. with electrodes) two sensors operating in displacement mode (first peak used) are required for a thickness measurement. By first using a calibration piece of known thickness, the thickness of unknown objects in the measurement range can be realized. See Figure 7.10.

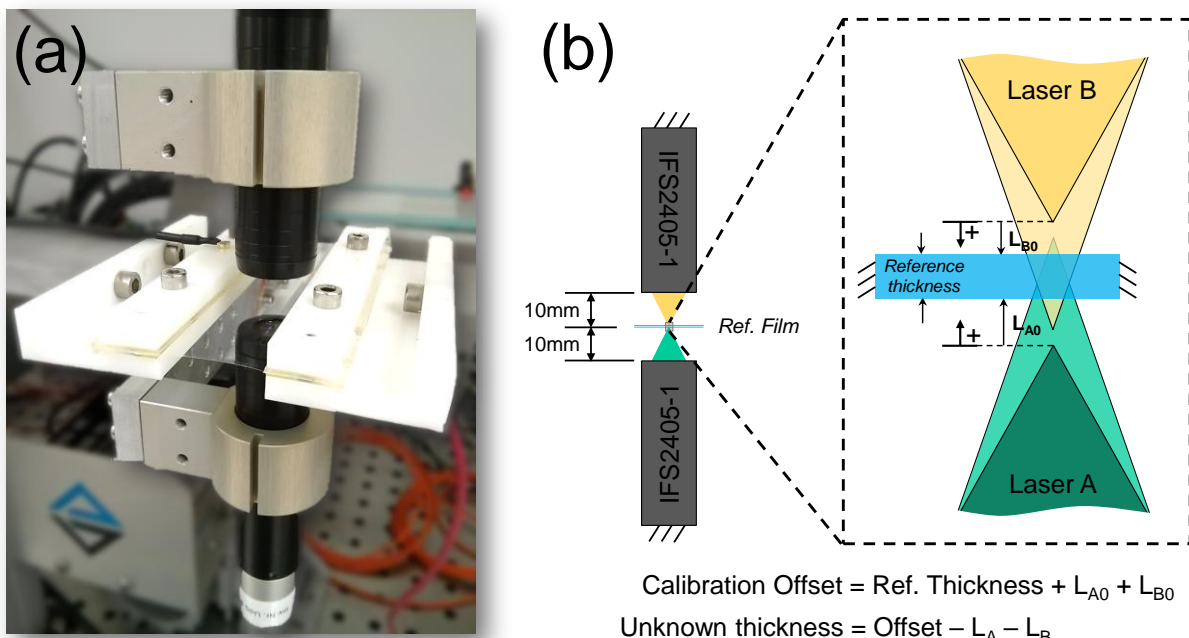


Figure 7.10: Calibrating thickness measurement sensors (a) photo and (b) measurement schematic.

With the y-axis linear actuator the membrane thickness was measured across the specimen width. The thickness profile was at a given cross-section of the specimen. See Figure 7.11. The tensile force on the specimen was measured with a load cell (Futek LSB-302, 25lbf). High voltage signals were supplied to the DE using an Ultravolt® HVA series amplifier (shown in Figure 7.9(c)). For resistance and capacitance measurements a Hameg HM8118 LCR meter was utilized. A video camera (Logitech® B910HD) was employed to continuously observe one electrode surface throughout the tests. The actuator and sensor signals were processed through a National Instruments™ 7852R Field Programmable Gate Array (FPGA) board which was programmed from a Windows 7® desktop computer running LabVIEW 2012™.

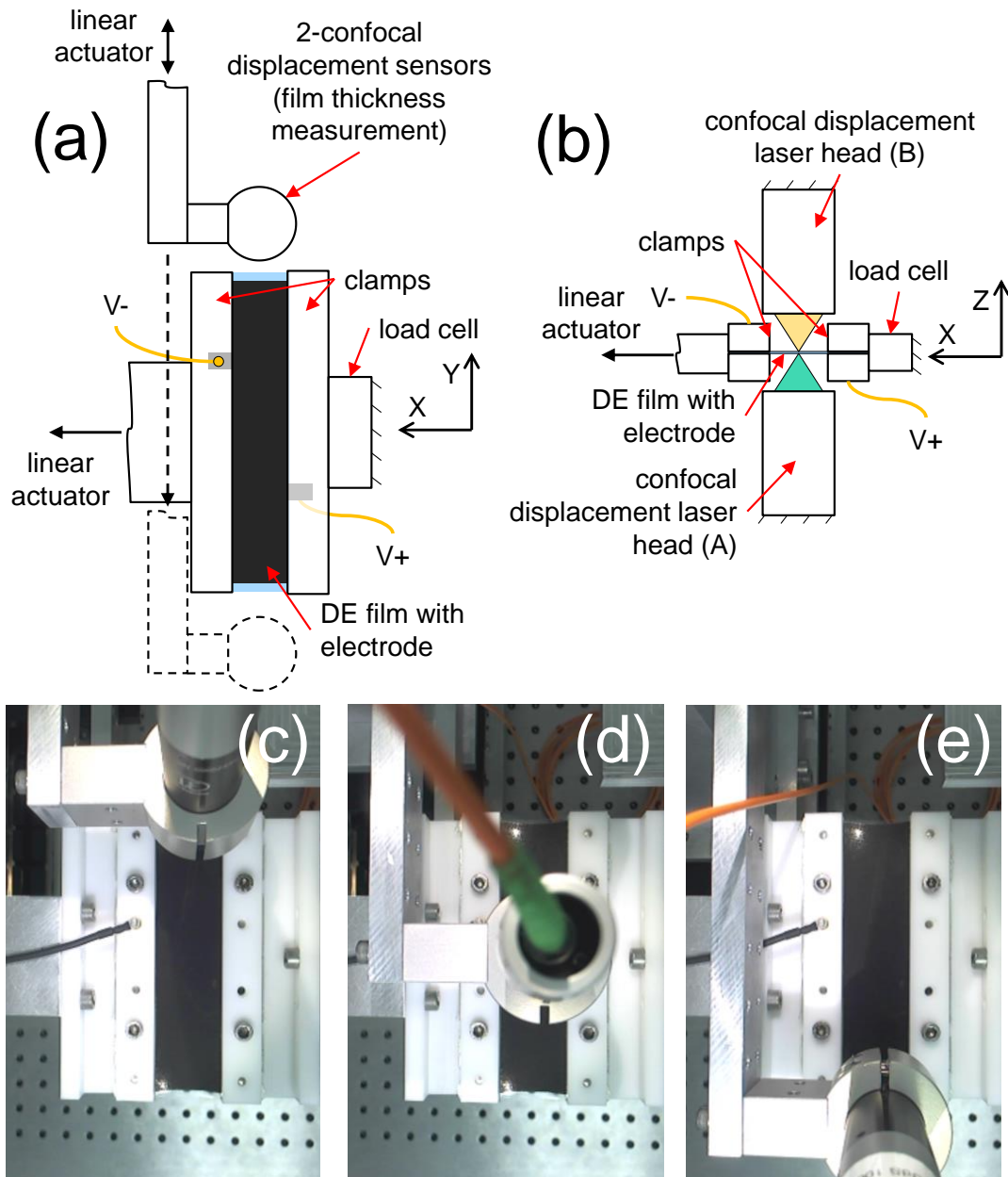


Figure 7.11: Thickness scan of membrane (a) sketch from above, (b) sketch from side, (c-e) photos from above as membrane is scanned.

7.4 EXPERIMENTAL RESULTS

This section presents an overview of some tests which can be performed with the device as well as a summary of the results and analysis. The prepared pure-shear specimens were first placed in the clamps, the four clamp screws were carefully tightened and the x -axis linear actuator was enabled (fixed). This initial starting position was maintained as the zero stretch reference for all the following tests. The sacrificial connecting tabs were clipped, freeing the two halves of the specimen. Figure 7.12 shows the specimen before and after clipping.

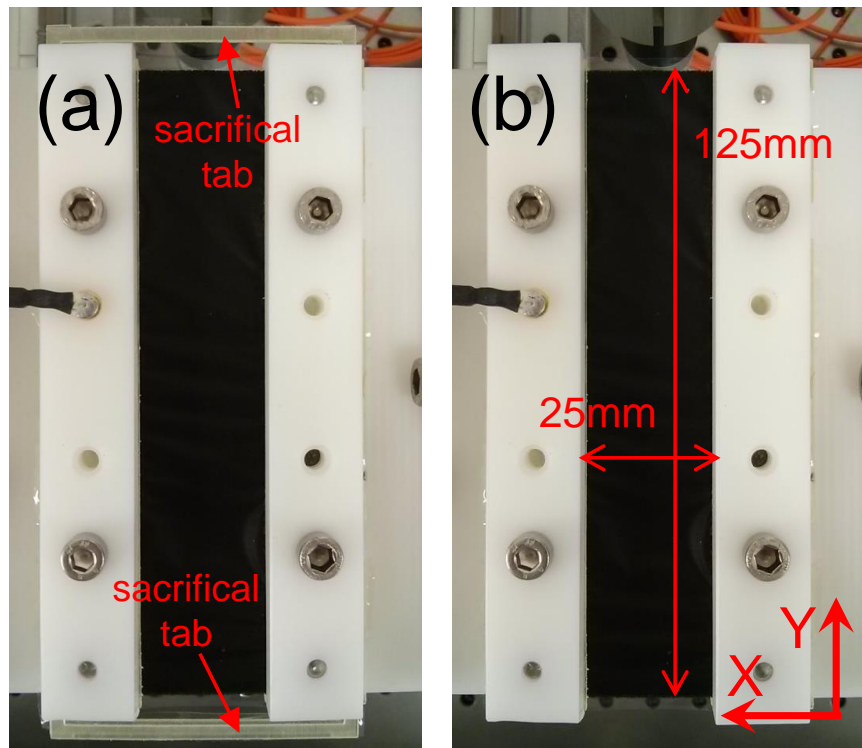


Figure 7.12: View of specimen (with electrodes) in clamps (a) before, and (b) after removing the sacrificial connection tabs.

The following set of tests were executed for several identical specimens (same film, electrode mix and fabrication procedure):

1. Scan across the specimen width, measuring thickness profile.
2. Mechanically load the specimen at various sinusoidal rates.
3. Perform isometric (constant position) tests at different pre-stretch levels and at various electrical loading rates.
4. Perform isotonic (constant force) actuation tests at various loads.

7.4.1 Thickness profile test

Thickness profile scans were performed to check the repeatability of the specimen fabrication process. To do this thickness sensors were moved in a linear manner (at 5mm/s) from one side of the specimen and back again. The scan crossed the specimens at their undeformed mid-section (Figure 7.13(a-b)) from the right to the left and back again. Figure 7.13(c) presents a profile without electrodes compared with three specimens with electrodes. The specimen without electrode is thinner and shows a significantly lower roughness than specimens 1-3. This added roughness on specimens 1-3 is an artifact of the screen printing. Figure 7.13(d) shows a close-up photo of the screen printed surface which leads to the uneven measurement. Even though specimens 1-3 are rough, they are similar in roughness which suggests that the printing process is consistent. It is also interesting to note the total electrode thickness is $\sim 9\mu\text{m}$, meaning the screen print process applied a $\sim 4.5\mu\text{m}$ thick electrode to each side.

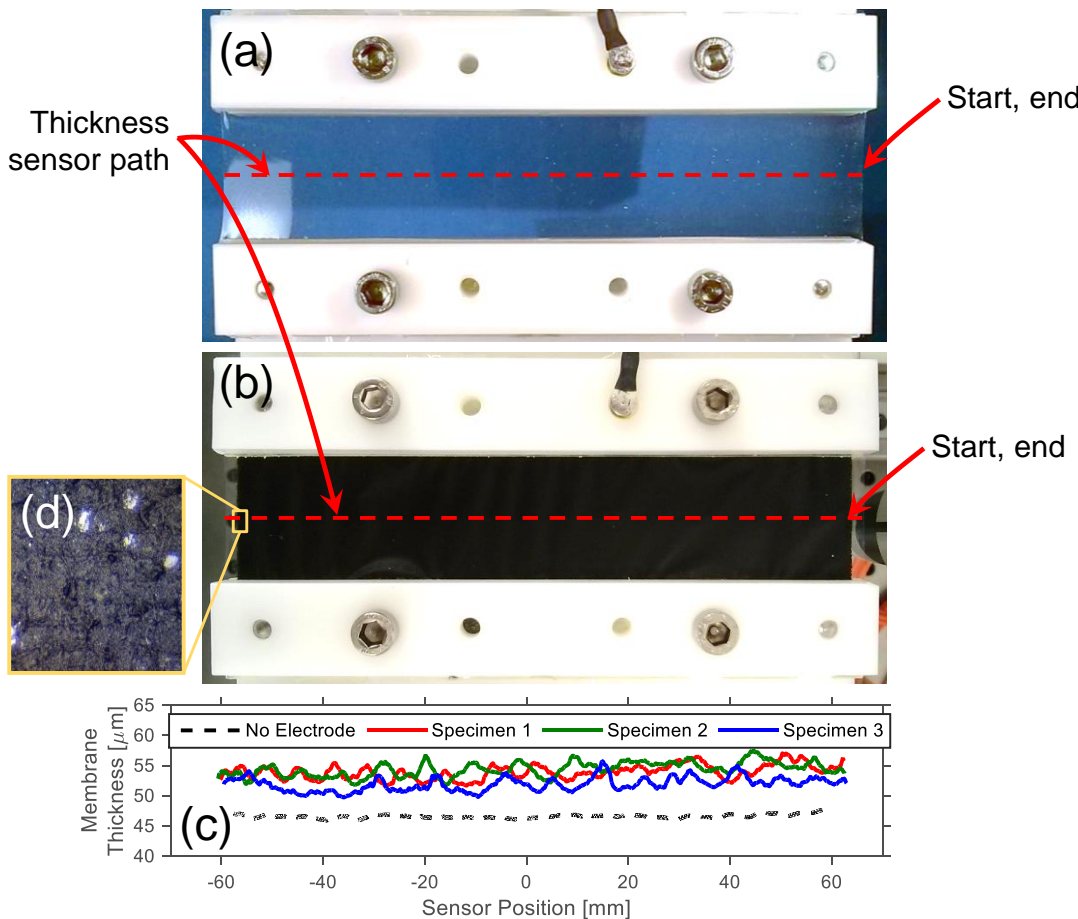


Figure 7.13: Average membrane thickness measurements when un-stretched ($\lambda = 1$), (a) for specimen without electrodes, (b) for specimen with electrodes, (c) specimen profiles compared and (d) close-up of screen printed electrode surface.

A second type of thickness profile measurement was performed in which a stretched membrane thickness was measured and compared with the calculated thickness. The calculated thickness was found assuming the material maintained constant volume while stretched.

$$\lambda_1 \lambda_2 \lambda_3 = 1 \quad (11)$$

Where λ_1 , λ_2 and λ_3 are the principle stretches of the sample in the x , y and z directions respectively. Since it is a pure-shear specimen with a width-to-length ratio of 5:1, the width is approximated to be constant [149], [157]. Therefore, $\lambda_2=1$ and consequently the thickness can be calculated as follows:

$$\lambda_3 = \frac{1}{\lambda} \rightarrow z = \frac{z_0}{\lambda} \quad (12)$$

Where λ is the stretch in the x -direction (λ_1), z_0 is the original membrane thickness and z is the new thickness.

For this test the specimen was stretched and allowed to rest for 1 minute before being scanned. This was performed for four different λ_1 values. See Figure 7.14. The dashed horizontal lines

represent the calculated thickness found using Eqn. 10 while z_0 ($52.9\mu\text{m}$) was the measured average thickness before stretching ($\lambda = 1$).

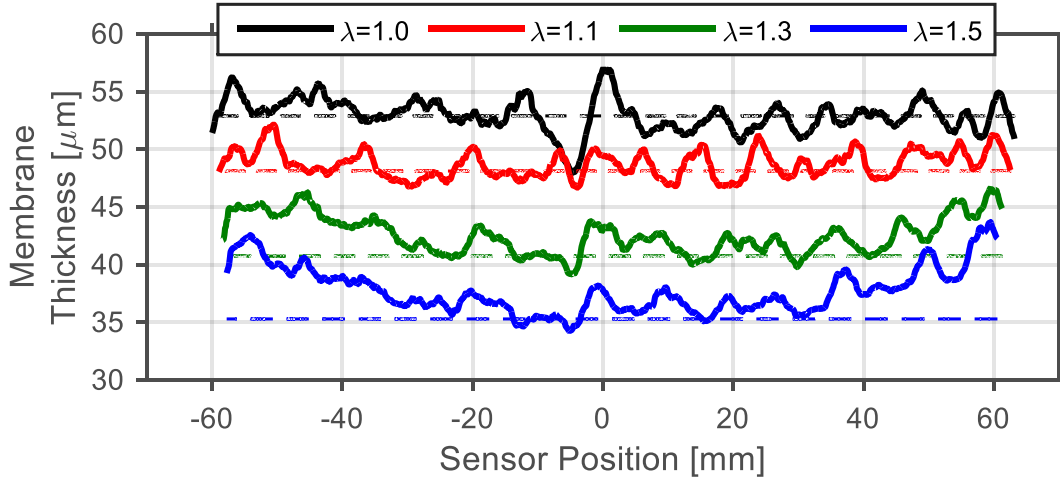


Figure 7.14: Measured thickness profile when stretched to 4 different stretch levels. Dashed lines are calculated thickness.

The linear actuator performing the scan was fixed and did not move in the x -direction as the specimen was stretched. Therefore, the thickness profiles recorded were at different cross-sectional “cuts” of the membrane. Nevertheless, the reduction in thickness due to the stretch can be realized by this measurement. Note for higher stretch levels the thickness deviates from the calculated thickness, especially at the free-ends. This is attributed to the necking of the specimen’s width. It compromises the plane-shear approximation and results in a thicker membrane at the free edges. The calculated thickness is most similar to the measured thickness at the middle of the specimen.

7.4.2 Force vs. displacement test

Next the specimens were stretched at rates of 0.02Hz up to 12.5mm ($\lambda = 1.5$) while measuring force, displacement, thickness, resistance and capacitance. Figure 7.15 presents the time resolved results for one specimen when the voltage was on and off. This plot is valuable when predicting voltage induced stroke for different counter loads as discussed in Hodgins *et al* [84]. While the tensile test was performed, the “local thickness” of the specimen was measured. It is termed “local thickness” because the sensors measured the thickness continually along a 2mm line at the approximate middle of the specimen width. The sensors were oscillating sinusoidally along the line at a rate of 2Hz to obtain a better average reading of the electrode surface.

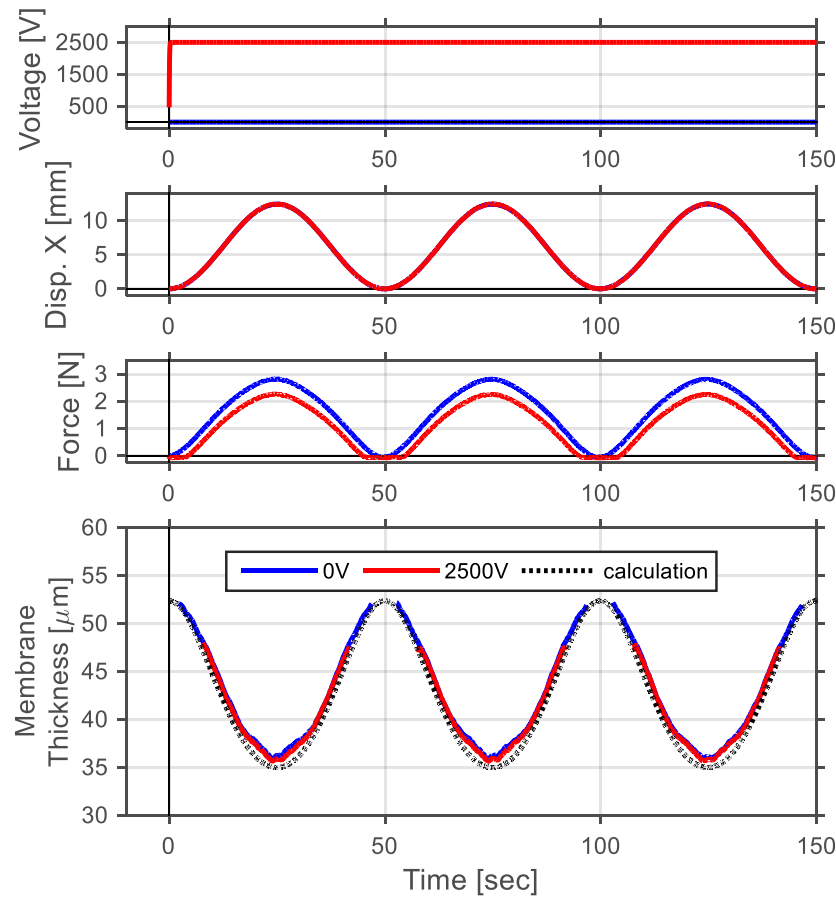


Figure 7.15: Time resolved force-displacement results of tensile test for one specimen.

As expected, with 2500V applied there is a noticeable decrease in the measured membrane force. The thickness change in the membrane was as expected: the thickness decreases as the specimen is stretched. The membrane thickness is quite similar in magnitude to the calculated thickness (Eqn. 11). As would be expected, the thickness deviation is greatest at the higher elongations because specimen has lost its original rectangular shape due to necking. The applied voltage has little to no impact on the thickness, as expected, because of the constrained boundaries and the pure-shear approximation. Hence the thickness change is dominated by the stretch in the x -direction. Due to the film wrinkling slightly out-of-plane at low elongations yielding irregular thickness readings, no results are shown for low stretches.

To examine and ensure the repeatability of the tensile test the 3 specimens were tested in the same manner. For comparison force vs. elongation is plotted in Figure 7.16(a).

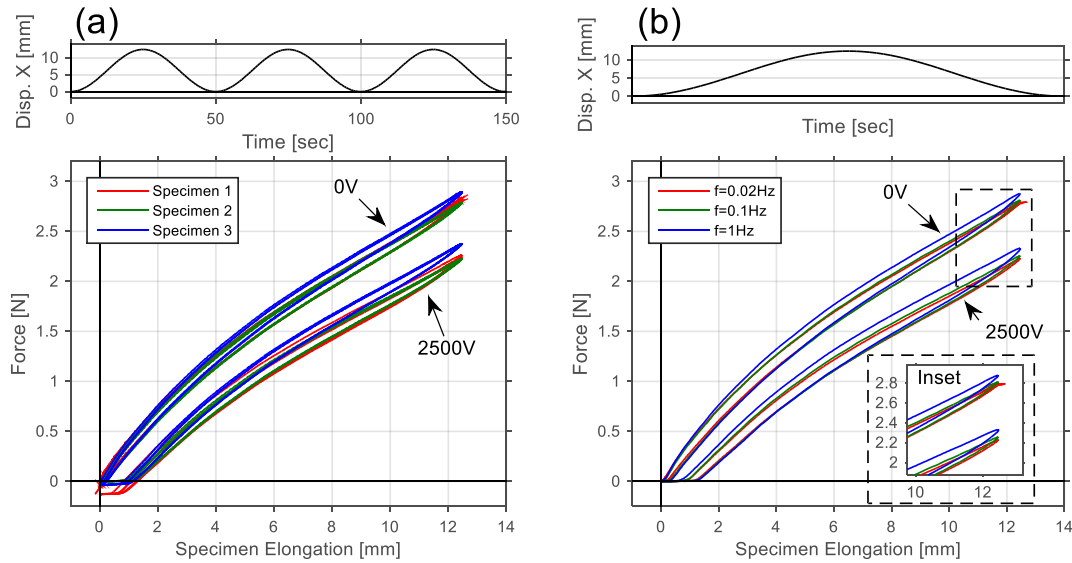


Figure 7.16: Force-Elongation plot for sinusoidal displacement of (a) three specimens showing repeatable results and (b) one specimen at different elongation frequencies showing increase in force with frequency.

The results for the three membranes are very similar and this is attributed to the repeatable electrode printing and fabrication. The small differences in force may be due to slight variations in membrane thickness from specimen to specimen. Figure 7.16(b) shows the results for Specimen 2 at different frequencies. The increase in the peak measured force is higher due to the viscoelastic response of the film. Since the setup is capable of testing high mechanical rates this can be helpful to identify parameters when modeling the viscoelastic response of elastomer materials.

The electrical properties of the DE membrane were tested when stretched to show another capability of the testing device, Figure 7.17.

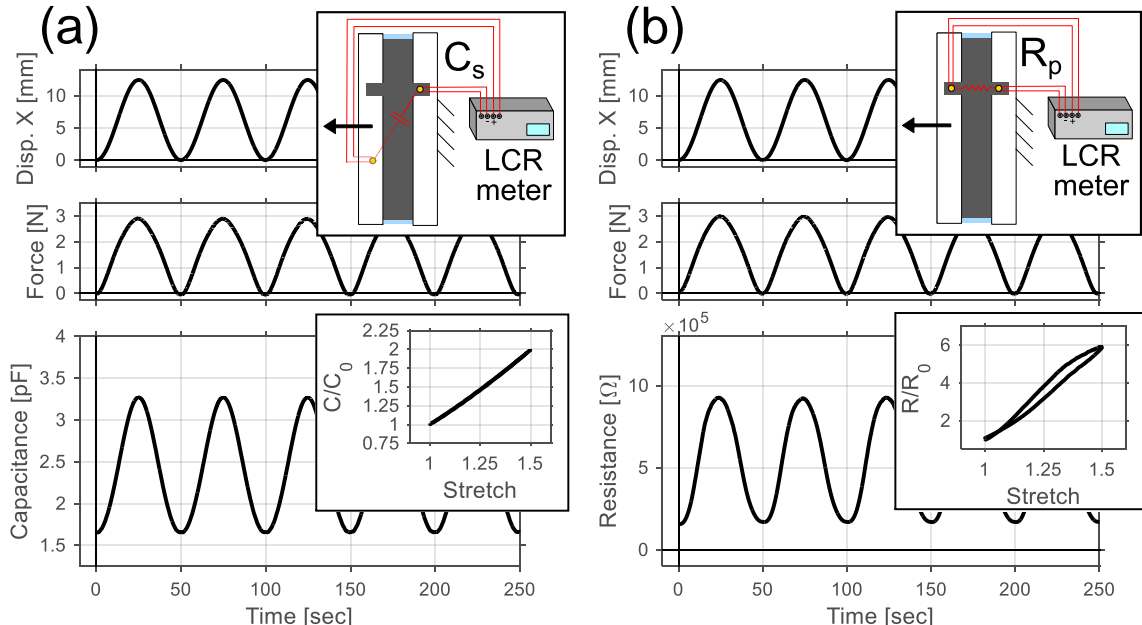


Figure 7.17: Measurement of capacitance and resistance change when sinusoidally stretched. For capacitance (a) the LCR measured the series capacitance, while when measuring resistance across one electrode (b) the LCR measured the parallel resistance.

First the capacitance of the DE was measured and secondly the electrode resistance was measured. The two tests were performed for sinusoidal oscillations with an amplitude of 12.5mm ($\lambda=1.5$) and 0.02Hz. The capacitance was measured with an LCR meter equipped with Kelvin clips and a 4-wire probe. The device was set to measure at 100Hz for capacitance and 1kH for resistance. The stretch induced capacitance change shows a very linear response without hysteresis. This is because the specimen area and thickness greatly influences the capacitance. The resistance change here is quite repeatable but not without hysteresis. The mechanism which leads to this is not known but future tests will examine this more closely. In general, this test procedure and other similar ones will be beneficial in benchmarking highly compliant and conductive electrode materials for DE devices.

7.4.3 Isometric tests

The blocking force was measured at different stretches while increasing and decreasing the voltage linearly. Figure 7.18 compares three specimens when stretched to three different stretches.

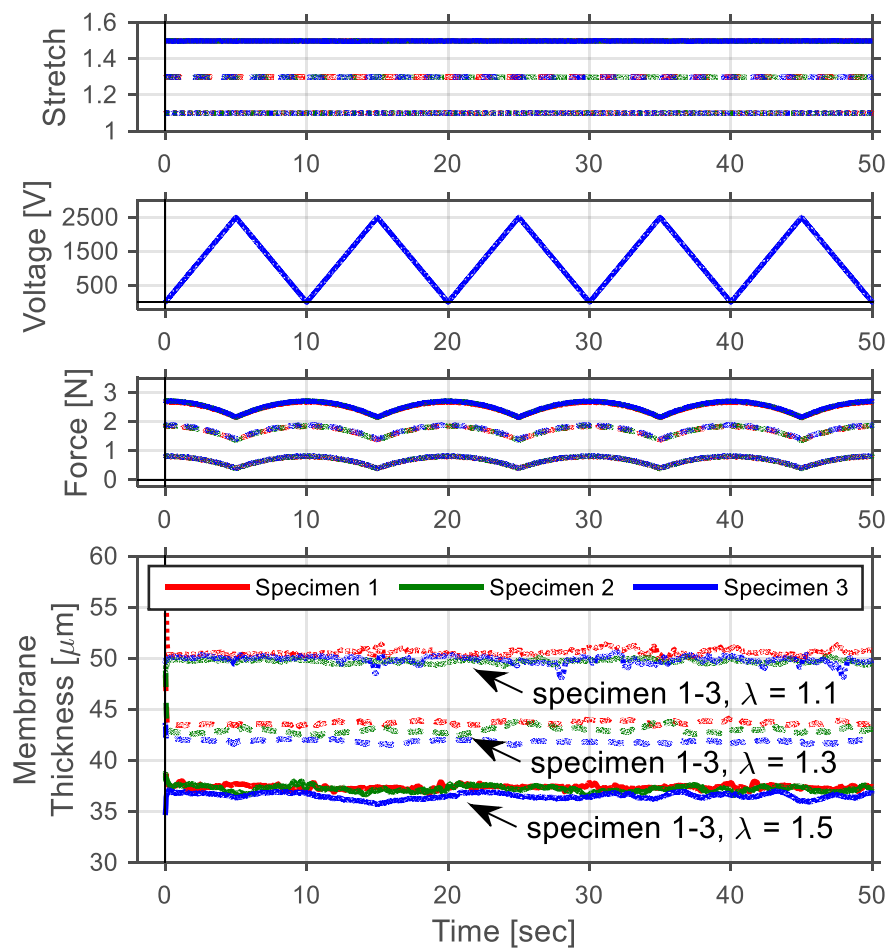


Figure 7.18: Comparing the blocking force results for three specimens at three different stretches for voltage frequency = 0.1Hz

The force level for each specimen lie directly over each other confirming a repeatable specimen fabrication. The measured “local thickness” (at the middle of specimen) shows only a small

variation between specimens. As expected with the fixed stretch there is practically a constant thickness even when actuated. This would show the pure-shear assumption is still maintained.

Figure 7.19 presents the results for one specimen at different stretches and voltage frequencies in terms of force vs. voltage. In Figure 7.19(a) five different stretch ratios are shown while voltage is varied in linear manner, at three different freq. (one cycle shown). Several trends can be seen here.

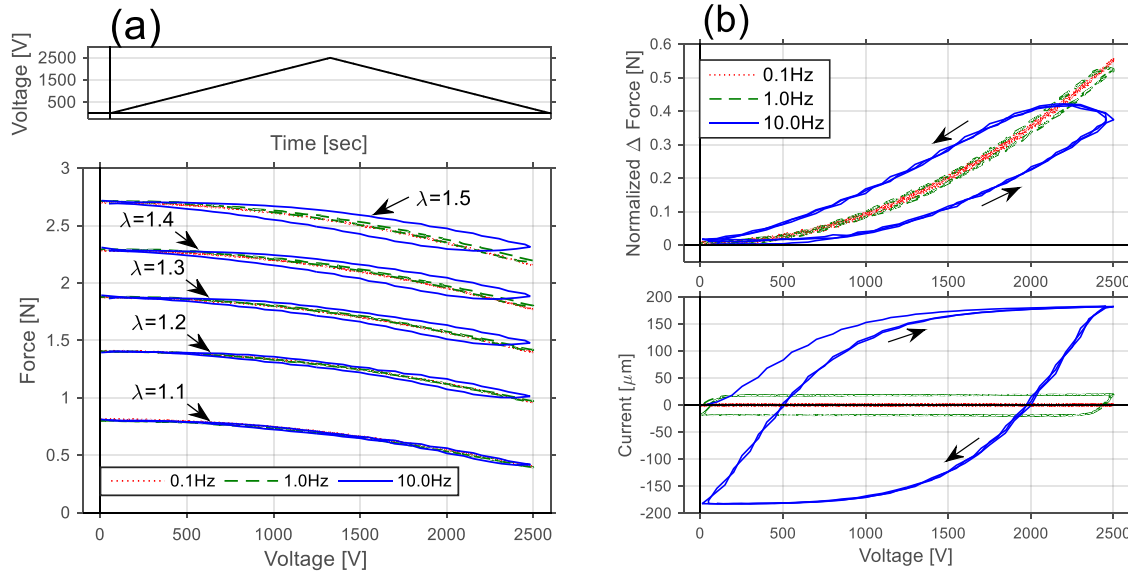


Figure 7.19: Blocking force measurement results (a) Force-voltage at different stretch levels and at 3 different driving frequencies, (b) Normalized force and current vs. voltage at $\lambda = 1.5$.

Firstly, the larger stretches produce a larger change in force. This observation agrees with the diverging constant voltage force-elongation characteristic seen in Figure 7.16 as well as in York *et. al.* [49]. Secondly, it can be seen in Figure 7.19(a) that the hysteresis increases with the stretch and in Figure 7.19(b) with voltage frequency. Also Figure 7.19(b) compares the Δ force along with the current draw for $\lambda = 1.5$ at three frequencies.

This plot clearly shows that the hysteresis observed in the force measurement is dependent on the driving frequency. As would be expected, the current draw increases with the voltage frequency. The hysteresis seen in the force is primarily attributed to the electrical dynamics of the DEA. Charging and discharging of the electrode surfaces is a time dependent process. This phenomenon is normal since DEs are effectively a variable RC-circuit with a time constant (τ) which increases with the stretch (due to the increase in capacitance and electrode resistance).

7.4.4 Isotonic tests

The actuation elongation was tested by applying a constant force while the voltage was cycled. This is a standard test for DEAs [149] and is helpful when comparing the electro-mechanical sensitivity of the DEAs. A custom LabVIEW algorithm (similar to the method reported in [84]) was written to operate the test rig in force control mode.

Figure 7.20 presents the time resolved constant force actuation results for a specimen at three different force levels. The higher the force (of stretch), the higher the actuation stroke was for a given maximum voltage. The average electric field calculation is a result of using the dielectric elastomer as the thickness. To get this the unstretched electrode thickness was removed from the known membrane thickness:

$$z_{DE} = \frac{z_0 - z_{Electrode}}{\lambda} \quad (13)$$

Where z_{DE} is the thickness of the DE film, z_0 is the average membrane thickness (from unstretched profile scan), $z_{Electrode}$ is the initial combined electrode thickness ($9\mu\text{m}$) and λ is the membrane stretch. Since the maximum voltage is 2.5kV the electric field approximation (V/z_{DE}) is higher for higher forces (or stretch).

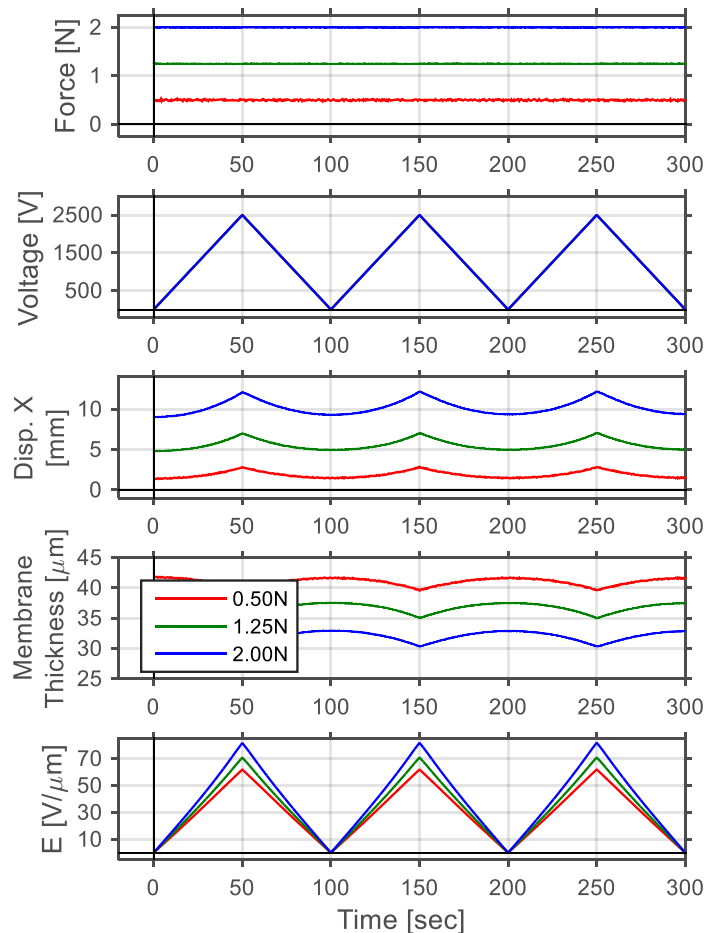


Figure 7.20: Time resolved constant force actuation test results at three different force levels. The voltage induces a stroke and a decrease in thickness. Based on this thickness (and the voltage) the electric field is determined as shown at the bottom frame.

In Figure 7.21(a) the results from Figure 7.20 are presented in terms of the actuation strain versus the electric field. This plot illustrates that the DEA is increasingly electromechanically sensitive the more the membrane is stretched. These results confirm as do several other studies [158]–[160] that the pre-stretch can increase the output of membrane DEAs.

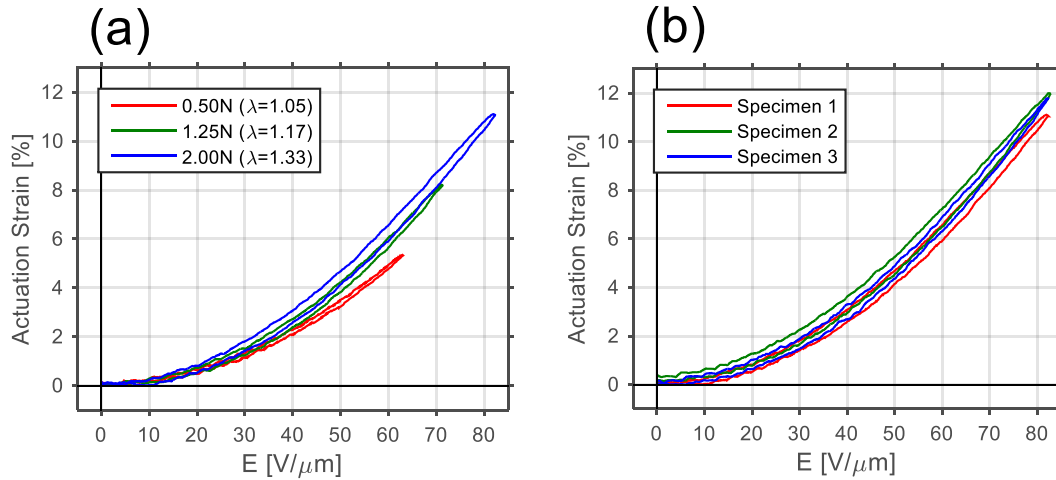


Figure 7.21: Actuation strain vs. Electric field for three isotonic tests, Maximum voltage applied is 2.5kV. (a) Specimen at different constant force levels. Pre-stretch increases the electromechanical sensitivity of the actuator. (b) Comparison of three specimens at constant load of 2.00N showing repeatability.

One can also notice that since the same was voltage applied for each test (2.5kV) it results in different electric fields due to the difference in membrane thickness. Figure 7.21(b) additionally demonstrates that the results of the isometric tests are repeatable. Specifically, three different specimens were tested at 2.00N. The slight deviations are attributed to the small differences in membrane thickness.

7.5 CONCLUSIONS

This paper presented the design, fabrication and initial results of a testing station which is capable of accurate and repeatable measurements of the mechanical and electrical properties of DE membranes. A systematic approach for preparing and mounting the test specimens in a way which minimizes measurement variation was realized. To demonstrate the functionality and types of repeatable measurements possible with the device, several pure shear specimens were characterized and the results were presented. The outcome showed the setup was capable of performing a variety of repeatable measurements to test DE membranes. Among others this included a novel ability to obtain a membrane thickness profile when the specimen was stretched or activated. Future work will use this testing station to characterize various elastomer and electrode materials and their applicability as DE sensors and DE actuators.

Chapter 8 DISCUSSION AND OUTLOOK

The results of this work and their contribution to the field of membrane DEAs are summarized in this chapter. Additionally, in light of the present development, further work packages are suggested for each parts of the thesis.

8.1 SUMMARY OF WORK

This work emphasized the design of membrane dielectric elastomers actuators (DEAs). The general introductory chapter provided a brief background of DEs and the motivation for investigating membrane DEAs. Specifically, it introduced the need for a compliant mechanism to increase membrane DEA stroke (covered in Part 1), as well as the importance of the new experimental test setups and techniques (covered in Part 2). Chapter 2 covered the fundamentals of DEAs including their electromechanical behavior and the role of the dielectric material and compliant electrodes. Various actuator configurations used and commonly studied in literature were similarly briefly discussed. In Chapter 3 the benefits and requirements of proper bias mechanisms for membrane DEAs (specifically diaphragm membrane DEAs) were shown experimentally. By comparing three types of bias mechanisms, trends were observed which led to a recommendation of a non-linear spring or negative-rate bias spring (NBS) for increasing actuator output stroke. Chapter 4 continued with the experimental study of the NBS as the bias element of the DEA. It was shown experimentally that when the NBS is assisted by a linear spring (LS) it can stabilize the actuator and allow for tuning of the DEA when operating against loads. The addition of the linear spring element allowed for easier modification of the output force and control of the stroke. Chapter 5 presented experimental and modeled actuation results of a membrane DEA demonstrator. The diaphragm DEA was biased by a NBS+LS mechanism. The force was measured for each element and was used to develop a potential energy based model of the actuator. From the potential energy model the stability and stroke of the actuator were predicted for three different NBS+LS combinations. The actuation stroke behavior modeled agreed qualitatively well with the experimental measurements.

Part two of the thesis concerned two test techniques for characterizing and benchmarking membrane DE actuators and materials. Chapter 6 presented a novel test device capable of applying programmable loads to DE membranes via a custom programmed electromagnetic motor. The design, setup and control were first explained before using the device to pre-load a diaphragm DEA. A range of strokes were observed when positive and negative stiffness mechanisms were tested. These results concurred with those found in Chapter 3 which concluded that the largest stroke can achieved by using a negative stiffness mechanism. It was

additionally shown that for the DEA to maintain overall mechanical stability the bias mechanism stiffness must be of *lower stiffness* (i.e. softer) than the membrane DEA. Chapter 7 presented the design of a uniaxial test device and procedure to repeatably test planar membrane DEs. The design included the new ability to obtain a membrane thickness profile when the specimen is stretched and/or actuated. The specimen fabrication procedure and tester design included features to eliminate human error during handling. Electromechanical characterization results were presented for pure-shear specimens. The tester showed very repeatable results which are promising for future material benchmarking and electrode mixture studies.

8.2 FUTURE WORK IN DESIGNING MEMBRANE DEAs

To progress on toward commercialization of membrane DE actuators several areas should continue to be addressed by the DE research community. Some have been touched on in this thesis and some not. One is on optimizing the design of the bias mechanism. This thesis presented one kind (i.e. shape) of bistable mechanism but there are more shapes and sizes possible. Considerable work can be performed to optimize the shape and size of the bistable mechanism. This can be done perhaps through finite element computer simulations.

Another area is designing the negative-stiffness mechanism to make the overall actuator more compact. This could be through a clever spring design or a combination of miniature compliant mechanisms to achieve the stroke desired while maintaining a small device footprint.

Related to this is the packaging of the membrane DEA system. The DEA system should be as small as possible and preferably smaller (if not smaller, then at least lighter) than the conventional actuator solution. This calls often for clever configuration and arrangement of the membrane DEAs and the bias mechanism to make use of the available space. It is recommended that the membranes be sized (via changing the diameter or area of electrode) based on the application's stroke requirements and/or stacked depending on the force requirements. The size is typically constrained by the maximum film strain and the force is limited by the maximum allowed electric field. Stacking the membranes increases the available force but, as is the case with stacked actuators (page 11), making a robust electrical contact between the layers can be challenging and thus should be thoroughly thought-out.

Use of negative-rate bias mechanisms with DEAs can be expanded to DE configurations other than diaphragm/circular/out-of-plane configurations. For example, a planar DEAs can also benefit from a well-designed negative-rate bias mechanism just as do the circular DEAs. Furthermore, because the out-of-plane force-displacement (F-D) response of circular DEAs is parabolic (due to the geometry), the achievable stroke, even with the NBS mechanism, is unnecessarily limited. The problem lies in fitting a linear NBS profile into a parabolic-shaped gap (see Figure 3.4, p.19). However, for the planar membrane DEAs tested in Chapter 7, this is not the case. They exhibit a relatively linear F-D response (see Figure 7.16, p.100). This

means the workable area for these actuators is more linear in shape, which allows for easier tuning the linear region of the NBS mechanism to the DEA.

8.3 FURTHER WORK IN EXPERIMENTAL TECHNIQUES

Considerable work is yet to be performed in the area of experimental testing of DEAs. The suggestions here are limited to the potential tests which can be performed using test setups described in part 2 of the thesis. Firstly, the programmable force motor presented in Chapter 6 can be applied to not only to simulate bias mechanisms, it can be also used to mimic a viscous load such as in a fluid pump. If the load was known (perhaps a non-linear one) the motor could be programmed to be the load as the membrane DEA acted against it. The advantage of this is that the programmable motor can measure the force and position while testing. This eliminates the need to somehow adding sensors to measure the DEA force or stroke when acting against the load. The load can be changed simply modifying the LabVIEW program.

Other tests using the programmable motor can be performed on planar membrane DEAs. As explained in the previous section, these membrane DEAs are more linear in their force-displacement response (e.g. Figure 7.16, p.100) than the diaphragm DEAs (e.g. Figure 6.6, p.75) and therefore when biased with a linear *negative-rate* spring they could exhibit actuation strains easily higher than 30%. This can be pursued as an alternative to diaphragm membrane DEAs. The programmable motor test rig could potentially help show the maximum actuation stroke achievable for planar DE membranes. Again this would not require the extra work to build the physical bias mechanism.

As presented in Chapter 7, the comprehensive DE tensile test device is capable of accurate and repeatable tests. The test rig will enable future investigations into the impact of DEA fabrication process parameters on the actuator performance. In the area of conductive electrode patterning, the parameters such as screen size and number of layers could have an impact on the stiffness and resistance of the DEA. Still, further tests could study different electrode mixtures to learn, for example, the impact the electrode components (carbon black or PDMS) have on the actuator or sensor electrical resistance, mechanical compliance and thickness per layer [161]. Other investigations, some of which are ongoing, will delve into answering questions like how the film thickness, film pre-stretch and planar specimen geometry impact the actuator performance.

The test rig was built so that extra motors and/or sensors could be added. An incremental improvement step is to add a second motor axis to control the position of the thickness sensors not only in the *y-direction* but also the *x-direction*. This would ultimately enable an *x-y* thickness profile map of the stretched/activated membrane. Such results could aid in validating a FE model of the membrane.

Another interesting study to perform is to map the strain fields of a membrane DEAs using digital image correlation (DIC). To date little work has been reported in this area [162]–[164]

but investigating this topic could help in understanding the effect of membrane pre-stretch, boundary conditions, specimen geometry and electrode stiffening.

The test rig would also be a good platform to study joule heating of the membrane electrodes using thermal camera systems. The electrode resistance of the specimen can be varied by stretching the specimen and the cameras could observe where the resistance is highest. These studies could lead to observation of thermally induced dielectric breakdown as shown in [165].

Additionally, self-sensing, as presented in [166], could be implemented into the test rig to provide useful information into how the capacitance and resistance change while the actuator is driven. These could be very interesting also if the change in capacitance could be verified by digital image techniques.

As one can see there is practically no limit to the number of investigations possible. These experimental results can be modeled in a finite element analysis (FEA) program such as COMSOL to develop detailed material models.

APPENDICES

Appendix A: MINIATURIZATION THROUGH INCLINED BEAM FLEXURES

In an effort to reduce the length and overall size of the DEA actuator system, a new kind of NBS mechanism was designed. For this design the same X-shaped beam mechanism was used, but with new boundary conditions. In this case the clamped ends of the NBS were inclined, therefore producing an asymmetric bistable mechanism, as discussed in Section 4.3.3. The advantage of this method is that the mechanism is initially asymmetric, potentially eliminating the need for a linear spring. Work by Beharic *et al* showed that at a certain angle the bistability is lost, therefore giving it only one stable solution [167].

The linear spring (as used in Section 4.4.2 and the chapter on DEA Prototypes) adds to the length of the overall actuator. For instance, the DEA prototype in Chapter 5 is approximately 50mm long (including the support structure) and the stroke for this actuator ranged from 2mm for a stable stroke and 5mm for a bistable stroke, therefore giving the actuator 4-10% elongation. Figure A.1 compares a DEA with the linear spring and one with an inclined NBS.

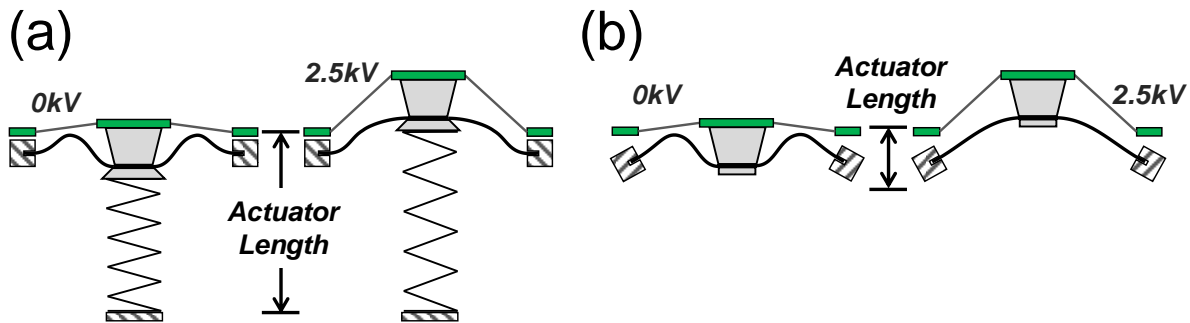


Figure A.1: Comparing the actuator length for two bias mechanism designs (a) NBS+LS and (b) an inclined NBS (iNBS).

To evaluate this design, several small prototypes were built. The buckling frames were designed with an inclined surface and a cover to clamp them down. Figure A.2 shows the buckling frame design and photos of the frame with 0° and 30° inclination angles.

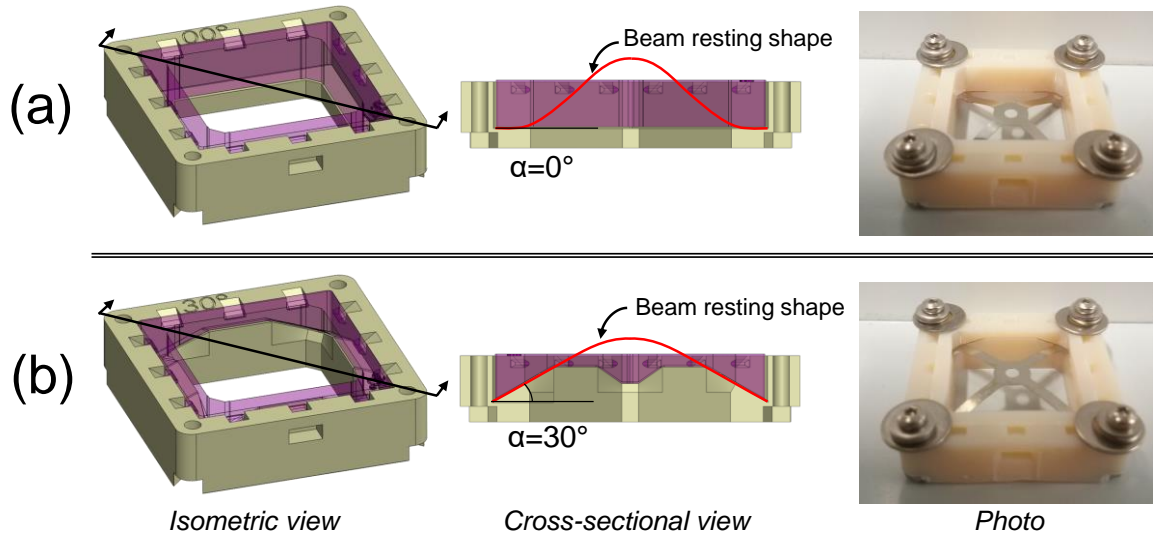


Figure A.2: Buckling frame design (a) 0° and (b) 30°.

Frames with angles ranging from 0° to 30° in steps of 5° were printed, assembled and tested. Figure A.3(a) presents the results for each mechanism. Figure A.3(b) shows a profile of the DEA and two appropriate iNBS elements together.

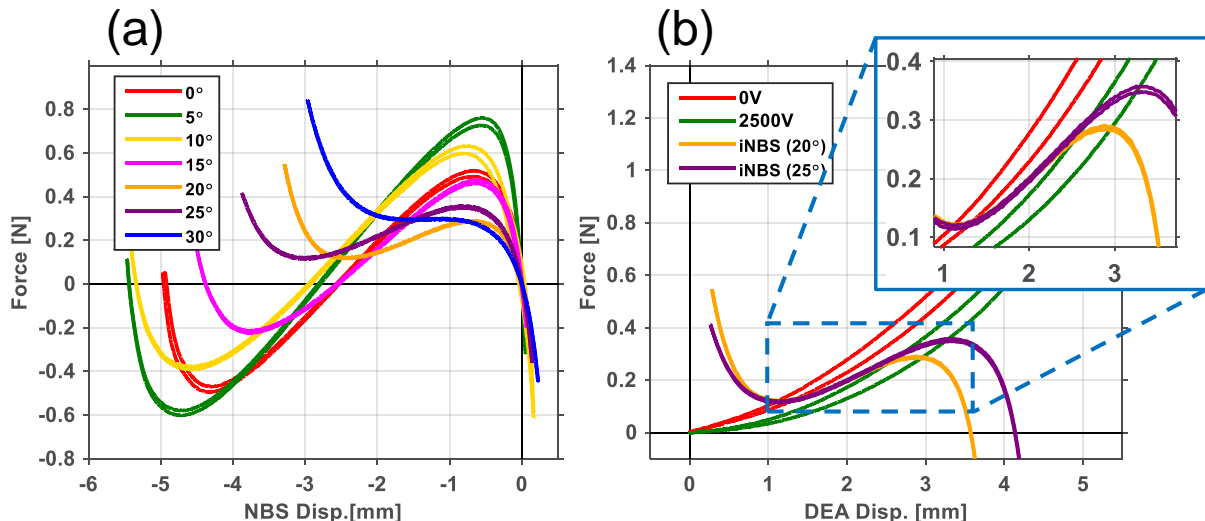


Figure A.3: Inclined NBS test results (a) force-displacement, (b) DEA coupled with 20° and 25° inclined NBS

The somewhat irregular trend seen in Figure A.3(a) shows that as the angle increases, the NBS stiffness in the linear region decreases. Also the distance between stable force equilibrium points decreases. Between 15° and 20° the mechanism loses the second stable position. These mechanisms can be stable when coupled to the DEA just as the NBS+LS mechanisms were in Section 4.4.2 and Chapter 5 on DEA Prototypes.

The DEA actuator coupled with the iNBS has a force profile which appears to have a similar stiffness as the 20° and 25° mechanisms when properly pre-deflected as shown in Figure A.3(b). A small actuator prototype was designed in SolidWorks and printed on the 3D printer. Figure A.4 shows the design which is similar to the ones before. The inclined NBS mechanism

and the DEA are fastened in a frame. The DEA pre-deflection is made adjustable thanks to the four screws which connect the two frames.

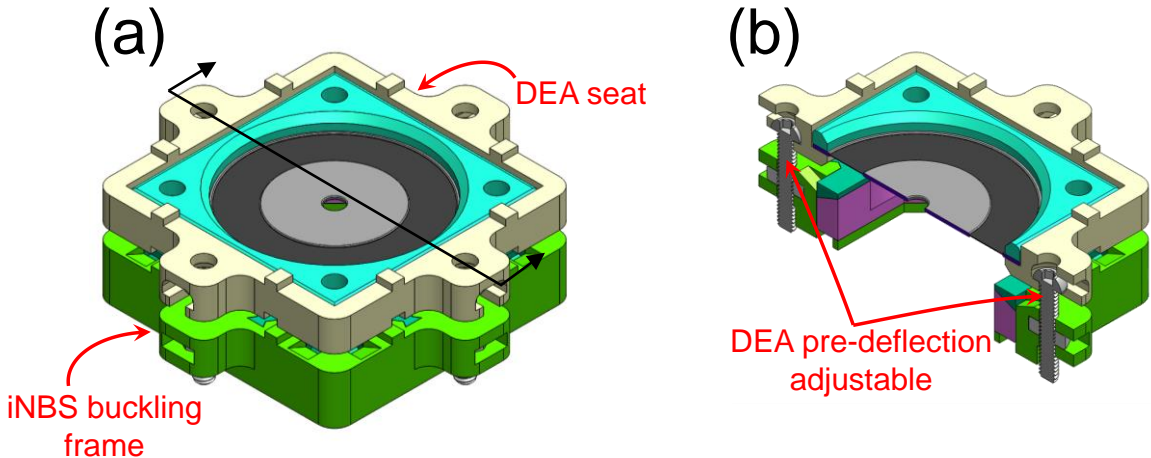


Figure A.4: Solidworks sketch of demonstrator (a) Isometric view, (b) cross-sectional view (iNBS not modeled)

Figure A.5 and Figure A.6 shows photos of the assembled demonstrator at 0V and at 2500V.

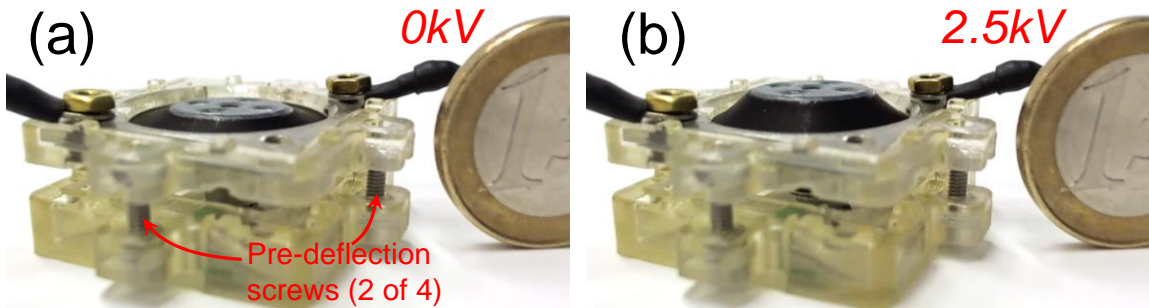


Figure A.5: Photo of inclined NBS demonstrator (a) 0V and (b) 2500V.

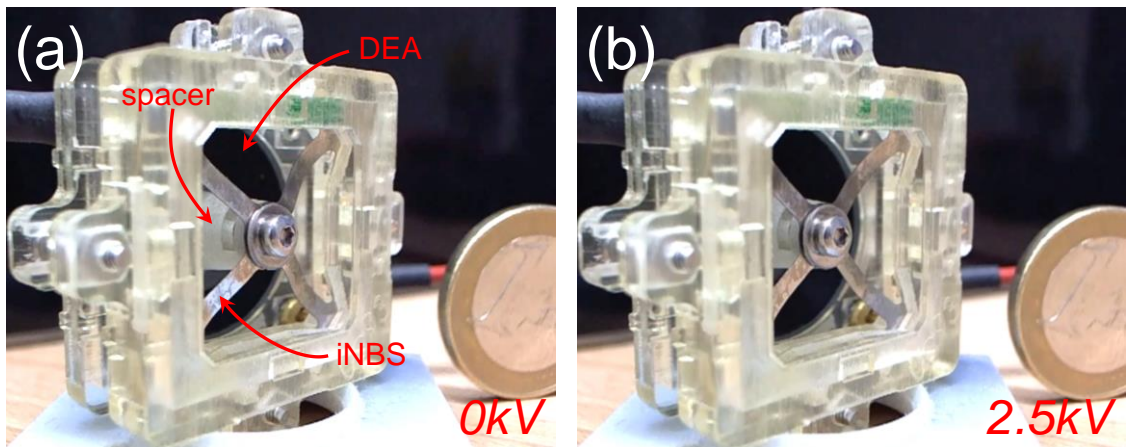


Figure A.6: Photo of inclined NBS demonstrator from rear (a) 0V and (b) 2500V.

Below are the stroke results when applying different voltage inputs to the DEA biased with the iNBS.

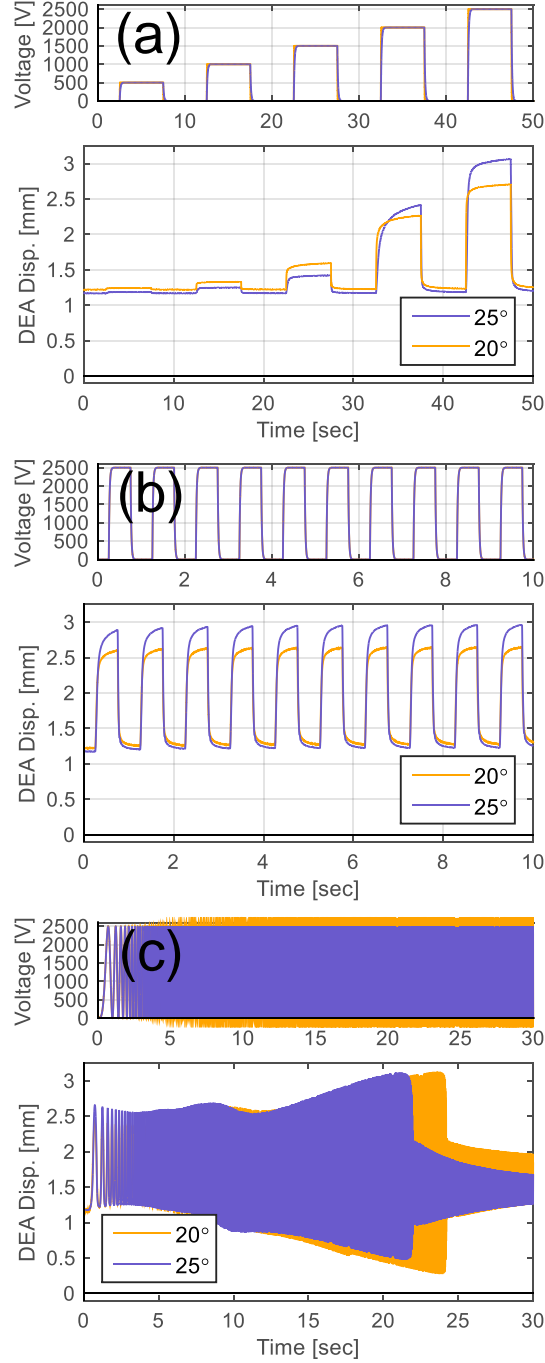


Figure A.7: Stroke results for iNBS demonstrator for different voltage inputs, (a) amplitude modulated square wave, (b) square wave (1Hz), and (c) sine-sweep from 0-60Hz.

Another advantage of this actuator is that the inertial forces are smaller because the linear spring is absent. As seen in the sine-sweep, the actuator responds well at higher frequencies. A maximum stroke is measured at resonance (~48 and 44Hz for 20° and 25° respectively).

In summary, this design is clearly more compact without the linear spring behind the actuator. It produces around 1.8mm of stable stroke. From this design, as shown in Figure A.5 and the stroke shown in Figure A.7, this actuator exhibits stroke of about 14% of its length. This is 4% more than the prototype in Chapter 5 and could certainly be improved with further NBS tuning.

Appendix B: MAGNETIC BIAS FORCE

It has been shown that to increase the stroke of diaphragm membrane actuators, a negative stiffness and non-linear force mechanism is required. The NBS+LS bias mechanism which has been presented extensively here is non-linear and when coupled properly with the DEA, it will operate only in its linear region. Since the diaphragm DEA has a quadratic or a higher order force-displacement relationship, the stroke a linear mechanism can produce is limited by the gap between the force-displacement profiles.

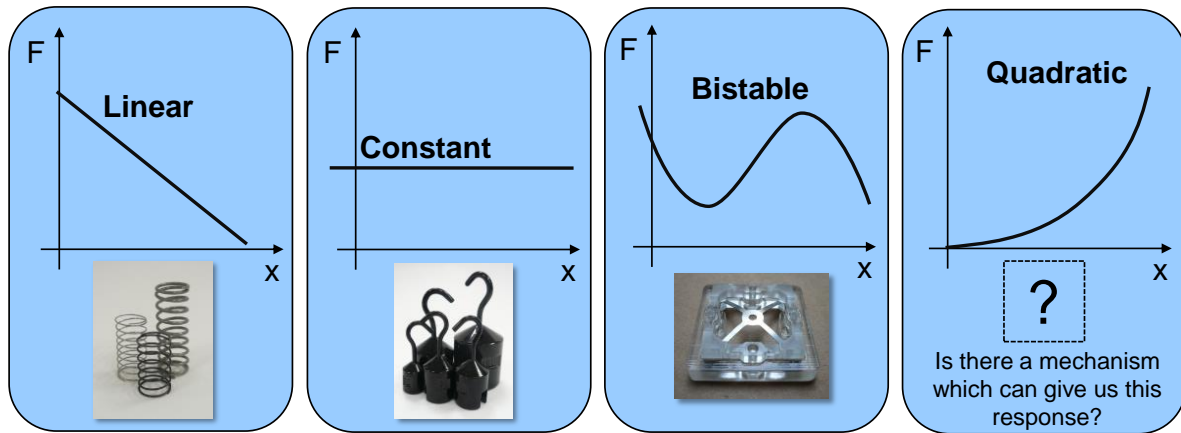


Figure B.1: Bias mechanism force profiles.

Given that the DEA stiffens at higher stretches, it would be desirable to use a bias mechanism which also stiffens with elongation. This could increase the stroke since the bias force would remain in the workable region for higher elongations. As previously seen, the NBS mechanisms increase in force but at a certain point must fall again due to the beam changing buckling modes. However *magnetic attraction force* is shown here to have a quadratic or a stiffening behavior, as seen in the test performed below.

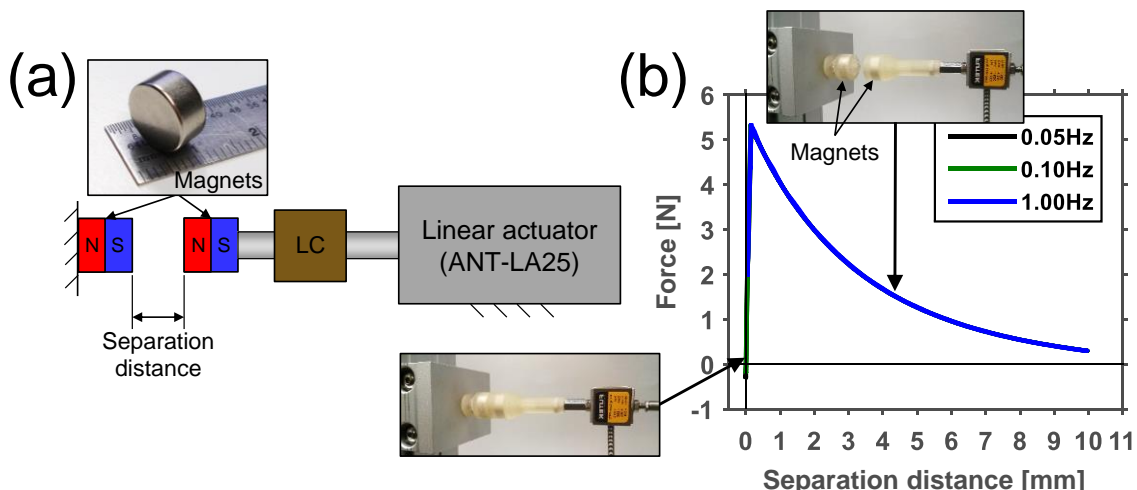


Figure B.2: Measuring magnet attraction force (a) setup and (b) results.

The magnetic attraction force was measured, as presented in Figure B.2. It decreases approximately quadratically as the separation distance increases. These results show that the

attraction force can be used as a non-linear bias force for DEAs. Some advantages are that it is non-contact, high force and rate independent.

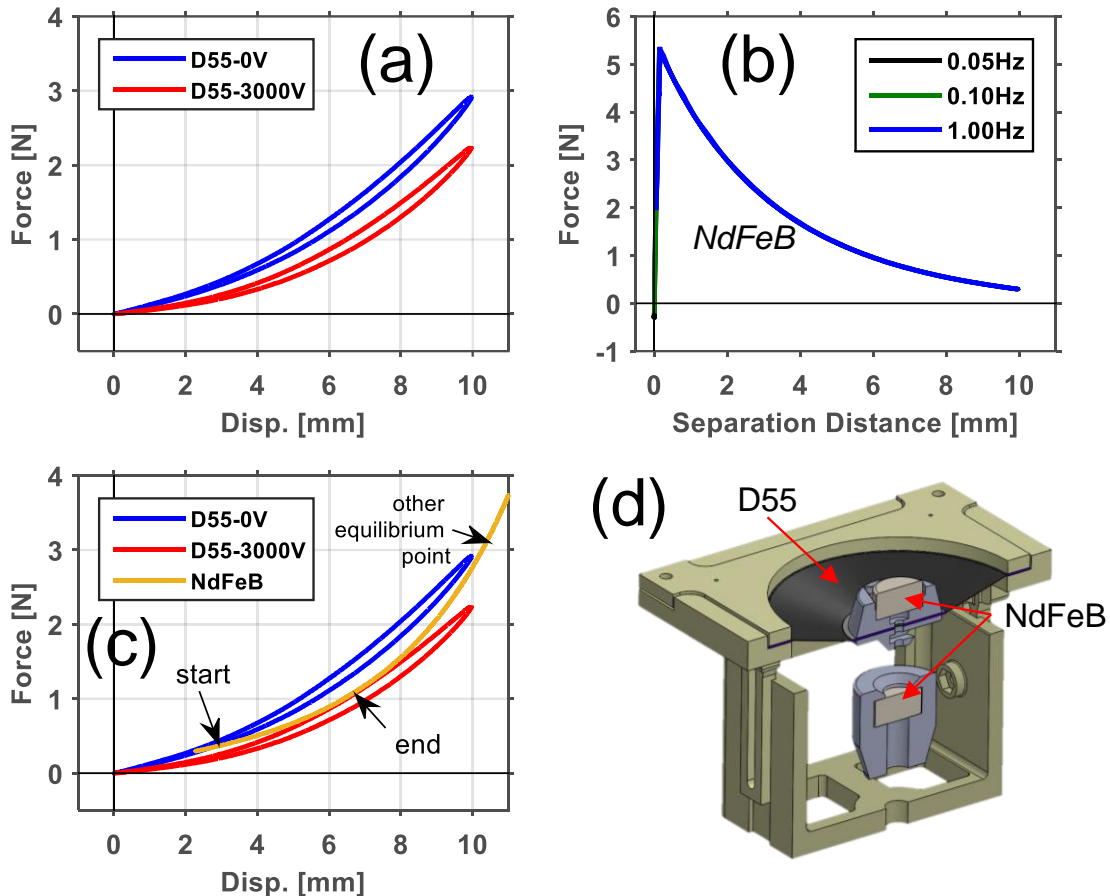


Figure B.3: Magnet demo tests and sketch, (a) DEA force response, (b) magnet attraction force response, (c) theoretical force equilibrium plot showing potential bistability, and (d) demonstrator sketch.

Figure B.3(c) presents the force-displacement results of a DEA biased with the magnetic attraction force. The theoretical stroke achievable with this magnet is around 4.5mm. To test the stroke, a demonstrator was designed in Solidworks, printed with the 3D printer and assembled using a single DEA. The NdFeB magnets are cylindrical with 5mm thickness and 10mm diameter.

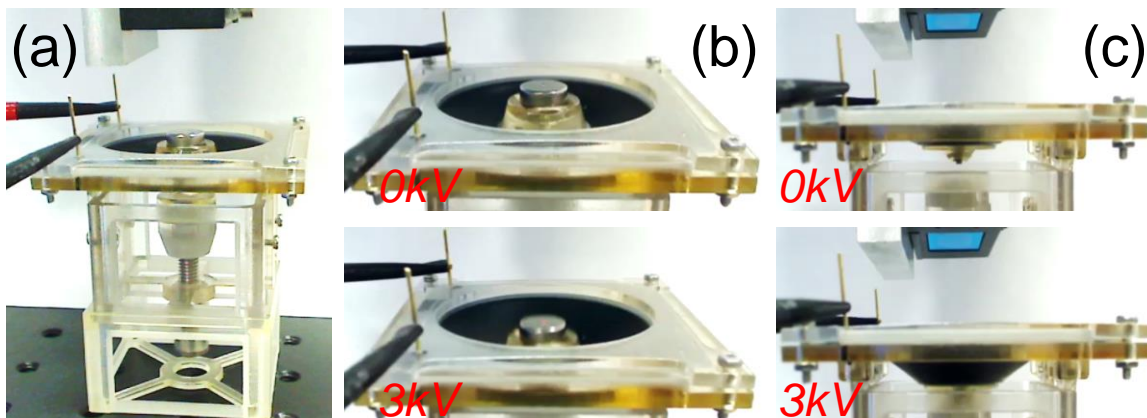


Figure B.4: Photos of magnetic bias demonstrator, (a) test setup, (b) photos capturing actuation from above, (c) and from below.

The work presented here is the first known DEA biased with magnetic attraction force. It is yet another method for biasing DEAs. Many configurations and applications can be conceptualized such as valves, pumps and miniature push-pull actuators, see Figure B.5.

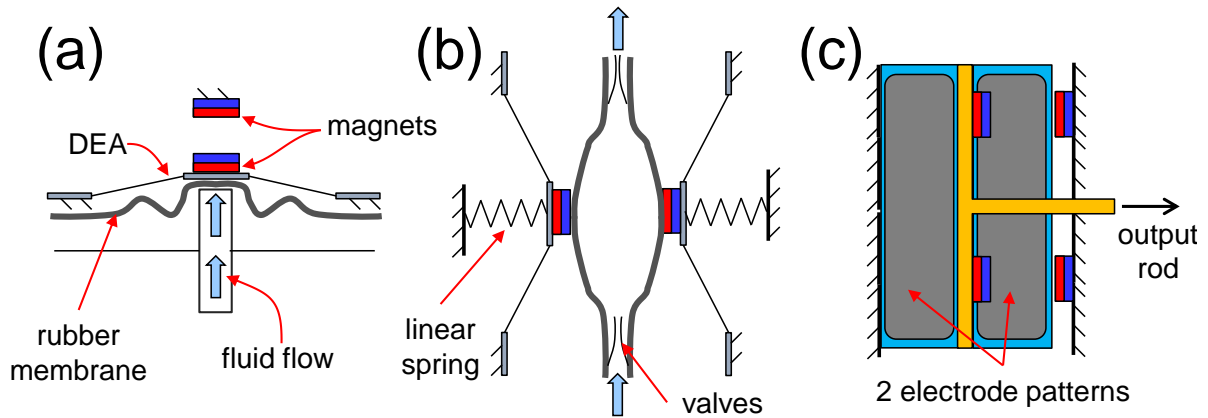


Figure B.5: Sketches of various magnetically biased DEAs such as, (a) DEA driving a fluidic valve, (b) 2-DEAs driving a diaphragm pump, (c) 2 planar DEAs configured antagonistically producing push-pull motion.

BIBLIOGRAPHY

- [1] R. E. Pelrine, R. D. Kornbluh, and J. P. Joseph, "Electrostriction of polymer dielectrics with compliant electrodes as a means of actuation," *Sensors and Actuators A: Physical*, vol. 64, no. 1, pp. 77–85, 1998.
- [2] K. Jung, K. Kim, and H. Choi, "A self-sensing dielectric elastomer actuator," *Sensors and Actuators A Phys.*, vol. 143, no. 2, pp. 343–351, May 2008.
- [3] A. York, J. Dunn, and S. Seelecke, "Systematic approach to development of pressure sensors using dielectric electro-active polymer membranes," *Smart Mater. Struct.*, vol. 22, no. 9, p. 094015, Sep. 2013.
- [4] G. Rizzello, D. Naso, A. York, and S. Seelecke, "Self-Sensing in Dielectric Electro-Active Polymer Actuator Using Linear-In-Parametes Online Estimation," in *IEEE/IES International Conference on Mechatronics*, 2015.
- [5] S. J. A. Koh, C. Keplinger, T. Li, S. Bauer, and Z. Suo, "Dielectric elastomer generators: How much energy can be converted?," *IEEE/ASME Trans. Mechatronics*, vol. 16, no. 1, pp. 33–41, 2011.
- [6] R. D. Kornbluh, R. Pelrine, H. Prahlad, A. Wong-Foy, B. McCoy, S. Kim, J. Eckerle, and T. Low, "Dielectric elastomers: Stretching the capabilities of energy harvesting," *MRS Bulletin*, vol. 37, no. 03, pp. 246–253, 12-Mar-2012.
- [7] T. G. McKay, S. Rosset, I. a Anderson, and H. Shea, "Dielectric elastomer generators that stack up," *Smart Mater. Struct.*, vol. 24, no. 1, p. 015014, Jan. 2015.
- [8] "Smart Material." [Online]. Available: https://en.wikipedia.org/wiki/Smart_material. [Accessed: 01-Jun-2015].
- [9] GM, "Chevrolet Debuts Lightweight 'Smart Material' on Corvette," *GM Pressroom*, 2013. [Online]. Available: <http://media.gm.com/media/us/en/chevrolet/news.detail.html/content/Pages/news/us/en/2013/Feb/0212-corvette.html>. [Accessed: 26-Sep-2015].
- [10] T. Calkins and W. Polt, "Not so loud," *Boeing Frontiers--Tech Talk*, 2006. [Online]. Available: http://www.boeing.com/news/frontiers/archive/2006/march/i_tt.html. [Accessed: 26-Sep-2015].
- [11] Optotune AG, "Laser speckle reducers – Overview," *Optotune AG*, 2015. [Online]. Available: <http://www.optotune.com/products/laser-speckle-reducers>. [Accessed: 26-Sep-2015].
- [12] Parker, "Artifical Muscle," 2015. [Online]. Available: <http://promo.parker.com/promotionsite/artificialmuscle/us/en/home>. [Accessed: 26-Sep-2015].
- [13] N. C. Goulbourne, M. I. Frecker, and E. Mockensturm, "Electro-Elastic Modeling of a Dielectric Elastomer Diaphragm for a Prosthetic Blood Pump," in *Proc. SPIE 5385, Smart Structures and Materials 2004: Electroactive Polymer Actuators and Devices (EAPAD)*, 2004, pp. 122–133.
- [14] J. J. Loverich, I. Kanno, and H. Kotera, "Concepts for a new class of all-polymer micropumps.," *Lab Chip*, vol. 6, no. 9, pp. 1147–1154, Sep. 2006.
- [15] F. Carpi, C. Menon, and D. De Rossi, "Electroactive Elastomeric Actuator for All-Polymer Linear Peristaltic Pumps," *IEEE/ASME Trans. Mechatronics*, vol. 15, no. 3, pp. 460–470, Jun. 2010.
- [16] P. Lotz, M. Matysek, and H. F. Schlaak, "Fabrication and Application of Miniaturized Dielectric Elastomer Stack Actuators," *IEEE/ASME Trans. Mechatronics*, vol. 16, no. 1, pp. 58–66, 2011.
- [17] L. Maffli, S. Rosset, and H. R. Shea, "Zipping dielectric elastomer actuators: characterization, design and modeling," *Smart Mater. Struct.*, vol. 22, no. 10, p. 104013, Oct. 2013.

- [18] R. Pelrine, P. Sommer-Larsen, R. D. Kornbluh, R. Heydt, G. Kofod, Q. Pei, and P. Gravesen, "Applications of Dielectric Elastomer Actuators," in *Proc. SPIE 4329, Smart Structures and Materials 2001: Electroactive Polymer Actuators and Devices*, 2001, vol. 4329, pp. 335–349.
- [19] Y.-Y. Jhong, C.-M. Huang, C.-C. Hsieh, and C.-C. Fu, "Improvement of viscoelastic effects of dielectric elastomer actuator and its application for valve devices," in *Proc. SPIE 6524, Electroactive Polymer Actuators and Devices (EAPAD)*, 2007, p. 65241Y–65241Y–9.
- [20] M. Giousouf and G. Kovacs, "Dielectric elastomer actuators used for pneumatic valve technology," *Smart Mater. Struct.*, vol. 22, no. 10, p. 104010, Oct. 2013.
- [21] R. Heydt, R. Pelrine, J. Joseph, J. Eckerle, and R. Kornbluh, "Acoustical performance of an electrostrictive polymer film loudspeaker," *J. Acoust. Soc. Am.*, vol. 107, no. 2, pp. 833–9, Feb. 2000.
- [22] T. Sugimoto, A. Ando, K. Ono, Y. Morita, K. Hosoda, D. Ishii, and K. Nakamura, "A lightweight push-pull acoustic transducer composed of a pair of dielectric elastomer films," *J. Acoust. Soc. Am.*, vol. 134, no. 5, pp. EL432–7, Nov. 2013.
- [23] R. Pelrine, R. Kornbluh, Q. Pei, S. Stanford, S. Oh, J. Eckerle, R. Full, M. Rosenthal, and K. Meijer, "Dielectric elastomer artificial muscle actuators: toward biomimetic motion," in *Proc. of SPIE 4695*, 2002, vol. 4695, pp. 126–137.
- [24] A. Wingert, M. Licher, S. Dubowsky, and M. Hafez, "Hyper-Redundant Robot Manipulators Actuated by Optimized Binary Dielectric Polymers," in *Proc. SPIE 4695, Smart Structures and Materials 2002: Electroactive Polymer Actuators and Devices (EAPAD)*, 2002, vol. 4695, p. 415.
- [25] J.-S. Plante, "Dielectric Elastomer Actuators for Binary Robotics and Mechatronics," Massachusetts Institute of Technology, Cambridge, MA, 2006.
- [26] P. Zdunich, D. Bilyk, M. MacMaster, D. Loewen, J. DeLaurier, R. Kornbluh, T. Low, S. Stanford, and D. Holeman, "Development and Testing of the Mentor Flapping-Wing Micro Air Vehicle," *J. Aircr.*, vol. 44, no. 5, pp. 1701–1711, Sep. 2007.
- [27] G.-K. Lau, H.-T. Lim, J.-Y. Teo, and Y.-W. Chin, "Lightweight mechanical amplifiers for rolled dielectric elastomer actuators and their integration with bio-inspired wing flappers," *Smart Mater. Struct.*, vol. 23, no. 2, p. 025021, Feb. 2014.
- [28] F. Carpi, G. Frediani, C. Gerboni, J. Gemignani, and D. De Rossi, "Enabling variable-stiffness hand rehabilitation orthoses with dielectric elastomer transducers," *Med. Eng. Phys.*, vol. 36, no. 2, pp. 205–11, Feb. 2014.
- [29] J. Newton, J. Morton, J. Clark, and W. S. Oates, "Modeling and Characterization of Stiffness Controlled Robotic Legs Using Dielectric Elastomers," in *Proc. of SPIE Vol. 8340*, 2012, vol. 8340, no. 850, p. 83400Z–83400Z–12.
- [30] S. Dastoor and M. Cutkosky, "Design of dielectric electroactive polymers for a compact and scalable variable stiffness device," in *2012 IEEE International Conference on Robotics and Automation*, 2012, pp. 3745–3750.
- [31] H. Kim, J. Park, N. H. Chuc, H. R. Choi, J. D. Nam, Y. Lee, H. S. Jung, and J. C. Koo, "Development of dielectric elastomer driven micro-optical zoom lens system," in *Proc. SPIE 6524, Electroactive Polymer Actuators and Devices (EAPAD)*, 2007, vol. 6524, p. 65241V–65241V–10.
- [32] C. Keplinger, M. Kaltenbrunner, N. Arnold, and S. Bauer, "Rontgen's electrode-free elastomer actuators without electromechanical pull-in instability," in *Proceedings of the National Academy of Sciences of the United States of America*, 2010, vol. 107, no. 10, pp. 4505–10.

-
- [33] F. Carpi, G. Frediani, and D. De Rossi, "Bioinspired Tunable Lens Driven by Electroactive Polymer Artificial Muscles," *Biomim. Biohybrid Syst.*, pp. 74–82, 2012.
 - [34] S. Son, D. Pugal, T. Hwang, H. R. Choi, J. C. Koo, Y. Lee, K. Kim, and J.-D. Nam, "Electromechanically driven variable-focus lens based on transparent dielectric elastomer," *Appl. Opt.*, vol. 51, no. 15, pp. 2987–96, May 2012.
 - [35] G. Jordan, D. N. McCarthy, N. Schlepple, J. Krißler, H. Schröder, and G. Kofod, "Actuated Micro-optical Submount Using a Dielectric Elastomer Actuator," *IEEE/ASME Trans. Mechatronics*, vol. 16, no. 1, pp. 98–102, 2011.
 - [36] W. C. Röntgen, "Ueber die durch Electricität bewirkten Form- und Volumenänderungen von dielectrischen Körpern," *Ann. Phys.*, vol. 247, no. 13, pp. 771–786, 1880.
 - [37] R. Pelrine, R. Kornbluh, Q. Pei, and J. Joseph, "High-speed electrically actuated elastomers with strain greater than 100," *Science (80-.).*, vol. 287, no. 5454, pp. 836–839, Feb. 2000.
 - [38] Z. Ma, J. I. Scheinbeim, J.-W. Lee, and B. A. Newman, "High Field Electrostrictive Response of Polymers," *J. Polym. Sci. Part B Polym. Phys.*, vol. 32, pp. 2721–2731, 1994.
 - [39] R. Pelrine, R. Kornbluh, J. Joseph, R. Heydt, Q. Pei, and S. Chiba, "High-field deformation of elastomeric dielectrics for actuators," *Mater. Sci. Eng. C*, vol. 11, no. 2, pp. 89–100, 2000.
 - [40] R. Heydt, R. Kornbluh, R. Pelrine, and V. Mason, "Design and Performance of an Electrostrictive-Polymer-Film Acoustic Actuator," *J. Sound Vib.*, vol. 215, no. 1998, pp. 297–311, 1998.
 - [41] Y. Bar-cohen, T. Xue, M. Shahinpoor, J. O. Simpson, and J. Smith, "Low-mass muscle actuators using electroactive polymers (EAP)," in *Proc. SPIE 3324, Smart Structures and Materials 1998: Smart Materials Technologies*, 1998, no. 3324, pp. 1–5.
 - [42] SPIE, "SPIE Smart Structures/NDE conference." [Online]. Available: <http://spie.org/conferences-and-exhibitions/smart-structuresnde>. [Accessed: 17-Dec-2015].
 - [43] EuroEAP, "EuroEAP conference." [Online]. Available: <http://www.euroeap.eu/>. [Accessed: 17-Dec-2015].
 - [44] G. Kofod, P. Sommer-Larsen, R. Kornbluh, and R. Pelrine, "Actuation Response of Polyacrylate Dielectric Elastomers," *J. Intell. Mater. Syst. Struct.*, vol. 14, no. 12, pp. 787–793, Dec. 2003.
 - [45] S. Michel, X. Q. Zhang, M. Wissler, C. Löwe, and G. Kovacs, "A comparison between silicone and acrylic elastomers as dielectric materials in electroactive polymer actuators," *Polym. Int.*, vol. 59, no. 3, pp. 391–399, Dec. 2009.
 - [46] M. Wissler and E. Mazza, "Modeling and simulation of dielectric elastomer actuators," *Smart Mater. Struct.*, vol. 14, no. 6, pp. 1396–1402, Dec. 2005.
 - [47] J. Vogan, A. Wingert, J.-S. Plante, S. Dubowsky, M. Hafez, D. Kacher, and F. Jolesz, "Manipulation in MRI devices using electrostrictive polymer actuators: with an application to reconfigurable imaging coils," in *IEEE International Conference on Robotics and Automation, 2004. Proceedings. ICRA '04. 2004*, 2004, vol. 3, no. April, pp. 2498–2504.
 - [48] J. Plante and S. Dubowsky, "On the performance mechanisms of Dielectric Elastomer Actuators," *Sensors Actuators A Phys.*, vol. 137, no. 1, pp. 96–109, Jun. 2007.
 - [49] A. York, J. Dunn, and S. Seelecke, "Experimental characterization of the hysteretic and rate-dependent electromechanical behavior of dielectric electro-active polymer actuators," *Smart Mater. Struct.*, vol. 19, no. 9, p. 094014, Sep. 2010.

- [50] L. Patrick, K. Gabor, and M. Silvain, "Characterization of dielectric elastomer actuators based on a hyperelastic film model," *Sensors Actuators A Phys.*, vol. 135, no. 2, pp. 748–757, Apr. 2007.
- [51] M. Kollosche, G. Kofod, Z. Suo, and J. Zhu, "Temporal evolution and instability in a viscoelastic dielectric elastomer," *J. Mech. Phys. Solids*, vol. 76, pp. 47–64, Dec. 2015.
- [52] M. Wissler and E. Mazza, "Modeling of a pre-strained circular actuator made of dielectric elastomers," *Sensors Actuators A Phys.*, vol. 120, no. 1, pp. 184–192, Apr. 2005.
- [53] X. Zhao, S. J. A. Koh, and Z. Suo, "Nonequilibrium Thermodynamics of Dielectric Elastomers," *Int. J. Appl. Mech.*, vol. 03, no. 2, pp. 203–217, 2011.
- [54] M. Wissler and E. Mazza, "Electromechanical coupling in dielectric elastomer actuators," *Sensors Actuators A Phys.*, vol. 138, no. 2, pp. 384–393, Aug. 2007.
- [55] C. Jean-Mistral, A. Sylvestre, S. Basrour, and J.-J. Chaillout, "Dielectric properties of polyacrylate thick films used in sensors and actuators," *Smart Mater. Struct.*, vol. 19, no. 7, p. 075019, Jul. 2010.
- [56] J. Sheng, H. Chen, B. Li, and L. Chang, "Temperature dependence of the dielectric constant of acrylic dielectric elastomer," *Appl. Phys. A*, vol. 110, no. 2, pp. 511–515, Sep. 2012.
- [57] J. Qiang, H. Chen, and B. Li, "Experimental study on the dielectric properties of polyacrylate dielectric elastomer," *Smart Mater. Struct.*, vol. 21, no. 2, p. 25006, Feb. 2012.
- [58] T. Vu-Cong, C. Jean-Mistral, and A. Sylvestre, "Impact of the nature of the compliant electrodes on the dielectric constant of acrylic and silicone electroactive polymers," *Smart Mater. Struct.*, vol. 21, no. 10, p. 105036, Oct. 2012.
- [59] P. Lochmatter, G. Kovacs, and S. Michel, "Characterization of dielectric elastomer actuators based on a hyperelastic film model," *Sensors Actuators, A Phys.*, vol. 135, no. 2, pp. 748–757, Apr. 2007.
- [60] Q. M. Zhang, H. Li, M. Poh, F. Xia, Z.-Y. Cheng, H. Xu, and C. Huang, "An all-organic composite actuator material with a high dielectric constant," *Nature*, vol. 419, no. September, pp. 284–287, 2002.
- [61] G. Gallone, F. Carpi, D. Derossi, G. Levita, and a Marchetti, "Dielectric constant enhancement in a silicone elastomer filled with lead magnesium niobate–lead titanate," *Mater. Sci. Eng. C*, vol. 27, no. 1, pp. 110–116, Jan. 2007.
- [62] F. Carpi and D. D. Rossi, "Improvement of electromechanical actuating performances of a silicone dielectric elastomer by dispersion of titanium dioxide powder," *IEEE Trans. Dielectr. Electr. Insul.*, vol. 12, no. 4, pp. 835–843, 2005.
- [63] H. C. Nguyen, V. T. Doan, J. Park, J. C. Koo, Y. Lee, J. Nam, and H. R. Choi, "The effects of additives on the actuating performances of a dielectric elastomer actuator," *Smart Mater. Struct.*, vol. 18, no. 1, p. 15006, Jan. 2009.
- [64] F. Carpi, G. Gallone, F. Galantini, and D. De Rossi, "Silicone-poly(hexylthiophene) blends as elastomers with enhanced electromechanical transduction properties," *Adv. Funct. Mater.*, vol. 18, pp. 235–241, 2008.
- [65] J. E. Quinsaat, M. Alexandru, F. Nueesch, H. Hofmann, A. Borgschulte, and D. Opris, "Highly stretchable dielectric elastomer composites containing high volume fraction of silver nanoparticles," *J. Mater. Chem. A*, pp. 14675–14685, 2015.
- [66] J. Plante and S. Dubowsky, "Large-scale failure modes of dielectric elastomer actuators," *Int. J. Solids Struct.*, vol. 43, no. 25–26, pp. 7727–7751, Dec. 2006.

-
- [67] D. De Tommasi, G. Puglisi, and G. Zurlo, "Failure modes in electroactive polymer thin films with elastic electrodes," *J. Phys. D. Appl. Phys.*, vol. 47, p. 065502, 2014.
 - [68] L. Liu, Z. Zhang, Y. Liu, and J. Leng, "Failure modeling of folded dielectric elastomer actuator," *Sci. China Physics, Mech. Astron.*, vol. 57, no. 2, pp. 263–272, 2013.
 - [69] M. Kaltenbrunner, C. Keplinger, N. Arnold, and S. Bauer, "Analysis of safe and failure mode regimes of dielectric elastomer actuators," *2008 IEEE Sensors*, no. 1, pp. 156–159, 2008.
 - [70] M. Kollosche, J. Zhu, Z. Suo, and G. Kofod, "Complex interplay of nonlinear processes in dielectric elastomers," *Phys. Rev. E*, vol. 85, no. 5, p. 051801, May 2012.
 - [71] X. Zhao and Z. Suo, "Method to analyze electromechanical stability of dielectric elastomers," *Appl. Phys. Lett.*, vol. 91, no. 6, p. 061921, 2007.
 - [72] J. Huang, S. Shian, R. M. Diebold, Z. Suo, and D. R. Clarke, "The thickness and stretch dependence of the electrical breakdown strength of an acrylic dielectric elastomer," *Appl. Phys. Lett.*, vol. 101, no. 12, p. 122905, 2012.
 - [73] D. Gatti, H. Haus, M. Matysek, B. Frohnafel, C. Tropea, and H. F. Schlaak, "The dielectric breakdown limit of silicone dielectric elastomer actuators," *Appl. Phys. Lett.*, vol. 104, no. 5, p. 052905, Feb. 2014.
 - [74] S. Akbari, S. Rosset, and H. R. Shea, "Improved electromechanical behavior in castable dielectric elastomer actuators," *Appl. Phys. Lett.*, vol. 102, no. 7, p. 071906, 2013.
 - [75] A. York and S. Seelecke, "Experimental Investigation of Temperature Effects on Dielectric Electro-Active Polymer Actuators and Sensors," in *Volume 2: Mechanics and Behavior of Active Materials; Structural Health Monitoring; Bioinspired Smart Materials and Systems; Energy Harvesting*, 2013, p. V002T02A023.
 - [76] L. Liu, W. Sun, J. Sheng, L. Chang, D. Li, and H. Chen, "Effect of temperature on the electromechanical actuation of viscoelastic dielectric elastomers," *EPL (Europhysics Lett.)*, vol. 112, no. 2, p. 27006, Oct. 2015.
 - [77] L. Maffl, S. Rosset, M. Ghilardi, F. Carpi, and H. Shea, "Ultrafast All-Polymer Electrically Tunable Silicone Lenses," *Adv. Funct. Mater.*, pp. 1–10, 2015.
 - [78] Wacker Chemie, "Elastosil Datasheet," München, Germany, 2014.
 - [79] S. Rosset and H. R. Shea, "Flexible and stretchable electrodes for dielectric elastomer actuators," *Appl. Phys. A*, vol. 110, no. 2, pp. 281–307, Feb. 2013.
 - [80] M. Kujawski, J. D. Pearse, and E. Smela, "Elastomers filled with exfoliated graphite as compliant electrodes," *Carbon N. Y.*, vol. 48, no. 9, pp. 2409–2417, Aug. 2010.
 - [81] O. A. Araromi, S. Rosset, and H. Shea, "High-resolution, large-area fabrication of compliant electrodes via laser ablation for robust, stretchable dielectric elastomer actuators and sensors," *ACS Appl. Mater. Interfaces*, p. 150722072212009, 2015.
 - [82] M. Hodgins, A. York, and S. Seelecke, "Experimental comparison of bias elements for out-of-plane DEAP actuator system," *Smart Mater. Struct.*, vol. 22, no. 9, p. 094016, Sep. 2013.
 - [83] M. Rosenthal, C. Weaber, I. Polyakov, A. Zarrabi, and P. Gise, "Designing components using SmartMOVE electroactive polymer technology," in *Proc. SPIE 6927, Electroactive Polymer Actuators and Devices (EAPAD)*, 2008, vol. 6927, pp. 692704–692704–12.
 - [84] M. Hodgins, G. Rizzello, A. York, D. Naso, and S. Seelecke, "A smart experimental technique for the optimization of dielectric elastomer actuator (DEA) systems," *Smart Mater. Struct.*, vol.

- 24, no. 9, p. 094002, Sep. 2015.
- [85] T. Töpper, F. Weiss, B. Osmani, C. Bippes, V. Leung, and B. Müller, "Siloxane-based thin films for biomimetic low-voltage dielectric actuators," *Sensors Actuators A Phys.*, vol. 233, pp. 32–41, 2015.
- [86] F. M. Weiss, T. Töpper, B. Osmani, S. Peters, G. Kovacs, and B. Müller, "Electrospraying Nanometer-Thin Elastomer Films for Low-Voltage Dielectric Actuators," *Adv. Electron. Mater.*, p. n/a–n/a, 2016.
- [87] M. Bozlar, C. Punckt, S. Korkut, J. Zhu, C. Chiang Foo, Z. Suo, and I. a. Aksay, "Dielectric elastomer actuators with elastomeric electrodes," *Appl. Phys. Lett.*, vol. 101, no. 9, p. 091907, 2012.
- [88] A. Poulin, S. Rosset, and H. R. Shea, "Printing low-voltage dielectric elastomer actuators," *Appl. Phys. Lett.*, vol. 107, no. 24, p. 244104, Dec. 2015.
- [89] M. Hodgins and S. Seelecke, "Experimental Analysis of Biasing Elements for Dielectric Electro-Active Polymers," in *Proc. SPIE 7976, Electroactive Polymer Actuators and Devices (EAPAD)*, 2011, vol. 7976, pp. 797639–797639–14.
- [90] M. Hodgins, A. York, and S. Seelecke, "Improved Force-Displacement of a Dielectric Electro-active Polymer Actuator using a Negative- Rate Bias Spring Mechanism," in *Proceedings of ACTUATOR 2012, 13th International Conference on New Actuators & 7th Exhibition on Smart Actuators and Drive Systems*, 2012.
- [91] M. Hodgins, A. York, and S. Seelecke, "Experimental Investigation of a Loaded Circular Dielectric Electro-Active Polymer Actuator Coupled to Negative-Rate Bias Spring Mechanism," in *Volume 2: Mechanics and Behavior of Active Materials; Integrated System Design and Implementation; Bio-Inspired Materials and Systems; Energy Harvesting*, 2012, p. 259.
- [92] M. Hodgins, G. Rizzello, A. York, D. Naso, and S. Seelecke, "Modeling of Actuator System Based on a Dielectric Electro-active Polymer Circular Membrane when Operating Against a Constant Loading Force," in *Proceedings of ACTUATOR 2014, 14th International Conference on New Actuators & 8th Exhibition on Smart Actuators and Drive Systems*, 2014.
- [93] M. Hodgins, G. Rizzello, A. York, and S. Seelecke, "Experimental Analysis and Validation of a Circular Dielectric Electroactive Polymer Actuator Operating Against Various Loading Conditions," in *Volume 2: Mechanics and Behavior of Active Materials; Integrated System Design and Implementation; Bioinspired Smart Materials and Systems; Energy Harvesting*, 2014, p. V002T02A011.
- [94] M. Hodgins, A. York, and S. Seelecke, "Modeling and experimental validation of a bi-stable out-of-plane DEAP actuator system," *Smart Mater. Struct.*, vol. 20, no. 9, p. 094012, Sep. 2011.
- [95] M. Hodgins, G. Rizzello, D. Naso, A. York, and S. Seelecke, "An electro-mechanically coupled model for the dynamic behavior of a dielectric electro-active polymer actuator," *Smart Mater. Struct.*, vol. 23, no. 10, p. 104006, Oct. 2014.
- [96] M. Hodgins, G. Rizzello, A. York, D. Naso, and S. Seelecke, "A smart experimental technique for the optimization of dielectric elastomer actuator (DEA) systems," *Smart Mater. Struct.*, vol. 24, no. 9, p. 094002, 2015.
- [97] R. E. Pelrine, R. D. Kornbluh, and J. P. Joseph, "Electrostriction of polymer dielectrics with compliant electrodes as a means of actuation," *Sensors and Actuators A: Physical*, vol. 64, no. 1. Elsevier, pp. 77–85, 1998.
- [98] O. a. Araromi, I. Gavrilovich, J. Shintake, S. Rosset, M. Richard, V. Gass, and H. R. Shea, "Rollable Multisegment Dielectric Elastomer Minimum Energy Structures for a Deployable Microsatellite Gripper," *IEEE/ASME Trans. Mechatronics*, 2014.

-
- [99] J. Shintake, S. Rosset, B. Schubert, S. Mintchev, D. Floreano, and H. R. Shea, "DEA for soft robotics: 1-gram actuator picks up a 60-gram egg," in *Proc. SPIE 9430, Electroactive Polymer Actuators and Devices (EAPAD)*, 2015, p. 94301S.
 - [100] M. Matysek, P. Lotz, K. Flittner, and H. F. Schlaak, "High-precision characterization of dielectric elastomer stack actuators and their material parameters," in *Proc. SPIE 6927, Electroactive Polymer Actuators and Devices (EAPAD)*, 2008, vol. 6927, pp. 692722–692722–10.
 - [101] G. Kovacs, L. Düring, S. Michel, and G. Terrasi, "Stacked dielectric elastomer actuator for tensile force transmission," *Sensors Actuators A Phys.*, vol. 155, no. 2, pp. 299–307, Oct. 2009.
 - [102] F. Carpi, C. Salaris, and D. De Rossi, "Folded dielectric elastomer actuators," *Smart Mater. Struct.*, vol. 16, no. 2, pp. S300–S305, 2007.
 - [103] J. Maas, D. Tepel, and T. Hoffstadt, "Actuator design and automated manufacturing process for DEAP-based multilayer stack-actuators," *Meccanica*, 2015.
 - [104] W. Kaal, "Dielektrische Elastomer-Stapelaktoren mit gelochten Elektroden für strukturdynamische Anwendungen," Technischen Universität Darmstadt, 2014.
 - [105] G. Kovacs, L. Düring, S. Michel, and G. Terrasi, "Stacked dielectric elastomer actuator for tensile force transmission," *Sensors Actuators, A Phys.*, vol. 155, no. 2, pp. 299–307, Oct. 2009.
 - [106] E. Validation, "Journal of Intelligent Material Systems and Structures Optimal Design of Lozenge-shaped Dielectric Elastomer," *J. Intell. Mater. Syst. Struct.*, vol. 21, no. 5, pp. 503–515, Dec. 2010.
 - [107] C. Jordi, S. Michel, G. Kovacs, and P. Ermanni, "Scaling of planar dielectric elastomer actuators in an agonist-antagonist configuration," *Sensors Actuators, A Phys.*, vol. 161, no. 1–2, pp. 182–190, Jun. 2010.
 - [108] P. Wang and A. Conn, "Elastic Cube Actuator with Six Degrees of Freedom Output," *Actuators*, vol. 4, no. 3, pp. 203–216, 2015.
 - [109] G. Berselli, R. Vertechy, M. Babic, and V. Parenti Castelli, "Dynamic modeling and experimental evaluation of a constant-force dielectric elastomer actuator," *J. Intell. Mater. Syst. Struct.*, vol. 24, no. 6, pp. 779–791, Aug. 2012.
 - [110] J.-S. Plante and S. Dubowsky, "On the properties of dielectric elastomer actuators and their design implications," *Smart Mater. Struct.*, vol. 16, no. 2, pp. S227–S236, Apr. 2007.
 - [111] Q. Pei, R. Pelrine, S. Stanford, R. Kornbluh, and M. Rosenthal, "Electroelastomer rolls and their application for biomimetic walking robots," *Synth. Met.*, vol. 135–136, pp. 129–131, Apr. 2003.
 - [112] Q. Pei, M. Rosenthal, S. Stanford, H. Prahlad, and R. Pelrine, "Multiple-degrees-of-freedom electroelastomer roll actuators," *Smart Mater. Struct.*, vol. 13, no. 5, pp. N86–N92, 2004.
 - [113] J. P. Szabo, "Fabrication of Polyurethane Dielectric Actuators," Defence R&D Canada -Atlantic, Dartmouth, NS, CA, 2005.
 - [114] G. Kovacs, P. Lochmatter, and M. Wissler, "An Arm Wrestling Robot Driven by Dielectric Elastomer Actuators," *Smart Mater. Struct.*, vol. 16, no. 2, pp. S306–S317, Apr. 2007.
 - [115] A. Rajamani, M. D. Grissom, C. D. Rahn, and Q. Zhang, "Wound Roll Dielectric Elastomer Actuators : Fabrication , Analysis , and Experiments," *IEEE/ASME Trans. Mechatronics*, vol. 13, no. 1, pp. 117–124, 2008.
 - [116] G. Berselli, G. Scirè Mammano, and E. Dragoni, "Design of a Dielectric Elastomer Cylindrical Actuator With Quasi-Constant Available Thrust: Modelling Procedure and Experimental

- Validation," *J. Mech. Des.*, no. c, Aug. 2014.
- [117] K. Tadakuma, L. M. Devita, J. S. Plante, Y. Shaoze, and S. Dubowsky, "The Experimental Study of a Precision Parallel Manipulator with Binary Actuation: With Application to MRI Cancer Treatment," in *Proceedings - IEEE International Conference on Robotics and Automation*, 2008, pp. 2503–2508.
- [118] H. Wang, J. Zhu, and K. Ye, "Simulation, experimental evaluation and performance improvement of a cone dielectric elastomer actuator," *J. Zhejiang Univ. Sci. A*, vol. 10, no. 9, pp. 1296–1304, Sep. 2009.
- [119] M. Hodgins and S. Seelecke, "Mechanical behavior of a bi-stable negative-rate bias spring system," in *Proc. SPIE 7644, Behavior and Mechanics of Multifunctional Materials and Composites*, 2010, p. 76442H.
- [120] G. Berselli, R. Vertechy, G. Vassura, and V. Parenti-Castelli, "Optimal Synthesis of Conically Shaped Dielectric Elastomer Linear Actuators: Design Methodology and Experimental Validation," *IEEE/ASME Trans. Mechatronics*, vol. 16, no. 1, pp. 67–79, 2011.
- [121] P. Chouinard and J. S. Plante, "Bistable antagonistic dielectric elastomer actuators for binary robotics and mechatronics," in *IEEE/ASME Transactions on Mechatronics*, 2012, vol. 17, no. 5, pp. 857–865.
- [122] H. Godaba, C. C. Foo, Z. Q. Zhang, B. C. Khoo, and J. Zhu, "Giant voltage-induced deformation of a dielectric elastomer under a constant pressure," *Appl. Phys. Lett.*, vol. 112901, 2014.
- [123] M. Wissler and E. Mazza, "Mechanical behavior of an acrylic elastomer used in dielectric elastomer actuators," *Sensors Actuators A Phys.*, vol. 134, no. 2, pp. 494–504, Mar. 2007.
- [124] C. Keplinger, M. Kaltenbrunner, N. Arnold, and S. Bauer, "Capacitive extensometry for transient strain analysis of dielectric elastomer actuators," *Appl. Phys. Lett.*, vol. 92, no. 19, p. 192903, 2008.
- [125] S. Rosset, B. M. O'Brien, T. Gisby, D. Xu, H. R. Shea, and I. a Anderson, "Self-sensing dielectric elastomer actuators in closed-loop operation," *Smart Mater. Struct.*, vol. 22, no. 10, p. 104018, Oct. 2013.
- [126] J. Biggs, K. Danielmeier, J. Hitzbleck, J. Krause, T. Kridl, S. Nowak, E. Orselli, X. Quan, D. Schapeler, W. Sutherland, and J. Wagner, "Electroactive polymers: developments of and perspectives for dielectric elastomers.,," *Angew. Chem. Int. Ed. Engl.*, vol. 52, no. 36, pp. 9409–21, Sep. 2013.
- [127] K. Yuse, D. Guyomar, D. Audigier, A. Eddiai, M. Meddad, and Y. Boughaleb, "Adaptive control of stiffness by electroactive polyurethane," *Sensors Actuators A Phys.*, vol. 189, pp. 80–85, Jan. 2013.
- [128] R. Vertechy, M. Fontana, G. Stiubianu, and M. Cazacu, "Open-access dielectric elastomer material database," in *Proc. SPIE 9056, Electroactive Polymer Actuators and Devices (EAPAD)*, 2014, vol. 9056, p. 90561R.
- [129] Q. M. Zhang, J. Su, C. H. Kim, R. Ting, and R. Capps, "An experimental investigation of electromechanical responses in a polyurethane elastomer," *J. Appl. Phys.*, vol. 81, no. 1997, p. 2770, 1997.
- [130] R. Kaltseis, C. Keplinger, S. J. Adrian Koh, R. Baumgartner, Y. F. Goh, W. H. Ng, A. Kogler, A. Tröls, C. C. Foo, Z. Suo, and S. Bauer, "Natural rubber for sustainable high-power electrical energy generation," *RSC Adv.*, vol. 4, p. 27905, 2014.

-
- [131] G. Rizzello, M. Hodgins, D. Naso, A. York, and S. Seelecke, "Modeling of the effects of the electrical dynamics on the electromechanical response of a DEAP circular actuator with a mass-spring load," *Smart Mater. Struct.*, vol. 24, no. 9, p. 094003, Sep. 2015.
 - [132] E. Biddiss and T. Chau, "Dielectric elastomers as actuators for upper limb prosthetics: challenges and opportunities," *Med. Eng. Phys.*, vol. 30, no. 4, pp. 403–418, May 2008.
 - [133] O. Pabst, E. Beckert, J. Perelaer, U. S. Schubert, R. Eberhardt, and A. Tünnermann, "All inkjet-printed electroactive polymer actuators for microfluidic lab-on-chip systems," in *Proc. SPIE 8687, Electroactive Polymer Actuators and Devices (EAPAD)*, 2013, vol. 8687, p. 86872H.
 - [134] S. Hau, A. York, and S. Seelecke, "Rapid Prototyping and Characterization of Circular Dielectric Electro-Active Polymers (DEAP) With Different Geometries," *ASME 2014 Conf. Smart Mater. Adapt. Struct. Intell. Syst.*, p. V002T02A004, 2014.
 - [135] A. York, M. Hodgins, and S. Seelecke, "Electro-Mechanical Analysis of a Biased Dielectric EAP Actuator," in *ASME 2009 Conference on Smart Materials, Adaptive Structures and Intelligent Systems (SMASIS2009)*, pp. 1–9.
 - [136] N. Hu and R. Burgueño, "Buckling-induced smart applications: recent advances and trends," *Smart Mater. Struct.*, vol. 24, no. 6, p. 063001, 2015.
 - [137] H. W. H. Wang and C. L. C. Li, "A Linear Dielectric EAP Actuator with Large Displacement Output," *2009 Int. Conf. Meas. Technol. Mechatronics Autom.*, vol. 1, pp. 73–76, Apr. 2009.
 - [138] G. Berselli, R. Vertechy, G. Vassura, and V. P. Castelli, "A Compound-Structure Frame for Improving the Performance of a Dielectric Elastomer Actuator," in *Advances in Robot Kinematics: Analysis and Design*, Springer Netherlands, 2008, pp. 291–299.
 - [139] J. R. Heim, I. Polyakov, A. Zarrabi, and O. Hui, "Electroactive polymer transducers biased for increased output," US7492076 B2.2009.
 - [140] J. D. Vogan, "Development of Dielectric Elastomer Actuators for MRI Devices," MIT, 2004.
 - [141] G. Berselli, R. Vertechy, G. Vassura, and V. P. Castelli, "Design of a linear dielectric elastomer actuator of conical shape with quasi-constant available thrust," in *2009 International Conference on Intelligent Engineering Systems*, 2009, pp. 89–94.
 - [142] A. Wingert, M. D. Lichter, and S. Dubowsky, "On the design of large degree-of-freedom digital mechatronic devices based on bistable dielectric elastomer actuators," *IEEEASME Trans. Mechatronics*, vol. 11, no. 4, pp. 448–456, 2006.
 - [143] G. Scire Mammano and E. Dragoni, "Elastic compensation of linear shape memory alloy actuators using compliant mechanisms," *J. Intell. Mater. Syst. Struct.*, vol. 25, no. 9, pp. 1124–1138, 2013.
 - [144] J.-S. Plante, L. M. Devita, and S. Dubowsky, "A Road to Practical Dielectric Elastomer Actuators Based Robotics and Mechatronics: Discrete Actuation," in *Proc. SPIE 6524, Electroactive Polymer Actuators and Devices (EAPAD)*, 2007, vol. 6524, pp. 652406–652406–15.
 - [145] C. Jordi, "Biomimetic airship driven by dielectric elastomer actuators," ETH Zurich, 2011.
 - [146] Y.-H. Chen and C.-C. Lan, "An Adjustable Constant-Force Mechanism for Adaptive End-Effector Operations," *J. Mech. Des.*, vol. 134, no. 3, p. 031005, 2012.
 - [147] G. Rizzello, D. Naso, B. Turchiano, and S. Seelecke, "Robust Position Control of Dielectric Elastomer Actuators Based on LMI Optimization," *IEEE Trans. Control Syst. Technol.*, pp. 1–13, 2016.

- [148] Engineers Edge LLC, "Electric Motor Definitions and Terminology," www.engineersedge.com, 2015. [Online]. Available: http://www.engineersedge.com/motors/motors_definitions.htm. [Accessed: 22-Dec-2015].
- [149] F. Carpi, I. Anderson, S. Bauer, G. Frediani, G. Gallone, M. Gei, C. Graaf, C. Jean-Mistral, W. Kaal, G. Kofod, M. Kollosche, R. Kornbluh, B. Lassen, M. Matysek, S. Michel, S. Nowak, B. O'Brien, Q. Pei, R. Peltz, B. Rechenbach, S. Rosset, and H. Shea, "Standards for dielectric elastomer transducers," *Smart Mater. Struct.*, vol. 24, no. 10, p. 105025, 2015.
- [150] J. Zhu, M. Kollosche, T. Lu, G. Kofod, and Z. Suo, "Two types of transitions to wrinkles in dielectric elastomers," *Soft Matter*, vol. 8, no. 34, p. 8840, 2012.
- [151] H. Stoyanov, M. Kollosche, S. Risso, R. Waché, and G. Kofod, "Soft conductive elastomer materials for stretchable electronics and voltage controlled artificial muscles," *Adv. Mater.*, vol. 25, no. 4, pp. 578–83, Jan. 2013.
- [152] B. Kussmaul, S. Risso, G. Kofod, R. Waché, M. Wegener, D. N. McCarthy, H. Krüger, and R. Gerhard, "Enhancement of dielectric permittivity and electromechanical response in silicone elastomers: Molecular grafting of organic dipoles to the macromolecular network," *Adv. Funct. Mater.*, vol. 21, pp. 4589–4594, 2011.
- [153] Y. Wang, B. Chen, Y. Bai, H. Wang, and J. Zhou, "Actuating dielectric elastomers in pure shear deformation by elastomeric conductors," *Appl. Phys. Lett.*, vol. 104, no. 6, p. 064101, Feb. 2014.
- [154] G. Yang, G. Yao, W. Ren, G. Akhras, J. P. Szabo, B. K. Mukherjee, and N. Scotia, "The strain response of silicone dielectric elastomer actuators," in *Smart Structures and Materials 2005: Electroactive Polymer Actuators and Devices*, 2005, vol. 143, pp. 134–143.
- [155] B. Kim, Y. Park, J. Kim, S. M. Hong, and C. M. Koo, "Measuring true electromechanical strain of electroactive thermoplastic elastomer gels using synchrotron SAXS," *J. Polym. Sci. Part B Polym. Phys.*, vol. 48, no. 22, pp. 2392–2398, 2010.
- [156] R. Moser, "Plastic tests Plastics: A LEGO® Tensometer for Electromechanical Characterization of Dielectric Elastomers," Johannes Kepler Universität Linz, 2013.
- [157] G. Kofod, "The static actuation of dielectric elastomer actuators: how does pre-stretch improve actuation?," *J. Phys. D. Appl. Phys.*, vol. 41, no. 21, p. 215405, Nov. 2008.
- [158] J. P. Szabo, R. S. Underhill, M. Rawji, and I. A. Keough, "Effect of Pre-Strain on the Dielectric and Dynamic Mechanical Properties of HSIII Silicone," Defence R&D Canada - Atlantic, Dartmouth NS (CAN), 2006.
- [159] B. Li, H. Chen, J. Qiang, S. Hu, Z. Zhu, and Y. Wang, "Effect of mechanical pre-stretch on the stabilization of dielectric elastomer actuation," *Journal of Physics D: Applied Physics*, vol. 44, no. 15, p. 155301, 20-Apr-2011.
- [160] H. Stoyanov, P. Brochu, X. Niu, C. Lai, S. Yun, and Q. Pei, "Long lifetime, fault-tolerant freestanding actuators based on a silicone dielectric elastomer and self-clearing carbon nanotube compliant electrodes," *RSC Adv.*, vol. 3, no. 7, p. 2272, 2013.
- [161] B. Fasolt, M. Hodgins, and S. Seelecke, "Characterization of screen-printed electrodes for Dielectric Elastomer (DE) membranes: influence of screen dimensions and electrode thickness on actuator performance," in *Proc. SPIE 9798, Electroactive Polymer Actuators and Devices (EAPAD)*, 2016, p. 97983E.
- [162] T. Schmidt, J. Tyson, and K. Galanulis, "Full-Field Dynamic Displacement and Strain Measurement Using Advanced 3D Image Operation Dynamic Displacement," *Exp. Tech.*, no. June, pp. 47–50, 2003.

-
- [163] V. Nayyar, K. Ravi-Chandar, and R. Huang, "Stretch-induced wrinkling of polyethylene thin sheets: Experiments and modeling," *Int. J. Solids Struct.*, vol. 51, no. 9, pp. 1847–1858, 2014.
 - [164] A. Poulin, S. Rosset, and H. Shea, "Fully printed 3 microns thick dielectric elastomer actuator," in *Proc. SPIE 9798, Electroactive Polymer Actuators and Devices (EAPAD)*, 2016, p. 97980L.
 - [165] T.-G. La and G.-K. Lau, "Inhibiting electro-thermal breakdown of acrylic dielectric elastomer actuators by dielectric gel coating," *Appl. Phys. Lett.*, vol. 108, no. 1, p. 012903, 2016.
 - [166] G. Rizzello, D. Naso, A. York, and S. Seelecke, "Closed loop control of dielectric elastomer actuators based on self-sensing displacement feedback," *Smart Mater. Struct.*, vol. 25, no. 3, p. 035034, Mar. 2016.
 - [167] J. Beharic, T. M. Lucas, and C. K. Harnett, "Analysis of a Compressed Bistable Buckled Beam on a Flexible Support," *J. Appl. Mech.*, vol. 81, no. 8, p. 081011, Jun. 2014.

CURRICULUM VITAE

Micah Hodgins

Roonstraße 19, D-76137, Karlsruhe, Germany

Email: micah.hodgins@gmail.com

SUMMARY

Internationally-experienced American engineer completing doctorate in Germany and seeking to join an R&D team full time, as a mechatronics and/or new product development engineer. Strong R&D background with extensive hands-on experience with prototyping, smart materials, LabVIEW, MATLAB and SolidWorks.

EDUCATION

<i>Doctor of Engineering (Dr.-Ing.) in Mechatronics</i>	09/2016 (Expected)
Universität des Saarlandes	Saarbrücken, Saarland, Germany
<i>Master of Science in Mechanical Engineering</i>	12/2010
North Carolina State University	Raleigh, North Carolina, USA
▪ Magna Cum Laude (GPA: 3.7/4.0)	
<i>Bachelor of Science in Mechanical Engineering</i>	05/2008
University of South Carolina	Columbia, South Carolina, USA
▪ Summa Cum Laude (GPA: 3.97/4.0)	

EMPLOYMENT

<i>Doctoral Researcher/Scientific Associate</i> (40hrs/week)	01/2011 – 06/2016
Universität des Saarlandes	Saarbrücken, Saarland, Germany
<ul style="list-style-type: none"> ▪ Designed and fabricated DEA prototypes/demonstrators to customer requirements in cleanroom environment ▪ Designed and performed novel tests to electro-mechanically characterize dielectric elastomers actuators (DEAs) ▪ Presented work to other engineers at Universität des Saarlandes and conferences in Europe and North America ▪ Wrote and published six peer-reviewed articles on research findings ▪ Operated and maintained 3D printer (Objet500 Connex) on a regular basis ▪ Facilitated practicum lab sessions for students using German language 	
<i>Teaching Assistant-Dynamic Systems and Controls Lab</i> (20 hrs/week)	
08/2008 - 12/2010	
North Carolina State University	
Raleigh, North Carolina, USA	

<i>Teaching Assistant-Dynamic Systems and Controls Lab</i> (20 hrs/week)	08/2008 - 12/2010
North Carolina State University	Raleigh, North Carolina, USA
<ul style="list-style-type: none"> ▪ Taught approximately 36 students each semester, had regular office hours, and graded all technical lab reports ▪ Demonstrated to students concepts of Newton's Laws, vibrations, and fundamentals of PID control 	

- Supervised labs groups learning analog PID circuit design, LabView control, and introduction to microprocessors

Graduate Student Researcher (20 hrs/week) 08/2008 - 12/2010
North Carolina State University Raleigh, North Carolina, USA

- Tested smart materials using custom LabView code
- Statistically analyzed data to draw conclusions on key performance parameters
- Presented research results through technical posters, conference papers, and group presentations

Electro-Mechanical Machine Technician (40 hrs/week) 05/2008 - 8/2008
REI Automation Columbia, South Carolina, USA

- Fabricated and assembled metal machine structures according to engineering design in a hands-on setting
- Routed electrical wiring and pneumatic hoses to sensors and actuators
- Tuned and performed machine quality tests for customers in the nuclear power industry

Manufacturing Engineer (40hrs/week) 05/2007 - 8/2007
Cummins Turbo Technologies Charleston, South Carolina, USA

- Revised and improved process documentation at machines
- and fabricated “shadow boxes” at machining stations to reduce change over time and improve accuracy
- Performed machine capability studies in machining area resulting in cost savings

Structural Design Engineer (40 hrs/week) 05/2006 - 8/2006
Gulfstream Aerospace Corporation Savannah, Georgia, USA

- Improved the bulkhead and frame design in CATIA V5 based on current configuration
- Interfaced with stress analysis staff for formulation of preliminary design
- Catalogued current manufacturing process flow to determine impacts of new design

ADDITIONAL INFORMATION

Honors and Qualifications

- Honor Societies: Tau Beta Pi, Pi Tau Sigma, and Golden Key
- Scholarships: SC LIFE, SC State Fair, Lewis M. Caswell M.E., Dewy Campbell, and Abney Foundation
- Completion of FE exam

Qualities and Skills

Personal Qualities

- Superior work ethic
- Excellent interpersonal and organizational skills
- Detail-oriented, with a proven ability to multi-task

Language Skills

- English: native speaker
- German: good general and conversational knowledge

Computer Skills

- LabVIEW, MATLAB, SolidWorks, CATIA (v5)
- Excel, Word, PowerPoint, Inkscape

Volunteer Activities

- ESL volunteer/teacher
- NCSU international student orientation volunteer and group leader
- Raleigh Convoy of Hope volunteer
- Children and youth event volunteer in Germany

Interests and Hobbies

- Biking, basketball, inline skating and running
- Internationalism, cultures, worldviews and hosting guests
- Acoustic guitar
- Nature and being outdoors

